Improved identification of illicit materials using an X-ray backscattering technique

A thesis submitted to the University of Manchester for the degree of
Doctor of Philosophy in the Faculty of Science and Engineering

2021

Sarah L. Fisher

Department of Physics and Astronomy in the School of Natural Sciences
The University of Manchester

This page is intentionally left blank.

Contents

Abbreviations **9**

Declaration of Authorship **13**

Copyright Statement **14**

Acknowledgements **15**

1 Introduction **17**

2 Theory of x-ray imaging **21**

- 2.1 Generating x-rays . . . 21
  - 2.1.1 X-ray interactions . . . 22
    - 2.1.1.1 Bremsstrahlung emission . . . 22
    - 2.1.1.2 Characteristic x-ray emission . . . 23
    - 2.1.1.3 Auger emission . . . 24
  - 2.1.2 Example x-ray tube output spectrum . . . 24
  - 2.1.3 X-ray tube target design . . . 25
    - 2.1.3.1 Reflection target . . . 25
    - 2.1.3.2 Transmission target . . . 26
- 2.2 Photon-matter interactions . . . 26
  - 2.2.1 Photo-electric absorption . . . 26
  - 2.2.2 Compton scattering . . . 28
  - 2.2.3 Coherent scattering . . . 29
- 2.3 Photon-matter interactions in x-ray imaging . . . 30
  - 2.3.1 Transmitted intensity, I_T . . . 31
  - 2.3.2 Backscattered intensity, I_S . . . 32
  - 2.3.3 Effective atomic number definition . . . 33
  - 2.3.4 Effective atomic number and density relations . . . 33
  - 2.3.5 Energy dependence of I_S . . . 33
  - 2.3.6 Empirical fits for I_S, ρ and Z . . . 36
  - 2.3.7 Sample thickness dependence on I_S . . . 38
- 2.4 X-ray detectors . . . 39
  - 2.4.1 Semi-conductor detectors . . . 40
    - 2.4.1.1 Cadmium telluride and CZT . . . 41
  - 2.4.2 Scintillation detectors . . . 42

3 Backscatter imaging systems **45**
3.1 Image acquisition 45
3.2 Detector material and signal processing 46
3.3 Commercial systems 48
3.4 Example backscatter image 48

4 The energy spectrum reconstruction method **51**
4.1 Theory of inverse problems 51
  4.1.1 Finding the least squares solution 52
4.2 Tikhonov regularisation 54
  4.2.1 The L-curve method 55
  4.2.2 Morozov's discrepancy principle 56
  4.2.3 Evaluating errors in the Tikhonov solution 56
4.3 Spectrum reconstruction as an inverse problem 57
4.4 Choice of filters 59
4.5 Correcting for experimental effects (RCF) 60
4.6 Tikhonov regularisation for spectrum reconstruction 61
  4.6.1 δ parameter 61
  4.6.2 Non-negativity constraint 61
4.7 Behaviour of Tikhonov solutions 62
  4.7.1 Intrinsic errors 62
  4.7.2 Error parameter 64
  4.7.3 Stability 66
4.8 Other reconstruction methods 68
4.9 Chapter summary 69

5 Experimental approach **71**
5.1 Equipment 71
5.2 X-ray tube characterisation 72
  5.2.1 X-ray tube output spectrum 72
5.3 CdTe detector characterisation 76
  5.3.1 CdTe detector energy calibration 76
  5.3.2 CdTe energy resolution 76
  5.3.3 CdTe detector stability 78
5.4 Backscatter set-up 80
5.5 Measurements 83
  5.5.1 Example spectrum 84
  5.5.2 Calculating the detector response 85
5.6 Filters 86
  5.6.1 Filter manufacture 86
5.7 System calibration 87
5.8 Chapter summary 90

6 Simulation design **91**
6.1 Monte Carlo simulation theory 91
6.2 Geant4 simulation software 92
6.3 Simulation of materials in Geant4 93

6.4 Full geometry simulation . . . 93
6.4.1 Geometry details . . . 94
6.4.2 X-ray source simulation . . . 96
6.4.3 Detector simulation . . . 96
6.4.4 Energy spectrum validation . . . 96
6.4.4.1 Spectrum comparisons . . . 97
6.4.4.2 Analysis of spectral differences . . . 99
6.4.5 Simulation method . . . 100
6.4.5.1 Case 1: Testing the reconstruction method on additional materials . . . 101
6.4.5.2 Case 2: Investigation of systematic errors . . . 103
6.5 Simple simulation . . . 103
6.5.1 Simple simulation geometry . . . 104
6.5.2 Simple simulation validation . . . 105
6.5.3 Case 1: Use in RCF method . . . 105
6.5.4 Case 2: Use in understanding Tikhonov solutions . . . 106
6.6 Chapter summary . . . 106

7 Results 107
7.1 Note on spectra and comparison metrics . . . 107
7.2 Experimental detector response . . . 108
7.3 Experimental filtered detector response . . . 109
7.4 Experimental energy spectrum reconstructions . . . 110
7.4.1 HDPE reconstruction . . . 111
7.4.2 PVC reconstruction . . . 113
7.5 Comparison of simulation and experiment reconstructions . . . 114
7.5.1 HDPE . . . 114
7.5.2 POM, PVDF and PTFE . . . 116
7.5.3 PVC . . . 116
7.6 Determining material properties . . . 116
7.6.1 Density and C9 . . . 117
7.6.2 Effective atomic number and C3 . . . 119
7.7 Categorisation of explosive materials . . . 122
7.7.1 Explosive percentage likelihood . . . 123
7.7.2 Categorisation of experimentally tested materials . . . 123
7.7.3 General method performance . . . 124
7.8 Calculating atomic number and density . . . 124
7.9 Chapter summary . . . 127

8 Systematic error quantification 129
8.1 Static (non time-varying) systematic errors . . . 129
8.2 Simulations for investigating systematic errors . . . 130
8.2.1 Simulation I and II: x-ray tube alignment . . . 132
8.2.2 Simulation III and IV: Filter thickness . . . 132
8.2.3 Simulation V: Filter B thickness . . . 133
8.2.4 Simulation VI: Calibration material . . . 133
8.3 RCF response to systematic errors . . . 134

8.4 Reconstruction, Z_{eff} and ρ response to systematic errors . . . 135
8.4.1 Simulation I and II: x-ray tube alignment . . . 136
8.4.2 Simulation III and IV: Filter thickness . . . 136
8.4.3 Simulation V: Filter B thickness . . . 138
8.4.4 Simulation VI: Calibration material . . . 138
8.5 Summary and recommendations for static systematic errors . . . 138
8.6 Time varying systematic errors . . . 139
8.7 Chapter summary . . . 141

9 Discussion 143
9.1 Perspectives . . . 143
9.2 Reconstruction model . . . 146
9.2.1 Attenuation coefficient sampling . . . 146
9.2.2 Choice of filter thickness . . . 147
9.3 Reconstruction method choice . . . 150
9.4 Simulation input x-ray spectrum . . . 152
9.5 Measurements with higher energy beams . . . 152
9.6 Accounting for the sample thickness . . . 155
9.7 Material shielding effects . . . 156
9.8 Source-to-object and object-to-detector distances . . . 156
9.9 Scaling up to a field backscatter system . . . 156
9.10 Summary and recommendations . . . 157

10 Proposed future experiments and development 159
10.1 200 kV test system . . . 159
10.2 Multi-detector test on an M60 system . . . 161
10.3 Detector development . . . 162

11 Conclusions 163

Appendices 165

A Simulation validation by spectrum comparison 165
A.1 POM . . . 166
A.2 HDPE . . . 168
A.3 Nylon . . . 170
A.4 PVC . . . 172

B Experiment CdTe spectra and response measurements 175
B.1 HDPE . . . 176
B.2 POM . . . 178
B.3 PVC . . . 180
B.4 PVDF . . . 182
B.5 PTFE . . . 184
B.6 Nylon . . . 186
B.7 Acrylic . . . 188

C Experiment reconstruction data 191

Bibliography **193**

Final word count: 45,210 words

Abbreviations

Gadox	Gadolinium oxysulphide (scintillator material)
PVT	Polyvinyltoluine (scintillator material)
CsI	Cesium iodide (scintillator material)
CdTe	Cadmium telluride (semi-conductor detector material)
SNR	Signal-to-noise ratio ($\mathrm{SNR} = \mathrm{signal/error}$)
HDPE	High-density polyethylene (plastic)
POM	Polyoxymethylene (plastic)
PVDF	Polyvinylidene-fluoride (plastic)
PTFE	Polytetrafluoroethylene (a.k.a Teflon) (plastic)
PVC	Polyvinylchloride
TNT	Trinitrotoluene (explosive material)
RDX	Research department explosive or Royal demolition explosive (explosive material)
PETN	Pentaerythritol tetranitrate (explosive material)
PVA	Polyvinyl acetate (plastic)
PTFCE	Polychlorotrifluoroethylene (plastic)
C3	Number of counts between 10 and 15 keV in energy spectrum reconstructions
C9	Number of counts between 40 and 45 keV in energy spectrum reconstructions
RCF	Response correction factor (also referred to as α)
FWHM	Full width at half maximum height of Gaussian distribution
FG	Full geometry simulation
SG	Simple geometry simulation

This page is intentionally left blank.

Abstract

X-ray backscatter imaging has revolutionised screening procedures at security checkpoints across the world. It is used to acquire detailed x-ray images of the inside of vehicles and cargo in real time. Security personnel use these images to detect concealed illicit materials such as drugs, explosives and currency. However one downside to the technique is the limited ability to identify materials. Materials can only be classified as either organic or inorganic. As a result many unnecessary manual searches of vehicles and cargo are performed due to items being falsely identified as contraband. This causes extensive delays and reduced throughput at ports. Improved identification of illicit materials is needed to solve this issue.

This thesis describes the development of a technique to improve material identification in x-ray backscatter imaging. The problem with current backscatter systems is that no energy spectrum information can be measured by the x-ray detectors and energy spectrum information is critical to better material identification. The method presented involved taking several detector response measurements of a backscatter beam, each with a different amount of detector filtration. An approximate energy spectrum was calculated from the response measurements by a process known as "spectrum reconstruction" or "spectrum unfolding". The idea was tested in a proof-of-concept study using a 50 keV x-ray beam and five plastic test samples, including two explosive simulants.

Monte Carlo simulations were used to derive relationships between properties of the reconstructed spectrum, effective atomic number (Z_{eff}) and density (ρ). The Z_{eff} and ρ properties were calculated for the experimentally tested materials to within 0.5Z_{eff} and 0.12 $\mathrm{g\,cm^{-3}}$ of the true value. In the explosives material range this was improved to 0.1Z_{eff} and 0.04 $\mathrm{g\,cm^{-3}}$. This was a substantial improvement on the organic/inorganic separation currently achievable on commercial systems. The simulation results were also used to classify materials as explosive or inert. The two explosive simulant materials were correctly identified with a higher than 95% probability. Further analysis of simulated data suggested an up to 100% true positive detection rate and 7% false positive detection rate was possible using the technique.

A particular success of the method over other techniques proposed in the literature is that it does not rely on energy-resolving detectors, and therefore offers a cheaper and more practical solution for commercial systems. Work has started to test the technique using a 200 keV x-ray beam. Future work will focus on validation of the technique for cargo imaging.

Declaration of Authorship

I, Sarah L. Fisher , confirm that no portion of the work referred to in the thesis has been submitted in support of an application for another degree or qualification of this or any other university or other institute of learning.

Copyright statement

i. The author of this thesis (including any appendices and/or schedules to this thesis) owns certain copyright or related rights in it (the "Copyright") and s/he has given the University of Manchester certain rights to use such Copyright, including for administrative purposes. ii. Copies of this thesis, either in full or in extracts and whether in hard or electronic copy, may be made only in accordance with the Copyright, Designs and Patents Act 1988 (as amended) and regulations issued under it or, where appropriate, in accordance with licensing agreements which the University has from time to time. This page must form part of any such copies made. iii. The ownership of certain Copyright, patents, designs, trademarks and other intellectual property (the "Intellectual Property") and any reproductions of copyright works in the thesis, for example graphs and tables ("Reproductions"), which may be described in this thesis, may not be owned by the author and may be owned by third parties. Such Intellectual Property and Reproductions cannot and must not be made available for use without the prior written permission of the owner(s) of the relevant Intellectual Property and/or Reproductions. iv. Further information on the conditions under which disclosure, publication and commercialisation of this thesis, the Copyright and any Intellectual Property and/or Reproductions described in it may take place is available in the University IP Policy (see http://documents.manchester.ac.uk/DocuInfo.aspx?DocID=24420), in any relevant Thesis restriction declarations deposited in the University Library, the University Library's regulations (see http://www.library.manchester.ac.uk/about/regulations/) and in the University's policy on Presentation of Theses.

Acknowledgements

The work in this thesis would have not be possible without the support of many people. Firstly I would like to thank my supervisors Dr Dave Cullen and Dr Mark Procter for the opportunity to pursue this PhD, and for your support and guidance throughout the research and in the preparation of this thesis. I am grateful to STFC and industrial partner Rapiscan Systems for the funding support through the iCASE PhD studentship award under grant proposal ST/N00275X/1, and granting additional funding throughout the 2020 pandemic to allow the research to continue to completion.

Thank you to Dave Johnson at Rapiscan Systems for your help and patience with setting up the experiment, and to Colin Read at the University of Manchester for assisting with the design and 3D printing of the apparatus. Thanks to the PhD students in the Nuclear physics department for your support and friendship. Thanks to Mike Mallaburn for your guidance in the development of the spectrum reconstruction method and to James, Mike and Anthony at Rapiscan for your help with the experimental work.

Last but not least, thanks to my family and to Jacob. Without your support I can truly say I would have not got to where I am now.

Sarah Fisher
Home office, Woking
September 2021

Chapter 1

Introduction

X-ray imaging security systems have in recent years become part of everyday life. Airports, postal services, ports and some event venues all utilise x-ray technology to quickly and accurately detect threats and illegal activity. X-ray imaging involves using x-rays to create images of the inside of objects that are otherwise opaque, such as luggage, packages, vehicles and cargo. The x-ray images can be used to detect suspicious contents that would be otherwise concealed and go unnoticed. X-ray systems are an extremely efficient way of enforcing security protocols and are safer and more effective at detecting threats than traditional manual search methods.

The focus of this thesis is on one x-ray imaging technique called x-ray backscatter imaging. In x-ray backscatter imaging an x-ray beam is fired at the object of interest and the x-ray beam that scatters back off the surface of the object is recorded to create a greyscale image of the object interior. The intensity scattered beam is measured which corresponds to a particular greyscale level in the image. The idea was originally proposed in 1981 by B. C. Towe and A. M. Jacobs [1] and medical and non-destructive testing applications of the technique were soon realised [2, 3]. Nowadays x-ray backscatter imaging has a wide variety of uses from aerospace to petroleum engineering [4–8] (for example), as well as the focus of this work, imaging of vehicles and cargo for detection of contraband [9–11].

Backscatter imaging is typically a low-dose imaging technique, making it ideal for scanning vehicles such as trucks as it means drivers receive minimal radiation dose. Also backscatter imaging is used where space is tight, or for making portable inspection systems, as the object only needs to be accessible from one side. Backscatter imaging systems are best for imaging organic materials, including illicit materials such as explosives, narcotics and currency. This is because of the high scatter probability of low energy x-rays ($<$200 keV) from organic materials compared to inorganic materials such as metals. Hence x-ray backscatter imaging systems are used at ports and security checkpoints across the world to detect organic contraband material.

The images produced by backscatter systems are photographic in nature. When viewed by trained operators, they can be used to detect threats based on their shape and brightness in the image. There are two broad levels of material identification: organic materials, which appear white or light in the image (many x-rays scattered) and inorganic materials which appear dark (few x-rays scattered). This contrast between materials allows threats to be detected based on their shape. However further classification of what the object is made of is not possible.

Consider the backscatter image shown in Figure 1.1. This image shows a backscatter scan of six different organic materials. The objects are very different ranging from an apple to a bag of C4 explosive simulant. Nonetheless, all appear at the same brightness in the image. Those that are similar in shape, for example the bag of sugar and the bag of C4 simulant are indistinguishable. The result is that if any organic material of a suspicious shape is seen in an image this is flagged as a potential security alert, resulting in a large number of false positive detections.

High vehicle throughput at ports and security checkpoints is important to avoid long delays. All x-ray backscatter scans must be performed quickly but without compromising on detection

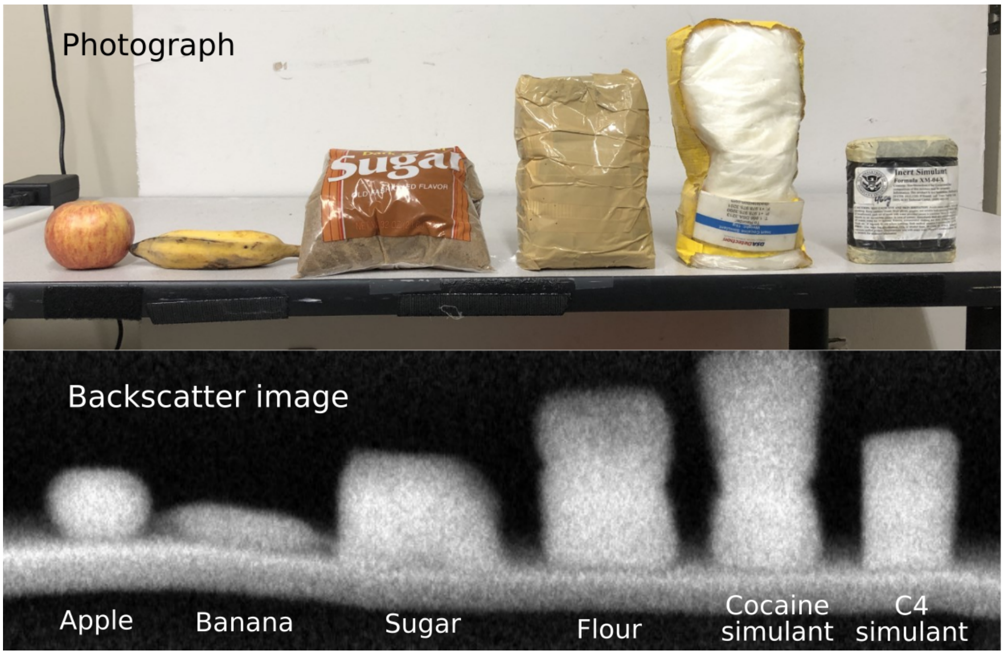

FIGURE 1.1: A backscatter image acquired from a handheld backscatter scanner [12]. Six different organic materials were scanned. From left to right these were an apple, banana, sugar, flour, cocaine simulant and C4 explosive simulant. Although the objects were all different the scatter intensity was the same so were indistinguishable from image brightness alone. Image courtesy of D. S. Gee and D. Palmer at AS&E, Billerica, US.

accuracy. The result is that any vehicle that is flagged up as containing potential contraband material must be manually searched. Manual searches can be up to 2 hours per vehicle [13] which can cause lengthy delays. Therefore it is of paramount importance to reduce the number of false positive detections by improving material identification.

Backscatter systems use x-ray detectors known as energy-integrating detectors. They are inorganic or plastic scintillator detectors made from materials such as gadolinium oxysulphide (gadox), polyvinyl toluene (PVT) or cesium iodide [14, 15]. These detectors measure the intensity of the scattered x-ray beam over a set time period ($\sim$20 µs). Detectors of this type are used due to their high efficiency, fast response times, low cost, environmental adaptability and ability to be manufactured into large sizes (backscatter detector panels typically cover 4 m^2 [15]).

Despite the many advantages of energy-integrating detectors they are also the main barrier to improving material identification. Studies have shown that the energy spectrum of the scattered beam is more specific to the material than the intensity [16], which suggests that spectral information could be used to discriminate between organic materials. This information is lost when energy integrating detectors are used. Previous studies have demonstrated improved material identification using an x-ray spectrometer with a cadmium telluride (CdTe) detector crystal [16, 17]. However, using CdTe in a real backscatter system would not currently be possible as current CdTe manufacturing methods mean crystal sizes are limited to mm^2 [18, 19] and are very expensive. Thus the ideal solution would be to use the existing energy-integrating detectors to retain efficiency and reduce cost, but also obtain spectral information to improve material identification capabilities.

This thesis presents a method that can do just that. Discussed is a novel technique for extracting x-ray spectrum information from energy-integrating detectors for application to x-ray backscatter imaging. The technique involves acquiring a series of scatter intensity measurements, each measurement with a different thickness of filter material in front of the detector. Placing material in front of the detector reduces the number of low energy x-rays incident on the detector which reduces the detected intensity. Changing the thickness of filter material changes the energy of the x-rays that are removed from the beam by the filter. By using a range of different filter thicknesses and comparing the measurements mathematically, the energy spectrum of the scattered x-ray beam can be calculated by a process known as "spectrum unfolding". This is the same process as techniques that use two filters or a sandwich detector arrangement for material identification in transmission imaging [20–23], however instead of two measurements, ten are acquired. A similar technique has also been applied to x-ray computed tomography by I. Kanno *et al.* which uses a single detector but with multiple detection segments along the beam direction [24–29]. The technique was developed independently and applied to x-ray backscatter imaging for the first time in this work.

A proof-of-concept study to test the energy spectrum reconstruction technique in x-ray backscatter imaging in a laboratory setting is presented in this thesis. This was the first demonstration of the spectrum reconstruction technique in x-ray backscatter imaging. A table-top backscatter geometry was set up using a 50 kVp x-ray source, CdTe detector operated in energy-integration mode and aluminium detector filters. Measurements for five different plastics samples were acquired and energy spectra were reconstructed from the data. A calibration process was also developed to account for experimental effects such as scattering, beam alignment and detector response to ensure valid spectra were obtained. Using the reconstructed energy spectra and the results of a Monte Carlo simulation, the samples were categorised as either explosive or inert and estimates of the sample atomic number and density were made. The results showed superior material identification was possible using this technique compared to what is currently achievable on commercial backscatter systems.

This thesis will firstly present the fundamental physics required for an understanding of the x-ray backscatter imaging process in Chapter 2. In Chapter 3, the physics will be put into practice to explain the operation of commercial backscatter systems. The concept of energy spectrum reconstruction and associated mathematical techniques for solving inverse problems are presented in Chapter 4. The experimental approach and results are discussed in Chapters 5 and 6 respectively. A detailed discussion of the experimental errors, areas for improvement and future work follows in Chapters 7, 8 and 9. Proposals for future experiments are outlined in Chapter 10. Finally this thesis is concluded in Chapter 11. Relevant raw data excluded from the main text for conciseness is given in Appendices A, B and C.

This research was undertaken as part of a collaboration project between the Nuclear Physics Department at the University of Manchester, UK and industry partner Rapiscan Systems Cargo Division, Stoke-on-Trent, UK. The project was funded through an STFC iCase award by STFC and Rapiscan Systems under grant proposal ST/N00275X/1. This project is the first PhD project in a newly established research field at the university. The work presented in this thesis draws on many techniques across a variety of different fields of mathematics, x-ray imaging, Monte Carlo simulation and detector science. It is hoped that this work provides a good basis for which backscatter imaging research can develop at the university.

Chapter 2

Theory of x-ray imaging

The following chapter describes the physical theory required to understand the x-ray imaging process and the methods used in this thesis. The generation of x-rays, x-ray interactions with matter and x-ray detection are discussed in detail. Concepts discussed in this chapter are put into practice in the discussion of commercial x-ray backscatter systems in Chapter 3. Relationships between the number of x-rays scattered at a particular energy and properties of the scatter object such as atomic number and density are also derived which are used in the analysis of the results in Chapter 7.

2.1 Generating x-rays

X-rays can be generated on demand using X-ray tubes. X-ray tubes are used in a wide range of non-destructive testing application such as x-ray imaging, x-ray fluorescence analysis and x-ray diffraction. An x-ray tube consists of an electron source (cathode) and an electron target (anode) inside an evacuated glass or ceramic tube. The cathode is typically a filament that is heated to approximately 2400 K by passing a current though it [30]. At this temperature the thermal energy of the electrons on the surface of the cathode becomes larger than the surface binding energy and electrons are released from the surface of the cathode. This process is known as thermionic emission. A large negative voltage is applied to the cathode with the anode at ground [31]. This generates an electric field between the cathode and anode. Electrons ejected from the cathode are accelerated by the electric field towards the anode. The electrons hit the anode and lose their kinetic energy through interactions within the anode material. Some of these interactions produce x-rays.

2.1.1 X-ray interactions

In 99% of interactions, the electron's kinetic energy is absorbed by the anode lattice which causes the anode to heat up [30]. Only 1% of interactions are with the atoms of the anode material. There are three interactions which occur when an incoming electron interacts with an anode atom: bremsstrahlung, characteristic x-ray emission and Auger emission. These processes are summarised in Figure 2.1. X-rays are generated either through characteristic x-ray emission or by bremsstrahlung. Auger emission is a non-radiative competing process. Each will now be discussed.

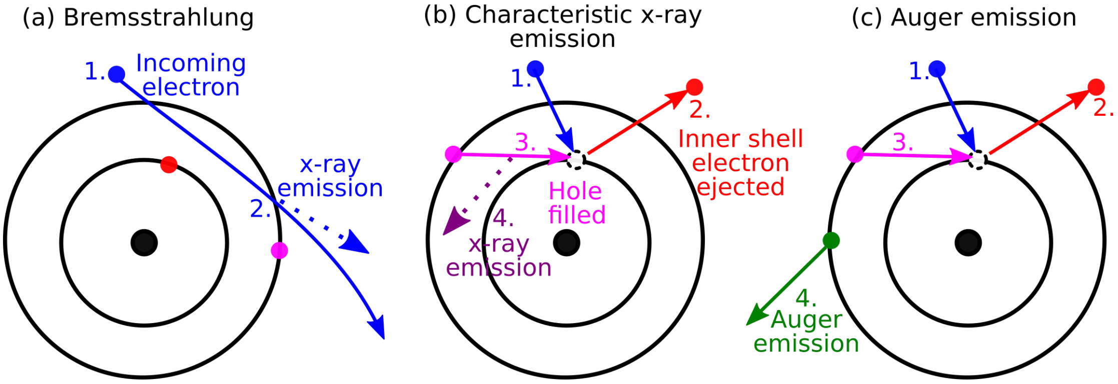

FIGURE 2.1: A diagram showing the three possible interactions incoming electrons undergo with the atoms of the anode material, (a) bremsstrahlung, (b) characteristic x-ray emission and (c) Auger emission. See the main text for details.

2.1.1.1 Bremsstrahlung emission

The bremsstrahlung process is illustrated in Figure 2.1a. As an electron moves through the anode material, the electric fields of the atomic electrons and nuclei of the anode material cause the electron to slow down and eventually stop. The kinetic energy of the electron is converted into radiation according to electromagnetic theory [32]. This is known as bremsstrahlung radiation.

If the potential difference between the anode and cathode is U volts, the kinetic energy of the electron when it reaches the anode is U eV. If the electron is stopped by a single interaction, all its energy is lost and converted into a single photon with energy U eV. More often though, the electron will lose its kinetic energy in multiple interactions so multiple photons are produced. Therefore the bremsstrahlung spectrum produced is continuous as a function of energy with the maximum energy of U eV.

The conversion efficiency of electron kinetic energy to bremsstrahlung radiation η depends on the atomic number of the anode material and the x-ray tube voltage [30],

$$\eta = KZU. \tag{2.1}$$

K is the Kramers constant $K = 9.2 \times 10^{-7}$ kV^{-1} [33] and Z is the atomic number of the anode material. Therefore the higher the atomic number of the anode material the higher the bremsstrahlung yield.

2.1.1.2 Characteristic x-ray emission

Sometimes the incoming electron can collide with an inner shell electron in an atom of the anode material. Characteristic x-ray emission can result as shown in Figure 2.1b. In the collision the incoming electron's kinetic energy is transferred to the inner shell electron and the inner shell electron is liberated from the atom leaving a shell vacancy. An electron from a higher electron shell will de-excite to fill the vacancy. The binding energy of the inner shell is higher than the outer shell and to conserve energy an x-ray photon is emitted in the de-excitation process. The energy of the emitted photon is the difference in the binding energies of the outer and inner atomic shells. The binding energy difference depends on the electron shell configuration therefore it is discrete and unique to the anode material. Often vacancies can be filled by electrons from multiple outer shells which results in many characteristic lines in the x-ray spectrum. Figure 2.2 is an illustration of the possible electron transitions that result in x-ray emission. The probability of characteristic x-ray emission is proportional to Z^4 where Z is the atomic number of the anode material.

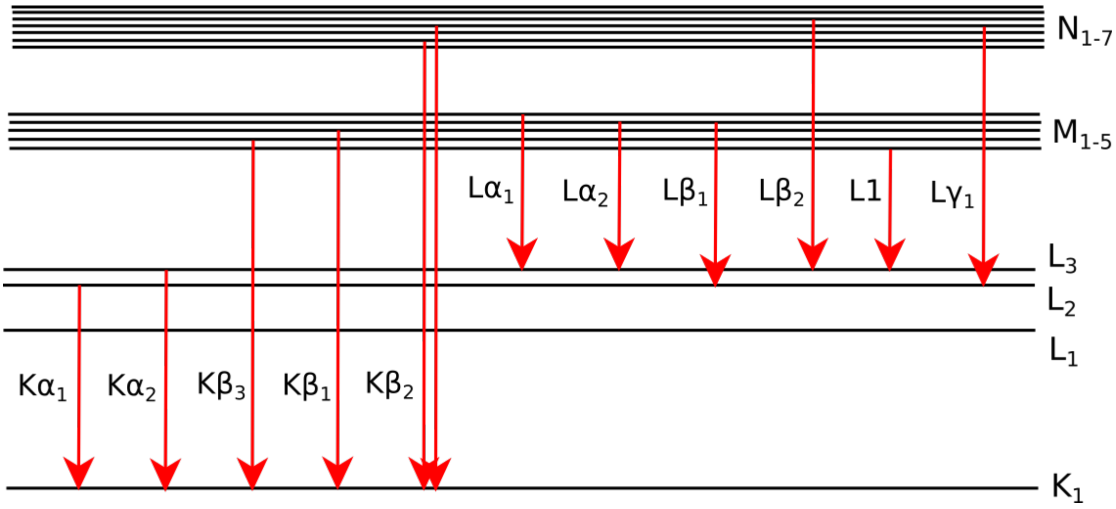

FIGURE 2.2: The electron transitions resulting in characteristic x-ray emission. The labels on the right give the names of the electron energy levels. The labelled arrows indicate possible transitions.

2.1.1.3 Auger emission

When a vacancy is created in an inner electron shell by an incoming electron, the atom can also de-excite in a non-radiative process known as the Auger effect, as shown in Figure 2.1c. When the atom de-excites to fill the inner shell vacancy, the excess energy can be transferred to another electron in an outer shell causing it to be emitted from the atom. This process competes with characteristic x-ray emission and hence limits the x-ray yield. The probability of Auger emission is approximately independent of atomic number [31]. The fraction of transitions that produce x-rays is given by

$$F_{xray} = \frac{Z^4}{C_A + Z^4}, \tag{2.2}$$

where C_A is the Auger emission constant. For a vacancy in the K shell, $C_A \sim 10^6$ and for a vacancy in the L shell $C_A \sim 10^8$ [31]. Hence the x-ray yield from characteristic x-ray emission will be high when Z is large.

2.1.2 Example x-ray tube output spectrum

An example x-ray tube output spectrum is shown in Figure 2.3. The anode material was gold and the operating voltage was 50 kV. A continuum is produced by the bremsstrahlung process which has a maximum energy of 50 keV. Characteristic x-ray lines are also produced on top of the bremsstrahlung continuum. This is due to characteristic x-ray emission from the anode material. The characteristic x-rays appear at 8.5 (gold L1), 9.7 (gold Lα), 11.5 (gold Lβ) and 13.4 (gold Lγ) keV [34].

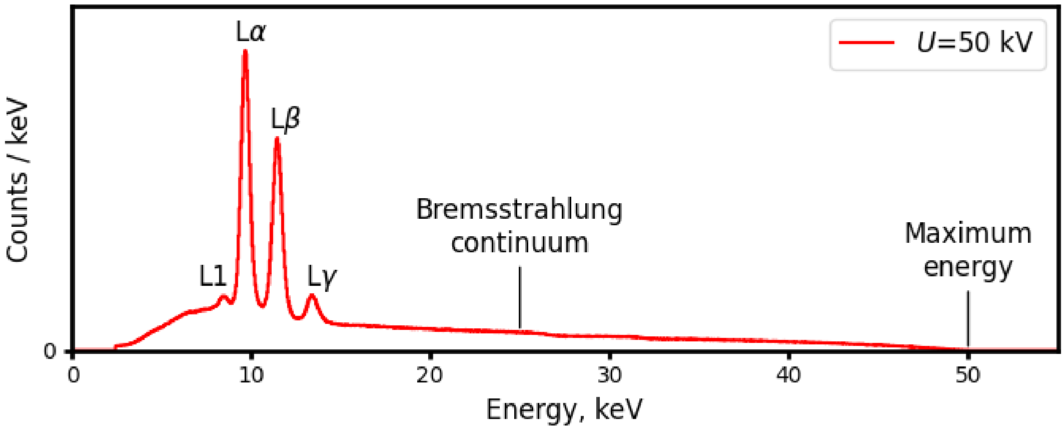

Figure 2.3: The energy spectrum emitted from an x-ray tube with a gold anode operating at a potential of 50 kV. A continuous bremsstrahlung spectrum is emitted with an end point at 50 keV. Characteristic x-rays appear at 8.5 (L1), 9.7 (Lα), 11.5 (Lβ) and 13.4 (Lγ) keV [34].

2.1.3 X-ray tube target design

The anode material strongly influences the intensity and shape of the x-ray tube output spectrum. As discussed in Section 2.1.1, the higher the atomic number the higher the x-ray yield from bremsstrahlung and characteristic x-ray emission. The anode must also have a high heat capacity in order to withstand the heat generated by the electron-lattice interactions. Tungsten has both these attributes and is most commonly used as an anode material, especially in x-ray imaging applications. For x-ray fluorescence analysis, other high Z materials such as gold, silver or rhodium are used [35]. The x-ray tube used in this work had a gold anode.

There are two types of anode geometry: reflection target geometry and transmission target geometry. A schematic diagram of both geometries is shown in Figure 2.4. A transmission target x-ray tube was used for the experimental work in this project. Reflection targets are commonly used to generate higher energy x-ray beams (~200 keV) and are used in commercial backscatter systems.

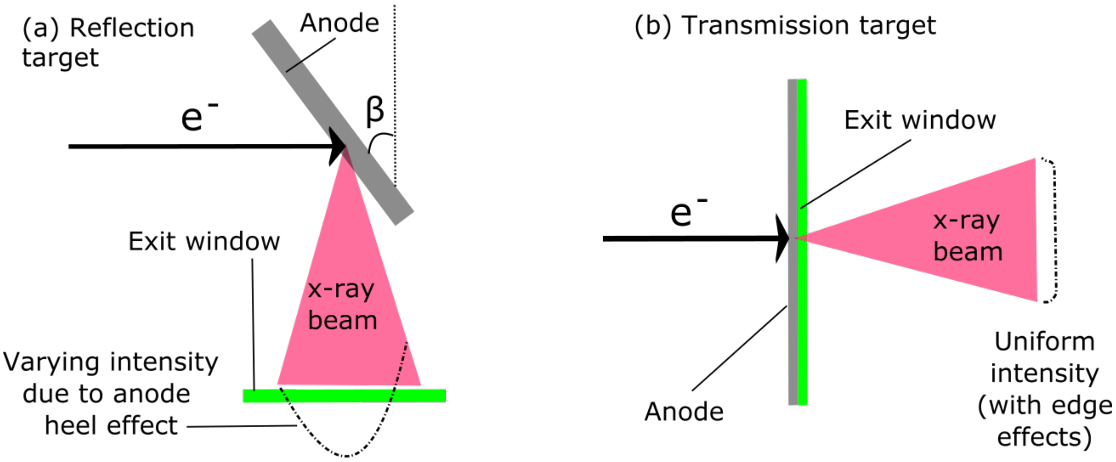

FIGURE 2.4: The two different types of x-ray tube anode configurations. In the reflection target configuration (a) the anode is thick and orientated at an angle $\pi/2-\beta$ to the electron beam. The x-ray beam produced has a varying spatial intensity due to the anode Heel effect, as discussed in the main text. In the transmission target configuration (b) the target is a thin deposit on the exit window surface. The electron beam strikes perpendicular to the anode surface and hence produces a beam with an approximately uniform spatial intensity with a reduction on the outer edges of the beam spot.

2.1.3.1 Reflection target

In reflection geometry the anode is positioned at an acute angle to the incident electron beam. The anode is typically thick (~mm) to ensure efficient removal of heat from the electron impact site. The x-ray beam used is the beam produced perpendicular to the electron beam. The x-ray beam produced from reflection geometries is not uniform due to a phenomenon known as the anode Heel effect. The electrons typically penetrate a few µm into the surface before interaction [30]. This means the x-rays produced are attenuated by the few µm of anode material surface before exiting the anode. The attenuation is greater on one side than the other due to the tilt of the anode; one side of the x-ray beam passes through more of the anode material before escape than the other side. A schematic beam profile demonstrating this effect is shown in Figure 2.4a. Reflection target systems typically operate at a power of above 100 W [36] and are used in x-ray imaging systems.

2.1.3.2 Transmission target

In transmission geometry x-ray tubes the anode material is deposited in a thin layer ($<\sim$0.1 µm) on the exit window [36]. As shown in Figure 2.4b, the x-ray beam intensity can slightly decrease in intensity at the edges of the focal spot due to the beam traversing a longer path length through the target, but otherwise the spatial distribution is uniform. Transmission targets are typically operated at low power (below 100 W) as a thin anode cannot withstand high heat [36]. The transmission target configuration is used in miniature x-ray sources used for x-ray fluorescence analysis [37–39].

2.2 Photon-matter interactions

The interactions between x-rays and matter are essential for x-ray imaging and material identification. In the energy range of interest for this work ($<$ 200 keV) there are three types of photon-matter interactions: photo-electric absorption, Compton scattering and coherent scattering. Coherent scattering is composed of two subprocesses, Rayleigh and Thomson scattering. Schematic diagrams of each process are shown in Figure 2.5 and each will be explained in this section. Pair production can also occur at higher x-ray beam energies ($>$ 1.022 MeV) but will not be discussed as x-rays above this energy threshold are not typically used for backscatter imaging in security applications.

2.2.1 Photo-electric absorption

Photo-electric absorption (PE) occurs when an x-ray photon interacts with an electron in the K shell of an atom. All the photon's energy is transferred to the K shell electron and the electron is liberated from the atom. This leaves a vacancy in the K shell. This is analogous to the electron-electron interaction discussed in Section 2.1.1.2 and the atom will de-excite in the same way by the emission of characteristic x-rays or Auger electron emission. This process is summarised in Figure 2.5a. Photo-electric absorption results in the complete absorption of

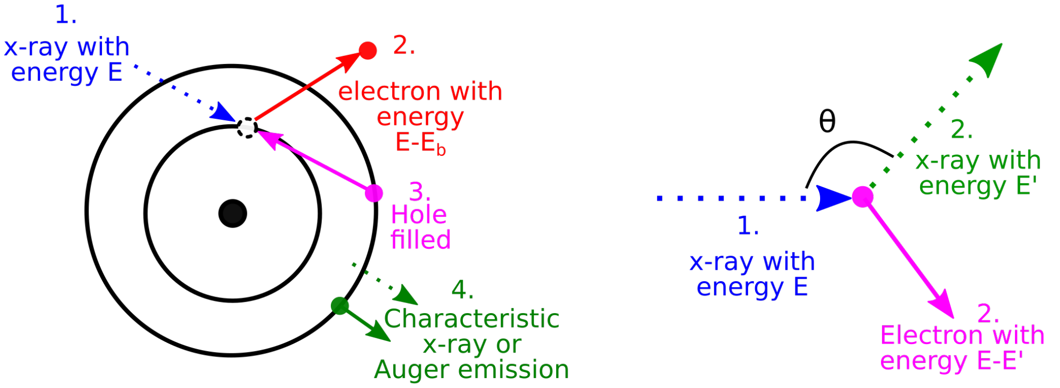
(a) Photo-electric effect

(b) Compton scattering

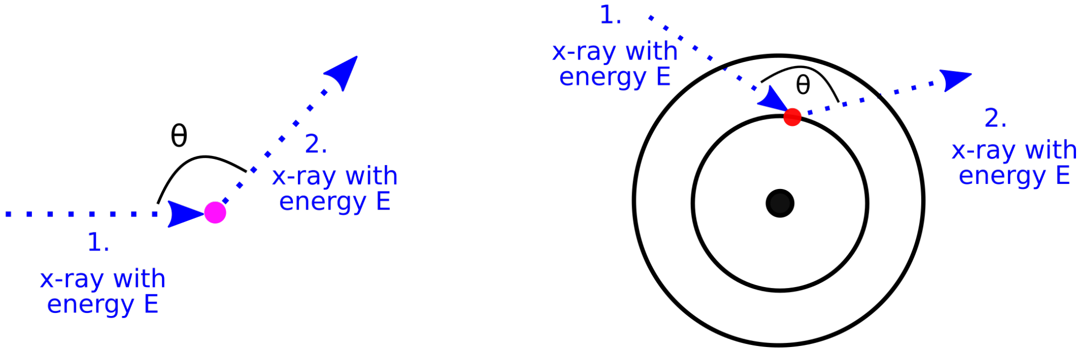
(c) Thomson scattering

(d) Rayleigh scattering

FIGURE 2.5: Schematic digrams of the X-ray interactions with matter when the x-ray energy E is less than 200 keV. (a) shows the photo-electric effect, (b) Compton scattering, (c) Thomson scattering and (d) Rayleigh scattering. Throughout E is the initial energy of the x-ray, E' is the energy of the scattered x-ray, E_b is the electron binding energy and θ is the scattering angle with respect to the direction of the incident x-ray. See the main text for a description of each process.

the x-ray photon's energy. To conserve momentum it can only occur when a photon interacts with a bound electron. The amount of energy transferred to the electron is E-E_b where E is the initial energy of the x-ray and E_b is the electron binding energy.

The cross-section for the photo-electric effect is

$$\sigma_{PE} \simeq k \frac{Z^n}{E^m} \tag{2.3}$$

where Z is the atomic number of the material, E is the x-ray photon energy and k, m and n are constants [40]. Experimental studies determined n to be between 4 and 5 and m to be between 3 and 3.5 [40, 41]. Therefore the photo-electric effect is the dominant interaction for high Z materials and for photon energies below 100 keV.

Discontinuities in the photoelectric cross section occur at discrete photon energies due to the effect of electron shell structure. When the photon energy is increased above the binding energy of an electron shell there is an increase in the photoelectric cross section as the photon can now interact with more of the atomic electrons.

2.2.2 Compton scattering

In the energy region 100 keV$\leq E \leq$4 MeV and for $Z \leq 20$ the dominant photon-matter interaction is Compton scattering [42, 43]. The x-ray photon interacts with an outer shell electron and scatters at an angle θ with respect to the initial photon direction. Part of the photon's energy is transferred to the electron and the scattered photon has a lower energy E'. The interaction is described as inelastic or incoherent because the photon loses energy. A schematic diagram of the Compton scattering process is shown in Figure 2.5b. The scattered photon energy is given by

$$E' = \frac{E}{1 + \frac{E}{m_e c^2}(1 - \cos\theta)}, \tag{2.4}$$

where E and E' are the incident and scattered photon energies respectfully. θ is the angle between the incident and scattered photon directions. m_e is the electron rest mass and c is the speed of light. The derivation of Equation 2.4 assumes the electron is unbound and at rest [42]. This is a good approximation when E is much less than the binding energy of the electron, for example in outer shell electrons in high Z atoms.

The angular dependence of the Compton scattering cross section is described by the differential cross section [44]

$$\left(\frac{d\sigma}{d\Omega}\right)_{KN} = \frac{r_e^2}{2}\left(\frac{E'}{E}\right)^2\left(\frac{E'}{E} + \frac{E}{E'} - \sin^2\theta\right). \tag{2.5}$$

The variable r_e is the classical electron radius ($r_e = 2.8 \times 10^{-15}$ m). Equation 2.5 is known as the Klein-Nishina equation [45]. Again it is assumed that the electron is free and at rest.

Figure 2.6 shows the Compton scattering cross section for three different x-ray energies. The Compton scattering cross section is given by the blue line. The Thomson scattering cross section is shown by the green line, which will be explained in Section 2.2.3. Photons are more likely to be Compton scattered in the forward direction as energy increases due to the greater influence of relativistic effects. Nonetheless a significant fraction are back-scattered even at 200 keV.

The free, stationary electron assumption holds for high Z atoms at high E. The assumption is less valid for low Z at low E as the binding energy of outer shell electrons becomes significant. A function $S(\vec{q}, Z)$, known as the incoherent scattering function is added to the

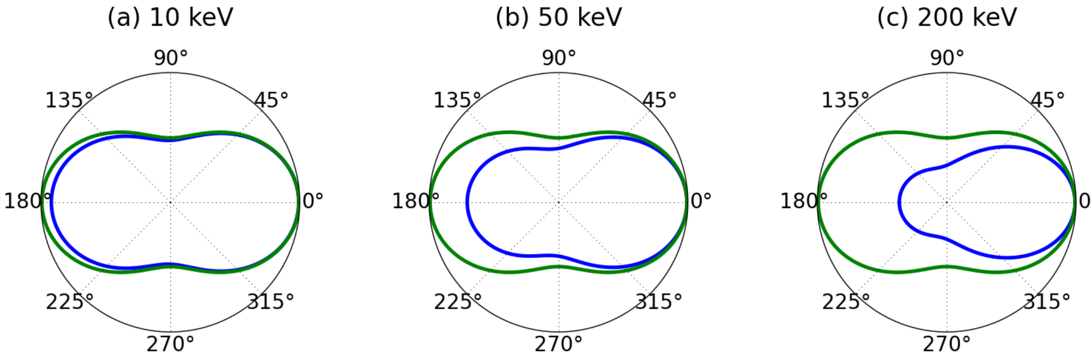

Figure 2.6: Differential cross section for Thomson scattering (green) and Compton scattering (blue) for three different energies: (a) 10, (b) 50 and (c) 200 keV. The differential cross sections were calculated using Equation 2.5 and Equation 2.8. The differential cross section for Thomson scattering is independent of energy. The differential cross section for Compton scattering becomes more forward angle focused as energy increases.

Klein-Nishina equation for a free electron to account for this,

$$\left(\frac{d\sigma}{d\Omega}\right)_{CS} = \left(\frac{d\sigma}{d\Omega}\right)_{KN} S(\vec{q}, Z). \tag{2.6}$$

$\vec{q}$ is the recoil momentum of the electron that the x-ray photon scatters from. The function $S(\vec{q}, Z)$ is a measure of the electron binding in the atom and is a probability that the atom will be ionised by the interaction [43, 46]. It can be calculated using theoretical models such as [47–51].

Integrating Equation 2.6 over the solid angle range gives the interaction cross section for Compton scattering per electron, $\sigma_{CS/e}$. The probability of Compton scattering in a material is proportional to the number of electrons in the material or the electron density ρ_e. Hence the cross-section for Compton scattering is [41]

$$\sigma_{CS} = \sigma_{CS/e}\ \rho_e. \tag{2.7}$$

2.2.3 Coherent scattering

There are two processes where a photon scatters off an electron without losing energy. These processes are Thomson and Rayleigh scattering and are known collectively as coherent scattering. Thomson scattering occurs when a photon is scattered by a weakly bound or outer shell electron. A diagram of the process is shown in Figure 2.5c. Thomson scattering occurs when the energy of the photon is greater than the electron binding energy but much less than the electron rest mass energy.

The differential cross section for Thomson scattering is [44]

$$\left(\frac{d\sigma}{d\Omega}\right)_{TS} = \frac{r_e^2}{2}\left(1+\cos^2\theta\right), \tag{2.8}$$

where r_e is the classical electron radius and θ is the angle of the scattered photon with respect to the incident photon, assuming the incident radiation is unpolarised. The cross section is independent of photon energy [44].

In the Rayleigh scattering process the x-ray photon scatters off an inner shell electron. A diagram of the process is shown in Figure 2.5d. As the scattering occurs far within the electron cloud of the atom, the charge distribution of the other electrons in the atom will affect the Rayleigh scattering process. The differential scattering cross section for Rayleigh scattering is the same as for Thomson scattering but modified by a form factor $F(\vec{q}, Z)$,

$$\left(\frac{d\sigma}{d\Omega}\right)_{RS} = \left(\frac{d\sigma}{d\Omega}\right)_{TS}[F(\vec{q}, Z)]^2. \tag{2.9}$$

$F(\vec{q}, Z)$ is known as the coherent scattering form factor and is the probability a momentum $\vec{q}$ is transferred to the electron but does not cause ionisation [42, 43]. Like the incoherent scattering cross section, $F(\vec{q}, Z)$ can also be calculated from theoretical models [51]. Rayleigh scattering is an important interaction at low x-ray energies [46] and high Z as the cross section is proportional to Z^2. Rayleigh scattering occurs predominantly at small forward angles due to the angular dependence of $F(\vec{q}, Z)$ [44].

2.3 Photon-matter interactions in x-ray imaging

Figure 2.7 shows the cross sections for coherent scattering, Compton scattering and photo-electric absorption as a function of atomic number for three different beam energies (a) 10, (b) 50 and (c) 200 keV. Photoelectric absorption is the dominant interaction for all materials at 10 and 50 keV, with the exception of materials with Z_{eff} <8 at 50 keV. There are discontinuities in the photo-electric cross section due to electron shell effects. Photo-electric absorption is also dominant at 200 keV where Z >40 but Compton scattering dominants for Z <20 at 200 keV. At all energies, the higher the atomic number of the material the higher the total cross section. These differences in cross section are exploited in x-ray imaging to determine what material an object is made from.

X-ray images are typically acquired by either measuring the x-ray beam that has passed through an object (transmission imaging), or by measuring the x-ray beam that has scattered off an object (backscatter imaging). This section will now explain the theoretical basis of both techniques.

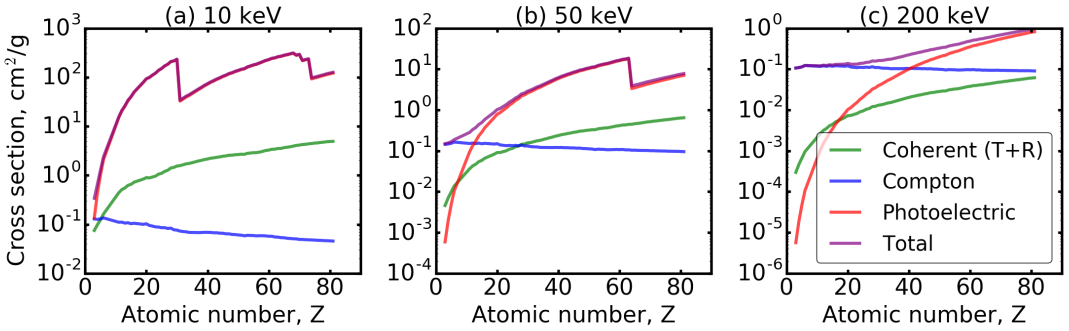

FIGURE 2.7: Cross section as a function of atomic number for the photo-electric effect (red), Compton scattering (blue) and coherent scattering (both Thompson (T) and Rayleigh (R) scattering) (green). Three different x-ray energies are shown (a) 10 keV, (b) 50 keV and (c) 200 keV. The total cross section is shown in purple. All data was taken from the NIST database [52].

2.3.1 Transmitted intensity, I_T

Consider an object of thickness L. An x-ray beam with intensity I_0 is incident on the object as shown in Fig. 2.8. If the x-ray beam is monochromatic with energy E the intensity of the x-ray beam after traversing the full length of the object is

$$I_T(L,E) = I_0(E)e^{-\sigma(E)\rho L}, \tag{2.10}$$

where σ is the total interaction cross section and ρ is the material density. Equation 2.10 is known as the Lambert-Beer law [30, 53]. The total interaction cross section is the sum of all the interaction cross sections for all processes that remove x-rays from the primary beam, $\sigma(E) = \sigma_{PE}(E) + \sigma_{CS}(E) + \sigma_{TS}(E) + \sigma_{RS}(E)$. The Lambert-Beer law is often written in terms of the quantity $\mu(E) = \sigma(E)\rho$, known as the attenuation coefficient. The greater the atomic number, the smaller the transmitted intensity. Additionally, thicker, higher density samples will also highly attenuate the beam.

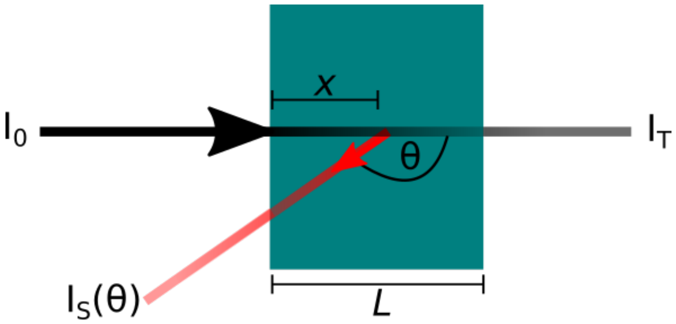

FIGURE 2.8: Schematic of an x-ray beam with intensity I_0 incident on an object. The x-ray beam that traverses the full length of the object L has intensity I_T. The part of the beam that is scattered at a distance x into the material through an angle θ has an intensity $I_S(\theta)$.

The intensity of the transmitted beam is also strongly dependent on the beam energy. A comparison of the scales in Fig. 2.7 shows the magnitude of the total cross section decreases rapidly with increasing energy from of the order 10^{-1}- 10^{3} cm^{2} g^{-1} at 10 keV to of the order 10^{-6}- 1 cm^{2} g^{-1} at 200 keV. Hence the transmitted intensity is higher the higher the x-ray energy. In the case of a polychromatic x-ray beam with a maximum energy E_{max}, the transmitted intensity is

$$I_T(L) = \int_0^{E_{max}} I_0(E) e^{-\mu(E)L} dE. \tag{2.11}$$

2.3.2 Backscattered intensity, I_S

Now consider the scatter intensity, I_S, off the same object of thickness L as shown in Figure 2.8. For simplicity, we consider the x-ray backscatter case where θ=180° and assume x-rays scatter once via the Compton scattering process. The beam undergoes three stages of interactions within the sample before detection. The first is attenuation up to a scatter point x. Secondly, the beam must scatter at point x. Finally the scattered beam is attenuated by the sample as it travels back in the direction of the primary beam. The intensity of the beam scattered at point x is therefore given by

$$I_S(x, E) = I_0(E) e^{-\mu(E)x} \rho_e \left(\frac{d\sigma}{d\Omega}\right)_{KN} e^{-\mu(E')x}. \tag{2.12}$$

Here ρ_e is the electron density, $(d\sigma/d\Omega)_{KN}$ is the Klein-Nishina cross-section as given by Equation 2.5 and E' is the energy of the scattered beam. The beam can scatter at any point in the sample along the beam direction, therefore the total backscatter intensity is calculated by integrating Equation 2.12 between $x = 0$ and $x = L$,

$$I_S(E) = \rho_e \left(\frac{d\sigma}{d\Omega}\right)_{KN} \int_0^L I_0(E) e^{-(\mu(E)+\mu(E'))x}\, dx. \tag{2.13}$$

Performing the integration and replacing $(d\sigma/d\Omega)_{KN}$ with Equation 2.5 with θ=180° gives [8]

$$I_S(E) = I_0(E) \frac{r_e^2}{2} \left(\frac{E'}{E}\right)^2 \left(\frac{E'}{E} + \frac{E}{E'}\right) \frac{\rho_e}{\mu(E) + \mu(E')} \left(1 - e^{-(\mu(E)+\mu(E'))L}\right). \tag{2.14}$$

The electron density is $\rho_e = \rho N_A Z_T / M$ where N_A is Avogadro's constant (N_A= 6.02×10^{23} atoms per molecule), M is the molar mass and Z_T is the total number of electrons in each molecule. For elements $Z_T = Z$ and for compounds $Z_T = \sum_i Z_i$ where Z_i is the atomic number of the i^{th} atom in the molecule. The backscatter intensity is a function of ρ and Z through the dependence on the electron density and attenuation coefficients $\mu(E)$ and

$\mu(E')$. Coherent scattering was not considered in the derivation of I_S as the cross section for Thomson scattering is small compared to Compton scattering and the cross section for Rayleigh scattering is negligible at large scatter angles.

2.3.3 Effective atomic number definition

Atomic number is a parameter associated with pure elements, however effective atomic numbers can also be calculated for compounds. The effective atomic number parameter used in this work was calculated as

$$Z_{eff} = (\sum_i N_i \beta_i Z_i^m)^{\frac{1}{m}}, \tag{2.15}$$

which is known as the XMuDat definition [54,55]. The effective atomic number was calculated by considering each individual element in the molecule, denoted by the subscript i. Z_i is the atomic number of element i and N_i is the number of atoms of element i in one molecule of the material. β_i is defined as the ratio of the atomic number of element i to the total proton number of the molecule, $\beta_i = Z_i / \sum_i Z_i$. m is a coefficient and for the materials of interest (organic materials with $Z_{eff} < 15$) m=3.5. There are many different ways to calculate the effective atomic number, for example [56–58]. The XMuDat definition was used because it is constant with energy and was used in similar work on material identification in x-ray transmission imaging [59].

2.3.4 Effective atomic number and density relations

As shown in Equation 2.14, the intensity of the scattered beam is dependent on the atomic number of the material and the electron density. However, these two properties are also related. The relationship between the density and electron density is approximately linear due to the near constant ratio Z_T/M over all materials, as shown in Figure 2.10. The relationship between atomic number and density is complex as the density is affected by chemical properties of the material, as shown in Figure 2.9.

2.3.5 Energy dependence of I_S

The scatter intensity as a function of Z and ρ at 10, 50 and 140 keV was calculated for solid materials with Z=3-82 using attenuation coefficient data given in the NIST XCOM database [52] and Equation 2.14. The sample thickness L was 10 mm. The results are shown

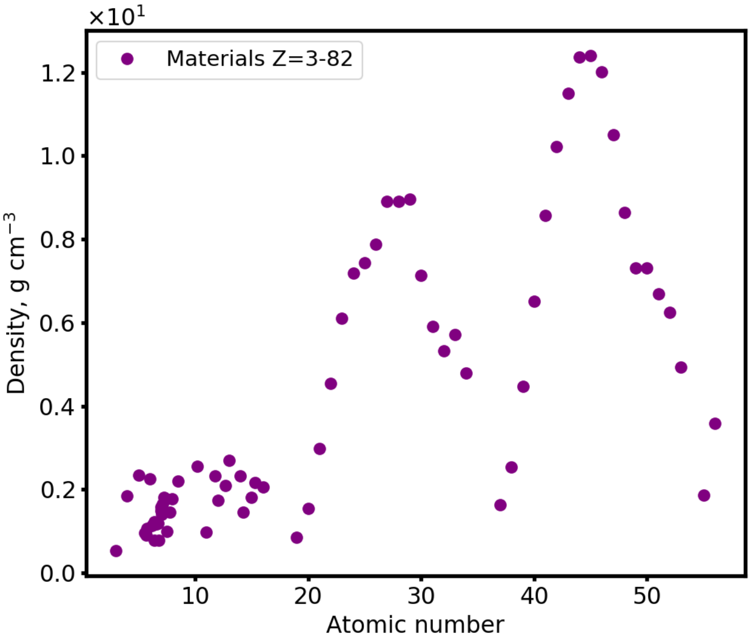

FIGURE 2.9: Atomic number as a function of density for materials with Z=3-82.

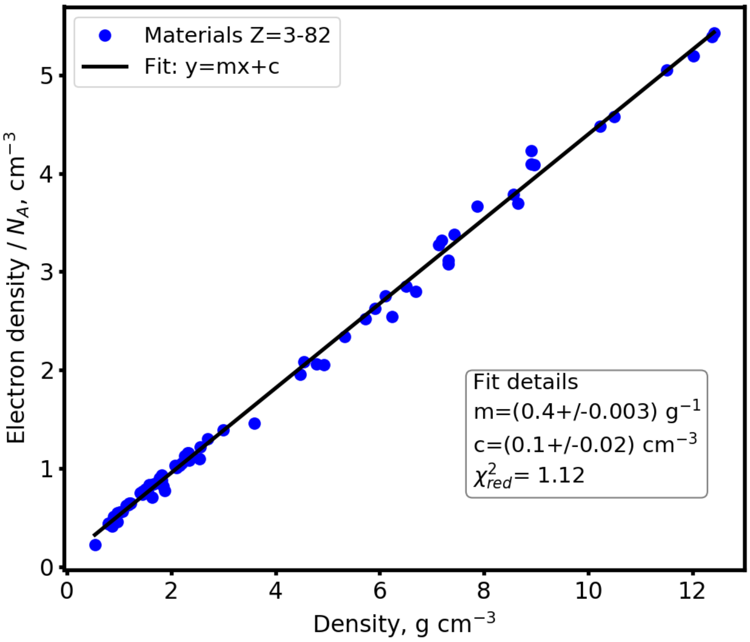

FIGURE 2.10: Electron density as a function of physical density for materials with Z=3-82. The electron density was normalised by N_A where N_A is Avogadro's number. The relationship between electron density and physical density showed good linearity with χ^2_{red}=1.12.

in Figure 2.11. The scatter intensity is shown for organic materials (3$\leq Z \leq$16) as a function of density (see Figure 2.11a) and atomic number (see Figure 2.11b). The scatter intensity is shown for both organic and inorganic materials (3$\leq Z \leq$82) as a function of density (see Figure 2.11c) and atomic number (see Figure 2.11d).

Backscatter intensity is a complex function of Z and ρ generally, as seen in Equation 2.14. However, approximate empirical relationships were derived from the theoretical backscatter intensity at certain x-ray beam energies. For example consider the relationship between scatter intensity and density shown in Figure 2.11a and Figure 2.11c. For Z <20 and E ~140 keV Compton scattering dominates over photo-electric absorption. In this case the backscatter intensity becomes proportional to the probability of Compton scatter, which is linearly dependent on density as shown in Figure 2.11a (blue points).

For Z <20 and E ~50 keV, as shown in Figure 2.11a (red points), this linear relationship becomes less defined, especially for materials with 10 <Z< 20. As E decreases photo-electric absorption and Compton scattering become more comparable so the intensity starts to also depend on the atomic number. For E ~10 keV photo-electric absorption is the dominant interaction for almost all materials, therefore the scatter intensity depends almost entirely on Z and there is no clear trend with ρ.

Next consider Z_{eff} as a function of I_S for low E ($E \leq$ 10 keV), as shown in Figure 2.11b and Figure 2.11d (green points). Photo-electric absorption is the dominant interaction for all materials where $Z \geq 4$. This is because the chance of a photon scattering within the material and the scattered photon escaping the material without being absorbed decreases rapidly with Z. Hence there is a rapid decline in the calculated scattered intensity as a function of Z. The exception is $Z = 3$ (Lithium) where the cross sections for photo-electric absorption and Compton scattering are similar. The electron density is so low due to a low physical density (ρ=0.534 g cm^{-3}) that the beam has a higher chance of passing straight through the material without scattering compared to $Z = 4$ (Beryllium, ρ=1.848 g cm^{-3}).

As the energy of the beam increases the atomic number for which the photo-electric cross section and Compton scattering cross section become comparable increases. The Z corresponding to the maximum scatter intensity and the start of the exponential decrease increases as E increases. The Z corresponding to the start of the exponential decay occurs at Z=4, 9 and 23 for 10, 50 and 140 keV respectively. For Z lower than this value the relationship with scatter intensity also depends on density effects so there is no clear relationship with atomic number.

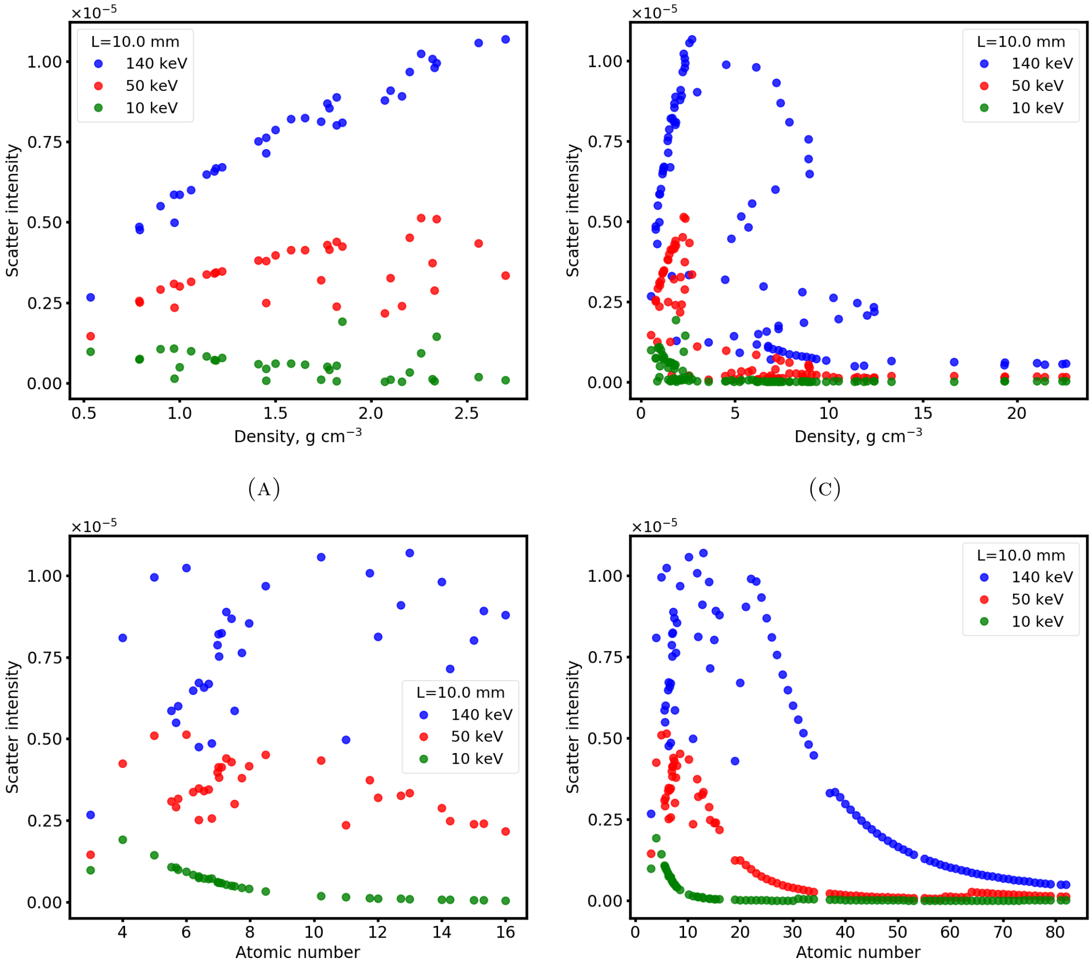

(A) (C)

(B) (D)

FIGURE 2.11: Backscatter intensity as a function of material density (A and C) and atomic number (B and D) for scattering off a 10 mm thick sample. The intensity is shown for three different x-ray beam energies, 10 (green), 50 (red) and 140 (blue) keV. Data are shown for two atomic number regions, Z=3-16 (A and B) and Z=3-82 (C and D). All intensities were calculated using Equation 2.14 using attenuation coefficient data from NIST XCOM [52] and Z, ρ and ρ_e information shown in Figure 2.9 and Figure 2.10.

2.3.6 Empirical fits for I_S, ρ and Z

In the two energy regions considered, where there were unique relationships between I_S and ρ and Z (10 and 50 keV for organic materials 3< Z_{eff} ≤16) empirical fits were applied to the theoretical data. I_S was plotted as a function of ρ for E=50 keV and L=10 mm, as shown in Figure 2.12. The equation $\mathrm{y} = \mathrm{m}\ln(\mathrm{x}) + \mathrm{c}$ was fit to the data for 3≤ Z ≤10, shown by the black line in Figure 2.12. This functional form was chosen empirically. The data appeared to follow a log-linear trend by eye and the function was the one with the fewest number of variables to describe the data. For Z >10, there was no clear trend with ρ so these points were omitted from the fit. The calculated fit parameters were m=0.437±0.013 and c=0.591±0.006. The χ^2_{red} statistic was 1.00. Using the Compton scattering energy

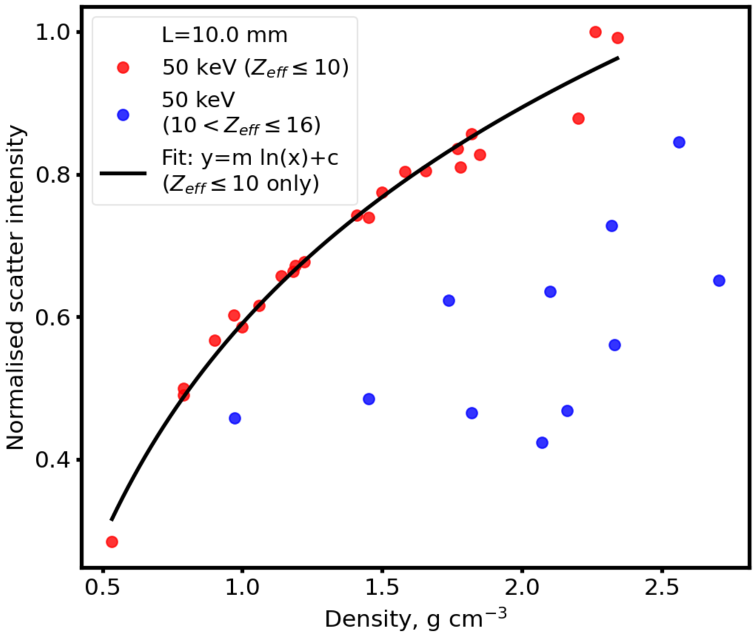

FIGURE 2.12: Scatter intensity as a function of density calculated at 50 keV for all materials with $3 \leq Z_{eff} \leq$16. Materials with $Z_{eff} \leq$10 are shown in red and those with 10$<$ $Z_{eff} \leq$16 shown in blue. The scatter intensity was normalised to the maximum scatter intensity point. An empirical fit $\mathrm{y = m ln(x) + c}$ was fit to the data with $Z_{eff} \leq$10. See the main text for information about the fit parameters.

equation given in Equation 2.4, for an incident beam energy of E=50 keV, the scattered beam has energy E'=42 keV. Therefore the scatter intensity of x-rays detected at 42 keV was shown to be proportional to the material density for 3$\leq$ Z $\leq$10 in the theoretical case.

Similarly for Z, I_S was plotted as a function of Z for 3$\leq$ Z $\leq$16, as shown in Figure 2.13. The equation $\mathrm{y = Ae^{-b(x-4.00)} + c}$ was fit to the data, as shown by the black line in Figure 2.13. Similarly to the density equation above, the functional form was chosen empirically for the same reasons. The point Z=3 (Lithium) was excluded from the fit. The calculated fit parameters were A=1.01±0.01, b=0.397±0.009 and c=0.017±0.006. The χ^2_{red} statistic was 0.1063. From Equation 2.4, for E=10 keV E'=9.6 keV. Therefore the intensity of the scattered x-rays detected at approximately 10 keV was shown to be proportional to Z_{eff} for 4$\leq$ Z $\leq$16 in the theoretical case.

These relationships with I_S, ρ and Z are key theoretical results which provided the basis of the material identification analysis in this thesis. These two examples demonstrate that if energy information is measured from a backscatter signal, it is possible to obtain information about the material properties of the scatter object.

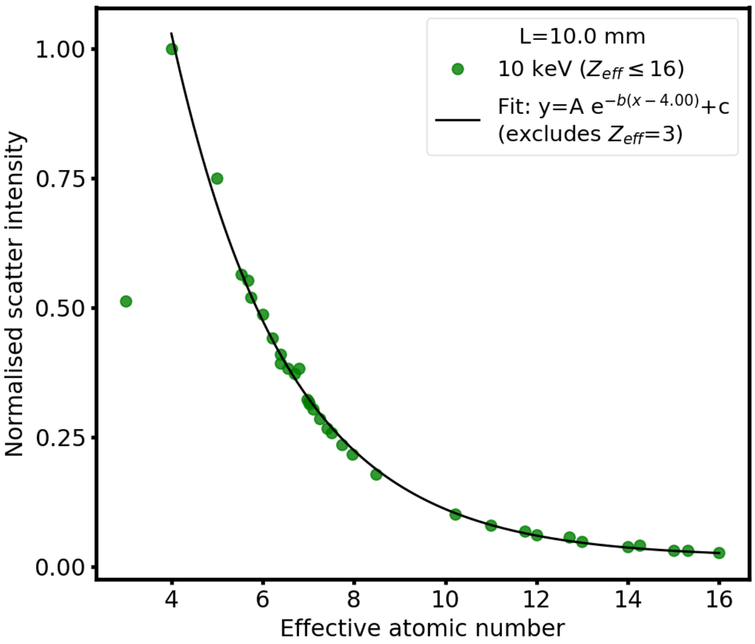

FIGURE 2.13: Scatter intensity as a function of density calculated at 10 keV for all materials with 3< $Z_{eff} \leq$ 16. The scatter intensity is normalised to the maximum scatter intensity point. An empirical fit $y{=}Ae^{-b(x-4.00)}{+}c$ was fit to the data. The point Z_{eff}=3 was excluded from the fit. See the main text for information about the fit parameters.

2.3.7 Sample thickness dependence on I_S

Sample thickness is an important factor in the detected scatter intensity. Figure 2.14 shows the relationship between scatter intensity and Z at 10 keV (Figure 2.14a) and ρ at 50 keV (Figure 2.14b) for four different sample thicknesses, L=1.0, 5.0, 10.0 and 50.0 mm.

As shown in Figure 2.14a, at 10 keV the scatter intensity is similar regardless of the sample thickness for materials with Z >8. This is because the atomic number is sufficiently large that even very small amounts of material cause considerable absorption of the x-ray beam. The scatter observed is only occurring from the surface of the material. The dominant interaction at 10 keV is photo-electric absorption for all materials with the exception of Z=3. As the atomic number decreases, the deviation from the exponential decay occurs at higher Z the smaller the sample thickness. For 1.0 mm the deviation is at Z=8, for 5.0 mm around Z=5, and for 10.0 and 50.0 mm at Z=3. The gradient of the exponential is also larger the larger the sample thickness. Therefore in theory the relationship between scatter intensity and atomic number follows an exponential trend regardless of the sample thickness, but the parameters of the exponential trend depend on the sample thickness. Hence for some materials knowing the thickness of the material is extremely important for determining the atomic number.

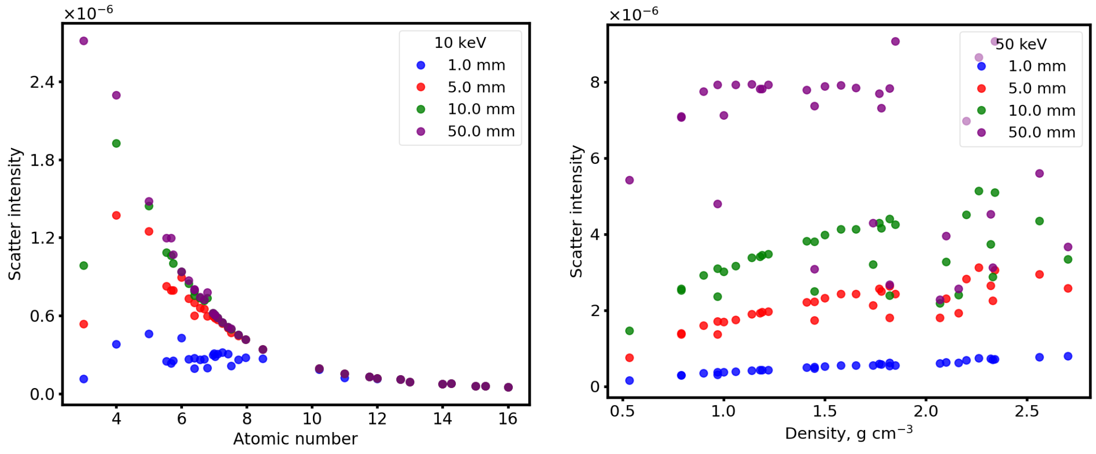

(A) (B)

FIGURE 2.14: Backscatter intensity as a function of atomic number with (A) E=10 keV and as a function of density for (B) E=50 keV. For both intensities were calculated for sample thicknesses of 1.0 mm (blue), 5.0 mm (red), 10.0 mm (green) and 50.0 mm (purple). All intensities were calculated using Equation 2.14 using attenuation coefficient data from NIST XCOM [52] and Z, ρ and ρ_e information shown in Figure 2.9 and Figure 2.10.

In addition, consider the relationship between ρ and I_S at 50 keV for different thicknesses, as shown in Figure 2.14b. The scatter intensity changes with L considerably here too. For $L \leq$10 mm the scatter intensity increases with increasing sample thickness, and follows a similar trend for all thicknesses. The dominant interaction for most of the organic materials at 50 keV is Compton scattering and hence the thicker the material the greater the amount of Compton scattering as there is more material to scatter off. This is the case only up to a point, as for L=50.0 keV the scatter intensity saturates at a density of approximately 1.0 g cm^{-3}, and fluctuates more with increasing density from ρ=1.5 g cm^{-3}. As the sample is so thick, the scatter intensity is limited by the penetration depth, which is dependent on Z_{eff}. Again, knowing the thickness of material is of high importance for determining the density, as in cases of large sample thickness, can limit the measurement altogether.

As these theoretical results show, the sample thickness has a significant effect on the scatter intensity. In practice, a backscatter system with perfect material identification capabilities would also need to account for sample thickness. Sample thickness estimation was not studied in the main part of this thesis, however adaptations to the technique to estimate the sample thickness are reviewed at length in the discussion (see Section 9.6).

2.4 X-ray detectors

There are two main types of x-ray detectors: scintillator and semi-conductor detectors. Scintillation detectors are used in commercial backscatter imaging systems. In this application they are operated in a way where the time-integrated beam intensity is measured, known as energy-integration mode. A semi-conductor detector with a cadmium telluride crystal (CdTe) was also used in the development work discussed in this thesis. CdTe detectors typically operate in photon-counting mode where the energy of each individual photon is measured. The theory of operation of both detectors will be discussed in detail.

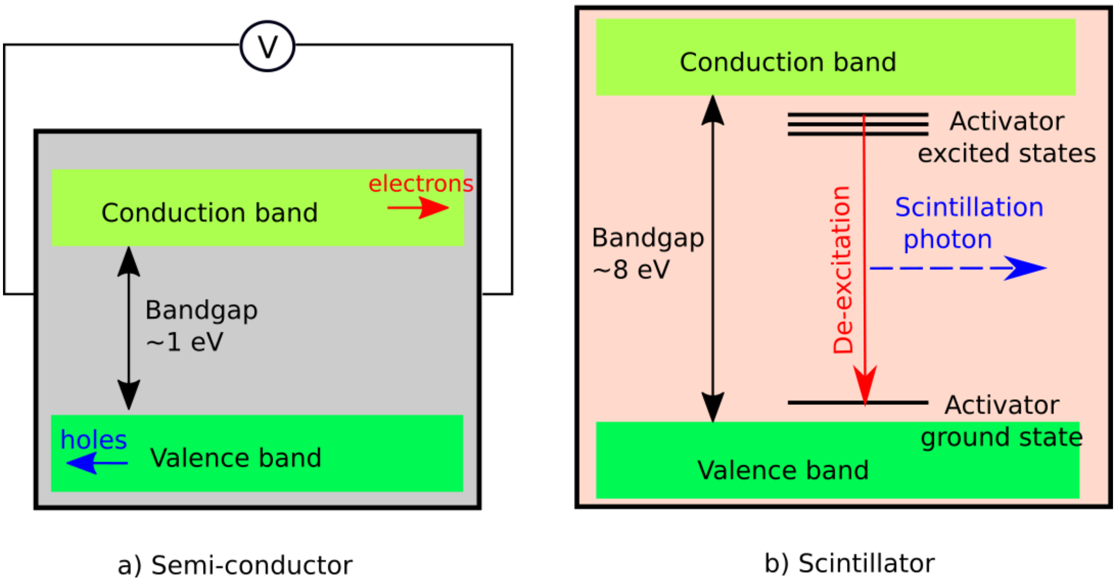

FIGURE 2.15: Schematic diagram of (a) a semi-conductor and (b) a scintillator x-ray detector. The valence and conduction bands are shown with the different band gaps. When an x-ray photon interacts with a semi-conductor detector material it creates electron hole pairs which are collected directly. When an x-ray photon interacts with a scintillation detector, scintillation light is produced in a multi-step process. See the main text for further details.

2.4.1 Semi-conductor detectors

A semi-conductor material is a material in which the energy difference between the valence and conduction band (called the bandgap) is approximately 1 eV [40]. At non-zero temperature, there are a number of electrons in the conduction band due to thermal excitation, and an equal number of holes in the valence band. The material can be used to detect x-rays by attaching an anode and cathode to either side of the semi-conductor material and applying a potential difference. The applied potential difference creates an electric field in the semi-conductor which causes the electrons to be attracted towards the positive anode and holes to the negative cathode. A charge-free area is created in the centre of the semi-conductor material called the depletion region.

When an x-ray photon is incident on the detector, the photon interacts with the material in the depletion region by photo-electric absorption or Compton scattering (as discussed in Section 2.2). Both interactions result in the ejection of an electron from an atom in the material with a high kinetic energy. This ejected electron is known as the primary electron. The primary electron travels through the depletion region and loses its energy by ionising the atoms of the semi-conductor material, creating many electron-hole pairs. The electrons generated in this step are known as secondary electrons. The secondary electrons and holes are swept to the anode and cathode respectively by the applied electric field. If the electrodes are connected to a circuit, a current pulse is generated with an amplitude proportional to the number of electron-hole pairs generated. The number of electron-hole pairs created is proportional to the primary electron energy which is in turn proportional to the energy of the incident photon. Hence the amplitude of the generated current is proportional to the incident x-ray photon energy.

2.4.1.1 Cadmium telluride and CZT

Cadmium telluride (CdTe) is a semi-conductor material that is used to make semi-conductor radiation detectors. A crystal of CdTe contains Cadmium (Z=48) and Tellurium (Z=52) in equal stoichiometric ratio. The bandgap for CdTe is 1.44 eV [60]. One of the biggest advantages of CdTe is that radiation detectors can operate at room temperature and maintain high energy resolution of typically $\sim$0.5 keV for x-rays $<$40 keV in energy [61]. As a result, CdTe detectors are used in many different scientific disciplines, for example in astronomy, nuclear security and medical imaging [19, 62–64]. CdTe detectors have also been used in prototype explosives detection systems for x-ray transmission and x-ray backscatter imaging [17, 22]. Nonetheless CdTe is not currently used in field systems due to cost and efficiency constraints.

Current CdTe manufacturing methods mean that crystals can only be produced in relatively small sizes. For example, 5×5 mm and 1 mm thickness is the standard dimensions of a commercially available CdTe detector [60]. Although the photo-electric absorption efficiency is $>$90% for x-rays with energies below 65 keV [60], individual crystals of CdTe are still inefficient compared to inorganic scintillators that can be manufactured into larger sizes. This is particularly problematic for backscatter imaging where the incident beam to scattered beam ratio is typically less than 10^{-5} [65]. Additionally, CdTe is a very expensive detector material compared to most commonly used inorganic scintillators.

Energy spectra acquired from CdTe detectors are affected by peak distortion due to a process called hole tailing. Single energy peaks can appear skewed from a perfect Gaussian with a peak tail or shoulder appearing on the low energy (left hand) side of the centroid. This is caused by impurities in the CdTe crystal. Impurity sites can capture holes as they migrate through the crystal. This can result in incomplete signal collection, and hence some energies are recorded lower than they should be as part of the signal has been lost. The hole tailing effect increases with increasing x-ray energy [60].

Polarisation is also a problem in CdTe [66]. Polarisation occurs when negative charges are trapped by cadmium vacancies over a period of sustained bias voltage [19, 60]. This effect reduces the overall electric field strength across the crystal which reduces the size of the depletion region [40]. Thus the total overall charge that can be collected is reduced. The effect is most noticeable at low bias voltage ($\sim$200 V) where peak shifts of up to $>$2% per hour have been recorded (on a commercially available 1 mm thick CdTe crystal). At higher bias voltages ($\sim$750 V), which were used in this work, the effect is negligible [60].

One way to overcome the polarisation effect in CdTe is to replace some of the Cd sites with zinc (Zn) to create CdZnTe (known as CZT). The chemical equation is $\mathrm{Cd}_{1-x}\mathrm{Zn}_x\mathrm{Te}$ where x ranges from 0.1 to 0.2 [19]. The bandgap in CZT with x=0.1 is 1.57 eV [19] therefore it can also be operated at room temperature. CZT is also used in a wide range of x-ray and gamma ray applications [18]. However, CZT suffers from a larger hole tailing effect than CdTe due to decreased hole mobility. The hole lifetime is typically 2×10^{-6} s for CdTe, an order of magnitude smaller than for CZT [67]. Costs of CZT are also high due to manufacturing methods.

At present, due to the cost and low efficiency of CdTe and CZT compared to inorganic scintillator materials that can be manufactured into large sizes, use of this material in x-ray backscatter systems would not be viable. CdTe was in this proof-of-concept study however because full energy resolution was required for diagnostic purposes.

2.4.2 Scintillation detectors

Scintillation detectors for x-ray detection are made from insulator materials (bandgap $\sim$8 eV) which are doped with an activator. The activator introduces energy levels in between the valence and conduction band. The activator ground state lies just above the valence band and activator excited states lie just below the conduction band. An illustration of this band structure is given in Fig. 2.15b.

When an x-ray interacts with the scintillator material a primary electron is emitted through a photo-electric absorption or Compton scattering interaction. Similar to the semi-conductor case, the primary electron loses energy by creating electron-hole pairs in the medium. Electrons are excited to the conduction band and populate the activator excited states. De-excitation then occurs from the activator excited states to the activator ground state, and a photon is released in the process [68]. The photon wavelength is in the visible light range. The intensity of visible light emitted by the crystal upon interaction with an x-ray is proportional to the number of electron-hole pairs created by the primary electron, and hence proportional to the energy of the incident photon.

The scintillation light must then be converted into a current pulse in order to be processed by an electronic circuit, unlike in the semi-conductor case where the collected electrons and holes form the electronic signal directly. Photo-multiplier tubes (PMTs) are used for this purpose. Other devices such as silicon photo-diodes (SiPMs) can also be used, but these devices are not commonplace in commercial x-ray backscatter imaging due to cost.

A PMT is a device that converts and amplifies the scintillation light pulse. It consists of a metal cathode and several metal dynodes with a concave shape. A diagram is of the inside of a PMT is shown in Figure 2.16. A scintillation photon exits the scintillator crystal and impinges on the photo-cathode. The scintillation photon interacts with the photo-cathode surface via the photo-electric effect and a photo-electron is released. The photo-electron is then accelerated through a potential difference to the first dynode. The photo-electron hits the surface of the first dynode and a number of secondary electrons are released (approximately 5 per photo-electron [69]). The secondary electrons are then accelerated to the next dynode, upon which more electrons are released from the surface upon electron impact. PMTs typically have 10 dynodes and this process repeats until the electrons reach the last dynode, known as the anode. The electrons collected at the anode induce a current in the analysis circuit.

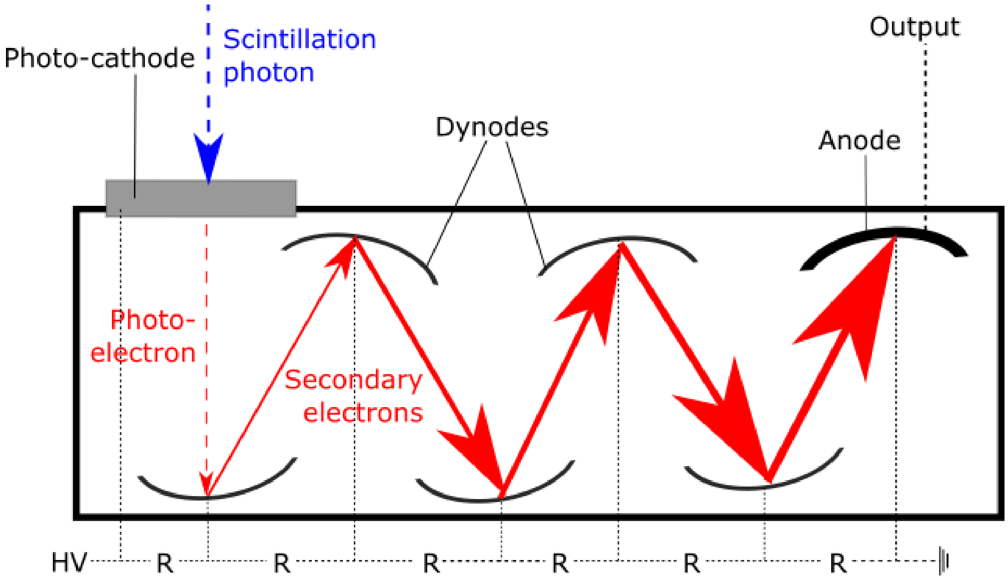

FIGURE 2.16: A scintillation photon is converted into an electronic signal using a photo-multiplier tube (PMT). A potential difference is applied across the cathode and anode. A series of resistors (R) are used so that each dynode is at a higher potential than the previous [69]. PMTs typically contain about 10 dynodes. The number has been reduced in this diagram for clarity. HV stands for high voltage.

Due to the multi-step process of signal collection and a larger bandgap, scintillation detectors have lower energy resolution compared to semi-conductor detectors. However, scintillation detectors are typically less expensive and can be manufactured more easily into larger sizes. As is the case with CdTe/CZT (but not most semi-conductor detectors), inorganic scintillator detectors can be operated at room temperature and temperatures suited to field environments without cooling. As a result, scintillation detectors are often more efficient than semi-conductor detectors and have more practical applications.

Currently, only inorganic or plastic scintillation detectors are used on commercial x-ray backscatter field systems. Detector materials include Cesium iodide (CsI), Calcium tungstate ($CaWO_4$), BaFCl, gadolinium oxysulphide (Ga_2O_2S or also known as Gadox) and plastic scintillator polyvinyl toluene (PVT) [10, 14, 15, 70, 71]. Details of commercial systems will now be explained in Chapter 3.

Chapter 3

Backscatter imaging systems

This chapter discusses the operation of commercial backscatter systems building on the physical theory from Chapter 2. An overview of the imaging technique and detector system is provided. Technical challenges in industrial backscatter imaging are also discussed. A test backscatter image is presented to highlight the basic organic/inorganic material separation achievable on current systems, and demonstrate the need for improved material identification.

3.1 Image acquisition

All types of backscatter system consists of an x-ray source and a detector panel on the same side of the object as the source. The x-ray beam is fired at the object to be scanned and the x-rays that are scattered in the backward direction are detected by the detector panel. There are two methods of image acquisition: space-multiplexing and time-multiplexing. Time-multiplexing is by far the most common method so will be described in full in what follows. A description of space-multiplexing can be found in reference [10].

In the time-multiplexing method, the x-ray beam is highly collimated. A typical beam spot has a 8 mm diameter 1 m from the source. The x-rays irradiate an $\sim$8 mm area of the object. The x-rays interact with the material within the irradiated area via the photon-matter interactions discussed in Section 2.2. Some x-rays are scattered back in the direction of the incoming x-ray beam by Compton scattering. The scattered x-ray intensity is measured by the detector through a series of signal processing steps. The intensity is used to assign a greyscale value to the pixel in the backscatter image. This is shown in Figure 3.1a.

The x-ray source collimator can rotate, and in doing so generates a sweeping pencil beam of x-rays. To perform a line scan which creates one line in the backscatter image, the x-ray beam is swept down the height of the object. Typical backscatter images are 1000 pixels tall,

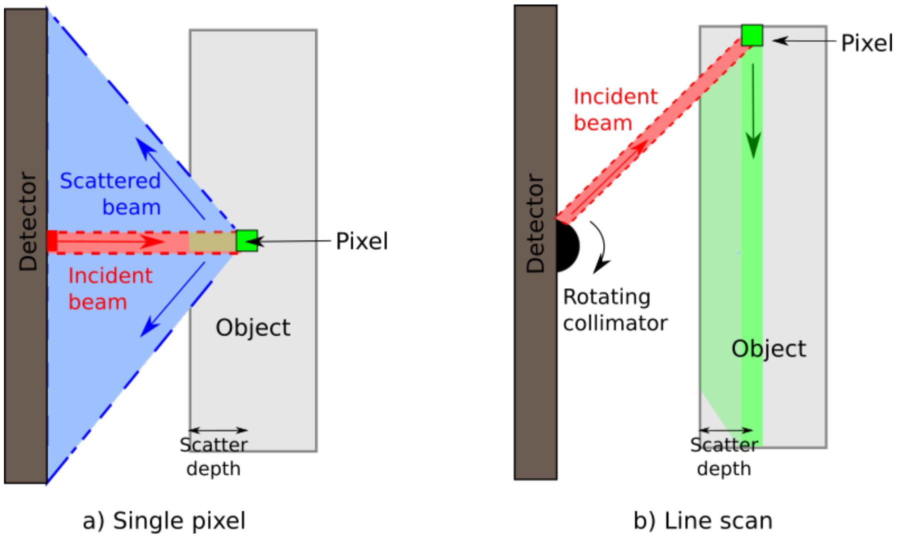

FIGURE 3.1: Schematic diagram showing time multiplexing method for backscatter imaging. Fig. a) shows the collimated x-ray beam incident on a small area of the object (pixel). Some of the beam is scattered back towards the detector and this is detected. To acquire a line scan of the image, a rotating collimator is used which sweeps the beam down the height of the object, Fig. b).

so 1000 different samples are acquired down the object length. For each sample selected, the detectors collect and processes the scattered beam before the beam moves on to the next pixel. To create a 2-dimensional image, the object is moved relative to the x-ray beam and multiple line scans are acquired along its length. For a vehicle scan, this could involve the vehicle driving slowly past the backscatter imager. For a scan using a handheld scanner, this could involve the operator slowly moving the device across the object of interest.

The collimator on a backscatter system typically rotates at 3000 rpm. Each line of the image is acquired in $\sim$0.02 s and each pixel in $\sim$20 μs. The radiation dose for a backscatter scan is low enough for scans to be performed on vehicles without the driver leaving the vehicle. For example, a scan using the AS&E ZBV backscatter scanner (which will be discussed in more detail in Section 3.3) the dose to the driver is $<$0.04 μSv per scan at a driving speed of 5 $\mathrm{km\,h^{-1}}$ [72], and 0.07 μSv per scan at 1.5 $\mathrm{km\,h^{-1}}$ [10] (assuming a scan distance of 1.5 m in both cases). In both cases this adheres to the American National Standards Institute limit of $<$0.1 μSv per backscatter scan (ANSI standard N43.17) [72].

3.2 Detector material and signal processing

As discussed in Section 3.1, the acquisition time per pixel in the backscatter system is $\sim$20 μs. The signal must be collected and processed by the electronics in 20 μs before the beam moves on to the next pixel to avoid the signals overlapping. It is therefore paramount that detectors with fast response times are used. Scintillation detectors are used such as $CaWO_4$, BaFCl, Gd_2O_2S (gadox) and PVT (as discussed in Section 2.4.2). The response times for these materials are 6 µs [73], 7 µs [74], 3 µs [75] and 1.6 ns [76] respectively.

In order to measure the energy spectrum of an x-ray beam using a Gadox detector for example, one photon should arrive no more rapidly than every 3 µs. If the excitation of the detector crystal is caused by one single photon then the amplitude of the scintillation pulse is directly proportional to that photon's energy. If multiple photons arrive before the crystal has a chance to decay, the amplitude of the scintillation pulse will not be proportional to one photon's energy but many different photon energies. The energy information for each photon is lost because there is no way of telling how the energy of each individual photon contributed to the pulse.

This is exactly what happens in the backscatter imaging process. The number of photons incident on the detector is of the order 600 photons μs^{-1} (calculated from signal-to-noise ratios reported in [77]), much higher than the 1 photon per 3 µs threshold for complete energy resolution. The result is the detectors can measure the intensity of the scattered beam but not any spectral information.

As a result the detector is operated in energy integration mode regardless of the detector material used. This is done to ensure high x-ray collection efficiency of the scattered beam which allows the time per scan to be kept to a minimum. A diagram of the energy-integration process in the data acquisition system is shown in Figure 3.2. The current pulse from the photo-multiplier tube (PMT) is converted in a voltage signal by a trans-impedance amplifier (TIA). The voltage pulse is then sent to an analog-to-digital converter (ADC). The ADC is sampled by a FPGA (field-programmable gate array which is a standard programmable circuit board) at a frequency of 5 MHz. The FPGA integrates over all the ADC samples in a 20 µs time window (100 samples) [78]. The total integrated value is the output detector response. The detector response value is then sent to image processing software and a greyscale value is

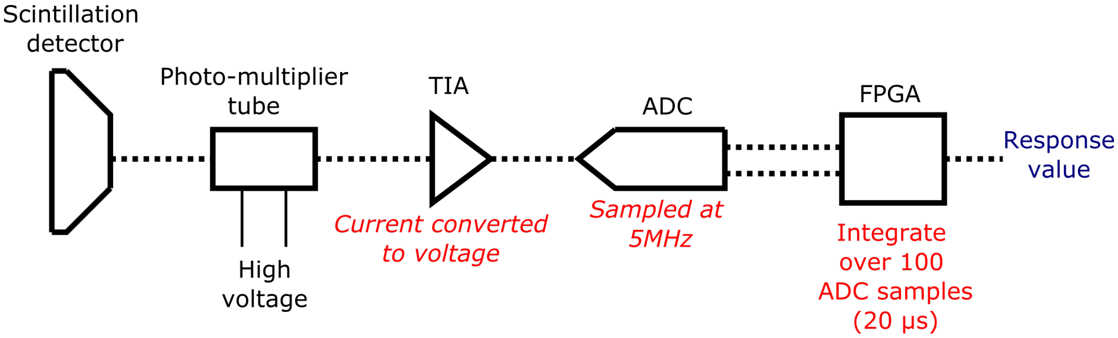

FIGURE 3.2: Data acquisition system flowchart for acquiring an energy-integrated detector response measurement [78]. From the photo-multiplier tube the signal passes to the trans-impedance amplifier (TIA) then to the analog-to-digital converter (ADC). The ADC is sampled at a rate of 5 MHz by the FPGA. The output detector response value is an integration over 100 samples of the ADC over a 20 µs time window.

assigned to the response to create one pixel in the image. On systems with multiple detectors, the response from all the individual detectors is summed and the sum is used by the image processing software.

3.3 Commercial systems

There are many x-ray backscatter imaging systems commercially available for security scanning of vehicles and cargo. One such system is the Rapiscan and AS&E Mobile-ZBV system [79]. The system has a 225 kVp x-ray source and a BaFCl scintillator detector panel which are mounted on the side of a van. The system is portable as it can be driven easily on public roads, and has a maximum vehicle scanning speed of 10 $\mathrm{km\,h^{-1}}$ [79]. The system is routinely used to scan trucks, lightly loaded cargo and passenger cars [9, 72].

Backscatter portal systems are also employed to scan passenger vehicles [80] and trucks and cargo [81]. Such systems utilise multiple detectors at different angles relative to the source in order to obtain up to six different views of the subject. These systems are extremely high throughput. Passenger systems of this type can scan up to 400 cars per hour [80], and cargo systems up to 250 trucks per hour [81]. Systems making use of both backscatter and transmission imaging (dual imaging systems) are also commonplace, such as the Eagle P60 ZBx portal system [82] and the Eagle M60 ZBx mobile system [83].

An example of a handheld device is the Mini-Z backscatter imaging system [12]. This system uses a 70 kV x-ray source and BaFCl detector panel. During operation the device is moved across the object of interest by the user and images are obtained in real time. The Mini-Z device can be used for scanning vehicle tyres, abandoned luggage and other areas of vehicles that are difficult to access.

3.4 Example backscatter image

An example backscatter system is shown in Figure 3.3. This system was a mobile backscatter system that was under development at Rapiscan Systems Cargo Division, Stoke-on-Trent, UK in April 2019. A picture of the full system is shown in Figure 3.3a. The backscatter imaging system was mounted on the chassis of a Mercedes truck.

The detector panel had 14 Gadox detectors each $300 \times 300\ \mathrm{mm}^2$ in area. Each detector had a PMT and signal processing unit connected behind it, as shown in Figure 3.3c. The x-ray beam collimator was behind the two empty central detector spaces on the second row of the detector panel. A picture of the collimator is shown in Figure 3.3b. The imaging unit

(A) Photograph of a backscatter image system in development showing the detector panel, position of x-ray source collimator and x-ray beam and path. The detector panel contains 14 detectors. The x-ray tube fires x-rays through the vertical gap in the detector panel. The rotating collimator (Fig. B) is used to generate a sweeping pencil beam. The x-ray tube cooling system and the detector acquisition system (Fig. C) are housed behind the detector panel in the container.

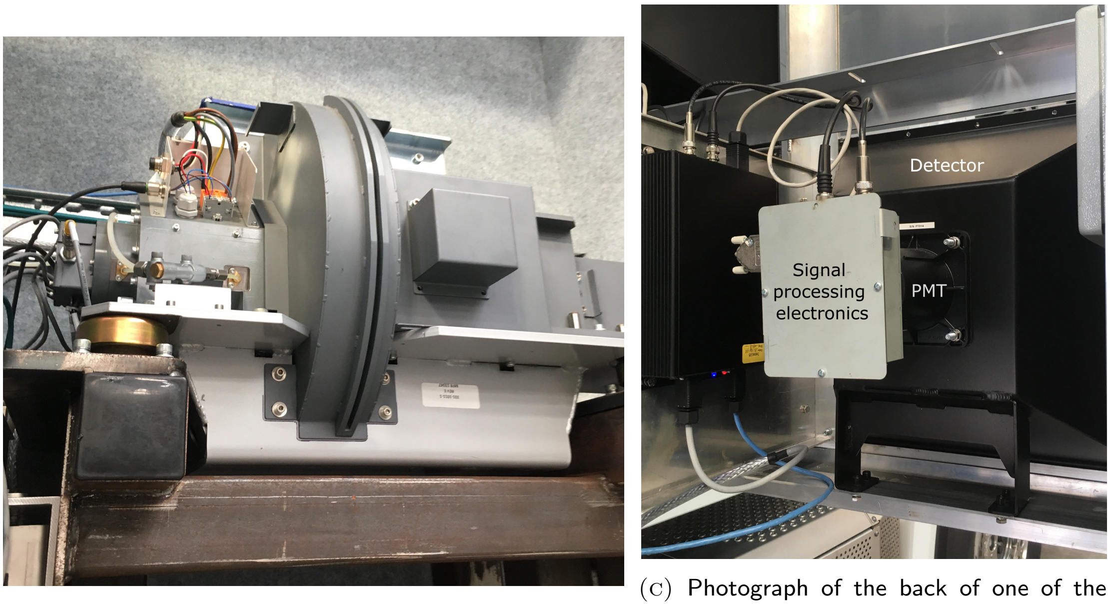

(B) Photograph of the rotating collimator used on the backscatter system. The device is used to create a sweeping pencil beam of x-rays.

(C) Photograph of the back of one of the backscatter detectors shown in the panel in (A). The white box shows the signal processing electronics and the black tube houses the PMT.

FIGURE 3.3: Labelled images of a backscatter system in development at Rapiscan Systems, Stoke-on-Trent. (A) is the full backscatter system, (B) is the x-ray source collimator and (C) is the back of one of the backscatter detectors. All author's own images.

also contained a cabin behind the detector panel which housed image processing and system monitoring computers. The cabin was accessible for personnel and was adequately shielded to ensure negligible radiation dose to the occupants while the system was scanning. Inside the cabin the acquired images were viewed.

Figure 3.4 shows a backscatter image of a forklift truck acquired using the development system. The forklift truck was carrying a test piece as part of an image performance analysis. The bottom section of the test piece was 50 mm thick HDPE. The top plate was 6 mm steel. A test piece containing HDPE rods of varying thickness was mounted on the front of the steel, and a HDPE diamond shaped test piece on the back of the steel. The forklift truck was driven forwards through the x-ray beam and then reversed back through the beam. A single image was acquired so the truck appeared twice. The truck was reversed at a slower speed than it was driven forwards which is why the right hand image of the truck was wider than the left hand image. The total acquisition time was approximately 30 s.

FIGURE 3.4: Backscatter image of a forklift truck carrying a test piece comprised of steel (top) and HDPE (bottom).

The image demonstrates the level of material identification that is currently achievable with field backscatter systems. The image clearly shows the distinction between organic and inorganic materials. The organic materials such as the HDPE plastic on the test piece and the driver's body appear bright in the image indicating a high-intensity of backscattered beam. The inorganic materials such as the steel part of the test piece and the body of the forklift truck appear much darker as the backscatter signal from these materials is much lower in intensity. This level of separation is clearly adequate to pick out shapes in the image. However, the person's body and the HDPE plastic test piece appear the same brightness even though they are made from very different organic materials. Therefore materials can only be broadly classified as organic or inorganic and in order to improve material separation beyond this the technology must be improved. The next chapter will discuss how this can be achieved using spectrum unfolding methods.

Chapter 4

The energy spectrum reconstruction method

To improve material identification in x-ray backscatter imaging, spectral information about the x-rays that are being scattered is required. Spectral information cannot be acquired directly from the detectors used on field systems as these detectors are energy integrating. The central idea of this work is to acquire spectral information from detector response measurements using a series of detector filters and a spectrum reconstruction algorithm. This chapter will present the theory behind how this is achieved.

Firstly the theory of inverse problems is discussed. The Tikhonov regularisation method is presented as a way of solving such problems. The theory is then applied to the energy spectrum reconstruction problem. The features of Tikhonov solutions when applied to this problem are then investigated through a discussion of solution intrinsic error, measurement error and stability. Practical considerations such as the choice of filters are discussed in depth.

It should be noted that throughout this chapter the mathematical definition of "consistent" is used which means there is at least one solution to the system of equations. The term "inconsistent" means there is no solution to the system of equations.

4.1 Theory of inverse problems

Consider the linear system

$$\mathbf{A}\vec{x} = \vec{b}. \tag{4.1}$$

The system describes how a set of measurements can be related to a physical model and a set of parameters. The physical model is given by the matrix $\mathbf{A}$, the parameters by the vector $\vec{x}$

and the measurements by the vector $\vec{b}$. Often it is necessary to find the parameters of a model given a set of measurements, hence find $\vec{x}$ given an assumed model $\mathbf{A}$ and measurements $\vec{b}$. This is known as the inverse problem.

In the case where the system is consistent, the solution is $\vec{x} = \mathbf{A}^{-1}\vec{b}$. However in practice measurement errors and model simplifications mean that the system is more likely an inconsistent system that can be described as

$$\mathbf{A}\vec{x} \simeq \vec{b}. \tag{4.2}$$

Complex systems in many scientific fields are modelled using this type of linear system. Solving the inverse problem is therefore fundamental to many scientific methods, including geological surveying [84], image deblurring [85] and x-ray tomographic imaging [30].

4.1.1 Finding the least squares solution

Consider the inconsistent system given in Equation 4.2, $\mathbf{A}\vec{x} \simeq \vec{b}$. $\mathbf{A}$ is taken to be a square matrix of size n, and $\vec{x}$ and $\vec{b}$ vectors with length n. This is the case where there are as many unknown model parameters as data measurements.

The system $\mathbf{A}\vec{x} \simeq \vec{b}$ has no solution $\vec{x}$ so that $\mathbf{A}\vec{x} = \vec{b}$. Instead the least squares solution to the problem can be found. This is the solution that minimises the difference between the recorded data, $\vec{b}$ and the calculated solution, $\mathbf{A}\vec{x}$, known as the residual vector $\vec{r}$,

$$\vec{r} = \mathbf{A}\vec{x} - \vec{b}. \tag{4.3}$$

This is equivalent to minimising the length of the vector $\vec{r}$, given by the 2-norm of $\vec{r}$,

$$||\mathbf{A}\vec{x} - \vec{b}||_2 = ||r||_2 = \sqrt{\sum_i r_i^2}. \tag{4.4}$$

Here $||\vec{r}||_2$, is the 2-norm of $\vec{r}$ and r_i represents the projection of $\vec{r}$ along $\hat{\imath}$. All $\hat{\imath}$ are orthogonal basis vectors. The matrix $\mathbf{A}$ can be written as $\mathbf{A} = [\vec{a_1}, \vec{a_2}, ..., \vec{a_n}]$, where $\vec{a_i}$ are column vectors. The column space of $\mathbf{A}$ is defined as the space spanned by these column vectors. A representation of the column space of $\mathbf{A}$ is shown in Figure 4.1. The column space is shown as 2-dimensional for ease of visualisation however this does not have to be the case generally.

All the vectors $\vec{c}$ for which the system $\mathbf{A}\vec{x} = \vec{c}$ is consistent lie within the column space of $\mathbf{A}$, $\mathrm{Col}(\mathbf{A})$, meaning they lie in the space spanned by the column vectors $\vec{a_i}$. In order to find the vector c that is closest to b, b is projected onto $\mathrm{Col}(\mathbf{A})$. This projection is denoted $\hat{b}$. The

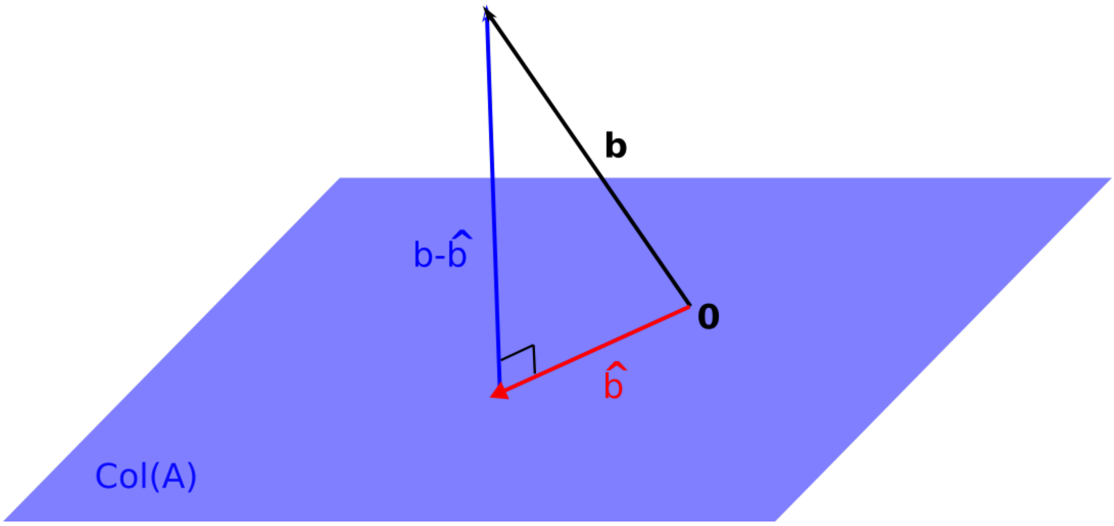

FIGURE 4.1: A diagram showing the projection of $\vec{b}$ onto the column space of $\mathbf{A}$, $\mathrm{Col}(\mathbf{A})$. The projection is $\hat{b}$. $\hat{b}$ is the least squares solution to $\mathbf{A}\vec{x} = \vec{b}$. The vector $\vec{b}-\hat{b}$ is perpendicular to $\hat{b}$ and the plane $\mathrm{Col}(\mathbf{A})$ [86]. $\mathrm{Col}(\mathbf{A})$ is shown as a 2-dimensional plane for ease of visualisation, however in general can be any dimension.

least squares solution is given by $\hat{x}$ where $\mathbf{A}\hat{x} = \hat{b}$ because $\hat{b}$ is the vector in $\mathrm{Col}(\mathbf{A})$ most similar to $\vec{b}$ so $\vec{r}$ is minimised. This process is shown in Figure 4.1.

$\vec{b} - \hat{b}$ is perpendicular to $\hat{b}$ and hence is orthogonal to the column vectors of $\mathbf{A}$. Therefore for every a_i, $\vec{a_i} \cdot (\vec{b} - \hat{b}) = 0$. Hence,

$$\mathbf{A}^T(\vec{b} - \hat{b}) = \begin{bmatrix} \vec{a_1} \\ \vec{a_2} \\ \dots \\ \vec{a_n} \end{bmatrix} \cdot (\vec{b} - \hat{b}) = 0. \tag{4.5}$$

Rearranging Equation 4.5 and substituting $\mathbf{A}\hat{x}$ for $\hat{b}$ gives,

$$\mathbf{A}^T\mathbf{A}\hat{x} = \mathbf{A}^T b \tag{4.6}$$

Equation 4.6 defines a consistent system which can be solved for $\hat{x}$,

$$\hat{x} = (\mathbf{A}^T\mathbf{A})^{-1}\mathbf{A}^T\vec{b}, \tag{4.7}$$

the least squares solution which minimises $||\vec{r}||_2$. Although a solution exists, the solution may not be unique. There are multiple least squares solutions when the column vectors a_i are co-planar rather than orthogonal, and in almost all physical applications this will be the case.

Therefore there are may ways to write the solution $\hat{b}$ as a linear combination of $[\vec{a_1}, \vec{a_2}, ..., \vec{a_n}]$. If $\vec{a_i}$ are orthogonal there is only one way to write $\hat{b}$ and hence only one least squares solution.

4.2 Tikhonov regularisation

In most real-world applications of inverse problems, there are many least squares solutions to the problem $\mathbf{A}\vec{x} \simeq \vec{b}$, especially if the dimensions of $\mathbf{A}$ are large. Tikhonov regularisation [87] (also known as ridge regression) is one well established method that can be used to choose the most suitable least squares solution. This will now be explained by following references [88–90]. As in Section 4.1.1, $\mathbf{A}$ is a square matrix of size n and $\vec{x}$ and $\vec{b}$ are vectors of length n.

The Tikhonov solution can be written as

$$min\ ||\mathbf{A}\vec{x} - \vec{b}||_2^2 + \beta||\vec{x}||_2^2 \tag{4.8}$$

where β is a factor known as the regularisation parameter. This controls how much the solution $\vec{x}$ is regularised by the $||\vec{x}||_2^2$ term.

Equation 4.8 can be written as

$$min\ || \begin{bmatrix} \mathbf{A} \\ \beta \vec{I} \end{bmatrix} \vec{x} - \begin{bmatrix} \vec{b} \\ 0 \end{bmatrix} ||_2^2 \tag{4.9}$$

where $\mathbf{I}$ is the identity matrix. Rewriting $[\mathbf{A}\ \beta\mathbf{I}]^T$ as the matrix $\mathbf{P}$, we obtain,

$$min\ ||\mathbf{P}\vec{x} - \vec{b}||_2^2 \tag{4.10}$$

which is the same as solving the problem $\mathbf{P}\vec{x} = \vec{b}$ for the least squares solution. As discussed in Section 4.1.1, the least squares solution is

$$(\mathbf{P}^T\mathbf{P})^{-1}\vec{x} = \mathbf{P}^T\vec{b}. \tag{4.11}$$

Substituting back in for $\mathbf{P}$ and multiplying out yields,

$$[\mathbf{A}^T\ \beta\mathbf{I}] \begin{bmatrix} \mathbf{A} \\ \beta\mathbf{I} \end{bmatrix} x = [\mathbf{A}^T\ \beta\mathbf{I}] \begin{bmatrix} \vec{b} \\ 0 \end{bmatrix}, \tag{4.12}$$

$$(\mathbf{A}^T\mathbf{A} + \beta^2\mathbf{I})\vec{x} = \mathbf{A}^T\vec{b}. \tag{4.13}$$

Rearranging for $\vec{x}$ gives the Tikhonov solution,

$$\vec{x_\beta} = (\mathbf{A}^T\mathbf{A} + \beta^2\mathbf{I})^{-1}\mathbf{A}^T\vec{b}. \tag{4.14}$$

4.2.1 The L-curve method

The Tikhonov solution depends entirely on the value of the regularisation parameter β. The L-curve method can be used to decide on the best value of β for the particular application. Figure 4.2 shows the relationship between $||A\vec{x} - \vec{b}||_2^2$ and $||\vec{x}||_2^2$, known as the L-curve. The "L" shape is characteristic of all inverse problems. For the lowest $||A\vec{x} - \vec{b}||_2^2$ there is a very rapid increase in $||\vec{x}||_2^2$ as $||A\vec{x} - \vec{b}||_2^2$ decreases. For larger $||A\vec{x} - \vec{b}||_2^2$, in the region to the right of the corner of the 'L', solutions to $\vec{x}$ are much smoother and low values of $||\vec{x}||_2^2$ result.

To find β all the solutions where $||A\vec{x} - \vec{b}||_2^2 \geq \delta$ are considered. Here δ is the total error in the data (if $\vec{b}$ is the measured data where $\vec{b} = \{b_1, b_2, ..., b_n\}$, then $\delta = \sum_{i=1}^{n} \sigma_{b_i}$ where σ_{b_i}

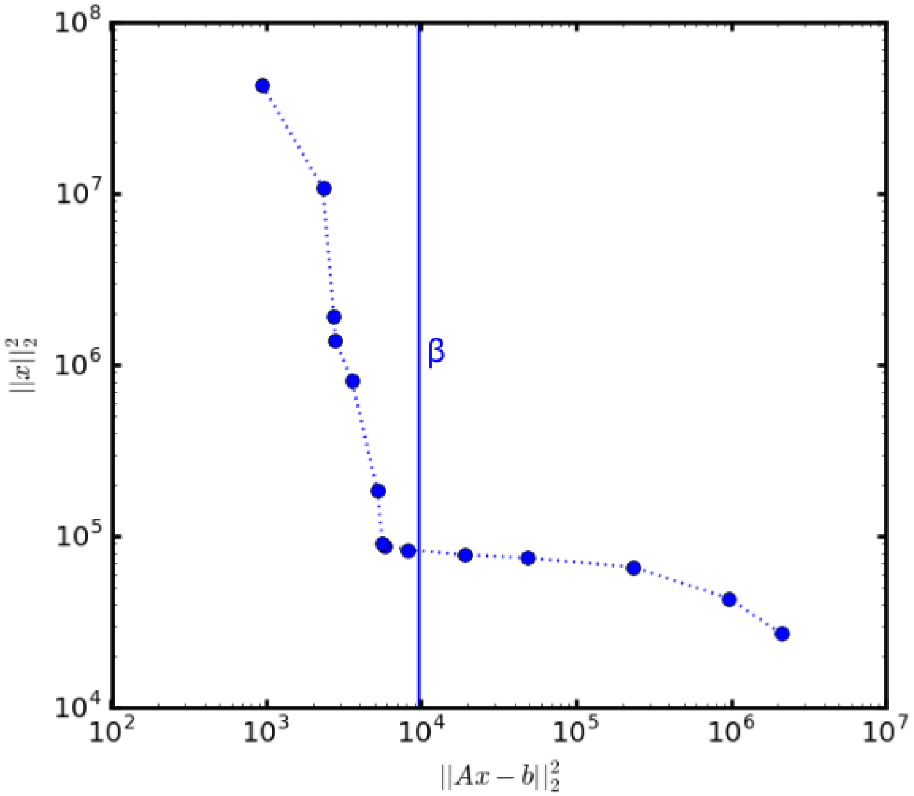

FIGURE 4.2: The relationship between the 2-norm of the residual $||Ax-b||_2^2$ and the 2-norm of the solution $||x||_2^2$ for an example inverse problem. The curve shape is characteristic of all inverse problems. The vertical line labelled β marks the value of β calculated using Morozov's discrepancy principle using an error δ, as discussed in Section 4.2.1. The point is just to the right of the corner of the L meaning the solution will have a small residual and also be stable.

is the error associated with the measurement b_i). When $||A\vec{x} - \vec{b}||_2^2$ becomes smaller than δ, the solution is no longer an accurate representation of the data. Because the residual is now smaller than the errors in the data, the noise in the data is now being fitted rather than the data itself. However, if $||A\vec{x}-\vec{b}||_2^2$ is too large, the Tikhonov solution will be overly regularised meaning any features in the solution will be smoothed over. The Tikhonov solution is the solution out of the set of solutions with $||A\vec{x} - \vec{b}||_2^2 \ \geq \ \delta$ with the smallest $||\vec{x}||_2^2$.

The optimum solution lies just to the right of the corner of the L on the L curve where both $||A\vec{x} - \vec{b}||$ and $||\vec{x}||$ are small. This should correspond to the point where $||A\vec{x} - \vec{b}|| = \delta$, where δ is the noise in the data. The value for β must be chosen so the $||A\vec{x} - \vec{b}|| = \delta$ solution is selected, which is typically done using numerical methods. One such method is an implementation of Morozov's discrepancy principle [91, 92], although other methods do exist such as the triangle method [93].

4.2.2 Morozov's discrepancy principle

Following [91], in the Morozov discrepancy principle method, an initial value for $\beta = \beta_0$ and a step size d are defined. The initial value is arbitrary, but greater than zero. An initial solution, x_0 is found using Equation 4.14, and the residual $||A\vec{x_0} - \vec{b}||$ is evaluated. If this residual is greater than δ then β is increased by a factor of d, $\beta_1 = \beta_0 d$. A solution $\vec{x_1}$ found using Equation 4.14. The residual $||A\vec{x_1} - \vec{b}||$ is evaluated, and if it is again less than δ, β is increased again by the step size d, $\beta_2 = \beta_0 d^2$. This process is repeated k times until β_k yields a residual less than δ. Therefore we have $||A\vec{x}_{\beta_{k-1}} - \vec{b}|| > \delta$ and $||A\vec{x}_{\beta_k} - \vec{b}|| < \delta$.

The next stage is to hone in on the value of β to get as close to the $||A\vec{x}_\beta - \vec{b}|| = \delta$ solution as possible. An average value β_l is selected where $\beta_{min} = \beta_{k-1}$ and $\beta_{max} = \beta_k$,

$$\beta_l = \frac{(\beta_{min} + \beta_{max})}{2}, \tag{4.15}$$

and x_{β_l} is evaluated. If $||A\vec{x}_{\beta_l} - \vec{b}|| < \delta$, then $\beta_{min} = \beta_l$. If $||A\vec{x}_{\beta_l} - \vec{b}|| > \delta$ then $\beta_{max} = \beta_l$. β_l is then recalculated using Equation 4.15 with the new values of β_{min} or β_{max}. The process is repeated until $||A\vec{x}_{\beta_l} - \vec{b}|| = \delta$ and $\beta = \beta_l$.

4.2.3 Evaluating errors in the Tikhonov solution

In order to determine the error in the Tikhonov solution based on the error in the data, the covariance matrix of x must be evaluated, $Cov(x)$. $Cov(x)$ is a diagonal matrix $Cov(x) = diag(\sigma_{x_1}^2, \sigma_{x_2}^2, ..., \sigma_{x_n}^2)$, where σ_{x_i} is the error in the measurement of x_i.

As discussed in Section 4.2, the Tikhonov solution is given by

$$\vec{x}_\beta = (A^T A + \beta^2 I)^{-1} A^T \vec{b}, \tag{4.16}$$

therefore, $Cov(\vec{x_\beta})$ is

$$Cov(\vec{x}_\beta) = Cov((A^T A + \beta^2 I)^{-1} A^T \vec{b}). \tag{4.17}$$

Using the relationship $Cov(A\vec{x}) = ACov(\vec{x})A^T$ [88], Equation 4.17 can be written as

$$Cov(\vec{x}_\beta) = (A^T A + \beta^2 I)^{-1} A^T Cov(\vec{b}) A (A^T A + \beta^2 I)^{-1}. \tag{4.18}$$

$Cov(\vec{b})$ is a diagonal matrix $Cov(\vec{b}) = diag(\sigma_{b_1}^2, \sigma_{b_2}^2, ..., \sigma_{b_n}^2)$, where σ_{b_i} is the error in the measurement of b_i. The errors in each x_{β_i} are given by the elements of $Cov(\vec{x}_\beta)$. Note that the errors given in $Cov(\vec{x}_\beta)$ are only due to the errors in the measurement of $\vec{b}$ and do not take into account the choice of β which will add additional bias to the solution.

4.3 Spectrum reconstruction as an inverse problem

The following section will show how the energy spectrum reconstruction problem can be formulated and solved as an inverse problem. The method in this section was independently formulated by the author but since discovered a similar formulation by I Kanno *et al.* The technique is called "energy spectrum unfolding" and has been applied to x-ray CT for medical applications [24–29], and recently shown promising developments in material identification in x-ray CT [94, 95].

The detector response from an energy integrating detector D, can be written as [26]

$$D = \int_0^{E_{max}} EN(E)\, dE, \tag{4.19}$$

where E is the photon energy, $N(E)$ is the number of photons with energy E, and E_{max} is the maximum energy in the energy spectrum. The equation describes a perfect case that does not account for detector efficiency effects. Equation 4.19 can be discretised so that

$$D \approx \sum_{i=0}^{m} E_i N_i \tag{4.20}$$

where N_i is the number of counts in bin i and E_i is the bin energy (usually the bin centre) over the energy range 0 to E_{max}. The total number of bins in the spectrum is m.

Consider a hypothetical energy spectrum where m=2. The spectrum consists of two bins with the midpoint energy of each bin as E_0 and E_1. The number of counts in each bin is N_0 and N_1. In order to reconstruct (or "unfold") the energy spectrum, two different detector response measurements are required, each with a different thickness of filter. If the spectrum is passed through two different filters, one with thickness x_0 and the other with thickness x_1, we obtain the following relations

$$\begin{aligned} D_{x_0} &= E_0 N_0 e^{-\mu(E_0)x_0} + E_1 N_1 e^{-\mu(E_1)x_0} \\ D_{x_1} &= E_0 N_0 e^{-\mu(E_0)x_1} + E_1 N_1 e^{-\mu(E_1)x_1} \end{aligned} \tag{4.21}$$

through Equation 4.20 and the Lambert-Beer law given in equation Equation 2.10. Equation 4.21 is a set of two simultaneous equations which can be solved for N_0 and N_1 provided D_{x_0} and D_{x_1} are known. D_{x_0} and D_{x_1} are the filtered response measurements so can be measured experimentally. Equation 4.21 can be written in matrix form as

$$\begin{pmatrix} D_{x_0} \\ D_{x_1} \end{pmatrix} = \begin{pmatrix} E_0 e^{-\mu(E_0)x_0} & E_1 e^{-\mu(E_1)x_0} \\ E_0 e^{-\mu(E_0)x_1} & E_1 e^{-\mu(E_1)x_1} \end{pmatrix} \begin{pmatrix} N_0 \\ N_1 \end{pmatrix}. \tag{4.22}$$

This demonstrates that in order to calculate an energy spectrum with two bins, a detector response measurement D should be acquired for two different filters and the above system of linear equations solved for N_0 and N_1. N_0 and N_1 give the number of photons with energy E_0 and E_1 respectively, hence an estimation of the energy spectrum.

This can be generalised for a spectrum with m bins calculated using n different filtered detector response measurements. The system of linear equations

$$\begin{pmatrix} D_{x_0} \\ D_{x_1} \\ \ldots \\ D_{x_n} \end{pmatrix} = \begin{pmatrix} E_0 e^{-\mu(E_0)x_0} & E_1 e^{-\mu(E_1)x_0} & \ldots & E_m e^{-\mu(E_m)x_0} \\ E_0 e^{-\mu(E_0)x_1} & E_1 e^{-\mu(E_1)x_1} & \ldots & E_m e^{-\mu(E_m)x_1} \\ \ldots & \ldots & \ldots & \ldots \\ E_0 e^{-\mu(E_0)x_n} & E_1 e^{-\mu(E_1)x_n} & \ldots & E_m e^{-\mu(E_m)x_n} \end{pmatrix} \begin{pmatrix} N_0 \\ N_1 \\ \ldots \\ N_m \end{pmatrix}. \tag{4.23}$$

is then solved to reconstruct an energy spectrum with m bins. For clarity Equation 4.23 can be written as

$$\vec{D} = \mathbf{W}\vec{N}, \tag{4.24}$$

or, when taking into account measurement uncertainties in $\vec{D}$,

$$\vec{D} \simeq \mathbf{W}\vec{N}, \tag{4.25}$$

where $W_{ij} = \sum_i^n \sum_j^m E_j e^{-\mu(E_j)x_i}$. $\mathbf{W}$ is known as the system matrix. As the energy spectrum is continuous, $\mathbf{W}$ can be thought of as a sample of the filtered detector response at particular energies and material thicknesses. This method for generating $\mathbf{W}$ is known as the quadrature method [89]. Equation 4.25 is the same form as the general inverse problem presented in Section 4.1. The number of counts in each energy bin (the spectrum) can be found by solving the inverse problem.

4.4 Choice of filters

An integral part of the reconstruction problem is the choice of filters $\{x_0, x_1, ...x_n\}$. The choice of filters depends on the spectrum reconstruction problem, particularly on the x-ray spectrum energy range and the number of energy bins required. The filter material is also a consideration to ensure the experiment can be carried out practically. This section provides some practical details about the choice of filter thickness. Further experimental details are explained in Section 5.6.

The chosen spectrum energy range was 0-50 keV. This was because a 50 kVp x-ray tube was used in the experiment, thus the maximum energy scattered (coherently) was 50 keV. In this work, only the case where $m{=}n$ was considered. Ten filters were used ($m{=}n{=}10$), determined to be the minimum number of bins to see detail in the energy spectrum. Aluminium was chosen as the filter material to provide appropriate filtration within the energy range of interest without the filters being too thin or thick within the geometry constraints.

The thicknesses of aluminium were chosen so that for each energy bin the percentage of gamma rays transmitted at the bin-centre energy was 10%. This transmission percentage was chosen to ensure a measurable difference between filters and a reasonable detection rate for each filter. The same transmission percentage was used for each filter to ensure linear bin spacing. As this was a proof-of-concept study, a constant transmission percentage was used as the simplest case. Other combinations of transmission percentages and non-linear bin spacing were not considered but will be the subject of discussion and future work (see Section 9.2.2).

This filter thickness x_f was calculated by considering the attenuation equation given by the Lambert-Beer law (Equation 2.10),

$$x_f = \frac{1}{\mu(E_C)} ln(10) \tag{4.26}$$

where $\mu(E_c)$ is the attenuation coefficient for aluminium at the bin centre energy, E_c, as quoted in the NIST XCOM database [52]. The thinnest filter (filter A) was 0.0066 mm thick (10% of 2.5 keV x-rays transmitted through 0.0066 mm of aluminium), and the thickest filter (filter J) was 21.1 mm thick (10% of 47.5 keV x-rays transmitted through 21.1 mm of aluminium). All other the filter thicknesses are given in Table 4.1.

#	E_C, keV	Filter thickness, mm
A	2.5	0.0066 ± 0.0015
B	7.5	0.14 ± 0.01
C	12.5	0.63 ± 0.02
D	17.5	1.68 ± 0.09
E	22.5	3.47 ± 0.16
F	27.5	6.0 ± 0.22
G	32.5	9.26 ± 0.28
H	37.5	13.0 ± 0.34
I	42.5	17.0 ± 0.38
J	47.5	21.1 ± 0.43

TABLE 4.1: Thicknesses of aluminium filter used for the ten bin spectrum reconstruction. Errors quoted are due to experimental uncertainties and are discussed in Section 5.6.

4.5 Correcting for experimental effects (RCF)

The spectrum reconstruction formulation discussed in Section 4.3 assumes the detector response is only due to the proportion of the backscattered beam that has traversed the entire thickness of the filter. However, experimentally additional factors such as scattering will increase the detector response above this. In addition, experimental factors change the detector response compared to what is expected from the simple model. Such effects include the x-ray tube alignment, errors in the filter thickness and detector efficiency effects (for example escape events, charge trapping and polarisation in CdTe [61, 67, 96]).

In order to account for these effects, a response correction factor, referred to as the RCF or by the variable α in what follows, was introduced into the system of linear equations to give,

$$\vec{\alpha}\vec{I} = \mathbf{W}\vec{N}. \tag{4.27}$$

$\vec{I}$ is a vector with elements I_j and $\mathbf{W}$ is a matrix of calculated attenuation factors describing how each of the bin centre energies is attenuated by each filter, and $\vec{N}$ is the vector representation of the m bin energy spectrum, all as in Section 4.3. $\vec{\alpha}$ is a vector with elements α_j where α_j is the RCF for filter j. If $\vec{I}$ and $\vec{N}$ are both known then α_j can be calculated as

$$\alpha_j = \frac{\left(\sum_{k=1}^{m} W_{jk} N_k\right)}{I_j}. \tag{4.28}$$

The error in the RCF was calculated through error propagation to be

$$\sigma_{\alpha_j} = \alpha_j \sqrt{\frac{\sum (W_{jk}\sigma_{N_k})^2}{(\sum W_{jk} N_k)^2} + \left(\frac{\sigma_{I_j}}{I_j}\right)^2}, \tag{4.29}$$

where σ_{α_j} is the error on α_j and σ_{N_k} is the error on N_k. Here $\sum_{k=1}^{m}$ has been shortened to $\sum$.

Following [25] a calibration process was developed to determine α_j for each filter. The scatter geometry was simulated for a calibration material using a simple scatter geometry (see Section 6.5 for details). The resulting simulated spectrum (binned to m energy bins) was used for $\vec{N}$. Response measurements for the same calibration material were acquired experimentally for each of the filters in Table 4.1 giving $\vec{I}$. $\vec{\alpha}$ was then calculated using Equation 4.28. In essence the calibration method involved comparing the perfect case (simulation) to what was actually measured experimentally, filter by filter. The factor by which the simulation and experiment were different was the correction factor α_j. Details of the experimental measurements performed for the calibration are provided in Section 5.7.

4.6 Tikhonov regularisation for spectrum reconstruction

Tikhonov regularisation was used in this project to solve the inverse problem and hence calculate the energy spectrum. Tikhonov regularisation was used as solutions were expected to be smooth from the knowledge of the backscatter spectra (this will be discussed in more detail in Section 5.5.1). Additionally, Tikhonov regularisation has been used with success in other applications of spectrum unfolding using x-ray tube spectra [97, 98]. The method was also familiar to the author from previous work.

4.6.1 δ parameter

The error parameter δ, used to calculate the β regularisation parameter, was calculated by considering the total error in the data. This included contributions from the detector response measurements and the error in the alpha correction factor. Hence

$$\delta = \sqrt{\sum (\alpha_j I_j)^2 \left[\left(\frac{\sigma_{\alpha_j}}{\alpha_j} \right)^2 + \left(\frac{\sigma_{I_j}}{I_j} \right)^2 \right]}. \tag{4.30}$$

4.6.2 Non-negativity constraint

All elements of $\vec{N}$ must be positive because negative values for the number of counts in a spectrum is unphysical. In Tikhonov regularisation it is not possible to directly incorporate this information into the process of finding the solution. Therefore for the Tikhonov solution the non-negativity constraint was implemented after the solution was found by setting all the negative components of $\vec{N}$ to zero.

4.7 Behaviour of Tikhonov solutions

To understand the behaviour of Tikhonov solutions in the backscatter problem, a simplified backscatter geometry was simulated. Details of this simulation will be given in Section 6.5. Energy integrated measurements for ten filters given in Table 4.1 were simulated for a 10 mm Nylon scatter object using the simple simulation geometry (as before, see Section 6.5). No filters or detector effects were simulated and filters were added mathematically post-simulation in a process that is described in Section 6.5.4. The simulation allowed understanding of the Tikhonov solutions in the perfect case energy spectrum reconstruction problem and provided insight into how reconstructions from experimental data would behave. From this intrinsic errors, effect of the error parameter and stability were investigated. As the simulation was simplified, no RCF was required (e.g. $\vec{\alpha} = \vec{1}$ and $\vec{\sigma_\alpha} = \vec{0}$).

Spectra were compared by calculating the difference parameter, d. The difference parameter is a modified Euclidean distance measure and is defined as

$$d = \frac{\sqrt{\sum_{j=1}^{10}(N_{1_j} - N_{2_j})^2}}{\sqrt{\sum_{j=1}^{10}(N_{1_j})^2}}. \tag{4.31}$$

Here N_{1_j} and N_{2_j} are the number of counts in bin j of spectrum 1 and spectrum 2 respectively. The parameter d is expressed as a percentage difference. In imaging applications typically the root-mean-squared deviation (RMS) is used to compare solutions, however the RMS is dependent on the number of counts in the spectrum so would not allow a fair comparison across materials in this particular application. As the d metric contains a normalisation term in the denominator it avoids dependence on the total counts.

4.7.1 Intrinsic errors

Figure 4.3 shows the detector response as a function of filter thickness for the 10 mm Nylon simulation. The detector response decreased with increasing filter thickness at a decreasing rate. For example, between filters A-E the detector response changed from (2.171±0.007)$\times 10^6$ for filter A and (4.921±0.040)$\times 10^5$ for filter E with an average change of (-4.847±0.043$\times 10^5$) mm^{-1}. For filters F-J the change was less rapid with a response of (2.507±0.029)$\times 10^5$ for filter F and and (1.127±0.065)$\times 10^4$ for filter J with an average change of (-1.586±0.093)$\times 10^4$ mm^{-1}. This is just one example however. The exact shape of the detector response curve with filter thickness depends on the particular energy distribution of the x-rays being measured.

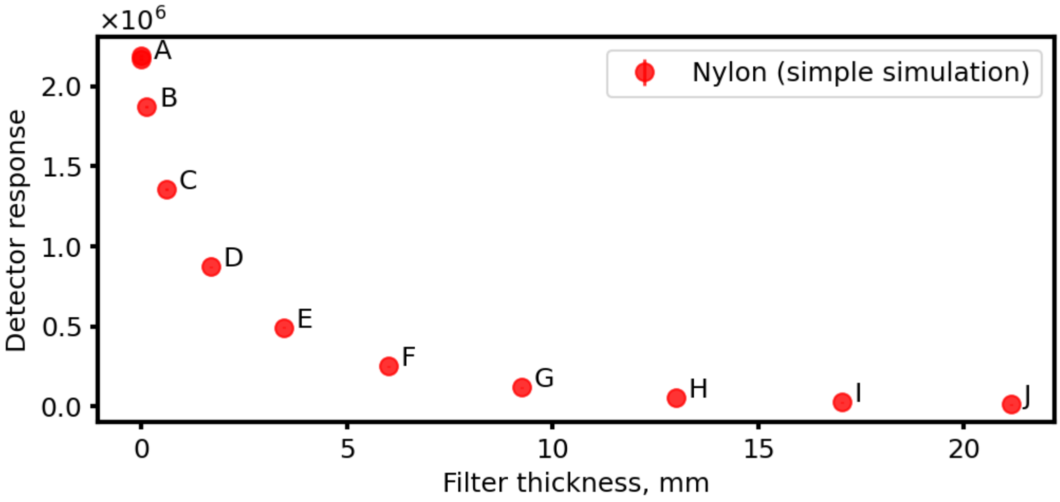

FIGURE 4.3: Simulated detector response as a function of filter thickness for a 10 mm thick Nylon sample with filters mathematically added. There is a rapid decrease in the detector response with increasing filter thickness for filters A-E. For filters F-J the decrease with increasing filter thickness is more gradual.

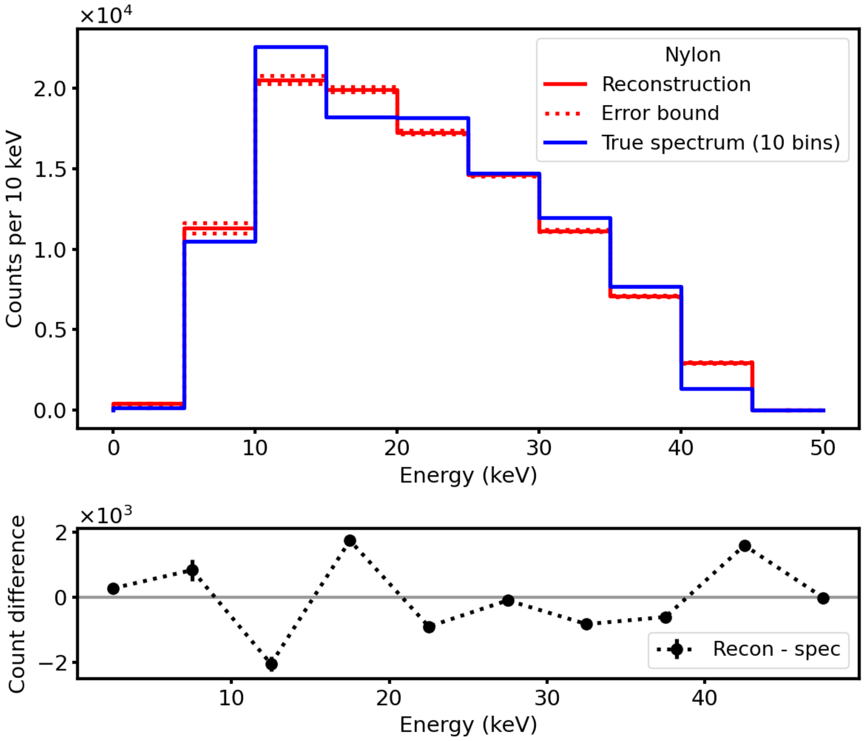

FIGURE 4.4: Reconstruction of the detector response data shown in Figure 4.3 with δ as the total Poisson error. The difference between the reconstruction and true spectrum is calculated as shown in black.

The detector response data in Figure 4.3 was then reconstructed using Tikhonov regularisation. The δ parameter was 0.1%, equivalent to the size of the Poisson error in the data. The result is shown in Figure 4.4 (red) compared to the true solution (blue). There are differences between the reconstruction and true spectrum with the percentage difference d at 8.7%. This is to be expected even in the perfect case given that the model used (the matrix $\mathbf{W}$) is an approximation and, to a greater extent, the fact that Tikhonov solutions are regularised. This means that deviations between bins will be smoothed out.

In the true spectrum there is a peak in the third bin (10-15 keV) but this has not been reproduced in the reconstruction to the same extent. Instead the peak is spread over bins 3 and 4. In the third bin the reconstruction is 2040±233 counts (9%) lower than the true spectrum, and in the fourth bin the reconstruction is 1744±154 counts (10%) higher than the true spectrum.

Smoothing also causes problems at the lower and upper bounds of the spectrum. In the true spectrum there is a change of 6335 counts between bin 8 and bin 9, then a change of 1337 counts between bin 9 and bin 10. In the reconstruction this change is more gradual with a change of 4142±57 between bin 8 and 9 and 2941±46 between bin 9 and 10. As a result, the reconstruction of bin 9 is 1594±33 counts (118%) higher than the true spectrum. Similarly bin 1 is 280±16 counts (209%) higher and bin 2 837±332 counts (8%) higher to smooth out the change between bin 1 and bin 3. The area where the reconstruction is closest to the true solution is the 20-40 keV region (bins 5-8), with a maximum difference of 895±113 counts (bin 5). This region is reconstructed more closely as this part of the true spectrum is smooth.

In summary even in the perfect case considered here, the reconstruction still produces deviations from the true spectrum with the dominant contribution to this being the regularisation of the reconstruction method.

4.7.2 Error parameter

The error parameter δ has a large influence on the reconstruction process as it controls the regularisation. The simulated data set was reconstructed with different values for the error parameter δ to understand what this means for the Tikhonov solution calculated. Different δ values were calculated with δ as 5, 1, 0.1 and 0.001%. The reconstructions and corresponding L-curves for each δ are shown in Figure 4.5.

The smoothest solutions were found when δ was largest (Figure 4.5a). This corresponded to the solutions on to the right of the apex of the L on the L-curve (Figure 4.5b). Overly smooth solutions were characterised by more counts in the higher energy part of the spectrum

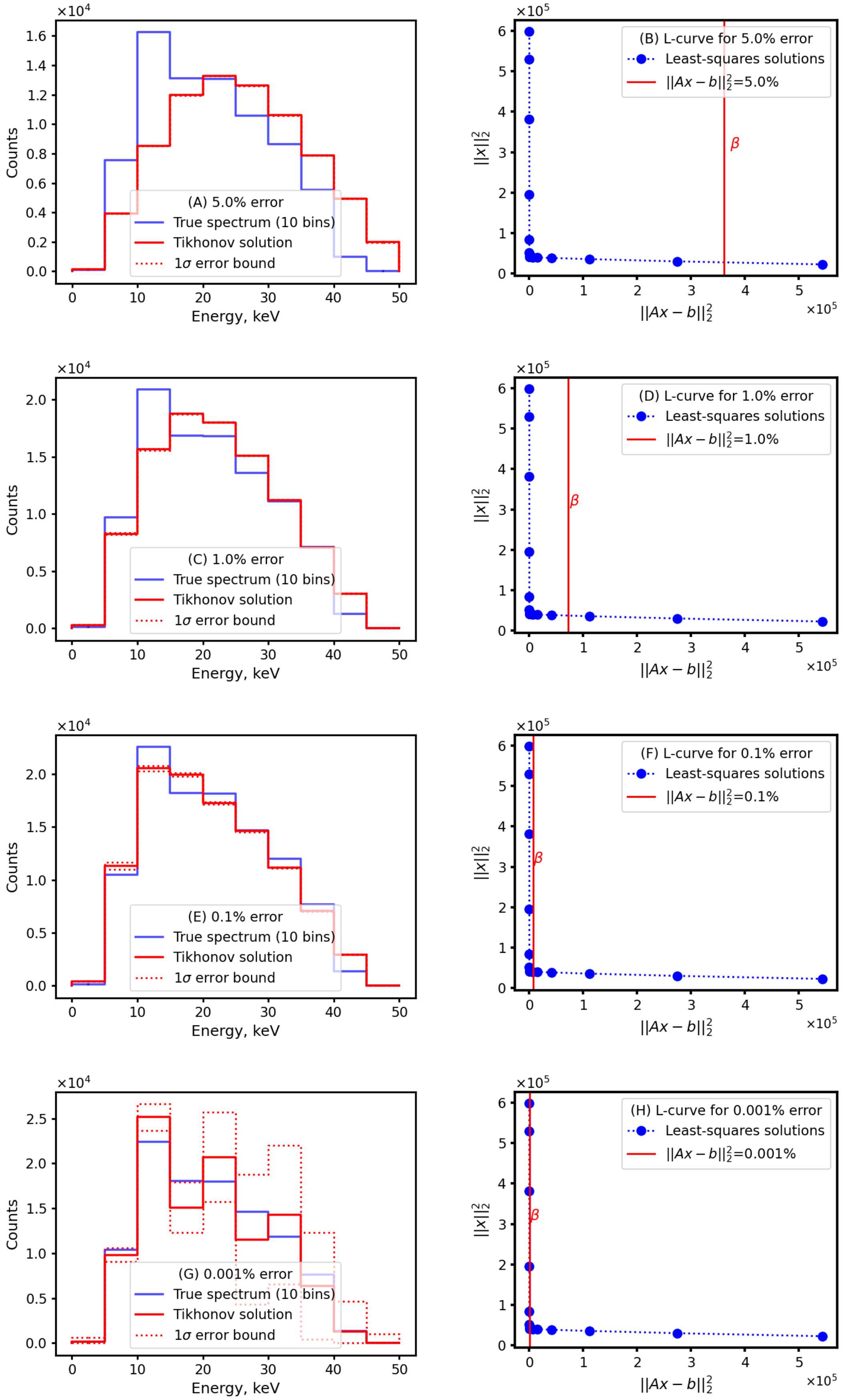

FIGURE 4.5: Reconstructions for different error parameters and associated L curves. (A) is the reconstruction when δ=5.0% and (B) the corresponding L curve. (C) shows the reconstruction and (D) the L-curve when δ=1.0%. (E)) shows the reconstruction and (F) the L-curve when δ=0.1% which is approximately equal to the Poisson error, or the true error in the data. (G) and (H) show the reconstruction and L-curve respectively when δ=0.001%.

than expected, particularly the 40-50 keV bins. A d value of (37.4±0.1)% represented a low similarity with the true spectrum.

As the error percentage was decreased, solutions became less smooth. As δ decreased from 5-0.1%, the Tikhonov solutions became more similar to the true spectrum with d=(16.9±0.2)% for δ=1% and d=(8.7±0.1)% for δ=0.1%. As δ decreased from 0.1-0.001% however, the solutions became less similar. For the smallest error, 0.001%, the chosen value of β was to the left of the apex of the L curve in the region where $||x||$ was changing very rapidly. As a result the reconstructed spectrum was less smooth than the true spectrum and less similar. This is because the as error was too small, the noise in the data was being fitted. Also note the error bounds for the 0.001% reconstruction. These are now much more significant demonstrating the reconstruction's sensitivity to noise in the initial solution. The d value was d=(15.2±31.5)% for δ=0.001%.

The actual value for the error in the data as calculated by Poisson statistics is approximately 0.1% which agrees with the correct position on the L curve for achieving a reconstruction that is not overly smooth but not fitting noise in the data. However, in some cases if the Poisson error is too large, the difference between an overly smooth solution and a solution where noise is being fitted may not be so distinct.

4.7.3 Stability

The stability of the reconstruction to perturbations was also investigated. Each detector response measurement was increased in turn by a certain percentage and the reconstruction performed. The percentage difference in the Tikhonov solution compared to the unperturbed solution was calculated. Figure 4.6 shows the percentage difference as a function of the filter with the perturbation. Perturbations of sizes 0.1, 0.5, 1.0 and 2.0% were investigated.

As shown in Figure 4.6, the thinnest filters were most sensitive to perturbations when compared to the thicker filters. This is in line with expectation as the greatest changes between detector response measurements occur for the thinnest filters in this example due to the spectral distribution (as shown in Figure 4.3). Perturbations to filters H-J caused little or no change to reconstruction even up to perturbations of 5% (maximum d was 0.7% for filter H at 5% perturbation). This is because the change in detector response measurements was less for thicker filters (as shown in Figure 4.3).

Multiple bins can be affected by a perturbation, not just the one corresponding to the filter the perturbation occurred in. This is due to the regularisation in the Tikhonov solutions; if one bin is changed then neighbouring bins will also change to smooth out the effect of the perturbation. For example, as shown in Figure 4.7a, when a 1% perturbation was applied to filter B, bins 2 and 3 changed by -61% and 16% respectively. However, as shown in Figure 4.7b, when a 1% perturbation was applied to filter E, bins 3 and 5 changed by 2% and -4% respectively.

To further quantify this effect, a perturbation of a certain percentage was applied to each of the filter measurements in turn and a reconstruction performed. Of the ten different reconstructions for that perturbation, the maximum and minimum values for each bin in the reconstruction were found. This is shown in Figure 4.8. This way it is possible to see how a perturbation of a certain size at any of the filters effects each bin. In agreement with the above discussion, Figure 4.8 showed the bins that were effected most by perturbations were the first four bins. For a perturbation of 0.1%, the count difference was 37 (9% of the total bin height) for bin 1, 715 (6%) for bin 2, 653 (3%) for bin 3 and 265 (1%) for bin 4. For a

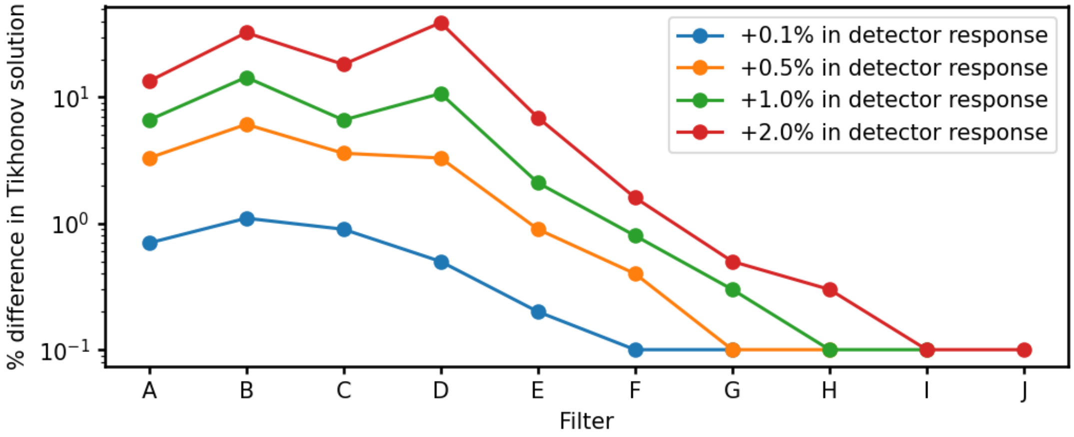

FIGURE 4.6: d as a function of perturbed filter measurement. Measurements for the thinner filters are more sensitive to perturbations than thicker filters.

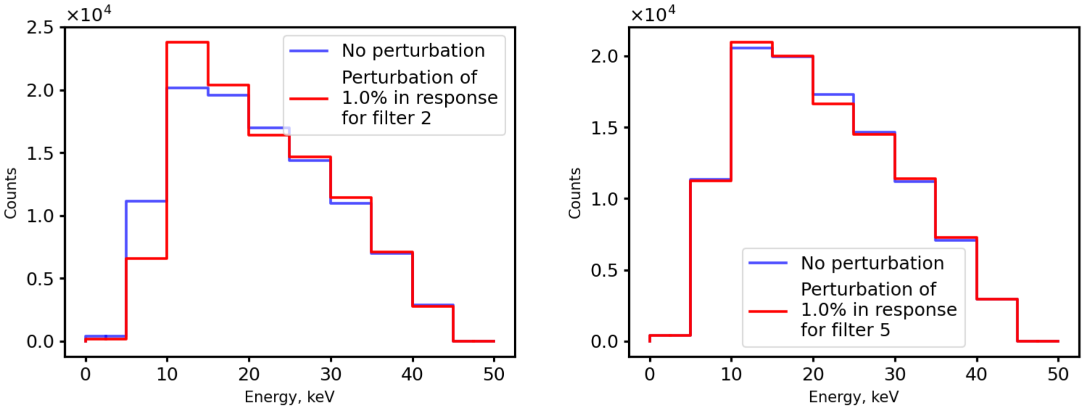

(A) (B)

FIGURE 4.7: Tikhonov solutions with a 1% perturbation in (A) filter B and (B) filter E. The solution with no perturbation is shown in blue and the perturbed spectrum in red. The difference parameter for each was (A) d=14.4% and (B) d=2.1%. The differences in the spectra are discussed in the main text.

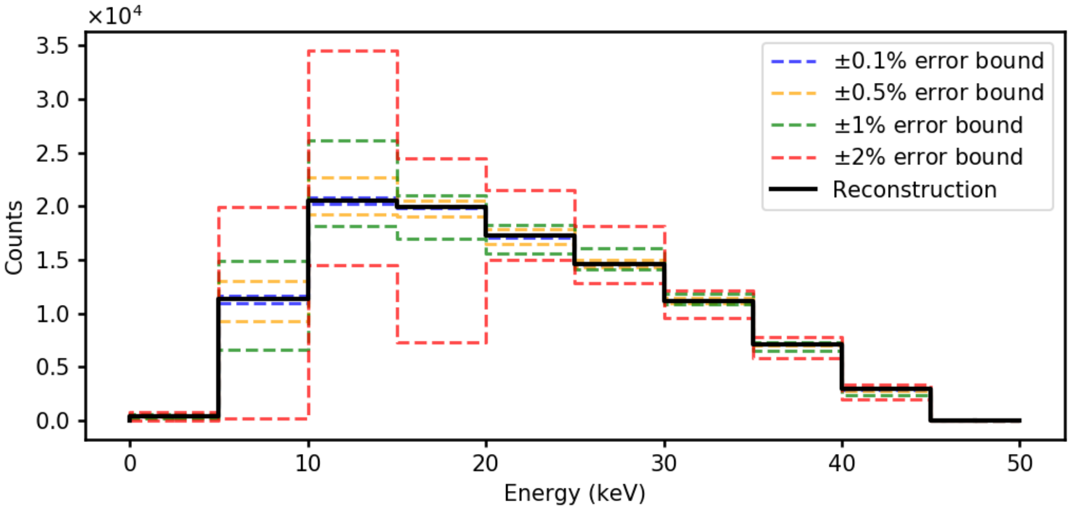

FIGURE 4.8: Spectrum reconstruction showing the maximum and minimum counts reconstructed in each bin for a certain percentage perturbation on each filter. Perturbations of 0.1, 0.5, 1 and 2% are shown by the dashed lines. The unperturbed reconstruction is shown by the black line.

2% perturbation this was up to a difference of 841 (204%) 19646 (173%) for bin 1, for bin 2, 20092 (98%) for bin 3 and 17178 (86%) for bin 4.

As this investigation demonstrates, the greater the change in the detector response between filters, the greater the effect perturbations to the detector response are likely to have. As a result spectral changes are complex to quantify exactly and would most likely be unique to the particular reconstruction problem. The investigation here was useful when evaluating the reconstruction results, in particular in understanding how systematic errors may effect the spectra that are attainable using this technique.

4.8 Other reconstruction methods

Solving inverse problems is a diverse area of mathematics and as a result there exist many different algorithms that can be used. Popular methods include iterative algorithms such as Landweber, ART (algebraic reconstruction technique) and CGLS (conjugate gradient least squares), matrix decomposition methods such as SVD (singular value decomposition) and TSVD (truncated-SVD), and back-projection methods such as FDK (Feldkamp-Davis-Kress) (with a particular application to x-ray CT imaging) to name but a few [89, 99–102]. Ultimately the choice of reconstruction method depends on many factors including the complexity of the problem, speed required for solution convergence and formulation of the problem. The matrices in this work are small (10×10) compared with those used in x-ray CT reconstruction where the number of elements can reach into the millions, so convergence speed was not an issue. Potential advantages of the other reconstruction methods will be a subject of later discussion (see Section 9.3).

4.9 Chapter summary

This chapter has shown how the energy spectrum reconstruction problem can be formulated as an inverse problem and demonstrated that energy spectrum reconstruction is possible through acquiring a series of filtered detector response measurements. A calibration method for accounting for experimental errors in the spectrum reconstruction problem was presented. The Tikhonov reconstruction algorithm was chosen for solving the spectrum reconstruction problem. Through use of a perfect case backscatter spectrum intrinsic errors in the Tikhonov solutions have been investigated. This showed that even in a perfect case the Tikhonov solution could not reproduce exactly the true spectrum mainly due to the effects of regularisation. The effect of the measurement error parameter and solution stability have also been discussed in depth, highlighting the importance of measurement error in the calculation of a valid spectrum.

Chapter 5

Experimental approach

This chapter presents the equipment and methods used to acquire the experimental scattering data for reconstruction. The set-up consisted of a CdTe detector, x-ray tube and sample arranged in a backscatter configuration. Aluminium filters were used to filter the scattered x-ray beam measured by the CdTe detector. Firstly, characterisation and calibration procedures for the CdTe detector and 50 keV x-ray tube are discussed in depth. The experiment design and procedure are then presented. Finally the calibration process for calculating the RCF is discussed.

5.1 Equipment

The x-ray detector used was the Amptek X-123 CdTe compact x-ray spectrometry system [60, 103]. A photograph of the device is shown in Figure 5.1. The device had a 1 mm thick cadmium telluride (CdTe) semi-conductor detector crystal with an active area of 25 mm^2. This detector crystal was located at the end of the detector arm. The main body of the detector contained the pre-amplifier, pulse processing electronics, multi-channel analyser (MCA) and thermo-electric cooler for room temperature operation [60]. The manufacturer quoted energy resolution was 0.6 keV full width at half maximum (FWHM) at 60 keV [103]. The device was operated via USB and spectra were acquired using Amptek acquisition software [104]. The portability of the device together with the high energy resolution at room temperature made the detector ideal for this application.

Although the primary aim of the experiment was to acquire response measurements from an energy integrating detector which has no energy resolution, the energy spectrum information was essential in the proof-of-concept study for diagnostic purposes. Therefore throughout the experiment, full energy spectra were acquired and an equivalent energy integrated response was calculated from each spectrum (see Section 5.5.2 for details). Spectral information allowed investigation of systematic errors in more detail and also was used to understand what spectrum was expected in order to compare the reconstructed spectrum to an actual measurement. Additionally, the energy spectrum was used to validate Monte Carlo simulations of the set-up.

(a) Mini-X x-ray tube

(b) X-123 CdTe spectrometer

FIGURE 5.1: Photographs of the Amptek Mini-X x-ray tube (a) and X-123 CdTe detector (b).

The x-ray tube used was the Amptek Mini-X miniature x-ray tube with a gold anode [38]. A photograph of the device is shown in Figure 5.1. The x-ray tube voltage range was between 10 kV and 50 kV. The maximum current was 200 µA or so that the power of the x-ray tube was no greater than 4 mW. The x-ray tube was small and portable due to the reflection target configuration of the anode making it ideal for the tabletop setup (section 2.1.3.1). The device was operated via USB using Amptek control software [105]. For operation a brass collimator with diameter 2 mm was inserted into the end of the x-ray tube producing a cone beam with 5° divergence.

5.2 X-ray tube characterisation

5.2.1 X-ray tube output spectrum

Before use the output spectrum of the x-ray tube was measured at five different voltages between 10-50 kV to check the device was operating as expected. This was done by taking a measurement with the CdTe detector directly in front of the x-ray tube for each voltage setting. The output spectrum at 50 kV was particularly important as it was used in the Geant4 simulations discussed in Section 6.4 and Section 6.5.

A set-up involving a system of motors was used to align the source and detector precisely. A schematic diagram of this is shown in Figure 5.2. As shown in Figure 5.2, two Velmex bi-slide motor devices (bi-slide) were used [106] each with a motorised movable platform that could be moved with an accuracy of 0.1 mm in one linear dimension. One bi-slide was attached to the movable platform of the other so that the free platform could be moved in two dimensions.

A collimator with an inner diameter of 400 µm was attached to the CdTe detector. A photograph of the collimator is shown in Figure 5.3. The collimator was used to reduce the count rate on the detector to avoid detector saturation and reduce pulse pile-up effects. The CdTe detector with collimator was secured to the free bi-slide platform with the detector arm pointing vertically upwards. The x-ray source was held directly above the detector with the x-ray beam pointing vertically downwards using a clamp. The distance between the x-ray tube and detector was 10.5 cm. Due to radiation safety, the experimenter could not be near

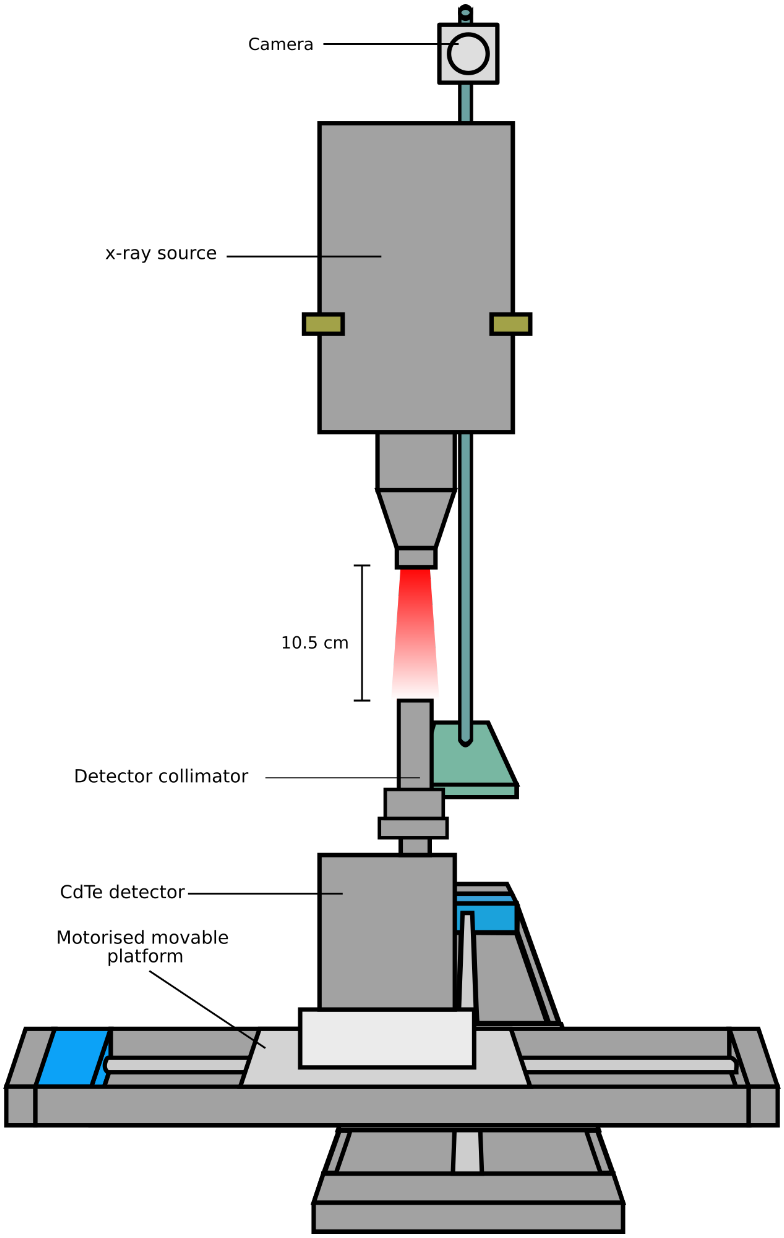

FIGURE 5.2: Schematic diagram of the experimental setup to measure the output spectrum of the Mini-X x-ray source.

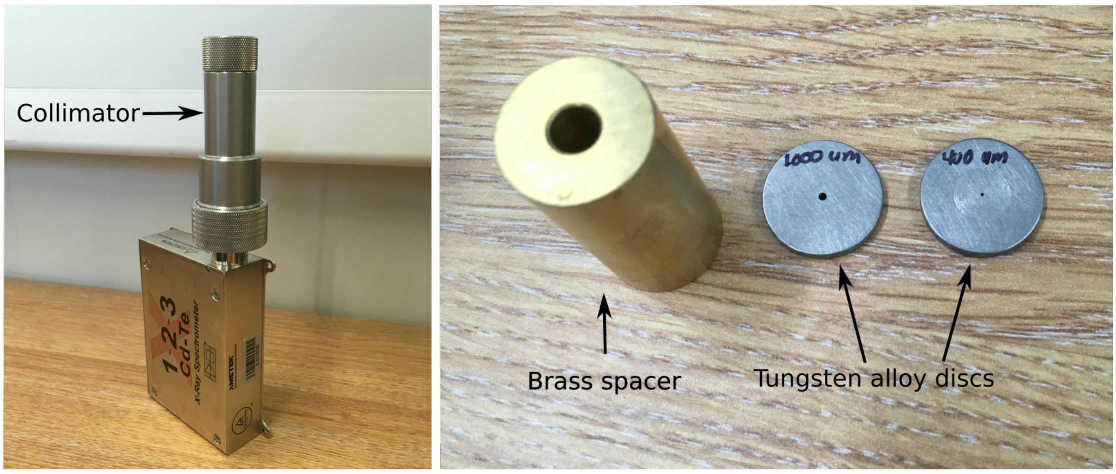

(a) CdTe detector with collimator (b) Collimator insert

FIGURE 5.3: Photographs of the X-123 CdTe detector with collimator (a) and the components of the collimator (b), a brass spacer and two tungsten alloy disks with diameters 1000 μm and 400 μm.

the x-ray tube while in operation therefore a camera was attached to the top of the clamp so the position of the detector could be monitored throughout the experiment.

The CdTe detector was moved around underneath the source to sample the x-ray spectrum at each point in the beam and find the aligned position. The aligned position was taken to be the position of maximum count rate. The maximum count rate was recorded at several points over a 1 mm region, consistent with a beam spot size of 2 mm and a 1 mm diameter collimator. The centre of this region (taken to be the beam centre point) was at the point (x, y)=(300,600)$\times 10^{-2}$ mm where x and y are coordinates in the horizontal plane relative to an arbitrary reference point. The x-ray beam was detectable up to 5.5 mm away from the beam centre point consistent with the spot size at 10.5 cm given a 5° beam divergence. The x-ray spectrum was measured at two places offset from the aligned position, (800,400) and (800,800)$\times 10^{-2}$ mm. The total counts detected was 11% and 19% of the total counts detected in the aligned position respectively.

The output spectrum was measured for five different voltages between 10 and 50 kV at the maximum power setting for 30 sec. Figure 5.4 shows the measured CdTe output spectrum at each voltage and current setting. For voltages above 20 kV, the spectra contained gold characteristic x-rays in the expected ratios. The characteristic x-rays all sat on a continuous bremsstrahlung background which terminated at the energy corresponding to the maximum voltage. In the spectrum at 10 kV only the bremsstrahlung background was observed because the maximum electron energy was below that of the K edge in gold so characteristic x-rays were not emitted from the gold target. These observations were consistent with theoretical predictions and example spectra given in the Mini-X data sheet [38] and therefore it was concluded that the x-ray tube was functioning as expected.

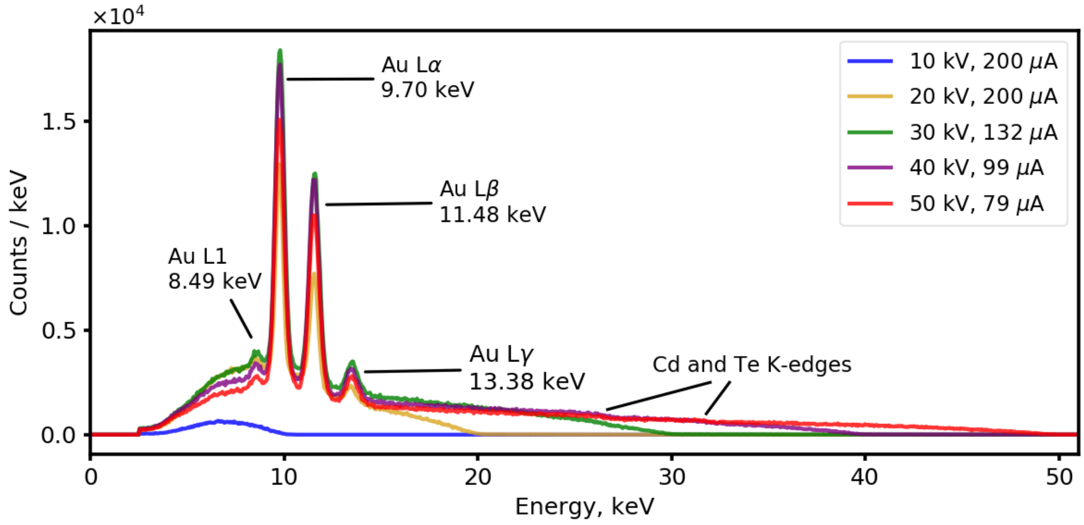

FIGURE 5.4: Output spectrum of the Mini-X x-ray tube as measured by the CdTe detector in the aligned position. The output is shown for five different tube voltages, 10, 20, 30, 40 and 50 keV.

The bremsstrahlung to characteristic x-ray ratio was estimated for the three measured spectra to understand the spatial profile of the beam. The area of the characteristic x-ray peaks was estimated using gf3 peak fitting software [107]. Theoretically the percentage bremsstrahlung background increases with increasing distance from the beam focal point. X-rays emitted off centre have to travel a greater distance through the anode and therefore undergo more

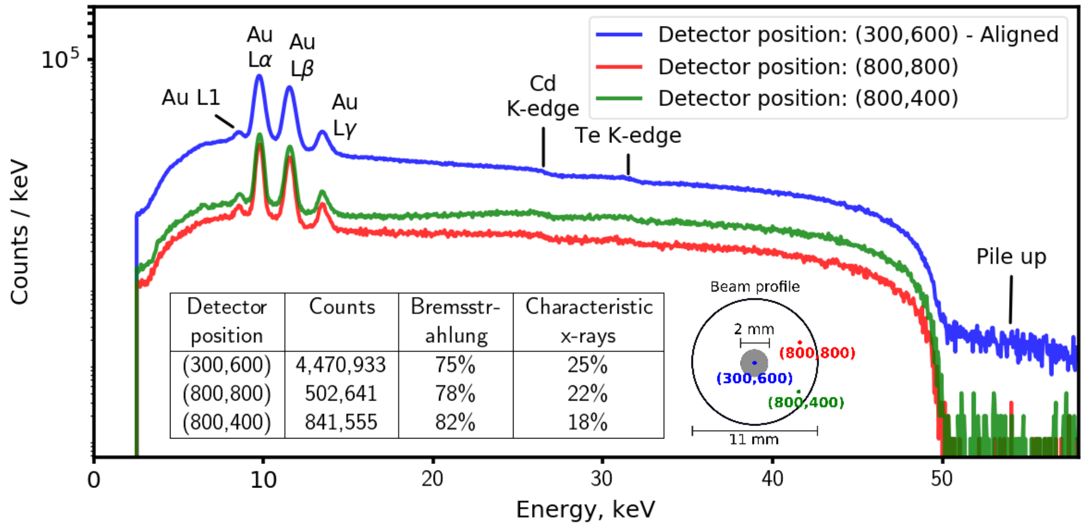

Detector position	Counts	Bremsstrahlung	Characteristic x-rays
(300,600)	4,470,933	75%	25%
(800,800)	502,641	78%	22%
(800,400)	841,555	82%	18%

FIGURE 5.5: Output spectrum of the Mini-X x-ray tube at different detector positions. The aligned position is (300,600) where the coordinates xy are relative to an arbitrary reference point in the horizontal plane. The beam profile shows the positions of the detector within the cone beam. The region within the black circle is the area where the x-ray beam can be measured at 10.5 cm away. The grey shaded area in the centre is the point of maximum beam intensity. The total counts and percentage of each spectrum that is bremsstrahlung background and characteristic x-rays is given in the table.

attenuation within the target (see Section 2.1.3 Figure 2.4b). The characteristic x-rays in the spectrum are of a lower energy compared to the bremsstrahlung background and low energy x-rays are more highly attenuated than higher energy x-rays. Therefore the characteristic x-ray intensity in the off-centre beam were reduced more in comparison to the bremsstrahlung background intensity. In the aligned position the characteristic x-rays made up 25% of the spectrum but this was reduced in the offset cases which were 22 and 18% respectively, as given in the table in Figure 5.5.. This observation was consistent with the theoretical prediction.

5.3 CdTe detector characterisation

5.3.1 CdTe detector energy calibration

Measurements to determine the relationship between detector channel number and gamma-ray energy (the energy calibration) of the CdTe detector were performed using the known gamma-ray emissions of ^{241}Am (up to 59 keV) [108] and ^{133}Ba (up to 81 keV) [109]. The known characteristic x-ray emissions of copper and tin (with energies approximately 8 and 25 keV respectively) [34] were also used in the calibration. The relationship between energy and channel number was assumed to be linear and of the form $E=g \times ch+f$ where E is the x-ray energy, ch is the channel number, g is the gain and f is the zero offset.

For the source calibration measurements the source directly in front of the detector and a spectrum measurement was acquired. For the copper and tin measurements, a copper or tin scattering plate was placed in the sample holder and the x-ray tube was fired onto the plate. Spectrum measurements were acquired at a 140° scattering angle. By far the most dominant feature of the x-ray scatter spectrum was the characteristic x-rays of tin and copper.

Calibrations were performed at the start of each experiment day. The experiments were performed over two experiment days. The calibration for the first day was g=(5.2$\times$10^{-2}$\pm$ 3.1$\times$10^{-5}) keV per channel and f=(-0.17$\pm$0.02) keV where g and f are the gain and offset respectively. For the second day the calibration was g=(5.2$\times$10^{-2}$\pm$3.4$\times$10^{-5}) keV per channel and f=(-0.16$\pm$0.02) keV. The error on the energy was thus 0.2% for energies less than 10keV and 0.1% for energies between 10 and 50 keV (for both experiment days).

5.3.2 CdTe energy resolution

Another important detector characteristic was the CdTe detector energy resolution. The energy spectrum of two radioactive sources, ^{241}Am and ^{133}Ba were acquired allowing resolution measurements to be obtained from 13 to 81 keV. For each the source was positioned 1 cm from the detector and each measurement was acquired for 700 s. The spectra obtained are shown in Figure 5.6. The peaks used to calculate the resolution are labelled. The energy units for all labels in Figure 5.6 is keV.

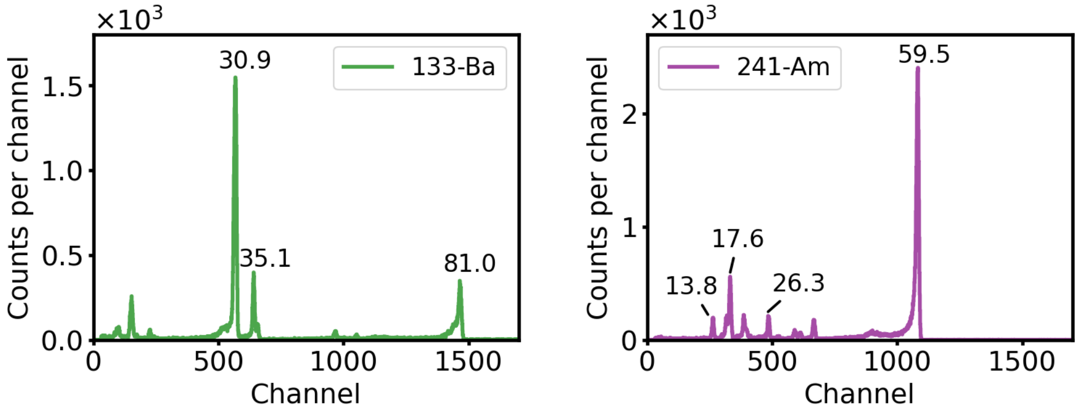

(A) (B)

FIGURE 5.6: (A) ^{133}Ba and (B) ^{241}Am spectra as measured using the X-123 CdTe detector. The energies used to estimate the detector resolution are annotated on each figure. The units for all are keV.

Peaks in the ^{133}Ba and ^{241}Am spectra were fit to a Gaussian function using the software gf3 [107] to obtain the peak full-width at half maximum (FWHM). A Gaussian function rather than a Voigt profile was used for the x-ray peaks at 13.8, 17.6 and 35.1 keV because the linewidths of these x-ray transitions are 16 eV or less [110] so negligible compared to the detector resolution. The x-ray peak at 30.9 keV was not used in the analysis because it

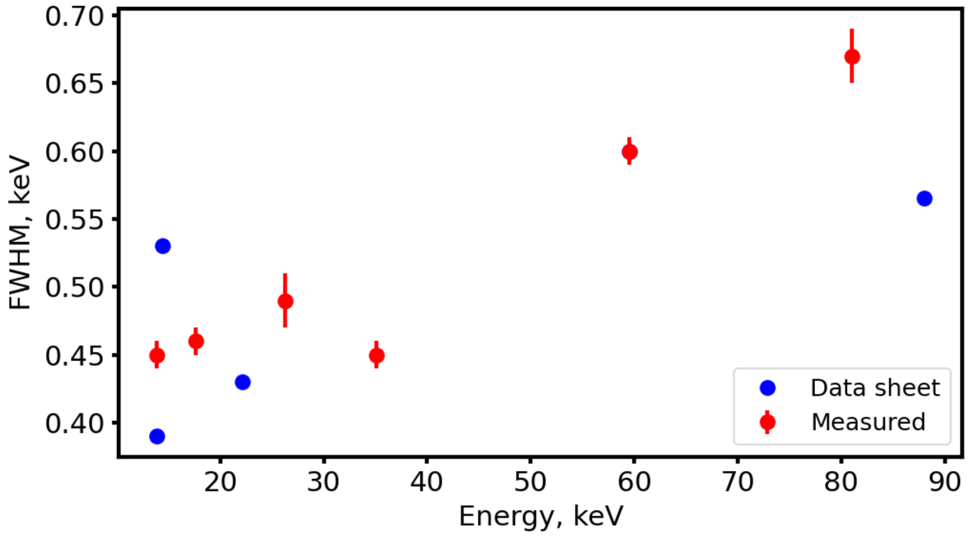

FIGURE 5.7: CdTe detector resolution (measured as FWHM) as a function of energy. In blue are the data sheet values given in the X123-CdTe detector manual [103]. In red are the measured values using a ^{241}Am and ^{133}Ba source.

consists of two Kα x-ray transitions of comparable intensity that could not be individually resolved (at 30.6 and 31.0 keV with an intensity ratio of 0.54 [109]). The FWHM as a function of energy is shown in Figure 5.7. The FWHM values as given in the detector manual [103] are shown in blue and the measured values are shown in red. From Figure 5.7, the measured FWHM increases as a function of energy. The measured FWHM varies slightly from the data sheet values, with the data sheet values being 0.05-0.1 keV lower than the measured values, with the exception of the 22.1 keV data point from the manual. This variation is to be expected as the data sheet values are quoted under laboratory test conditions so worse resolution can be expected in practice. Additionally, slight variation of FWHM is expected between detectors due to manufacturing processes [61, 67]. Nonetheless the CdTe detector used shows good energy resolution close to and of the same order of magnitude as expected.

5.3.3 CdTe detector stability

Experiments were performed to characterise the stability of the X-123 CdTe detector output spectrum over time. A 40 kBq ^{133}Ba source was positioned 3 cm in front of the detector. A measurement of the energy spectrum was made every 15 minutes over a period of 3 hours. Each spectrum was acquired for 2 minutes. The measurements were performed in an indoor laboratory, not in the outdoor test facility that will be discussed in Section 5.5.

The peak centroid for the 31 and 81 keV gamma rays was calculated using gf3 [107] for each spectrum. Figure 5.8 shows the change in channel number as a function of measurement start time for 31 keV and 81 keV. For both energies the channel number was found to increase for the first 90 minutes of the detector being switched on and approximately stabilise after this although there is some fluctuation, more so for the 81 keV compared to the 31 keV.

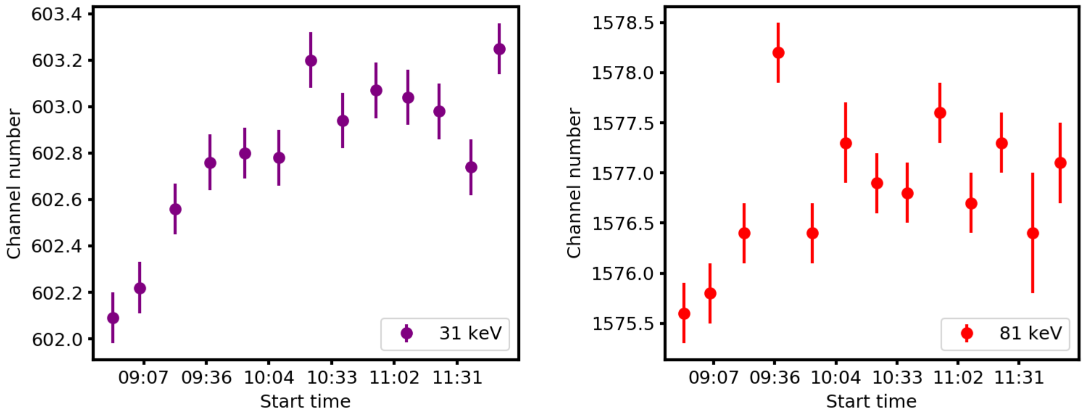

(A) (B)

FIGURE 5.8: Channel number of the peak centroid as a function of measurement start time for (A) 31 keV and 81 keV peaks of the ^{133}Ba source.

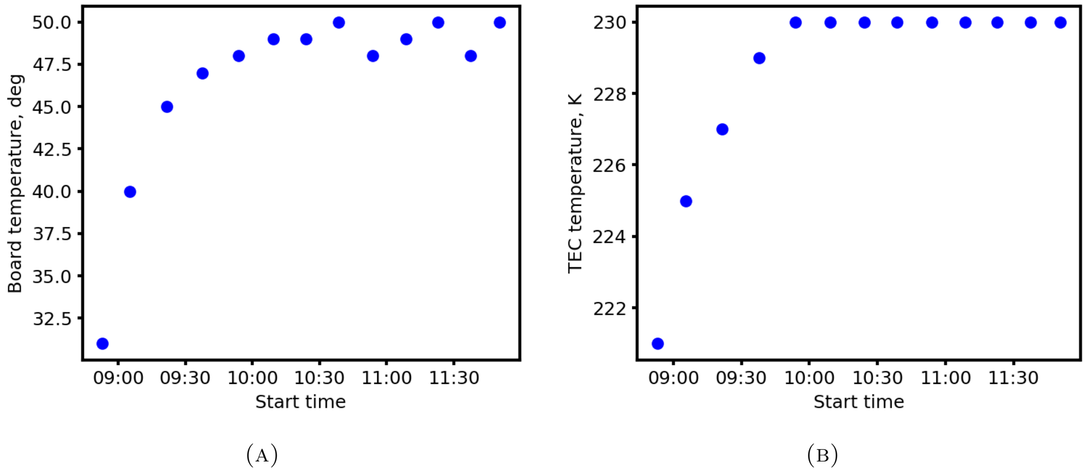

(A) (B)

FIGURE 5.9: Temperature as a function of time for (A) the detector circuit board and (B) the thermoelectric cooler.

The temperature of the detector circuit board (board temperature) and the temperature of the thermo-electric cooler (TEC) were recorded over the 3-hour measurement period. Figure 5.9 shows the change in both temperatures as a function of time. The board temperature and temperature of the TEC were also found to increase for the first 90 minutes and stabilise. Therefore the channel number increase shown in Figure 5.8 could correlate with increasing air temperature in the laboratory due to time of day, similar to the diurnal variation of the centroid position seen by the manufacturer in [60].

The total counts as a function of time was measured and is shown in Figure 5.10. As shown in Figure 5.10, the total counts did not undergo a measurable change over the 3 hour time period. The average value was 7202±34 counts (0.1% error) suggesting a negligible variation of the detector response over time. Consequently the effect was ignored in the

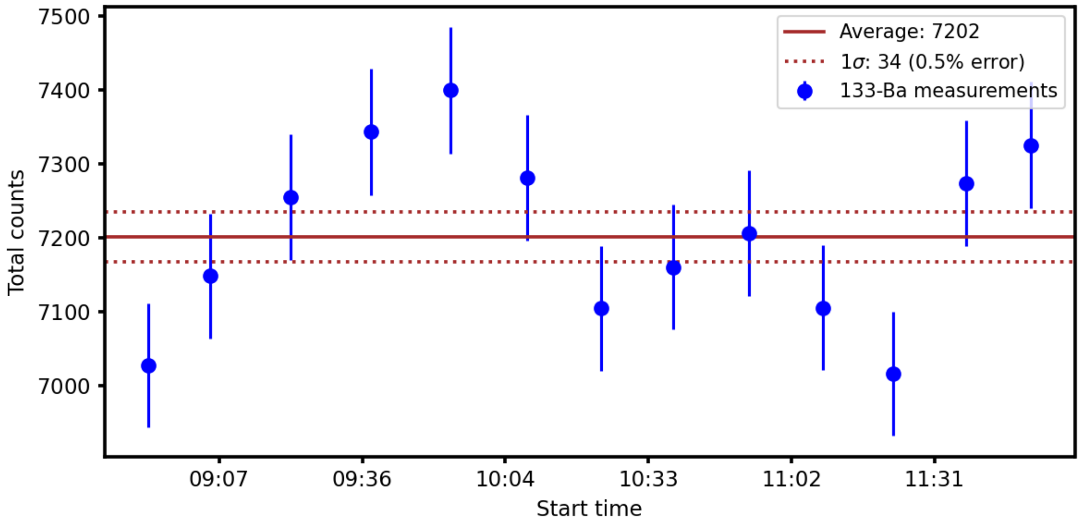

FIGURE 5.10: Total detected counts as function of time for the ^{133}Ba source measurements.

detector response measurements obtained from the scattered materials. In addition, taking the maximum and minimum channel numbers for both 31 and 81 keV showed an energy difference of 0.05 keV (0.2%)and 0.2 keV (0.2%). This is the same order of magnitude as the energy calibration error discussed in Section 5.3.1 and was thus also neglected.

5.4 Backscatter set-up

The experimental measurements were performed using a set-up consisting of an x-ray source, sample and detector in a arranged backscatter geometry. The 50 kVp Amptek Mini-X x-ray tube was used to irradiate the sample and the Amptek X-123 CdTe detector was used to measure the x-rays scattered from the sample. Aluminium plates (filters) were positioned in front of the detector to filter the scattered x-ray beam. A schematic diagram of the set-up is shown in Figure 5.11 and labelled photographs are shown in Figure 5.12.

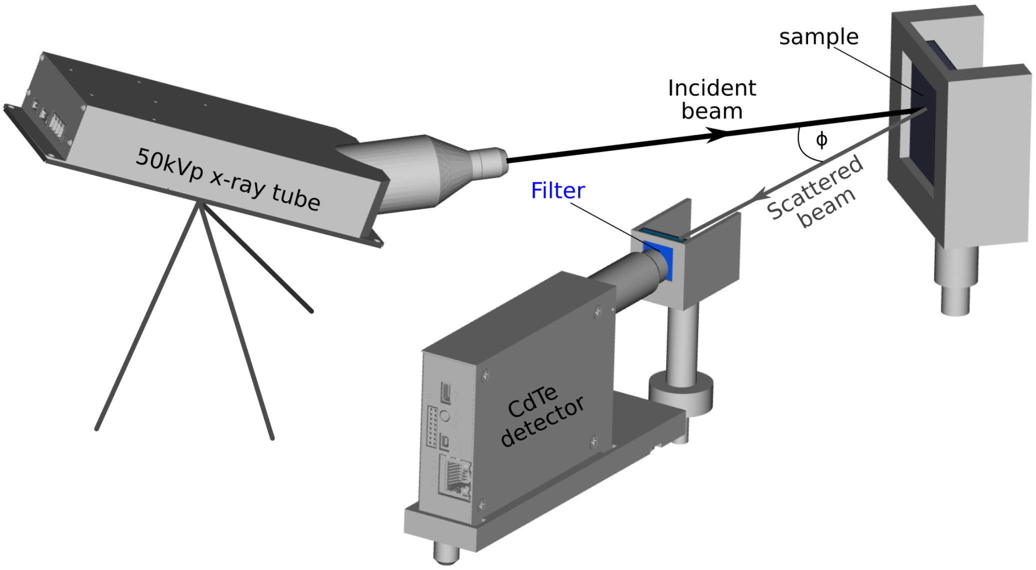

FIGURE 5.11: Schematic diagram of the experimental set-up used to acquire filtered detector response measurements in a scatter geometry.

In all experiments the source-to-object distance and detector-to-object distance were fixed at 17 cm and 10 cm respectively. Errors on both measurements were ±0.5 mm. These dimensions were chosen by considering the x-ray beam penetrability and beam divergence effects based on theoretical reasoning, as well as space limitations.The intensity of the x-ray beam decreased with increasing distance from the source, and the focal spot size increased with increasing distance from the source. Both effects required small source-to-object and detector-to-object distances to maximise the beam flux on the sample. However at too short a distance, the effect of multiple scattering events off the x-ray source casing would

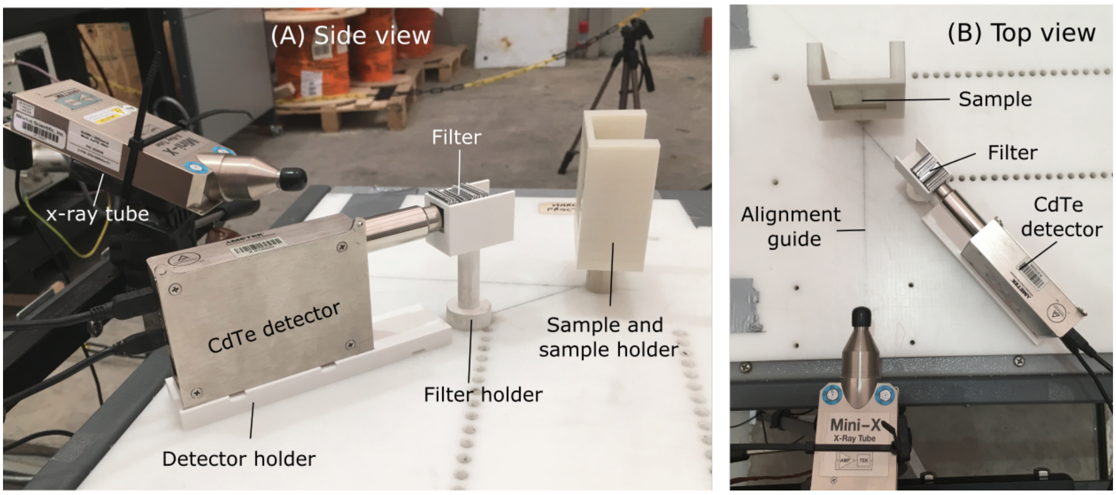

FIGURE 5.12: Photographs of the experimental set-up arranged according to the diagram in Figure 5.11. (A) is a side-on view and (B) is a top down view.

be noticeable. The source-to-object and detector-to-object distances were chosen within these constraints. The filters had a 20×26 mm area and variable thickness depending on the specific measurement. The error on the filter height and width dimensions was ±0.05 mm and the error on the filter thickness varied for each filter as will be discussed in Section 5.6.

The scattering angle was 140° and the acute angle between the incident and scattered beam was 40°, as shown by ϕ in Fig. 5.11. A scattering angle of 140° was used as it was the closest scattering angle to 180° possible within the space constraints. All samples were 45×45 mm in area with thickness 10 mm. Errors on dimensions of the plastic samples due to manufacturing tolerances were ±5%.

It was important to maintain a precise alignment of the x-ray source, sample, filter and detector to ensure repeatability across multiple measurements and to minimise systematic errors. The detector, sample and filters were held in position on a base plate using sample holders designed for the purpose. The x-ray source was mounted on a tripod so the height and firing direction could be fixed. The x-ray beam was aligned with the centre of the sample by eye using markers on the base plate as shown by the alignment guide label in Figure 5.12.

The plastic holders were designed for the application using computer aided design (CAD) software. Plastic holders were required to hold the detector, filter and sample. The CAD design for each is shown in Figure 5.13. The dimensions for each piece are given in Figure 5.13 have a ±0.1 mm error due to the printing process. Holes were drilled in precise positions in the base plate. Each holder was designed to fit into these holes to limit movement of the component. The holders were each printed in polylactide (PLA) plastic with a 10% density achieved by printing the component with an internal honeycomb structure. This was done to minimise x-ray scattering off the holders themselves while maintaining a strong structure.

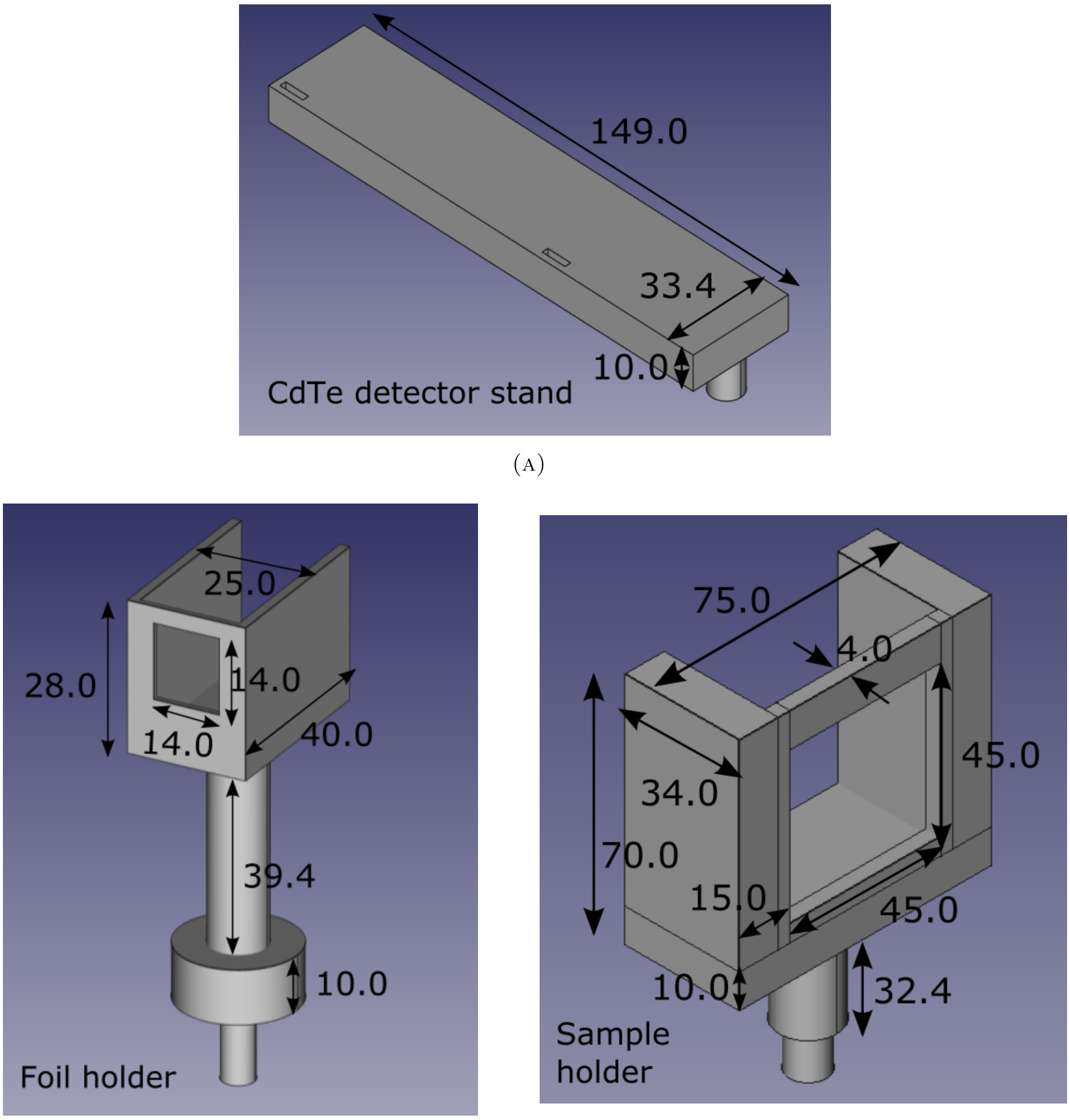

(A)

(B)

(C)

FIGURE 5.13: CAD designs for the experimental setup components (A) detector stand, (B) foil holder and (C) the sample holder. All dimensions shown are in mm.

All experiments were performed with the set-up assembled in a large warehouse. The set-up was operated remotely from a control cabin adjacent to the warehouse for radiation safety. The air temperature of the warehouse was not controlled. This is similar to the conditions commercial backscatter systems are operated in which are often operated outdoors and in harsh field environments.

5.5 Measurements

Seven different plastics were measured overall, two as calibration materials and five as test samples. The test materials were HDPE, POM, PVDF, PTFE and PVC. The measurements were performed over two experimental days. On the first day (4th February 2020), HDPE, POM and PVC were tested. Nylon was used as the calibration material for the first day. On the second day (5th February 2020), PVDF and PTFE were tested with Acrylic used as the calibration material. Each plastic sample had a thickness of 10 mm (±5% due to manufacturing tolerances).

The plastics were chosen based on their Z_{eff} and ρ properties within the selection of materials that could be sourced by the university supplier. The organic material range is typically $3< Z_{eff} <16$ and $(0.5< \rho <2.2)$ g cm^{-3}. The material densities ranged from 0.97 to 2.2 g cm^{-3} and effective atomic numbers Z_{eff} from 5.53 to 14.26 to fully sample the organic material range. The vast majority of explosive materials lie between $6.5\leq Z_{eff} \leq 8.0$ and $(1.4\leq \rho \leq 2.0)$ g cm^{-3} [17]. The plastics POM and PVDF were chosen because they have Z_{eff} and ρ properties indistinguishable from explosive materials despite being inert plastics so could be used to determine how well explosive materials could be identified. The properties of the sample materials are given in Table 5.1. The Z_{eff} was calculated following Section 2.3.3.

Ideally, it would have been best to keep the calibration materials the same for both days for consistency. The reason the calibration materials were different is because when the experiment was originally performed, it was not known that the RCF calibration process would be necessary as this was only discovered upon post-experiment analysis of the data. It was not possible to acquire further experimental data due to laboratory closures over the pandemic. Instead, Nylon and Acrylic were used as calibration materials as they had the most similar properties out of all the materials tested on the two days in terms of

Material	Z_{eff}	Density, g cm^{-3}
HDPE	5.53	0.97
Nylon	6.21	1.08
Acrylic	6.56	1.18
POM	7.03	1.41
PVC	14.26	1.45
PVDF	7.97	1.78
PTFE	8.48	2.20

Table 5.1: Effective atomic number (Z_{eff}) and density properties for each sample [54, 55, 59]. The Z_{eff} was calculated using the method outlined in Section 2.3.3.

Z_{eff} and ρ (Z_{eff}(Nylon)=6.21 and Z_{eff}(Acrylic)=6.56 and ρ(Nylon)=1.08 $\mathrm{g\,cm^{-3}}$ and ρ(Acrylic)=1.18 $\mathrm{g\,cm^{-3}}$). The effect of the different calibration material was found to have a negligible effect on the result, as will be discussed in Section 8.4.4.

The CdTe detector was used to measure the backscatter spectrum for each thickness of aluminium filter. Measurements were taken for an accumulation time of 60s per filter plus an additional 60s measurement with no filter to compare to the reconstruction later on in the analysis. Ten filters were used therefore the total measurement time for each material was 660s. An energy threshold of 2.5 keV was applied to the experimental spectra to reduce the effect of electronic noise on the spectrum.

The thicknesses of filter used are given in Table 5.2 in Section 5.6. Filter B was supposed to be (0.14±0.01) mm, as will be discussed in further detail in Section 5.6. On the 1st experimental day (HDPE, POM and PVC measurements) the filter B thickness was (0.14±0.01) mm as expected. However on the 2nd experimental day (PVDF and PTFE measurements) the filter B thickness was (0.05±0.005) mm due to a mistake in the experiment. The effect of this was investigated further in simulation studies in Section 8.4.3 and was found to have negligible effect on the overall result.

5.5.1 Example spectrum

Figure 5.14 shows three backscatter spectra acquired for a 10 mm POM sample. The spectrum acquired with no detector filtration is shown in green, and two other filtered

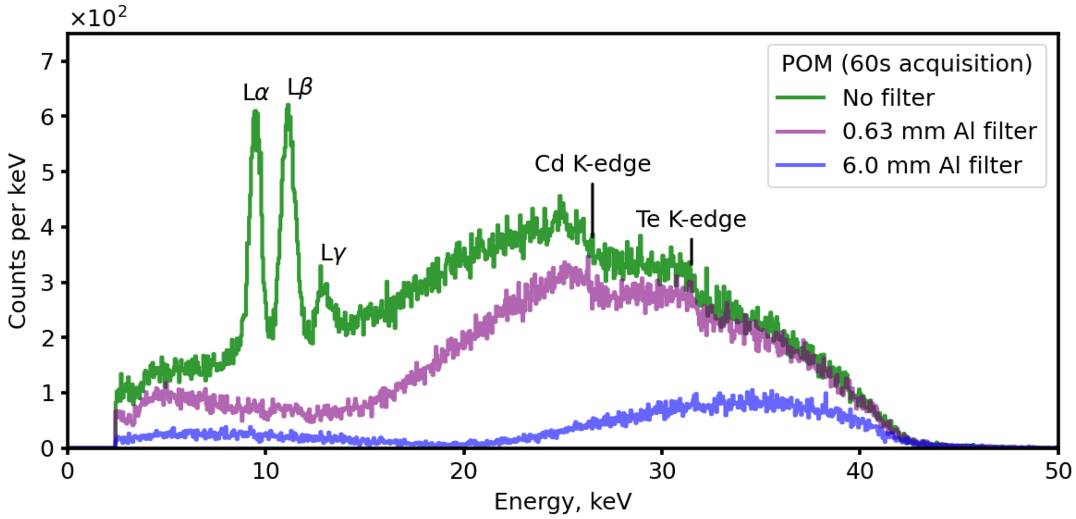

FIGURE 5.14: Experimental spectra for scattering off 10 mm POM with different filtrations. No filter is shown in green, 0.63 mm aluminium in purple and 6.0 mm aluminium in blue. Scattered Gold Lα, Lβ and Lγ peaks are seen in the unfiltered spectrum. K-edge effects are seen in the unfiltered and 0.63 mm spectra.

spectra at 0.63 mm and 6.0 mm are shown in purple and blue respectively. Below 15 keV in the unfiltered spectrum, peaks at 9.4, 11.0 and 12.8 keV are seen which are the scattered Gold Lα, Lβ and Lγ characteristic x-rays from the x-ray tube target. Above 15 keV the unfiltered spectrum is smoother as this is the region where the bremsstrahlung part of the x-ray tube spectrum is being scattered. There are discontinuities at 26.7 and 31.8 keV due to absorption edges in the CdTe detector material. The unfiltered spectrum reaches almost zero at approximately 42.6 keV, the energy of 140° scatter at the maximum 50 keV.

In the 0.63 mm spectrum in Figure 5.14 (purple trace), below 15 keV the characteristic x-rays seen in the unfiltered spectrum are not present. The number of counts in each bin above 15 keV is reduced compared to the unfiltered spectrum up to about 32 keV. These effects are due to the attenuation of the spectrum as it has passed through the 0.63 mm aluminium filter. The 0.63 mm filter attenuated all x-rays with energies below 12.5 keV by 90% or more. The number of counts seen below 15 keV is greater than expected given the attenuation effect. Most of the counts in this region are not coming from the part of the spectrum that has passed completely through the filter, but from x-rays that have hit the side of the filter and scattered into the detector. This will be discussed in more detail in Section 5.7. The 6.0 mm filter trace seen in Figure 5.14 has the same features as the 0.63 mm but with more attenuation due to the larger thickness of filter.

5.5.2 Calculating the detector response

An equivalent energy integrated response I_j was calculated as follows

$$I_j = \sum_{i=1}^{n} E_i N_{ij}. \tag{5.1}$$

Here E_i is the energy of bin i. N_{ij} is the number of counts in bin i for a filter j. n is the number of energy bins in the spectrum. The error on each energy integrated measurement, σ_{I_j}, is

$$\sigma_{I_j} = \sqrt{\sum_{i=1}^{n} (E_i \sqrt{N_{ij}})^2} \tag{5.2}$$

by assuming the number of counts in each bin follows Poisson statistics and adding the error for each bin in quadrature. The error in the energy due to the energy calibration was assumed to be negligible compared to the Poisson error (see Section 5.3.1). For filter A (thinnest filter) the error σ_I was between 0.3-0.5% for the plastics tested. For filter J (thickest filter) the error σ_I was between 2.9-3.6%. The error σ_I for the other filters were between these limits. All of the raw detector response data can be found in Table B.1 in Appendix B.

Spectrum measurements with no sample in the sample holder (background measurements) were also acquired for each thickness of filter (including no filter). These background measurements were used in the simulation validation process discussed in Section 6.4.

5.6 Filters

The detector filters were made from aluminium. Aluminium was chosen because suitable attenuation of x-rays below 50 keV could be achieved with manageable material thicknesses (a thickness range of 0.005 - 25 mm). Aluminium with thickness in this range were used following the discussion in Section 4.4. Other considerations were the filters should not be so thin that the filters were hard to manufacture or handle, but not too thick so as to be too big for the scatter geometry or cause excessive x-ray scattering.

#	Filter thickness, mm
A	0.0066 ± 0.0015
B	0.14 ± 0.01
C	0.63 ± 0.02
D	1.68 ± 0.09
E	3.47 ± 0.16
F	6.0 ± 0.22
G	9.26 ± 0.28
H	13.0 ± 0.34
I	17.0 ± 0.38
J	21.1 ± 0.43

TABLE 5.2: Thicknesses of aluminium filter used for the spectrum reconstruction.

5.6.1 Filter manufacture

To create all the different thicknesses of filter given in Table 5.2, five different base thicknesses were used: 1.5, 10 and 20 µm, and 0.1 and 0.9 mm. A photograph of the five base thicknesses is shown in Figure 5.15. Each foil was cut from a larger aluminium sheet to an area of 20×26 mm. The 1.5, 10 and 20 µm foils were all too fragile to be handled directly so were glued onto a PLA plastic support. The plastic support covered a 3 mm border around the edges and a 9 mm thickness from the bottom of the filter, leaving a 14 mm^2 central area free (Figure 5.15a-c). The error in each filter thickness, for all but the 1.5 µm filter, was taken to be the manufacturing tolerance which was 10%. The errors in the filters used given in Table 5.2 were calculated by combining the errors for the filters used in quadrature. For measurements involving the 1.5 µm filters, the error was taken to be 1 full filter (1.5 µm)

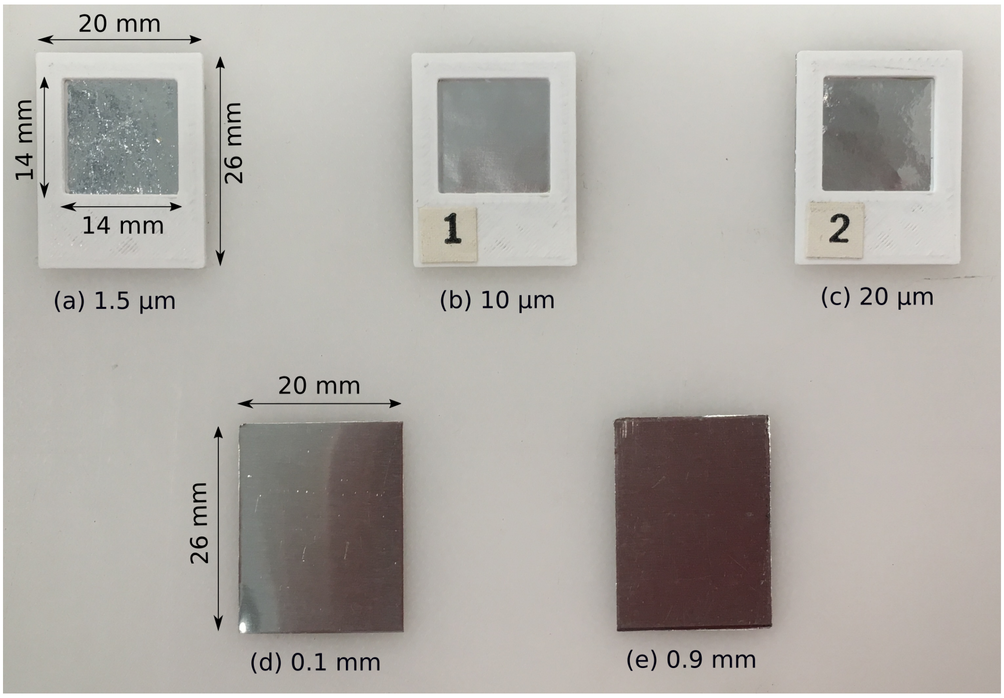

FIGURE 5.15: The five base aluminium filter thicknesses used to create all required filter thicknesses. Filters were cut to an area of 20×26 mm. The thinnest filters (a)-(c) were glued to a plastic support.

owing to the presence of pinholes. The only instance where the 1.5 µm filters was used was in filter #1 resulting in percentage errors of 23%.

5.7 System calibration

The reconstruction model assumed the detector response is only due to the proportion of the beam that has backscattered at 140°. However, experimentally there are other contributions to the detected x-ray signal. This is due to x-ray tube leakage or additional scatter from the filters and other components in the experiment. An illustration of the way x-ray tube leakage or additional scatter can enter the x-ray detector is shown in Figure 5.16a.

Simulation studies estimated scatter to be an insignificant fraction of the total detected counts for filter A, 3% of the total detected counts for filter C, up to 70% of the total detected counts filter J. The effect of scatter shows up as low energy counts below the energy threshold of the filter. Consider Figure 5.16b which shows an example of a detector response with filter C (0.63 mm) which has an energy threshold of around 10 keV. The expected spectrum assumed by the model is shown in blue. There are no x-rays detected below 10 keV as these have been completely removed by the detector filter. Contrast this to what is measured by the detector (red curve) where x-rays are observed below 10 keV. These

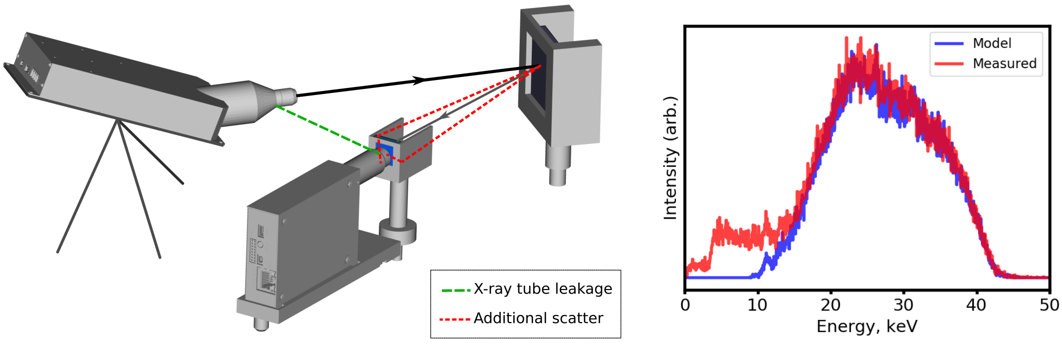

(A) (B)

FIGURE 5.16: (A) shows a diagram of the set-up showing possible paths of x-rays contributing to the detector response due to x-ray tube leakage or additional scatter. (B) shows the backscatter spectrum for the model in blue (that does not take into account x-ray scatter of the filter) and the experimentally measured spectrum in red.

are not coming from x-rays passing directly through the filter but rather from x-rays that have scattered off other components of the experiment and into the detector.

The response correction factor (RCF) was calculated to describe how all the aforementioned effects influence the detector measurement. The method for calculating the RCF was developed by the author for this application and a detailed discussion can be found in Section 4.5. Two calibration materials were used for the experimental measurements: Nylon (for HDPE, POM and PVC samples) and Acrylic (for PTFE and PVDF samples). The calculated RCF as a function of filter thickness are shown in Figure 5.17. The numerical values for the RCF as a function of filter thickness are given in Table 5.3. The response correction factor decreased with increasing filter thickness. This is to be expected as the thicker the filter the smaller the fraction of real signal in the detector response.

There is a difference the RCF between the two experiment days. The Acrylic (day 2) measurement is higher than Nylon (day 1) for all filters. The rate of decrease is approximately the same for both however. The most likely reason for this is due to a difference in x-ray tube alignment on the two experimental days. This will be discussed in more detail in Section 8.4.1. Additionally, environmental effects such as a ambient temperature may also play a role (see Section 8.6). The difference in energy spectra between the two scattered samples was thought to have a small effect on the RCF. Similarly, this will be discussed further in Section 8.4.4.

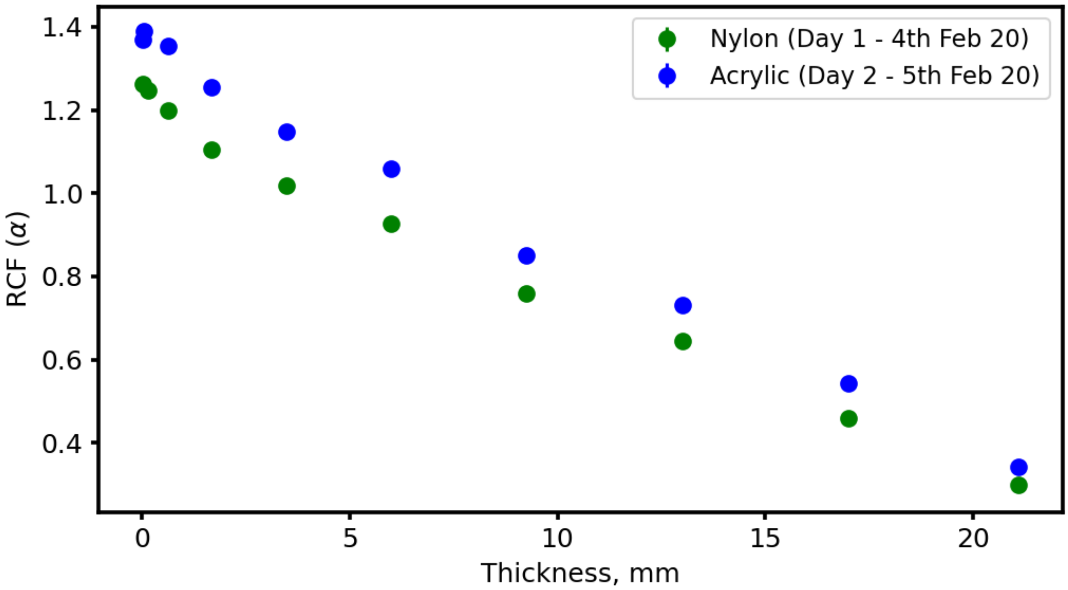

FIGURE 5.17: Response correction factor α as a function of filter thickness for Acrylic and Nylon samples. The numerical values are given in Table 5.3. Errors are too small to be seen but given in Table 5.3.

#	Filter thickness, mm	Correction factor, α (RCF)	
		Day 1 - Nylon	Day 2 - Acrylic
A	0.0066 ± 0.0015	1.263 ± 0.004	1.370 ± 0.005
B (day 1)	0.14 ± 0.01	1.248 ± 0.004	-
B (day 2)	0.05 ± 0.005	-	1.389 ± 0.005
C	0.63 ± 0.02	1.198 ± 0.005	1.353 ± 0.006
D	1.68 ± 0.09	1.105 ± 0.005	1.256 ± 0.006
E	3.47 ± 0.16	1.018 ± 0.006	1.147 ± 0.007
F	6.0 ± 0.22	0.928 ± 0.008	1.058 ± 0.009
G	9.26 ± 0.28	0.758 ± 0.009	0.850 ± 0.01
H	13.0 ± 0.34	0.644 ± 0.011	0.730 ± 0.014
I	17.0 ± 0.38	0.458 ± 0.011	0.542 ± 0.014
J	21.1 ± 0.43	0.298 ± 0.009	0.342 ± 0.011

TABLE 5.3: RCF as a function of filter thickness for both experiment days.

5.8 Chapter summary

This chapter has presented the techniques used to acquire experimental data for reconstruction using the energy spectrum reconstruction method. Calibration measurements for the x-ray source and CdTe detector were presented. Both devices were found to be functioning as expected. The set-up design was discussed along with the data acquisition process. Five materials were tested over two experimental days. The materials were HDPE, POM, PVDF, PTFE and PVDF. Eleven different measurements were acquired of the scatter spectra a scattering angle of 140° for 60 s each (ten filters and one unfiltered measurement). Calibration measurements were also acquired for each day using calibration materials Nylon and Acrylic.

Chapter 6

Simulation design

Two Monte Carlo simulations of the experimental geometry were written using the Geant4 simulation toolkit (version 10.3.1) [111]. One simulation that was run was a simulation of all the experimental components, known as the "full geometry simulation". The purpose of this was to simulate the experiment for materials that could not be tested in the laboratory due to their hazardous nature, or lack of availability of samples. The other simulation was a simplified geometry simulation, known as the "simple simulation". Only the detector, sample and x-ray source were simulated. This geometry was used to generate the expected spectrum model that was used in the calibration process for calculating the alpha correction factor, or RCF. This chapter explains how simulations were designed and validated.

6.1 Monte Carlo simulation theory

Monte Carlo is a technique for evaluating integrals using random numbers. A simple problem often used to introduce the Monte Carlo method is the calculation of π. To calculate π, N points are generated within a unit square by randomly generating the x and y positions. The ratio of the number of points within the quarter circle with r=1 and the number of random samples generated can be used to calculate π as $\pi = 4 \times N_c/N$ where N_c is the number of points in the quarter circle and r is the radius of the circle. This process is demonstrated in Figure 6.1a which uses N=5000 as an example. The error in the value of π is proportional to N_c, $\sigma_\pi = \pi/\sqrt{N_c}$. The red points represent N_c and the total number of points in the unit square (both red and blue points) is N. The accuracy to which π is calculated is dependent on the number of points generated. Figure 6.1b shows how the calculated value of π changes as a function of the number of points. As N increases the value of π converges to the true value and becomes more accurate with the error reducing.

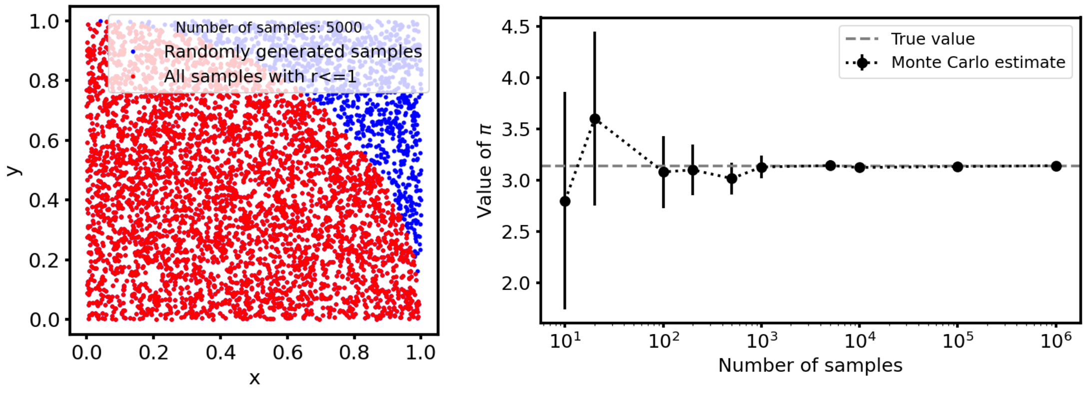

(A) (B)

FIGURE 6.1: Illustration of a simple Monte Carlo simulation to calculate π. (A) shows an example for N=5000 random samples. To calculate π the ratio of the number of points within the quarter circle of radius 1 (red points) is compared to the total number of points within the unit square. (B) shows how the estimate of π changes as a function of the number of points generated.

Monte Carlo methods are commonly used to simulate processes involving radiation transport [112, 113]. Radiation transport modelling involves integrating probability density functions associated with photon-matter interaction cross-sections [112]. Although the integrals are more complex compared to the simple example described, the technique is the same.

6.2 Geant4 simulation software

The Monte Carlo simulation software package Geant4 (version 10.3.1) [111] was used throughout this work. Geant4 is extensively used in high-energy physics and has been used with success in previous studies to simulate x-ray backscatter imaging geometries [113–115].

Geant4 allows the user to define the simulation geometry, either from a CAD file or by using pre-defined shapes. Materials for each part of the geometry must be specified. The geometry can contain any part of the experiment the user wishes to simulate, including any radiation detectors. Each simulation must have a source of radiation, for example a beam of x-rays. Using the x-ray beam as an example, in each run of the simulation, an x-ray photon is generated. The photon is then passed through the simulation geometry by simulating a set length of step through the geometry. At each step, the photon can undergo an interaction and the likelihood of interaction is determined by cross-sections using Monte Carlo methods. Detectors can be simulated by making part of the geometry "active", which means any photons incident on that part of the geometry are tracked and properties such as energy recorded.

Geant4 utilises a number of cross-section databases in order to model a range of radiation transport processes at different energies. These databases are known as physics lists. In this work the Livermore physics list was used [116] due to its suitability for modelling electromagnetic interactions in the energy region of interest (1-50 keV). The standard Livermore physics list step cuts and energy thresholds were used. The physics processes described by the Livermore physics list have been independently validated against experimental results, for example [117–119].

6.3 Simulation of materials in Geant4

Some materials are pre-programmed into the Geant4 simulation software and thus available from a materials database [120]. Other materials of interest not in the database were manually added to the simulation. Information about the molecular composition (type of element and how many atoms per molecule) and the material density was given. The materials manually added into the simulation in this work were TNT, hydrogen peroxide, PETN, RDX, cocaine, HDPE, cellulose, salt and sodium fluoride, as will be discussed later in Section 6.4.5.1. As the x-ray photon interactions with matter depend on material density and atomic number properties, this level of information was deemed appropriate to accurately simulate the backscatter spectra of these materials. Building materials in this way from their composite elements and properties in Geant4 has also been independently validated [117].

6.4 Full geometry simulation

A simulation of the experiment discussed in Section 5.4 was written in Geant4. This will be called the full geometry (or FG) simulation in what follows. The simulation was written for two purposes:

1. To acquire data for materials that could not be tested experimentally
2. To investigate systematic error effects (discussed in Chapter 8)

In each case, simulations were run for 1.25×10^{10} events to acquire scatter spectra with similar statistics to that measured in a 60 s acquisition in the experiment. This meant in each simulation 1.25×10^{10} individual x-rays were simulated. The total simulation time for each material (11 simulations in total) was approximately 12 h running on a computer cluster [1]

---

[1] 300-core computer cluster with a minimum of 500 MB of RAM per core and a clock speed of 2.2 GHz. Jobs controlled using HT Condor version 8.6.6 [121].

6.4.1 Geometry details

The FG simulation geometry was designed following the experimental geometry as discussed in Section 5.4 closely to model the scatter background as accurately as possible. The main components of the simulation were the scattering plate, filter and detector. Alongside these were the filter and sample holders, x-ray tube and detector cases, and plastic base plate and steel tabletop as shown in Figure 6.2. A detailed detector geometry was also used to accurately model the detector response as shown in Figure 6.3. The detector geometry model incorporated the detector beryllium window, platinum contact and copper heat sink as well as the CdTe crystal [122] following [123] to manufacturer specifications. Size and material composition details of each simulation component are given in Table 6.1. Following the experiment, the source-to-sample and sample-to-detector distances were 17.0 and 10.0 cm respectively.

Only components within the immediate vicinity (<30 cm away from the source) were included in the simulation. Objects in the test facility >30 cm away were not included, such as the walls, control PC and other equipment in the warehouse. This was done to minimise the simulation run time. The scatter off these object was thought to be minimal as if the x-ray beam were to reach to the objects in the distance it would most likely be absorbed. If it was scattered, due to the large distance away from the detector and small angular size of the detector, it was unlikely the rate would be significant. Additionally, experimental tests involving a lead beam stop ~30 cm away from the x-ray source saw no change in the detected spectrum with or without the beam stop supporting this decision.

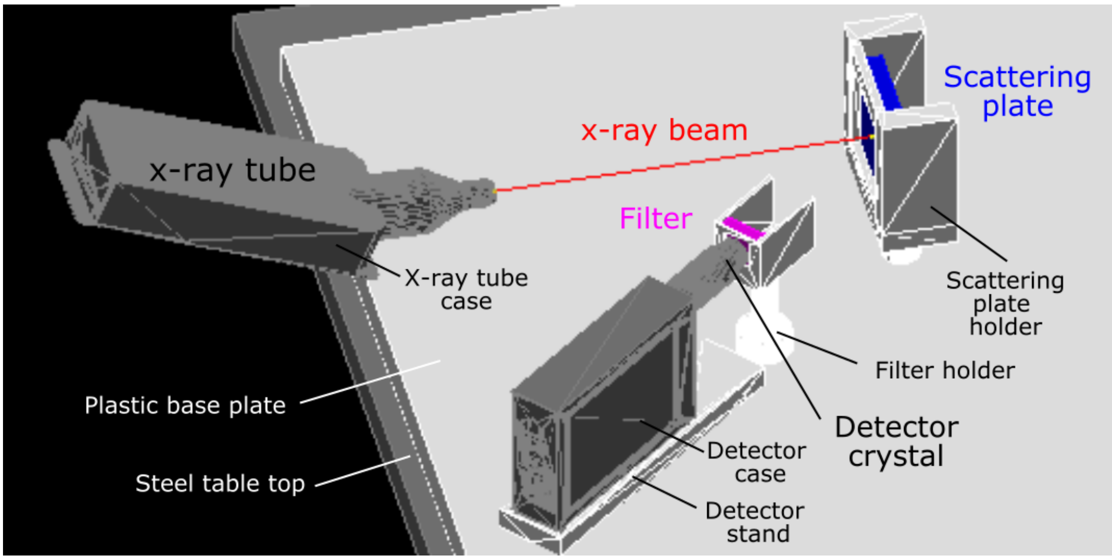

FIGURE 6.2: The full simulation geometry from the Geant4 Qt visualisation All components of the simulation geometry are labelled. See Table 6.1 for size and material information. The detector crystal consists of a more complex geometry as shown in Figure 6.3.

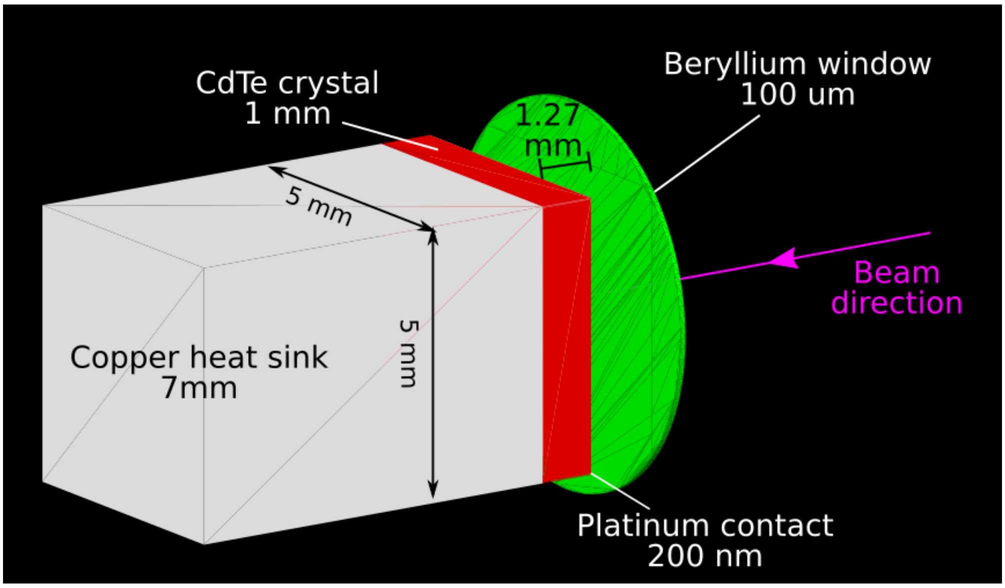

FIGURE 6.3: Schematic of the detector geometry used in the full geometry simulation. This part of the geometry makes up the detector crystal labelled in Figure 6.2. The dimensions of the components shown are given in Table 6.1.

Component	Size	Material
	Main geometry	
Sample	48×48×10 mm	Variable
Filter	20×25 mm, thickness variable	Aluminium
Detector case	To manufacturer CAD file [103]	Aluminium
X-ray tube case	To manufacturer CAD file [38]	Aluminium
Sample holder	To fit sample	PLA plastic 10% density
Filter holder	To fit filters	PLA plastic 10% density
Detector stand	To fit detector	PLA plastic 10% density
Base plate	50×2×40 cm	POM
Table top	60×2×60 cm	Stainless steel
	Detector geometry	
Detector crystal	5×5×1 mm	Cadmium telluride
Heat sink	5×5×7 mm [123]	Copper
Detector window	100 μm×3.45 mm^2 [122, 123]	Beryllium
Crystal contact	5×5 mm×200 nm [123]	Platinum

TABLE 6.1: Dimensions and material properties of all components included in the full geometry simulation. The components of the main geometry are shown in Figure 6.2 and the components of the detector geometry are shown in Figure 6.3.

6.4.2 X-ray source simulation

The x-ray source was simulated to be as close to the actual x-ray tube used in the experiment. The x-ray source was modelled as a circle with radius 1 mm. At the start of each event, the position of x-ray emission was chosen by randomly selecting a point within this circle. X-rays were emitted within a 5° cone. The x-ray emission direction at each event was chosen by randomly selecting a direction within this emission cone. The x-ray energy was chosen by randomly selecting an energy according to an energy distribution. The energy distribution used was the x-ray output spectrum in Section 5.2.1 which was measured by the CdTe detector in the aligned position (position (300,600) in Figure 5.5).

6.4.3 Detector simulation

The detector in the simulation was programmed to record the energy of the detected x-ray and such results were output as a histogram. An energy threshold of 2.5 keV for x-rays was also applied to the simulation histogram as this threshold was applied to the CdTe detector in the experimental measurements.

The detector resolution was added post-simulation. As discussed in Section 5.3.2, the measured CdTe energy resolution was not a clear function of x-ray energy over the measured energy range. When simulated and experimental spectra were compared (see Section 6.4.4 for more detailed analysis), it was clear that all of the measured FWHMs at any energy were too large because a resolution of 0.25 keV FWHM was found to best describe the widths of the characteristic x-rays in spectrum. This was because the x-ray spectrum input into the simulation already had in part some effect of the CdTe detector. The input spectrum used was the x-ray output spectrum as measured by the CdTe detector (see Figure 5.4 for a reminder of the input spectrum). The only way of correcting this would be to use an input spectrum with the measurement effects removed, and a detailed discussion of this can be found in Section 9.4. Note that the resolution was added at the last stage as part of spectrum processing and was not a component of the simulation. Therefore validation of the simulation geometry was still possible with an empirically determined resolution of 0.25 keV.

6.4.4 Energy spectrum validation

Before a Monte Carlo simulation can be trusted the results must be validated by comparison to experimental data. The simulation was validated by comparing simulated spectra to experimental spectra. Four materials and all eleven different filtration measurements for each (10 filters plus no filter) were compared. The materials were HDPE, Nylon, POM and PVC. The experimental spectrum used for the comparison was one with the background subtracted.

Material	Number of counts in the unfiltered spectrum (x=0)			f_n
	Experiment, $N_e(x=0)$ (60s acquisition) $\times 10^5$ counts	Simulation, $N_s(x=0)$ (1.25×10^{10} events) $\times 10^5$ counts	Difference (Sim-Expt) $\times 10^5$ counts	
HDPE	2.082 ±0.005	2.439±0.005	0.357±0.007	0.85
POM	1.991±0.005	2.169±0.005	0.178±0.007	0.92
Nylon	2.117 ± 0.005	2.296±0.005	0.179±0.007	0.92
PVC	0.604 ± 0.003	0.600±0.003	-0.004±0.004	1.01

Table 6.2: Number of counts in the spectrum for the experiment and simulation.

The background measurement was a measurement with no sample at the appropriate filter thickness. The similarity of the spectra were assessed by visual comparison of the two spectra. An exact bin-by-bin numerical comparison was not possible because the experiment and simulation had different bin widths (0.050 keV for the simulation and 0.052 keV for the experiment). Overall, 44 different spectra were compared. Only a few select examples are discussed in this section as the differences between all the materials and spectra were similar. For completeness all spectra that were used in the validation process are given in Appendix A.

To take into account the small differences between the number of counts in the experiment and simulation, all simulated spectra were normalised to the total number of counts in the spectrum by the normalisation factor $f_n = N_e(x=0)/N_s(x=0)$ Here $N_e(x=0)$ is the number of counts in the experiment spectrum for no filter and $N_s(x=0)$ is the number of counts in the simulated spectrum for no filter. The $N_e(x=0)$ and $N_s(x=0)$ values are given for all materials used in the validation in Table 6.2.

6.4.4.1 Spectrum comparisons

Consider the sample material 10 mm thick POM. Example spectra for no filter, and filters B, D and J are shown in Figure 6.4. The simulated spectra followed the same general trend as the experiment for all tested materials and thicknesses. Spectra were visually most similar in the 10-25 keV region. In the 2.5-10 keV and 25-40 keV regions the experiment had more counts than the simulation. For thicker filters, for example filter I in Figure 6.4d, the experiment was more noisy due to the smaller number of counts compared to the simulation. As given in Table 6.2, there was a difference of (0.179±0.007)$\times10^5$ counts between the simulation and experiment for the unfiltered measurement. Similar trends were seen across the other three materials.

In addition to the spectrum differences between 2.5-10 keV and 25-40 keV, the experimental spectrum for PVC had an additional peak at 25 keV. A comparison of the simulated and

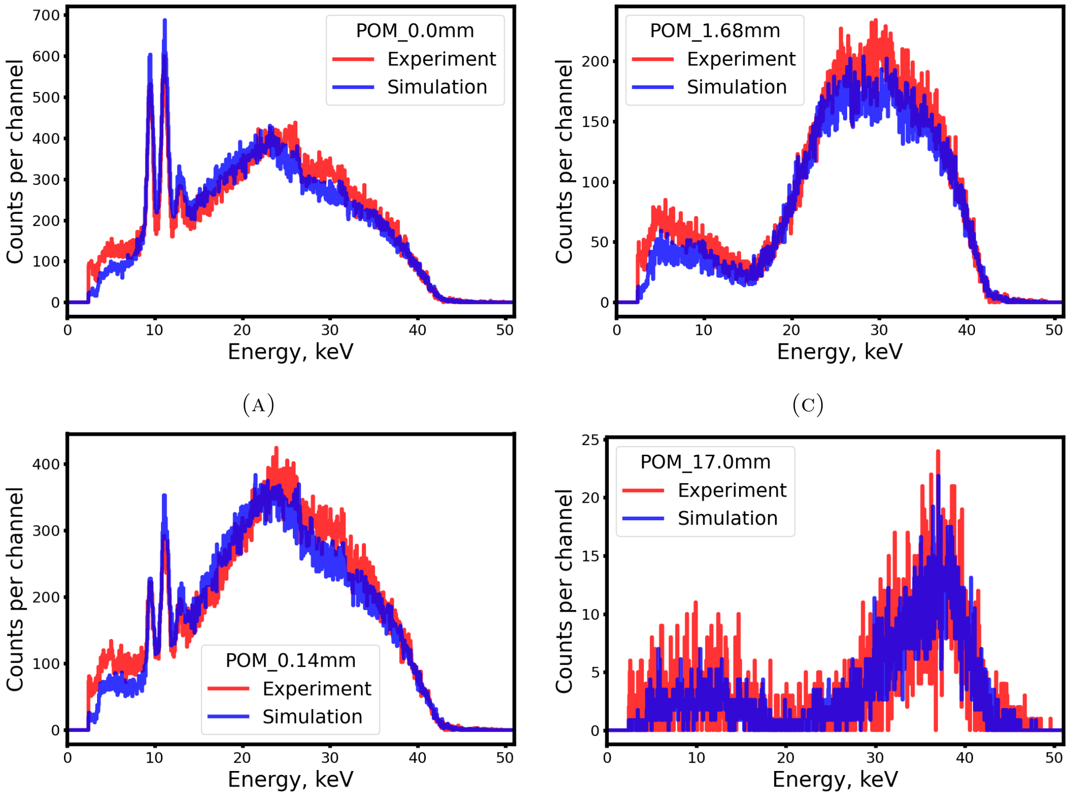

(A) (C)

(B) (D)

FIGURE 6.4: Comparison of simulated and experimental spectra for a 10 mm thick POM sample for (A) no filter, (B) filter B (0.14 mm), (C) filter D (1.68 mm) and (D) filter I (17.0 mm).

experimental spectra for PVC is shown in Figure 6.5a. The source of this is a tin impurity in the PVC sample as 25 keV corresponds to the Kα x-ray fluorescence line in tin [124]. Although exact elemental composition was not available from the supplier, tin is the most likely source as tin is often added as a stabiliser to PVC plastic to improve rigidity [125].

The HDPE spectrum comparison is shown in Figure 6.5b. The simulation and experiment show good agreement with the exception of the aforementioned areas at 2.5-10 keV and 25-40 keV. Nonetheless, the difference between the simulation and experiment in terms of total counts is 17% from the $N_e(x = 0)$ and $N_s(x = 0)$ values in Table 6.2. For the other three materials it is 9% or less. The most likely explanation for this is that the density for the experimentally tested material is not exactly the same as the HDPE sample simulated. There are a range of densities for HDPE (0.93-0.97 $\mathrm{g\,cm^{-3}}$) [126]. All the other materials were acquired directly from the manufacturer and hence the type of material, atomic number and density could be reliably confirmed. The HDPE sample came from a different source so the density and atomic number could not be confirmed. HDPE was the best estimate based on an inspection of the sample. As a range of HDPE properties exist, it could be that the HDPE was different to that simulated, hence a different spectrum was produced. To

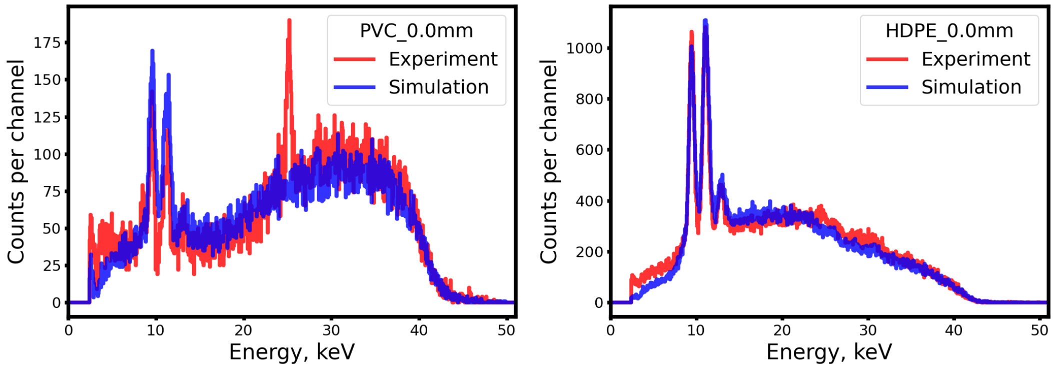

(A) PVC (B) HDPE

FIGURE 6.5: Comparison of simulated and experimental spectra for a 10 mm thick (A) HDPE and (B) PVC. Both spectra shown are unfiltered.

eliminate this issue, the HDPE sample should be weighed to confirm its density. This could not be carried out in this work due to restricted laboratory access over the pandemic.

6.4.4.2 Analysis of spectral differences

Further analysis of the spectral differences between 2.5-10 keV and 25-35 keV was performed using POM as an example. Figure 6.6 shows the simulated and experiment spectra for POM with no filter. Both spectra have been normalised to the channel with the largest number of counts to highlight differences in the distributions. In the energy region 0-10 keV (region(a) in Figure 6.6) and 25-35 keV (region (b) in Figure 6.6) there are more counts in the experimentally measured spectrum. In both spectra there are edge features at 26.7 keV and 31.8 keV corresponding to the K edge energies for Cd and Te, but these are much more prominent in the experiment spectrum.

Both these features were due to the x-ray spectrum input into the simulation. The simulation input spectrum was the output spectrum of the x-ray tube as measured by the CdTe detector (discussed in Section 5.2.1). This input spectrum contained features due to the detector response, namely edges at 26.7 and 31.8 keV, and more events at low energies. Both features were caused by escape events within the CdTe crystal [96]. The x-ray tube was therefore outputting more x-rays above 26.7 keV than what was measured by the CdTe detector [96]. When this input spectrum (with less high energy events than expected) was put into the simulation, there were then less escape events in the simulation as there were fewer x-rays above 26.7 keV being simulated. This resulted in a less pronounced K edge and fewer low energy counts. The low energy region was also increased in the experiment due to detector noise as this was not simulated in the experiment.

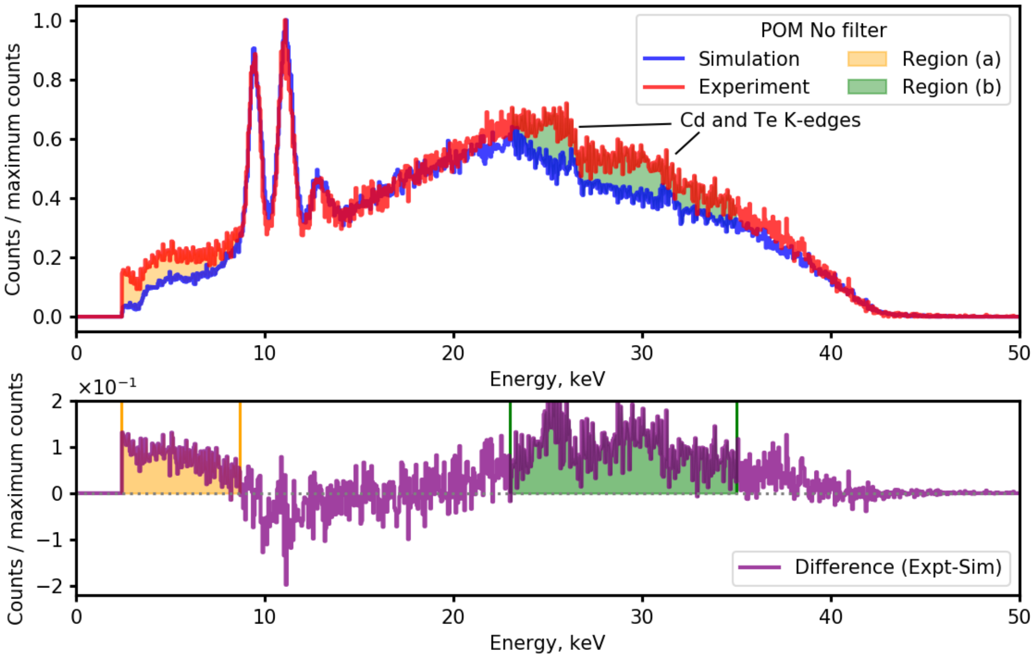

FIGURE 6.6: Simulated and experiment spectra for 10 mm POM (unfiltered). Both spectra are normalised to the channel with the largest number of counts to highlight the differences in the distributions of the two spectra. The two areas where the spectra differ most are indicated by the shaded regions. These are (a) 0-10 keV, shown in yellow and (b) 25-35 keV shown in green.

Overall, despite spectral differences in some regions, good agreement between the simulation and experiment was demonstrated. To improve in regions of differences, the simulation could instead use an x-ray tube input spectrum with the measurement effects removed. Applying spectrum processing software to remove the absorption edges [96], or using an x-ray tube spectrum model could achieve this, however both methods would introduce additional errors. This will be subject of further discussion in Section 9.4. Nonetheless the simulation reproduced the experimental spectrum shapes to high accuracy and it was concluded the simulation was suitable for the required uses.

6.4.5 Simulation method

The simulations were run following a process very similar to the experimental method. For each material, eleven different simulations were performed: one for each of the ten different filter thicknesses given in Table 5.2 and one with no filter.

The reconstruction of the energy spectra was the same as for the experimental spectra as outlined in Section 5.5. First an energy integrated detector response was calculated by adding the product of the number of counts and energy for each energy bin, $I=\sum^{i} E_i N_i$ where i is the number of bins in the spectrum (see Equation 5.1). The error in the detector response was calculated as $\delta{=}\sum^{i}\sigma_i$ where σ_i is the error in the detector response measurement I.The equation $\vec{\alpha}\vec{I} = \mathbf{W}\vec{N}$ was then solved using Tikhonov regularisation to calculate the energy spectrum $\vec{N}$. The RCF (or α) was calculated in the same way as the experiment as discussed in Section 4.5 to quantify how different the full simulation was to the model.

6.4.5.1 Case 1: Testing the reconstruction method on additional materials

In case 1, 33 different organic materials were simulated. The materials had atomic numbers between Z=3 and Z <16. The densities for the materials tested were between 0.534 g cm^{-3} (Lithium) and 2.699 g cm^{-3} (Aluminium). Among the simulated materials were all the experimentally tested materials (HDPE, POM, PVC, PVDF and PTFE) as well as explosives and narcotics (Hydrogen peroxide, RDX, TNT, PETN and cocaine). All samples were 10 mm thick and run for 1.25$\times$10^{10} simulation events. Nylon was used as the calibration dataset for calculating the RCF.

The atomic number and density properties for all simulated materials are given in Table 6.3. Most materials used were available from the Geant4 materials database [120]. A few materials (HDPE, cocaine, cellulose, TNT, RDX, PETN, hydrogen peroxide, sodium fluoride and salt) were not in the Geant4 materials database so were manually added by providing information about the atomic number, density and molecular composition. The chemical equation used for each material not in the Geant4 database is also given in Table 6.3.

Figure 6.7 shows the atomic numbers and densities for all simulated materials given in Table 6.3. The vast majority of explosives lie between 6.5$\leq Z_{eff} \leq$8.0 and (1.4$\leq \rho \leq$2.0) g cm^{-3} [17]. This region is marked in red in Figure 6.7. All explosive materials simulated lay within this region as well as two inert materials Sucrose and Cellulose, and two explosive simulants, POM and PVDF.

Material name	Z_{eff}	ρ, g cm^{-3}	In-built in Geant4?	Chemical equation (if not inbuilt)
Lithium	3	0.534	Yes	-
Beryllium	4	1.848	Yes	-
Boron	5	2.37	Yes	-
HDPE	5.53	0.97	No	$(C_2H_4)_n$
Polypropylene	5.67	0.9	Yes	-
Polystyrene	5.74	1.06	Yes	
Nylon	6.21	1.14	Yes	-
Acetone	6.39	0.7899	Yes	-
Cocaine	6.39	1.22	No	$C_{17}H_{21}NO_4$
Acrylic	6.56	1.18	Yes	-
PVA	6.7	1.19	Yes	-
Ethanol	6.79	0.7893	Yes	-
Cellulose	6.97	1.5	No	$(C_6H_{10}O_5)_n$
Sucrose	7.00	1.5805	Yes	-
POM	7.03	1.41	Yes	-
TNT	7.1	1.654	No	$C_7H_5N_3O_6$
RDX	7.25	1.82	No	$C_3H_6N_6O_6$
PETN	7.42	1.77	No	$C_5H_8N_4O_{12}$
Water	7.51	1	Yes	-
Hydrogen Peroxide	7.74	1.45	No	H_2O_2
PVDF	7.97	1.78	Yes	-
PTFE	8.48	2.2	Yes	-
Sodium fluoride	10.22	2.56	No	NaF
Sodium	11	0.971	Yes	-
Silica	11.75	2.32	Yes	-
Magnesium	12	1.74	Yes	-
Pyrex	12.17	2.23	Yes	-
PTFCE	12.71	2.1	Yes	-
Aluminium	13	2.699	Yes	-
PVC	14.26	1.45	Yes	-
Concrete	14.55	2.3	Yes	-
Gypsum	14.6	2.32	Yes	-
Salt	15.31	2.16	No	NaCl

TABLE 6.3: Density and atomic number properties for all materials simulated using the full geometry simulation case 1. Most materials were simulated using the in-built entry in the Geant4 materials database [120]. Some materials were manually added to the database by providing the density, Z_{eff} and molecular composition. This is indicated in the table.

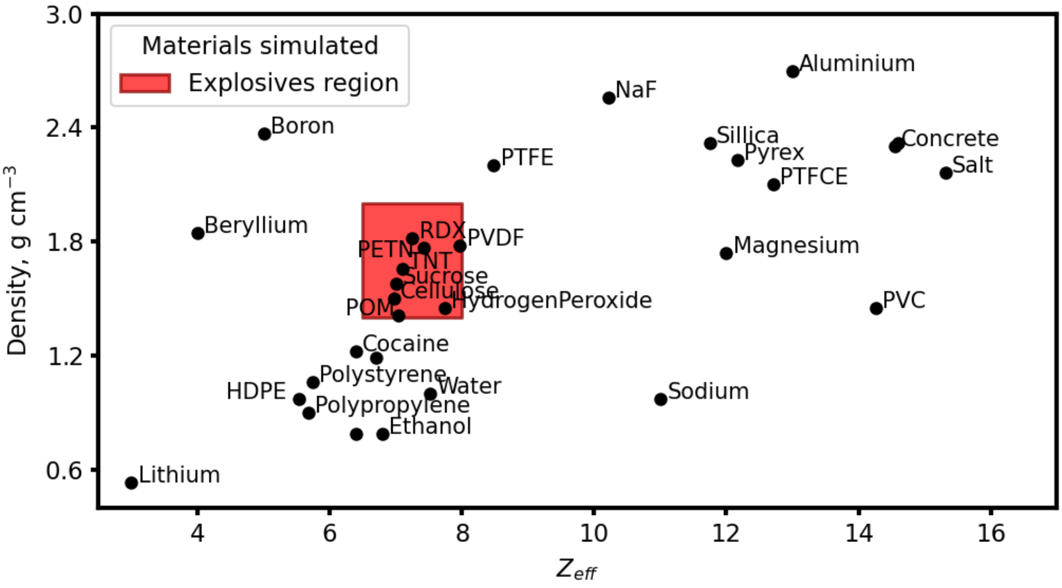

FIGURE 6.7: Atomic number and density properties for all materials simulated for full geometry case 1 as described in Section 6.4.5.1. Labels for materials Acetone, PVA and Gypsum have been omitted for clarity. The explosive material region is marked in red as explained in the main text. All Z_{eff} and ρ values are given in Table 6.3.

6.4.5.2 Case 2: Investigation of systematic errors

The full simulation geometry was also used in order to understand how systematic errors affected the accuracy of the energy spectrum reconstruction method. The sample material was 10 mm POM and all simulations were run for 1.25×10^{10} events. Minor modifications to the full geometry were made in order to simulate a specific systematic error. Further details of these simulations and modifications are provided in Chapter 10.

6.5 Simple simulation

A simulation of the 50 keV scattering experiment with a simplified geometry was also performed. This will be called the simple geometry (SG) simulation in what follows. The SG was used in cases where the full detail of the full simulation geometry was not necessary. The advantage of using the simplified simulation was the simulation run time was much shorter than the full geometry. Each simulation took approximately 1 h to run 1.25×10^{10} events (compared to 12 h for the same number of events in the full geometry). The two uses of the simple simulation were:

1. To calculate the theoretical spectrum for use when calculating the RCF (Section 5.7).

2. To understand the behaviour of the Tikhonov solutions in a simple case (Section 4.7).

Details for each case are provided in this section.

6.5.1 Simple simulation geometry

The simple simulation geometry consisted of a point x-ray source, sample and detector as shown in Figure 6.8. The dimensions of the set-up were the same as in the experiment and full simulation; the source-to-sample distance was 17 cm and sample-to-detector distance of 10 cm. The angle between the incident and scattered beams was 40 ° (scattering angle 140 °). The sample size was 48×48×10 mm and the detector volume was 5×5×1 mm.

The size and divergence of the x-ray beam was not modelled. Instead the x-ray beam was simulated as a point source emitting x-rays in a fixed direction in a straight line along the line connecting the point source and the centre of the sample. The energy of the x-rays was chosen by randomly selecting an energy from the aligned distribution spectrum at the start of each run, as done in the full simulation (see Section 6.4.2).

The CdTe detector material was not modelled in the simplified simulation so it could be used as the theoretical measurement. To do this the detector material was set as a vacuum and the energy of the x-rays incident on the surface of the detector volume were measured. The x-ray energies were then put into a histogram as in the full simulation to produce an energy spectrum.

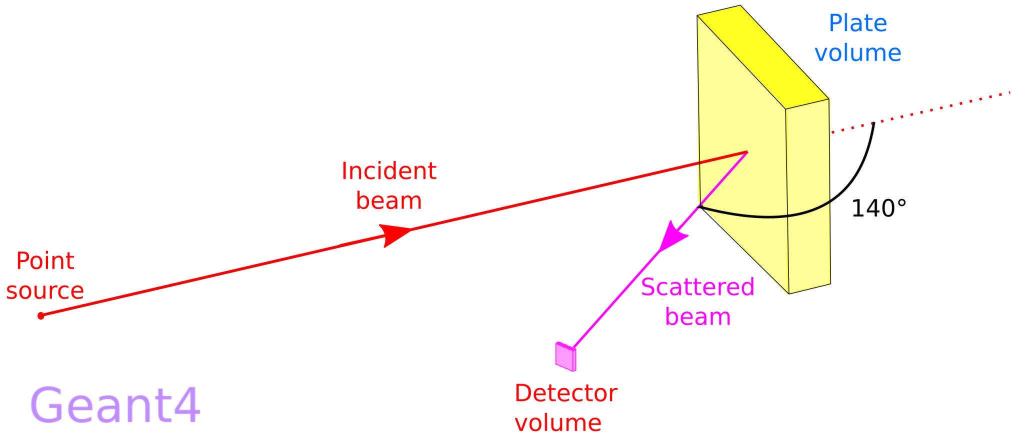

Figure 6.8: Geant4 simulation geometry for a simplified simulation of the experimental setup.

6.5.2 Simple simulation validation

The simulation was validated by comparison with spectra from the full simulation. The simulation was not validated by comparison with experimental data as it was a theoretical simulation with the sole purpose of not including any experimental effects. Both the simple and full simulations were run for 1.25$\times$10^{10} events each using POM as the sample material. The result is shown in Figure 6.9.

As shown in Figure 6.9 there are fewer x-rays with energy below 10 keV and more x-rays with energy above 25 keV in the simple simulation. This is because x-rays are now only scattering off the sample and not off other parts of the geometry as expected.

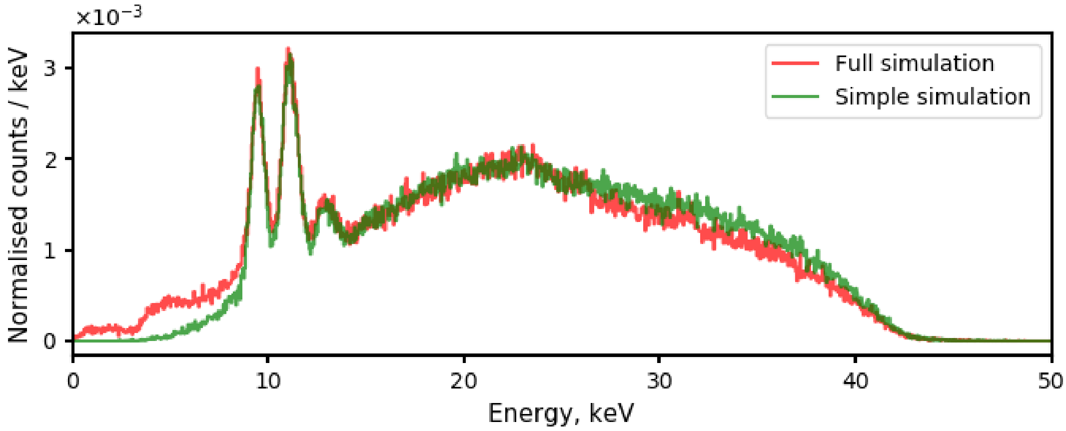

FIGURE 6.9: Simulated energy spectra for the full simulation (red curve) and the simple simulation (green curve) with POM as the sample material. Simulations were run for 1.25$\times$10^{10} events each. Both spectra have been normalised to the total number of counts in the spectrum to show the differences in the energy distribution.

6.5.3 Case 1: Use in RCF method

The SG was used to generate the theoretical scatter spectrum used to determine the calibration factor $\vec{\alpha}$. The method for calculating the RCF is discussed in Section 4.5. Two different calculations of α were required, one for each of the experimental days. The calibration material used on day 1 was Nylon, and for day 2 it was Acrylic. The simple simulation was run for both Acrylic and Nylon sample materials. For each material the simulation was run for 1.25$\times$10^{10} events. The resulting spectrum for each material was re-binned to 10 energy bins. This binned spectrum was the parameter $\vec{N}$ discussed in Section 4.5. The RCF could thus be calculated using Equation 4.28 in Section 4.5.

6.5.4 Case 2: Use in understanding Tikhonov solutions

The SG was also used to understand the behaviour of Tikhonov solutions in Section 4.7. One simulation was performed using a 10 mm Nylon sample material. The simulation was run for 5×10^9 events. Filters were added mathematically instead of simulating the filter in Geant4 in order to eliminate effects of scatter from the filters, as will be discussed in this section. By mathematically adding the filters, the detector responses was exactly as expected by the reconstruction model, allowing the intrinsic errors of the model to be investigated without the complications of additional scatter.

The filtered detector response measurements were simulated by taking each bin of the spectrum and mathematically applying the attenuation factor as follows,

$$N_j(x_k) = N_j e^{-\mu(E_j)x_k}. \tag{6.1}$$

Here N_j is the number of counts in bin j in the simulated spectrum, E_j is the energy of bin j, and x_k is the filter thickness of the filter to be simulated. $\mu(E_j)$ is the attenuation coefficient for aluminium at energy E_j as given by the NIST XCOM database [52]. $N_j(x_k)$ is the number of counts in bin j in the filtered spectrum. The detector response I_k was therefore

$$I_k = \sum^{j} N_j(x_k)E_j, \tag{6.2}$$

and the error in I_k, σ_{I_k} was

$$\sigma^2_{I_k} = \sum^{j} \left(E_j\sqrt{N_j(x_k)}\right)^2. \tag{6.3}$$

No RCF was required as no model corrections were necessary, therefore $\vec{\alpha} = \vec{1}$. Spectra were simulated in this way for all ten of the required thicknesses. The thicknesses are given in Table 4.1. The equation $\vec{\alpha}\vec{I} = \mathbf{W}\vec{N}$ was then solved for $\vec{N}$ using Tikhonov regularisation. See Section 4.7 for further details of the analysis.

6.6 Chapter summary

This chapter introduced the basic theory of Monte Carlo simulations and discussed the design and methods of the two Geant4 simulations used in this thesis: the full geometry (FG) and simple geometry (SG) simulations. The FG simulation followed the experimental geometry as precisely as possible and was used to simulate 33 additional organic materials and investigate systematic error effects. In addition, the SG simulation was used in the RCF calibration process and for understanding the behaviour of Tikhonov solutions. Both simulations were shown to produce valid results and are hence suitable for their desired uses.

Chapter 7

Results

This chapter presents the reconstructed experimental energy spectra acquired using the spectrum reconstruction method. The reconstructed spectra are discussed in depth drawing on the knowledge of the Tikhonov solution presented in Chapter 4. Using the simulated data set of 33 materials, relationships between spectrum properties and material properties were derived. These relationships were used to categorise the experimentally tested materials as either explosive or non-explosive with a certain probability. Additionally the relationships were used to estimate the Z_{eff} and ρ of the experimentally tested materials.

All raw CdTe spectra for the experimental measurements are shown in Appendix B along with the calculated detector response values. Not all energy bins in the spectrum reconstruction were relevant for the analysis but are provided in Appendix C for reference.

7.1 Note on spectra and comparison metrics

All energy spectrum reconstructions discussed had 10 bins which were numbered bins 1-10 in ascending energy order. The total energy range was 0-50 keV and each bin was 5 keV wide. The number of counts in bin n was referred to as Cn. For example, the number of counts in bin 3, which covers an energy range of 10-15 keV, was referred to as $C3$.

Throughout the analysis spectra were compared in several ways. The first spectrum comparison metric used was the difference parameter d where

$$d = \frac{\sqrt{\sum_{j=1}^{10}(N_{1_j} - N_{2_j})^2}}{\sqrt{\sum_{j=1}^{10}(N_{1_j})^2}}. \tag{7.1}$$

Here N_{1_j} and N_{2_j} are the number of counts in bin j of spectrum 1 and spectrum 2 respectively. The parameter d is expressed as a percentage difference. This is the same as that defined in Figure 4.7 Section 4.31.

The second measure was the average energy, $\bar{E}$ where,

$$\bar{E} = \frac{\sum_{j=1}^{10} E_{c_j} N_j}{\sum_{j=1}^{10} N_j} \tag{7.2}$$

where N_j is the number of counts in bin j and E_{c_j} is the bin centre energy. This was used as a measure of the overall distribution shape. A small d value and a similar average energy meant that the spectra followed a similar shape with little variation between bins.

In some cases individual Cn values were compared to evaluate the reconstruction quality in a particular bin. The most important bins in the reconstruction were bin 3 and bin 9 as these values were used to extract the effective atomic number and density of the material from the energy spectrum (an explanation of why C3 and C9 are used is provided in Section 7.6).

7.2 Experimental detector response

Unfiltered detector response measurements were first compared. This is equivalent to a measurement that is acquired on a field backscatter system. Differences between the detector responses were observed for each material within the experimental errors. For example, HDPE had a detector response of $(4.08\pm0.01)\times10^6$ keV counts and POM $(4.39\pm0.01)\times10^6$ keV counts. These detector response values for all materials are given in Table 7.1. As shown in Figure 7.1a, there is no clear unique relationship between density and detector response. Figure 7.1b shows no clear unique relationship between detector response and Z_{eff}, however the PVC point which has the highest Z_{eff} (Z_{eff}=14.26) has an approximately 2.8 times lower detector response compared to the other materials. On a commercial backscatter system materials of high and low atomic numbers are separated out via thresholding of the detector response. However more accurate categorisation, which is needed to identify explosive materials, is not possible using the current thresholding methods.

The signal-to-noise ratio (SNR), defined as $\mathrm{SNR} = \mathrm{response}/\mathrm{error}$, is often generally smaller for field backscatter systems compared to the measurements required here. For example, for a steel sample measured with a 160 keV x-ray source at a distance of 15 m, the SNR was 77 [77, 127] (see Section 9.9 for further discussion of this). In this investigation, even for PVC the SNR is much higher at 224. Therefore even in the best case scenario material identification is still very limited so is certainly not possible on field systems.

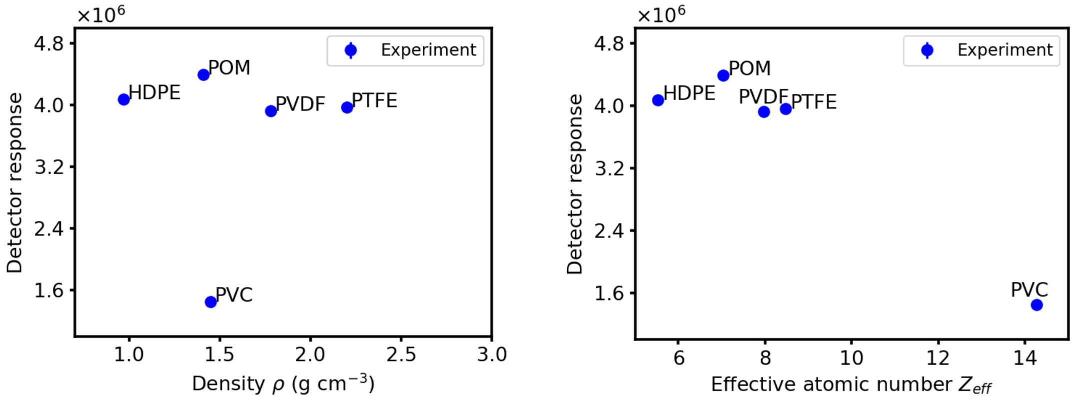

(A)

(B)

Figure 7.1: Detector response as a function of (A) density and (B) effective atomic number for experimentally tested materials. The detector response was acquired using an unfiltered CdTe detector. This represents the equivalent field measurement.

Material	Density	Z_{eff}	Detector response keV counts
HDPE	0.97	5.53	$(4.08 \pm 0.01)\times10^6$
POM	1.41	7.03	$(4.39\pm0.01)\times10^6$
PVC	1.45	14.26	$(1.45\pm 0.006)\times10^6$
PVDF	1.78	7.97	$(3.97\pm0.01)\times10^6$
PTFE	2.2	8.48	$(3.93\pm0.01)\times10^6$

Table 7.1: Detector response for the five experimental measurements as shown in Figure 7.1. The detector response was calculated from the unfiltered scattered spectrum for each material. The raw spectra are given in Appendix B.

7.3 Experimental filtered detector response

Figure 7.2 shows the detector response as a function of filter thickness for all filtered measurements for HDPE, POM, PVC, PVDF and PTFE. The values for all data points are given in Table B.1 in Appendix B. Errors are considered but too small to be seen on the plot. The percentage error on the detector responses ranged from 0.3 to 3.6%. The percentage error increased with increasing filter thickness, and was smaller as a percentage the larger the detector response. For all materials there was a decrease in the detector response as a function of filter thickness. The rate of decrease of the response also decreased as a function of filter thickness. The curves for PTFE, PVDF and POM are virtually indistinguishable. The HDPE curve has an initially steeper gradient compared to that of PTFE, PVDF and POM so is distinguishable from the others at thicknesses over ~2 mm. PVC has a much lower initial detector response and shallower gradient so is clearly distinguished from the other materials.

Similarly to that seen in the unfiltered detector response measurement, limited material discrimination is possible when using the raw filtered detector response measurements,

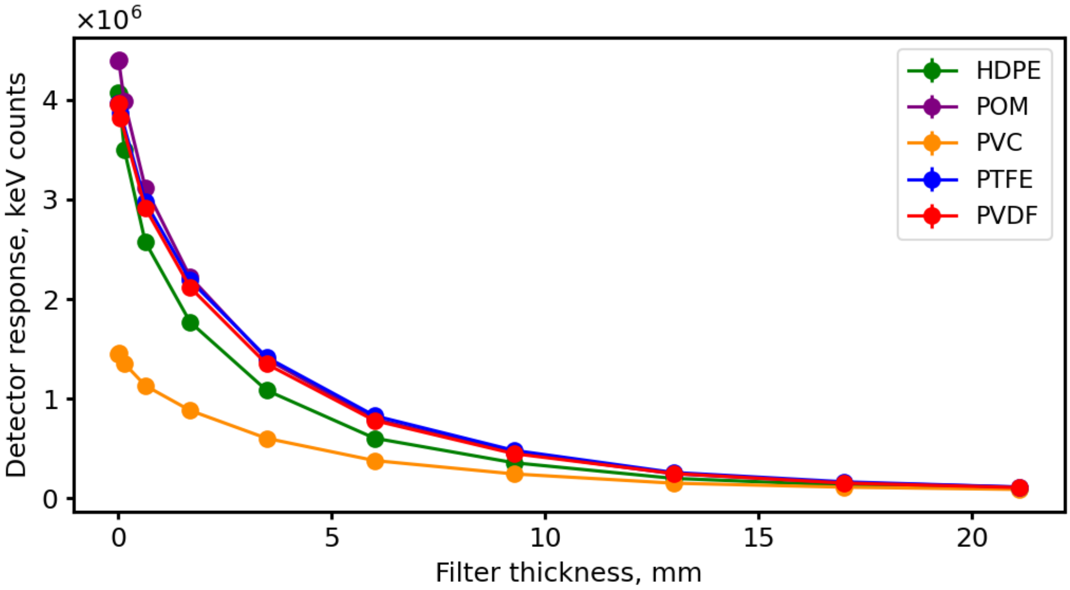

FIGURE 7.2: Detector response as a function of filter thickness for HDPE (green), POM (purple), PVC (yellow), PTFE (blue) and PVDF (red). The curves for POM, PVDF and PTFE are very similar. The percentage error on the detector response ranged from 0.3 to 3.6% as discussed in the main text.

especially for POM, PVDF and PTFE. These detector response measurements were used to perform the energy spectrum reconstruction for each material in order to improve the material separation.

7.4 Experimental energy spectrum reconstructions

The results of the energy spectrum reconstruction method showed improved material separation compared to that obtained using a single detector response measurement. This will be discussed in the following section. Reconstructions were performed using the detector response data given in Figure 7.2. Figure 7.3 shows the spectrum reconstructions from experimental measurements of HDPE, POM, PVDF, PTFE and PVC (solid line in Figure 7.3). The values for each bin in the spectrum are given in Table C.1 in Appendix C, and those relevant for the analysis (C3 and C9) are shown in Table 7.2. Each reconstruction was compared to an equivalent CdTe measurement of the energy spectrum binned to 10 bins (dashed line in Figure 7.3). The CdTe measurement was normalised so that the spectrum and reconstruction had the same number of total counts for ease of comparison. The difference between the reconstruction and spectrum was also calculated for each bin, shown below each spectrum plot in Figure 7.3.

Material	d	C3		C9		$\bar{E}$, keV	
	%	Spec	Recon	Spec	Recon	Spec	Recon
HDPE	18.6	53801 ± 232	48412 ± 1277	2228 ± 47	6369 ± 156	19.6±0.1	20.8±0.3
POM	19.5	33934 ± 184	32488 ± 1092	3233 ± 57	9444 ± 136	21.9±0.1	23.6±0.3
PVC	37.4	8010 ± 89	6424 ± 330	2026 ± 45	5264 ± 54	26.3±0.3	26.8±0.3
PVDF	23.8	26058 ± 161	21821 ± 1036	3935 ± 63	11288 ± 133	22.9±0.1	25.4±0.3
PTFE	25.9	23172 ± 152	19888 ± 1093	4494 ± 67	12222 ± 143	23.4±0.1	25.9±0.3

TABLE 7.2: Comparison of spectrum properties for experiment reconstruction (recon) and CdTe detector spectrum measurement (spec). See Figure 7.3 for the spectrum reconstructions.

The general spectrum shape was reproduced well for HDPE, POM, PVDF and PTFE (PVC is discussed separately in Section 7.4.2). The average energy was higher for the reconstructed spectrum than the measured spectrum by 1-2 keV. The spectrum differences ranged from 18.6-25.9%. The full comparison metrics are given in Table 7.2. Across all materials, the main differences are less counts in bins 1-3 and more counts in bins 4 and 9. Overall these spectrum differences are not surprising; the reconstruction is not expected to follow the spectrum measurement exactly. This is because firstly the model used in the reconstruction is an approximation, especially at low energies, and secondly because there are errors in the Tikhonov regularisation method as discussed in Section 4.7. These differences will now be evaluated in detail using the HDPE spectrum as an example.

7.4.1 HDPE reconstruction

Consider the HDPE reconstruction as shown in Figure 7.3a. The sharp peak in bin 3 in the CdTe spectrum is not reproduced in the reconstruction as a result of the regularisation. Instead the peak is wider and reaches a maximum in bin 4. The C3 value in the reconstruction is 5389±1277 counts which is 10% lower than the CdTe spectrum. The C4 value is 12782±841 counts which is 34% higher than the CdTe spectrum. C9 in the reconstruction is 4141±156 counts, 186% higher than the CdTe spectrum. This higher C9 value is as a result of the sharp change between bins 8 and 10 being smoothed out. Differences of this kind were observed in the perfect reconstruction case discussed in Section 4.7.1 as a result of the errors intrinsic to the Tikhonov solution due to regularisation.

The C1 value in the reconstruction is 5319±88 counts (85%) and C2 is 8958±1918 counts (25%) lower than the CdTe measurement. One reason for this could be noise in the lower energy bins in the CdTe measurement which has been removed by the calibration process in the reconstruction. Another reason could be inaccuracies in the reconstruction model. The model is less accurate at low energies as $\mu(E)$ varies most rapidly the lower the energy, so

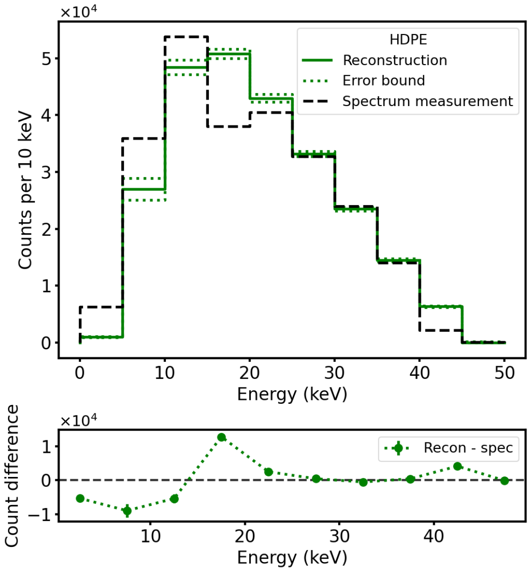

(A) HDPE

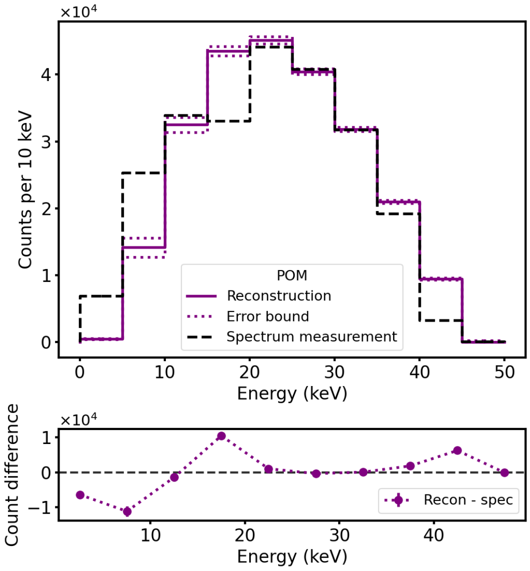

(B) POM

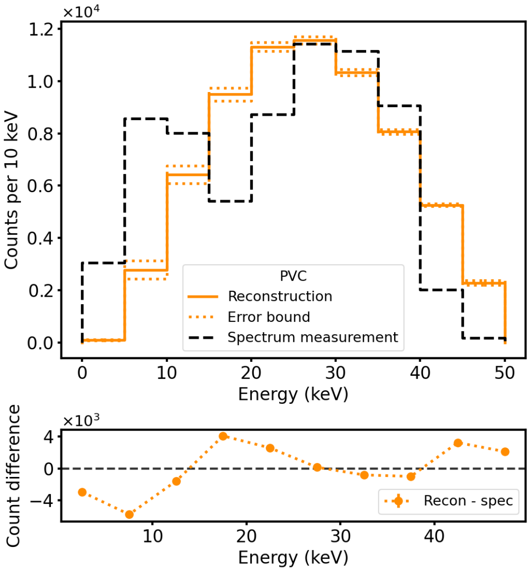

(C) PVC

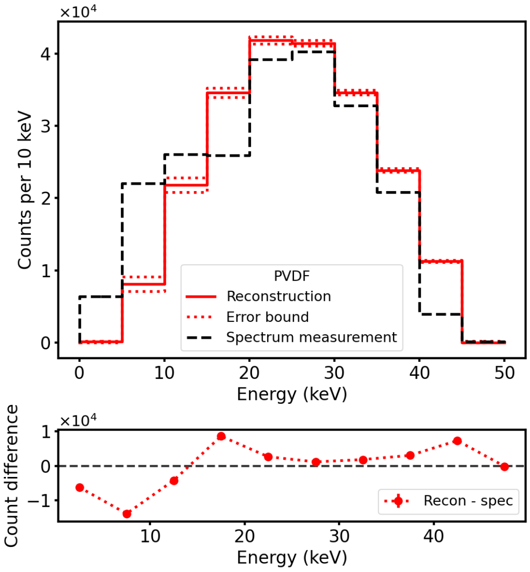

(D) PVDF

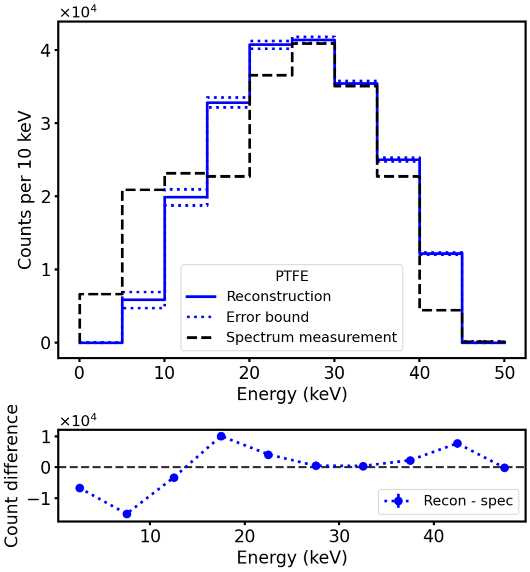

(E) PTFE

FIGURE 7.3: Energy spectrum reconstructions for (A) HDPE, (B) POM, (C) PVDF, (D) PTFE and (E) PVC. The reconstruction is shown by the solid colour line. The error in the reconstruction is shown by the coloured dashed line. The energy spectrum measurement is shown by the black dashed line for comparison. The spectrum measurement has been normalised to the total number of counts in the reconstruction for ease of comparison.

using the $\mu(E)$ corresponding to the bin centre is not representative of all the energies in the bin. The 20-40 keV (bins 5-8) region is more closely reconstructed. The maximum count difference across this range is 6.1% (bin 5). This is the smoothest part of the CdTe spectrum and hence is most accurately reproduced by the Tikhonov solution. Similar differences between the CdTe measurement and reconstructions are similar for POM (Figure 7.3b), PVDF (Figure 7.3d) and PTFE (Figure 7.3e).

7.4.2 PVC reconstruction

The PVC reconstruction as shown in Figure 7.3c is a poorer reconstruction as indicated by the d parameter value of 37.4%. Although the average energies given in Table 7.2 are similar it is clear that the structure on the lower energy side has not been reconstructed at all. The reconstruction was a different shape compared to the CdTe measurement. In the CdTe spectrum there are two distinct regions, the 0-15 keV region (region of characteristic x-ray scattering) and the region above 25 keV (region of bremsstrahlung scattering) with a clear transition between the two in the 20-25 keV. The reconstruction is too smooth to separate the two regions.

This is because the error in the data for PVC (the δ parameter) is larger than the error in the data for the other materials as there were fewer overall counts detected (δ error parameter was 0.77% for PVC compared to 0.43% for HDPE, for example). The larger δ the smoother the Tikhonov solution will be. Additionally, bin 10 in the reconstruction has a high number of counts with C10=2115±98, 1210% more than the CdTe spectrum. This is also an indication that the δ parameter is too large from the discussion in Section 4.7.2.

Analysis of the L-curve for the PVC data showed the δ parameter chosen to be representative of the data. Reconstructions with a smaller δ parameter contained artificial peaks similar to that shown in Figure 4.5g in Section 4.7.2 which is indicative of not enough regularisation. The δ parameter is proportional to the total number of detected x-rays as shown in Section 5.5 Equation 5.2. To get a δ value similar to that of the the other materials, and hence a reconstruction of similar accuracy, the PVC measurements would need to be acquired for 2.8 times longer (170 s per filter compared to 60 s). Increasing the time per measurement would reduce the scan efficiency however. This will be a subject of discussion in Section 9.9.

7.5 Comparison of simulation and experiment reconstructions

The experimental and simulated reconstructions were compared as a second validation check of the simulation. Simulations of the five experimentally tested materials were performed using the full geometry simulation. Energy spectra were reconstructed from the set of simulated detector response measurements. The reconstructions are shown in Figure 7.4. The experiment and simulated reconstructions were compared by calculating d, $\bar{E}$, $C3$ and $C9$. These parameters for all spectra shown in Figure 7.4 are given in Table 7.3. POM, PVDF and PTFE all showed good agreement between the simulation and experiment with all difference values less than 7%. This suggested the simulation was reproducing the experiment to high accuracy, supporting the results of the spectrum comparisons in Section 6.4.4. Discrepancies between the PVC and HDPE spectra were explained by a difference in the error parameter and a lack of information about the sample. Further details are provided in the following subsections.

Material	d %	C3 Sim	C3 Expt	C9 Sim	C9 Expt	$\bar{E}$, keV Sim	$\bar{E}$, keV Expt
HDPE	14.8	55590 ± 1350	48412 ± 1277	6953 ± 153	6369 ± 156	20.4±0.3	20.8±0.3
POM	5.6	31181 ± 1053	32488 ± 1092	9718 ± 126	9444 ± 136	23.6±0.2	23.6±0.3
PVC	9.3	6124 ± 297	6424 ± 330	4968 ± 43	5264 ± 54	26.3±0.3	26.8±0.3
PVDF	6.3	23355 ± 917	21821 ± 1036	11050 ± 116	11288 ± 133	24.8±0.2	25.4±0.3
PTFE	6.5	19842 ± 886	19888 ± 1093	12438 ± 117	12222 ± 143	25.7±0.2	25.9± 0.3

TABLE 7.3: Comparison of spectrum properties for simulation and experiment reconstructions. See Figure 7.4 for the reconstructions.

7.5.1 HDPE

In the case of HDPE shown in Figure 7.4a, the simulation reconstruction is greater than the experiment reconstruction in all bins. The d value suggests a 14.8% difference between the simulation and experiment. The C3 and C9 values are not consistent to within 3σ (see Table 7.3 for these values). However, the average energies are 20.4±0.3 keV for the simulation and 20.8±0.3 keV for the experiment and hence consistent to within 2σ suggesting the spectrum shapes are similar. As discussed in Section 6.4.4.1, the most likely explanation for this is a difference in the material density of what was simulated and what was measured experimentally.

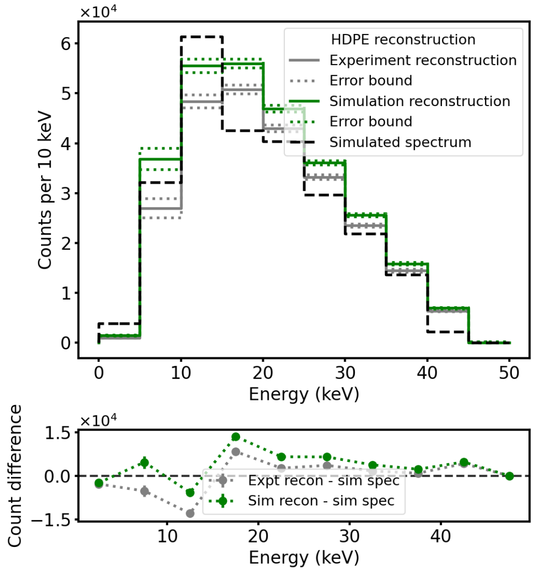

(A) HDPE

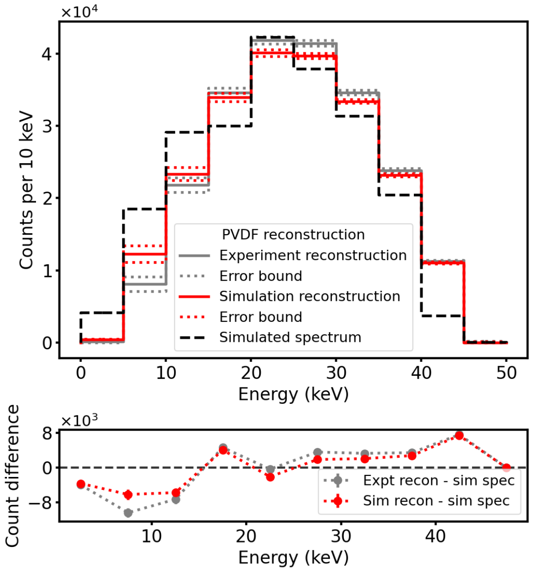

(D) PVDF

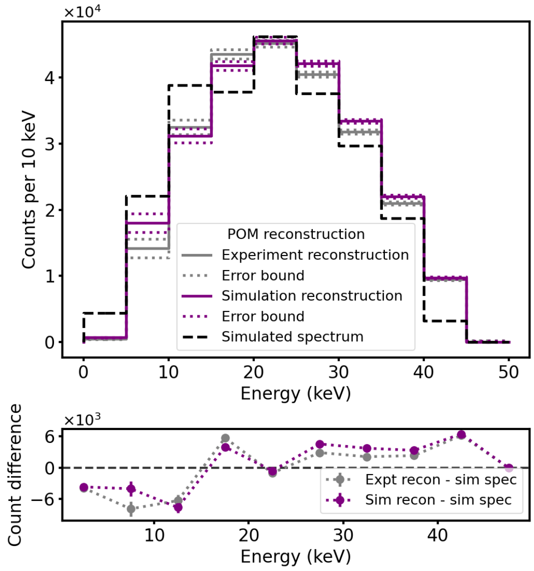

(B) POM

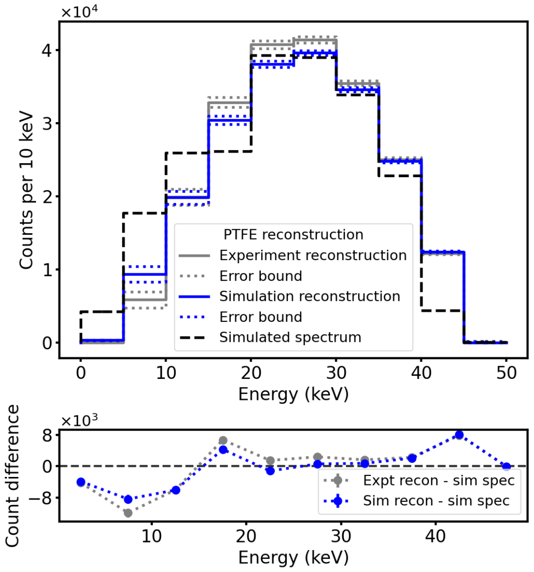

(E) PTFE

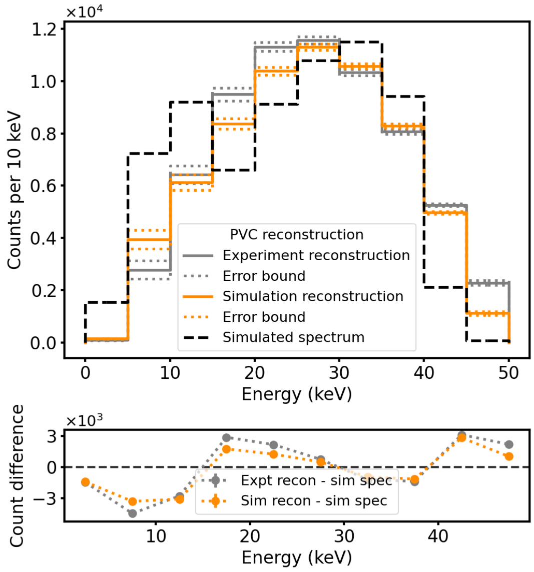

(C) PVC

FIGURE 7.4: Comparison of reconstructions from simulated (grey line) and experimental (coloured line) reconstructions. The simulated dataset was generated using the full geometry simulation (FG) discussed in Section 6.4. The dotted lines show the errors in the reconstruction due to the Poisson error. The dashed black line shows the simulated spectrum binned to 10 energy bins for comparison.

7.5.2 POM, PVDF and PTFE

Consider Figure 7.4. Upon visual inspection, the reconstructions that agree most closely are those for POM (Figure 7.4b), PVDF (Figure 7.4d) and PTFE (Figure 7.4e). The d values for these indicated a 5.6% difference for POM, 6.3% difference for PVDF and 6.5% difference for PTFE. The average energies were consistent to within 2σ. The C3 and C9 values were consistent within the reconstruction errors. Therefore there was good agreement between the experiment and simulation reconstructions suggesting the simulation was accurately reproducing the experiment.

7.5.3 PVC

For PVC, as shown in Figure 7.4c, visually the spectrum reconstructions are similar. The average energies are consistent and the d parameter indicated a 9.3% overall difference between the spectra. The C3 values were consistent, however the C9 value was higher for the experiment compared to the simulation at 5264±54 counts for the experiment compared to 4968±43 counts for the simulation. In both reconstructions the number of counts in bin 10 is much larger than expected at 2290±96 counts for the experiment reconstruction and 1126±66 counts for the simulation reconstruction compared to an expected 73±9 counts from the simulated spectrum. As discussed in Section 7.4, an increased number of counts in bin 10 is due to the size of the error in the data. The δ value for the simulation was 0.61% and for the experiment it was 0.77%.Therefore bin 10 was larger in the experiment because there was more smoothing of the solution as δ was larger. Bin 9 was also larger in the experiment as a result of the smoothing between bins 8 and 10.

7.6 Determining material properties

The full simulation geometry was used to simulate filtered backscatter spectra for a wider data set of organic materials. Thirty-three materials were simulated in total with spectrum reconstructions performed for each. The reconstructed spectra were then analysed to identify relationships between reconstructed spectrum properties and material properties. Analysis of the NIST data discussed in Section 2.3.6 showed theoretical relationships between the scatter intensity at 10 keV and Z_{eff} and the scatter intensity at 42 keV and ρ. As explained in the subsections below, C3 was chosen to represent the scatter intensity at 10 keV and C9 the scatter intensity at 42 keV.

The relationship between C3 and Z_{eff} and C9 and ρ is expected to deviate from the theoretical trends firstly because each bin represents a 5 keV window of energies so there will be more of a range of attenuation effects, and secondly because of errors intrinsic to the reconstruction model. Therefore lines of best fit were re-derived using the simulated material dataset. The Z_{eff} and ρ for the experimentally tested materials were then calculated using the re-derived equations.

7.6.1 Density and C9

The functional form $\mathrm{C9} = \mathrm{mln}(\rho) + \mathrm{c}_\rho$ was used to describe the relationship between C9 and ρ for materials with 3$\leq Z_{eff} \leq$10, based on a theoretical calculation using NIST data (Figure 2.12). C9 was chosen as the scatter energy of 42 keV was in this bin. Although bin 9 was greater than expected from the CdTe spectrum measurement, the effect was the same across all materials so was thought not to change the relationship with density significantly.

Consider Figure 7.5 which shows C9 as a function of density, ρ. The simulation data points are shown in black and the experiment data points in red. For all materials with $Z_{eff} \leq$10, C9 increased as a function of density. The fit $\mathrm{C9} = \mathrm{mln}(\rho) + \mathrm{c}_\rho$ was applied to all data points with $Z_{eff} \leq$10. The fit parameters were m=6668±162 and c_ρ=7351±69 with χ^2_{red}=4.13. This fit is shown by the solid black line and the errors are shown by the dashed black line. The explosive material density region 1.4$\leq \rho \leq$2.0 g cm^{-3} is shown by the grey vertical lines. The C9 values corresponding to a material with density in this range at 1σ is shown by the blue horizontal band. The 1σ confidence interval was (0.946<C9<1.206)$\times 10^4$ counts. This was calculated by putting ρ=1.4 g cm^{-3} and ρ=2.0 g cm^{-3} into the fit and calculating C9±1σ. The 2σ and 3σ confidence intervals are marked in lighter shades of blue at the top and bottom of the main band. The range of C9 values for the 2σ and 3σ confidence intervals were (0.933<C9<1.215)$\times 10^4$ counts and (0.920<C9<1.224)$\times 10^4$ counts respectively.

As shown in Figure 7.5, for materials with Z_{eff} >10 (materials such as PVC, Magnesium and Aluminium for example) no clear trend was seen with density. This shows it is not possible to acquire density information for materials with Z_{eff} >10 using x-rays with energy $\leq$50 keV. This is consistent with the theoretical prediction discussed in Section 2.3.5. Higher energy x-ray beams would need to be used to acquire this information. This will be a subject of discussion in Section 9.5.

The experimental data points are shown in red in Figure 7.5. The C9 values for each are also given in Table 7.4. The experimental C9 value for all materials was within 3σ of the simulated C9 value with the exception of PVC which was 296±69 (4.3σ) higher than the simulated value. The higher number of experimental counts in PVC is caused by a difference in the error parameters used in the reconstruction and simulation, as previously discussed in Section 7.5. This had no effect on the overall outcome however as it is not possible to acquire density information for PVC using this method anyway.

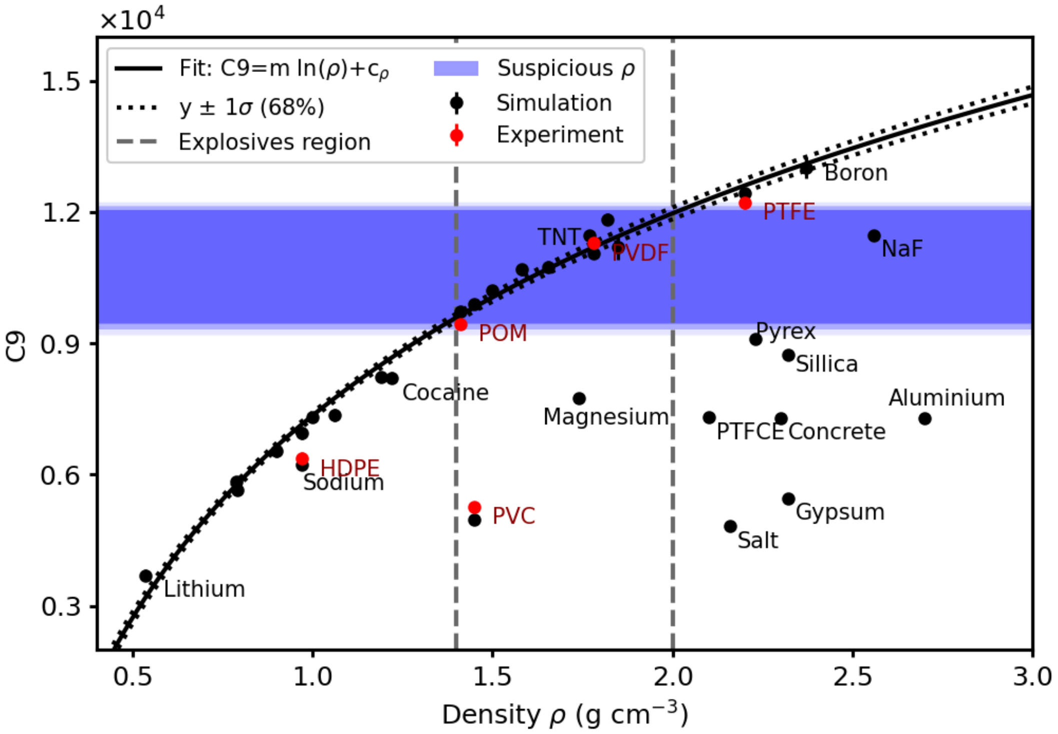

FIGURE 7.5: Plot of the number of counts between 40 and 45 keV (C9) and material density for reconstructions using the simulated data set (black points). The experiment data set is shown in red. The equation $\mathrm{C9} = \mathrm{m} \ln \rho + \mathrm{c}_\rho$ was fitted to all simulated data points with Z_{eff} ≤10. The fit parameters are given in the main text. The explosives region, 1.4≤ ρ ≤2.0 g cm^{-3}, is marked by the grey dashed lines. The region of C9 values corresponding to densities in the explosives region as calculated by the fit is marked in blue.

Material	Density	C9		
	g cm^{-3}	Experiment	Simulation	Difference (Expt-Sim)
HDPE	0.97	6369 ± 156	6953 ± 153	-584 ± 219 (2.7σ)
POM	1.41	9444 ± 136	9718 ± 126	-274 ± 185 (1.5σ)
PVC	1.45	5264 ± 54	4968 ± 43	296 ± 69 (4.3σ)
PVDF	1.78	11288 ± 133	11050 ± 116	238 ± 176 (1.4σ)
PTFE	2.2	12222 ± 143	12438 ± 117	-216 ± 185 (1.2σ)

TABLE 7.4: A comparison between the number of counts between 40 and 45 keV (C9) in the reconstructed spectrum for the experiment and simulation reconstructions. The data are shown in Figure 7.5. The difference between the experiment and simulation is also calculated for numerical comparison.

7.6.2 Effective atomic number and C3

The equation $\mathrm{C3} = \mathrm{Ae}^{-\mathrm{b}(\mathrm{Z_{eff}}-4.00)} + \mathrm{c_z}$ was used to describe the relationship between C3 and Z_{eff} for all materials with $Z_{eff} >3$ (see Figure 2.13). C3 was chosen to represent the number of counts at 10 keV. Bin 3 was chosen instead of bin 2 as the reconstructions were most similar to the spectrum measurement in bin 3, including PVC, in the experimental reconstructions. The greatest difference across HDPE, POM, PVDF and PTFE in bin 3 was a difference of -4237±1036 counts (16% reduction) for PVDF. The greatest difference in bin 2 was -8953±1918 counts (25% reduction) for HDPE. For PVC the difference in bin 2 was -5776±346 (77% reduction) and -1586±330 (20% reduction) for bin 3. Bin 3 was also slightly less sensitive to perturbations compared to bin 2 (see Section 4.7.3).

Consider Figure 7.6 which shows C3 as a function of Z_{eff}. The C3 value decreases with increasing effective atomic number, with the exception of Z_{eff}=3 (Lithium). Lithium is an outlying point, as discussed in Section 2.3.6. This is because the photo-electric absorption and Compton scattering cross-sections are a similar order of magnitude in Lithium, whereas for materials with $Z_{eff} >3$, photo-electric absorption dominates. The exponential function $\mathrm{C3} = \mathrm{Ae}^{-\mathrm{b}(\mathrm{Z_{eff}}-4.00)} + \mathrm{c_z}$ was fit to the data set (excluding the Z_{eff}=3 data point) with fit parameters A=119130±3890, b=0.47±0.02 and c_z=5602±335. The reduced χ^2 parameter was χ^2_{red}=323. The fit is shown by the solid black line in Figure 7.6. The 1σ error band for the fit is shown by the black dotted line. The range of effective atomic numbers for explosive materials is $6.5\leq Z_{eff} \leq 8$ [17] and this is marked by the vertical grey dashed lines. The blue horizontal band represents the range of C3 values that correspond to an explosive material at 1σ. This was calculated by putting Z_{eff}=6.5 and Z_{eff}=8 into the fit. The lighter shades of blue at the top and bottom of the horizontal band represent the 2σ and 3σ confidence levels. The values for the confidence intervals are given in Table 7.6.

The χ^2_{red} parameter of 323 suggests a poor model of the experimental data. This is not surprising. $C3$ is a complex function of atomic number, density, scatter angle and x-ray energy, and the model assumption relies on only an atomic number effect. That does not mean the fit is not useful though. A more accurate model that takes into account the small deviations in the data would require many more fit parameters and introduce additional fitting errors. It may also result in a non-singular relationship between Z_{eff} and C3 in places, (i.e. some C3 values could have more than 1 corresponding Z_{eff} value). Additionally, a large χ^2_{red} value suggests errors in C3 have been underestimated. This is also to be expected as the C3 values are affected by inaccuracies in the reconstruction process, errors for which have not been included. Despite the high χ^2_{red} the simplified fit clearly has a useful role in material identification using the C3 value. It serves as a good visual representation of the relationship between C3 and Z_{eff} that is a singular function and hence can be used to estimate Z_{eff} of an unknown material given a C3 value.

The experimental data points are shown in red on Figure 7.6. The C3 values for each material are given in Table 7.5. Both the simulated and experimental C3 values are given and the difference between the two is calculated. Within the experimental error there is no difference between the POM, PVDF, PTFE and PVC C3 values. The HDPE experimental C3 value is 7178±1858 counts lower than the simulation, and lies below the fit line on Figure 7.6. The most likely reason for this was a discrepancy between the simulated material and the material that was actually tested as discussed in Section 7.4.

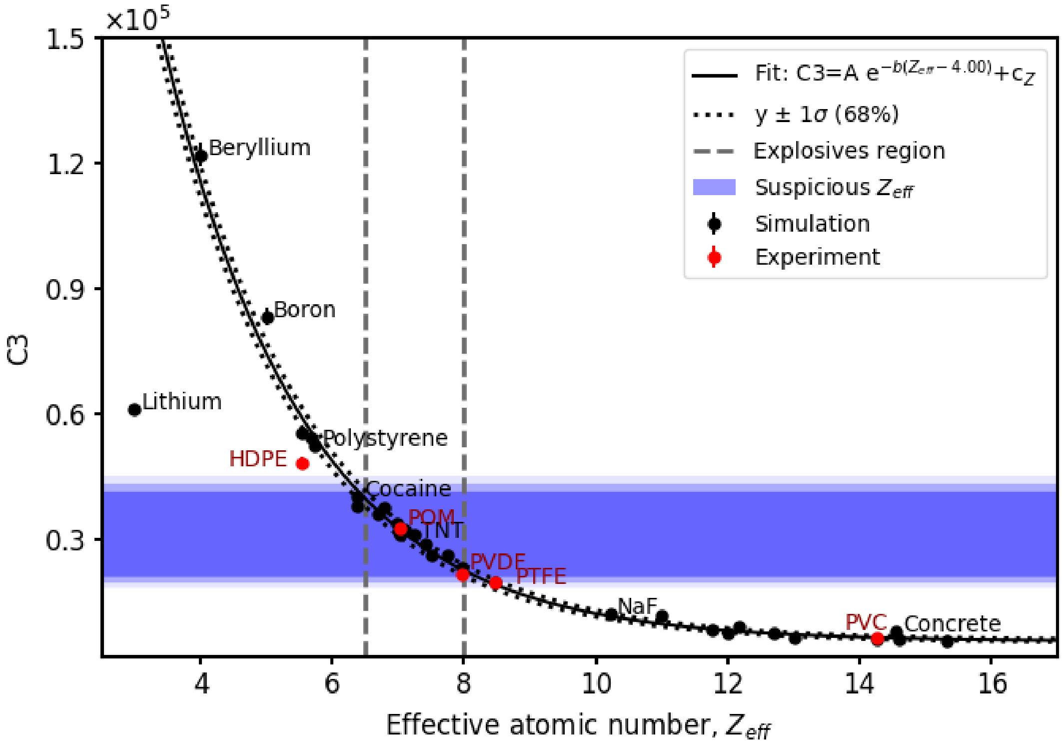

FIGURE 7.6: Plot of the number of counts in the 10-15 keV energy bin (C3) as a function of effective atomic number (Z_{eff}) for reconstructions using the simulated data set (black points). The experiment data set is shown in red. The simulated data points were fitted to the equation $\mathrm{C3} = \mathrm{A}\mathrm{e}^{-\mathrm{b}(\mathrm{Z}_{\mathrm{eff}}-4.00)} + \mathrm{c}_{\mathrm{Z}}$. The fit and 1σ error bound is shown by the solid and dashed black lines respectively. The lithium data point at Z_{eff}=3 was excluded from the fit. The fit parameters are given in the main text. The explosives region, 6.5$\leq Z_{eff} \leq$8.0, is marked by the grey dashed lines. The region of C3 values corresponding to Z_{eff} in the explosives region as calculated by the fit is marked in blue.

Material	Z_{eff}	C3		
		Experiment	Simulation	Difference (Expt-Sim)
HDPE	5.53	48412 ± 1277	55590 ± 1350	-7178 ± 1858 (3.9σ)
POM	7.03	32488 ± 1092	31181 ± 1053	1307 ± 1520 (0.9σ)
PVDF	7.97	21821 ± 1036	23355 ± 917	-1534 ± 1384 (1.1σ)
PTFE	8.48	19888 ± 1093	19842 ± 886	46 ± 1407 (0.03σ)
PVC	14.26	6424 ± 330	6124 ± 297	300 ± 444 (0.7σ)

TABLE 7.5: A comparison between the number of counts in the 10-15 keV energy bin (C3) in the reconstructed spectrum for the experiment and simulation reconstructions. The data is shown in Figure 7.6. The difference between the experiment and simulation is also calculated for numerical comparison.

7.7 Categorisation of explosive materials

Sections 7.6.1 and 7.6.2 have demonstrated that C9 is proportional to density for materials with Z_{eff} $\leq$10 and C3 is proportional to Z_{eff} for Z_{eff} >3. Figure 7.7 shows C3 as a function of C9. The simulation data set is shown by the black points. The region corresponding to explosive materials based on the C3 and C9 values is shown in blue. The 1, 2 and 3 σ confidence levels for explosive material identification are shown in different shades of blue. The experimentally tested materials are shown in red. The C3 and C9 values for the experiment are given in Table 7.7. The ranges of C3 and C9 values corresponding to a positive detection of an explosive material are given in Table 7.6 for each confidence level.

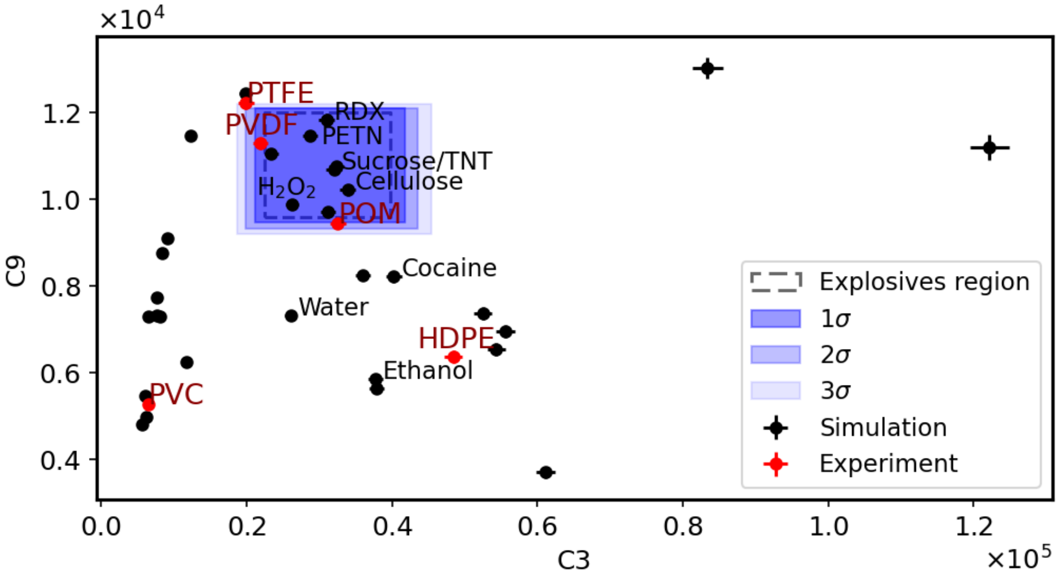

FIGURE 7.7: Number of counts between 10-15 keV in reconstructed energy spectrum (C3) as a function of number of counts between 40-45 keV in reconstructed energy spectrum (C9). Simulation points are shown in black and experiment points in red. The region of C3 and C9 values corresponding to a possible explosive material is shown in blue.

	Explosives region	1σ	2σ	3σ
C3, counts ($\times10^4$) C9, counts ($\times10^4$)	2.25 - 3.98 0.959 - 1.200	2.12 - 4.17 0.946 - 1.206	1.99 - 4.35 0.933 - 1.215	1.86 - 4.54 0.920 - 1.224

TABLE 7.6: Range of C3 and C9 values corresponding to the 1, 2 and 3σ bounds for explosives detection as illustrated in Figure 7.7.

7.7.1 Explosive percentage likelihood

A percentage likelihood of a material being explosive was calculated. This was done by calculating the percentage likelihood that the material lay within the explosive material range defined by the 3σ limits of C3 and C9. The 3σ limits on both C3 and C9 meant there was a 99% (0.997^2) chance if a material was explosive it would be detected within the 3σ region. All measurements were assumed to follow a normal distribution with the mean of the distribution either the C3 or C9 value (depending which was being analysed), and the standard deviation being the error on the value. The percentage of the Gaussian distribution of the measurement within the explosive region was calculated for both C3 and C9 ($p(C3)$ and $p(C9)$) and a percentage likelihood of the material being explosive was calculated by multiplying together both probabilities and the probability of an explosive material being detected within the 3σ region, $p(X) = p(C3) \times p(C9) \times 0.997^2$.

7.7.2 Categorisation of experimentally tested materials

Table 7.7 gives the percentage likelihood of explosive for all experimentally tested materials. As shown in Table 7.7, both explosive simulant materials (POM and PVDF) were detected as explosive with a higher than 95% chance. PTFE, which lay on the top left-hand edge of the explosive region in Figure 7.7, was detected with a 42.8% probability. HDPE and PVC were detected with a 0.0% probability owing to C9 values being at least 18σ away from the lower C9 3σ bound. Therefore at a detection threshold of $p(X)$ >95%, 2/2 materials were correctly identified as explosive and 3/3 materials were correctly identified as non-explosive. Therefore all the materials were correctly categorised meaning an extremely high success rate for the five samples tested.

Material	C3	C9	Percentage chance explosive, $p(X)$	Explosive?
HDPE	48412 ± 1277	6369 ± 156	0.0%	No
POM	2488 ±1092	9444 ± 136	95.8%	Yes
PVC	6424 ± 330	5264 ± 54	0.0%	No
PVDF	21821 ± 1036	11288 ± 133	99.3%	Yes
PTFE	19888 ± 1093	12222 ± 143	48.2%	No

Table 7.7: Table showing the percentage chance of an experimentally tested material being explosive based on the C3 and C9 values in the energy spectrum reconstruction. Whether or not the material is actually explosive simulant is indicated by the "Explosive?" column.

7.7.3 General method performance

The simulated dataset was studied to understand in more detail how successful the method may be over a larger range of materials in the best case scenario. This was because not enough experimental data were available to determine this experimentally. Out of the 33 materials simulated, eight were identified as being explosive at a higher than 95% chance, as illustrated in Figure 7.7. The $p(X)$ >95% threshold was chosen as this was the minimum probability observed for the experimental data, although in practice the threshold would be a value determined by the user based on the sensitivity required. The identified materials were POM, PVDF, Hydrogen peroxide (H_2O_2), RDX, PETN, TNT, Sucrose and Cellulose. Out of these materials Hydrogen peroxide, RDX, PETN and TNT are all explosive, POM and PVDF are explosive simulants, and Sucrose and Cellulose are non-explosive. PTFE was detected as having a 4.1% chance of being explosive from the simulated data. The number of true negatives was 25 and there were no false negatives. The overall method success rates are summarised in Table 7.8. The rate of true positive identification (at 95% chance or above) was 100% with a 0% false negative rate. The true negative identification rate was 93% and the false positive identification rate was 7%.

	Positive identification (>95% chance)	Negative identification
Explosive	Sim: 6/6 (100%) *Expt: 2/2*	Sim: 0/6 (0%) *Expt: 0/2*
Not explosive	Sim: 2 / 27 (7%) *Expt: 0/3*	Sim: 25 / 27 (93%) *Expt: 3/3*

TABLE 7.8: Method success rates. The simulated rates (sim) were based on data of 33 materials of which 6 were explosive materials and 27 were non-explosive materials. The experiment rates (expt) were based on experimental measurements of 5 materials of which 2 were explosive simulants and 3 were non-explosive.

7.8 Calculating atomic number and density

The derived relationships between C3 and Z_{eff} and C9 and ρ allow us to go one step further than a simple explosive/non-explosive categorisation and calculate an estimate of the Z_{eff} and ρ for the five experimentally tested materials.

The atomic number was calculated as

$$Z_{eff} = 4.00 + \frac{1}{b} \ln \left(\frac{A}{C3 - c_Z} \right), \tag{7.3}$$

where A=119130±3890, b=0.47±0.02 and c_Z=5602±335 as derived in Section 7.6.2. The error in Z_{eff} was calculated through standard error propagation of the errors in $C3$, A, b and c_Z. Similarly the density was calculated as

$$\rho = \exp\left(-\frac{C9 - c_\rho}{m}\right), \tag{7.4}$$

where m=6668±162 and c_ρ=7351±69 as derived in Section 7.6.1. The error in ρ was calculated through standard error propagation of the errors in $C9$, m and c_ρ.

Figure 7.8 shows Z_{eff} plotted against ρ. Each material is coloured (HDPE red, POM green, PVDF blue, PTFE purple and PVC pink). The shaded rectangles represent the confidence levels of the calculation with the inner rectangle the 1σ bound, the middle rectangle the 2σ bound and the outer rectangle the 3σ bound. The data sheet value is shown by the black marker. A left pointing arrow shows the range of possible density values for HDPE due to a lack of knowledge about the sample (see Section 7.5.1 for details). The calculated Z_{eff} and ρ values for HDPE, POM, PVC, PVDF and PTFE are given in Table 7.9 along with how many σ away the values are from the true value.

The Z_{eff} for all materials was calculated to $<0.7\sigma$ of the true value with the exception of HDPE (4.9σ). All materials are within $\pm0.5Z_{eff}$ of the true value demonstrating high accuracy for material identification as the greatest deviation in calculated Z_{eff} from the true value is $0.5Z_{eff}$ (HDPE). For density, POM, PVDF and PTFE are calculated to within 2σ of the true value. HDPE is between 3.5 and 5.5σ away. The greatest deviation between the calculated and true value of ρ is 0.12 g cm^{-3} (PTFE). The density of PVC could not be calculated using the discussed technique as $Z_{eff}(\mathrm{PVC}) > 10$.

Overall, Z_{eff} and ρ values for the experimental data points were calculated to a high accuracy using this method. In the explosive material range, the Z_{eff} and ρ calculations are the most accurate with a maximum deviation of $0.1Z_{eff}$ and 0.04 g cm^{-3} for POM and PVDF. This suggests highly accurate further categorisation of explosive materials may be possible with this information.

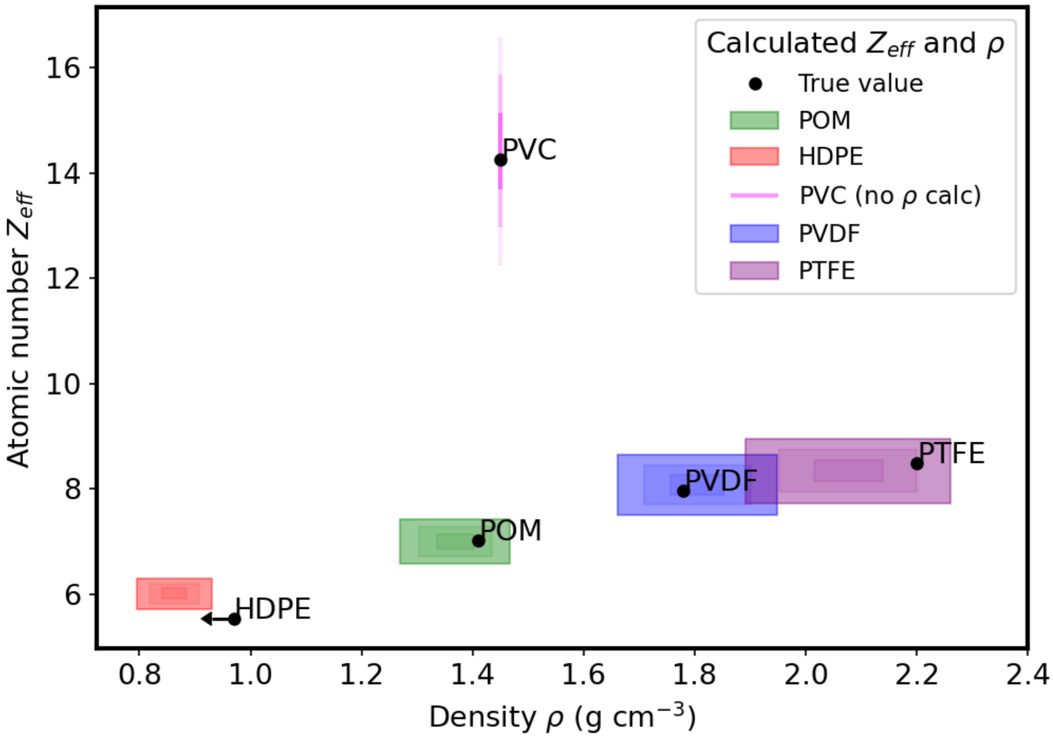

FIGURE 7.8: The figure shows the calculated effective atomic number and density values obtained by putting the C3 and C9 values for the experimental reconstruction into the fits dervied from the simulated reconstruction dataset. The 1,2 and 3 σ bands are shown by the coloured shaded regions. The true values are shown by the black points. For HDPE the true value for the density was thought to be 0.97 g cm^{-3}, although densities in the range 0.93-0.97 g cm^{-3} are possible [126] as indicated by the black left-pointing arrow. The Z_{eff} and ρ values shown in this figure are given in Table 7.9.

Material	Z_{eff}			Density, g cm^{-3}		
	True	Calculated	σ	True	Calculated	σ
HDPE	5.53	6.01 ± 0.10	4.9	0.93-0.97	0.86 ± 0.02	3.5-5.5
POM	7.03	7.00 ± 0.14	0.2	1.41	1.37 ± 0.03	1.2
PVC	14.26	14.42 ± 0.72	0.2	1.45	-	-
PVDF	7.97	8.08 ± 0.19	0.6	1.78	1.80 ± 0.05	0.5
PTFE	8.48	8.35 ± 0.20	0.7	2.20	2.08 ± 0.06	2.0

TABLE 7.9: Effective atomic number and density for experimentally tested materials as shown in Figure 7.8.. Z_{eff} and ρ were calculated using Equation 7.3 and Equation 7.4 respectively from the fits derived in Section 7.6.2 and Section 7.6.1. The σ column for both determines how many standard deviations the calculated value is from the true value.

7.9 Chapter summary

Energy spectra were reconstructed from a series of experimental filtered detector response measurements for five materials. The reconstructed spectra showed similar behaviour to equivalent CdTe spectra. The main cause of differences between the two was the smoothing effect of the Tikhonov solution. Using simulated data, bounds on C3 and C9 for explosive materials were derived and relationships between C3 and Z_{eff} and C9 and ρ were fitted. Two out of two explosive simulant materials were detected as being explosive with a higher than 95% probability. PTFE was detected as explosive with a 48% probability and HDPE and PVC had 0.0% chance of being explosive. From the simulated data set the method could expect a maximum true positive detection rate of 100% and a 7% false positive detection rate. The Z_{eff} and ρ of all experimentally tested materials were calculated to within $0.5Z_{eff}$ and 0.12 $\mathrm{g\,cm^{-3}}$, and in the explosive material range this was improved to within $0.1Z_{eff}$ and 0.04 $\mathrm{g\,cm^{-3}}$. Overall the fact that this method does not require energy information but can still achieve high accuracy is an extremely promising result.

This page is intentionally left blank.

Chapter 8

Systematic error quantification

A number of systematic errors were present in the experiment. These included uncertainties due to x-ray tube alignment and uncertainties in the filter thicknesses due to manufacturing tolerances. Simulations were performed to determine how well the response correction factor (RCF) corrected for these effects. Other factors such as the calibration material used to calculate the RCF and the choice of filter thicknesses were also investigated. All studies were used to understand how sensitive the measurements of Z_{eff}, ρ and the material classification were to these factors. Effects of time-varying systematic errors due to changes in the detector response or x-ray output over time were also studied using stability measurements.

8.1 Static (non time-varying) systematic errors

The main source of error in the experiment was random error due to the number of detected x-ray photons. One reason for introducing the RCF was to account for systematic errors. The systematic errors corrected for using the RCF were static systematic errors that did not change over time because the calibration measurement was only performed once per day. This section will discuss how different systematic errors affected the RCF and how this translated into the reconstruction.

The systematic errors investigated were

- The x-ray tube alignment - the position of the x-ray source relative to the centre of the sample,
- Filter thickness errors - the effect of changing the thickness of each filter filter by $x{\pm}1\sigma$, firstly reconstructing with the assumed filter thicknesses, x, and secondly reconstructing with the actual filter thicknesses, $x{\pm}1\sigma$,

- The effect of using a different thickness for filter B (0.05 vs 0.14 mm),
- The effect of the calibration material (Nylon vs Acrylic).

It is impossible to decouple all the different systematic errors and observe the exact effect they have in isolation, especially given the complex nature of the reconstruction process. In order to fully quantify systematic errors and understand their full experimental effect, one should perform the experiment multiple times in many different similar arrangements and environmental conditions. This was not possible within the time constraints of the project so simulations were performed instead.

8.2 Simulations for investigating systematic errors

The full geometry simulation (FG) was used for all error investigations (see Section 6.4 for details). For some systematic errors, aspects of this geometry were changed, as will be explained in more detail in the relevant sections. Each simulation was run firstly with a calibration material (either 10 mm thick Nylon or 10 mm thick Acrylic) and then with 10 mm POM. All simulations were run for 1.25×10^{10} events per filter per material, the same as the simulations run in the main part of the work. The calibration material data set was compared to a simple simulation of the same material to calculate the RCF (see Section 4.5).

Overall six different simulations were run as summarised in Table 8.1. The reconstructions were compared to the reconstruction acquired with no modifications. This simulation with no modifications was called simulation 0.

#	Simulation description	C3	C9	Z_{eff}	ρ g cm^{-3}	d %	$p(X)$ %
0	Full geometry (FG) POM (simulation with no changes)	31181 ±1053	9718 ±126	7.11 ±0.14	1.43 ±0.03	-	99.4
I	FG POM, x-ray source position to (-5,0)	33094 ±909	9578 ±118	6.95 ±0.14	1.40 ±0.03	3.8	99.3
II	FG POM, x-ray source position (+5,0)	32240 ±961	9857 ±121	7.02 ±0.14	1.46 ±0.03	4.6	99.4
III	FG POM, filter thicknesses changed by $x\pm1\sigma$ and reconstructed using x	min. 31026 ±1056	min. 9525 ±129	max. 7.12 ±0.14	min. 1.39 ±0.03	min. 3.5	98.8
		max. 33399 ±1043	max. 9867 ±126	min. 6.93 ±0.14	max. 1.46 ±0.03	max. 2.9	98.1
IV	FG POM, filter thicknesses changed by $x\pm1\sigma$ and reconstructed using $x\pm1\sigma$	min. 31067±1061	min. 9530±126	max. .12±0.14	min. 1.39±0.03	min. 3.0	99.0
		max. 33608±1039±126	max. 9878±0.14	min. 6.91±0.03	max. 1.46	max. 3.1	99.4
V	FG POM, filter B = 0.05 mm	31538 ±978	9773 ±119	7.08 ± 0.14	1.44 ± 0.03	2.3	99.4
VI	FG POM, Acrylic α correction	28932 ±1058	9631 ±127	7.32 ±0.15	1.41 ±0.03	3.6	99.4

TABLE 8.1: Summary of simulations run to investigate systematic error effects. A brief description of each simulation is provided. More detailed descriptions can be found in the main text in Section 8.2. The simulation with no modifications was labelled simulation 0. Other simulations are labelled in Roman numerals from I-VI. The C3, C9, Z_{eff} and ρ values calculated from the spectrum reconstructions are shown. The percentage difference (d) when compared to the reconstruction for simulation 0 was also calculated for simulations I-VI. The reconstructions are shown in Figure 8.3.

8.2.1 Simulation I and II: x-ray tube alignment

X-ray tube alignment was considered as the x-ray tube was aligned by eye. Two simulations were performed to quantify this effect. In the first simulation the geometry was modified to change the source position by -5 mm in the horizontal direction. This is labelled simulation I. In the second simulation, simulation II, the source position was changed by +5 mm in the horizontal direction. In both simulations I and II, the firing direction of the beam was kept the same so that the beam was hitting ±5 mm off the centre of the sample. A diagram of the change in geometry is shown in Figure 8.1. The beam divergence properties were kept the same as in the original simulation. The original unchanged filter thicknesses given in Table 5.2 were used. A schematic diagram showing the detector geometry for the simulations is shown in Figure 8.1.

The change in x-ray tube position changed the scattering angle. In simulation II the scattering angle was 138° and and in simulation I it was 142° (for a source position of (0,0) it was 140°). In practice, the alignment of the x-ray tube may also affect the x-ray tube output spectrum as well, as discussed in Section 5.2.1. This was not investigated as would require detailed knowledge about the x-ray tube beam profile which was not available experimentally.

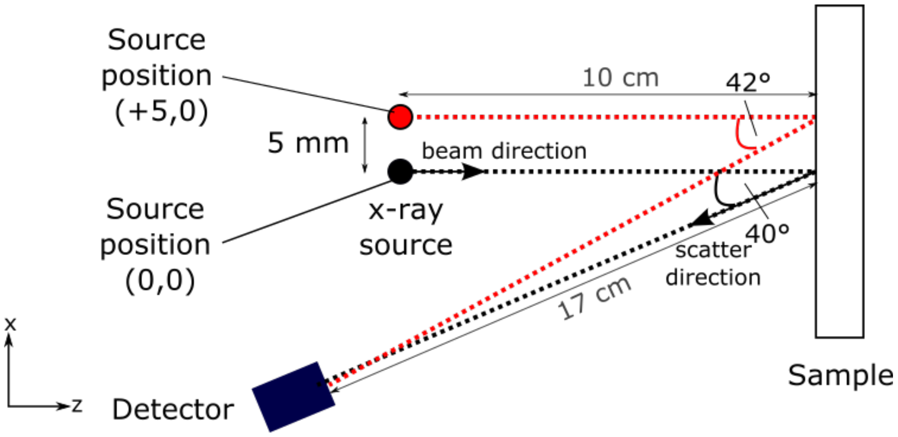

FIGURE 8.1: Schematic diagram of the simulation geometry used to understand the effect of the x-ray tube alignment errors. The viewpoint is looking downwards on the (x,z) plane. In black shows the x-ray beam path and scatter path for perfect alignment, source position (0,0)). In red shows the x-ray beam path and scatter path for a source position of (5,0) so that the source is misaligned by 5 mm in the x direction.

8.2.2 Simulation III and IV: Filter thickness

The filter thicknesses have an error due to manufacturing tolerances and the combination of filters that were used (as discussed in Section 5.6). The filters used are given in Table 5.2. Simulations were performed to understand how the filter thickness errors effected the calculation of α and the reconstruction. Filters of thickness $x - 1\sigma$ (thicknesses {0.0051, 0.13, 0.61, ..., 20.67} mm) and $x + 1\sigma$ (thicknesses {0.0081, 0.15, 0.65, ..., 21.53} mm) were simulated. Data sets of detector responses were created, each one with one of the filters changed by either $\pm 1\sigma$ (20 data sets in all). Then a reconstruction was performed on each data set with the appropriate RCF. This was completed over the full 20 data sets. Then out of the 20 resulting reconstructions, the maximum and minimum value of the reconstruction in each bin was found.

Two different reconstructions were performed. For simulation III, the reconstruction was performed using the assumed thicknesses in the system matrix, i.e. {0.0066, 0.14, ..., 21.1} mm. For example if the thickness of filter A was decreased to 0.0051 mm, the presumed value 0.0066 mm would be used in the reconstruction. This was to simulate what could happen if the filter thickness was actually thicker of thinner by the error 1σ but the experimenter was not aware so reconstructed the data using the filter thickness they thought it was.

In simulation IV, the reconstruction was performed using the actual thicknesses in the system matrix. For example if the thickness of filter A was decreased to 0.0051 mm then a thickness 0.0051 mm was used in the reconstruction. This was done to quantify how sensitive the reconstruction method was to the choice of filter thicknesses within the thickness errors.

8.2.3 Simulation V: Filter B thickness

In simulation V the thickness of filter B was 0.05 mm rather than 0.14 mm. All other filters were kept the same. For the materials tested on day 2 (PVDF and PTFE), a mistake in the experiment meant that a 0.05 mm filter was used instead of 0.14 mm for filter B. This simulation was used to quantify the effect of this change of filter B.

8.2.4 Simulation VI: Calibration material

The final simulation (VI) was a simulation of the full geometry with no changes, however the data was reconstructed using the RCF calculated with an Acrylic calibration material rather than Nylon. The plastic samples tested on the first experimental day used a Nylon calibration material whereas for those tested on the second experimental day an Acrylic calibration material was used. This simulation was used to quantify the effect of changing the calibration material.

8.3 RCF response to systematic errors

The RCF was calculated for each simulation. The results are shown in Figure 8.2 which shows RCF (denoted α) as a function of filter thickness. In each plot α for simulation 0 is shown in red.

Figure 8.2a shows α for simulation I (green) and simulation II (blue). The α is increased compared to simulation 0 for all filters for simulation II as expected. The number of x-rays scattered is reduced in simulation II according to the Klein-Nishina equation (see Section 2.2.2 and Figure 2.6 - blue line) due to the decrease in scattering angle (138°) hence the detector response is reduced and α is larger to correct for this. The converse is true for simulation I. The scattering angle is larger (142°) so the scattered intensity and therefore detector response is increased. The RCF is therefore smaller to counteract this. This shows the RCF is adapting to changes in the x-ray tube alignment in order to account for the systematic error.

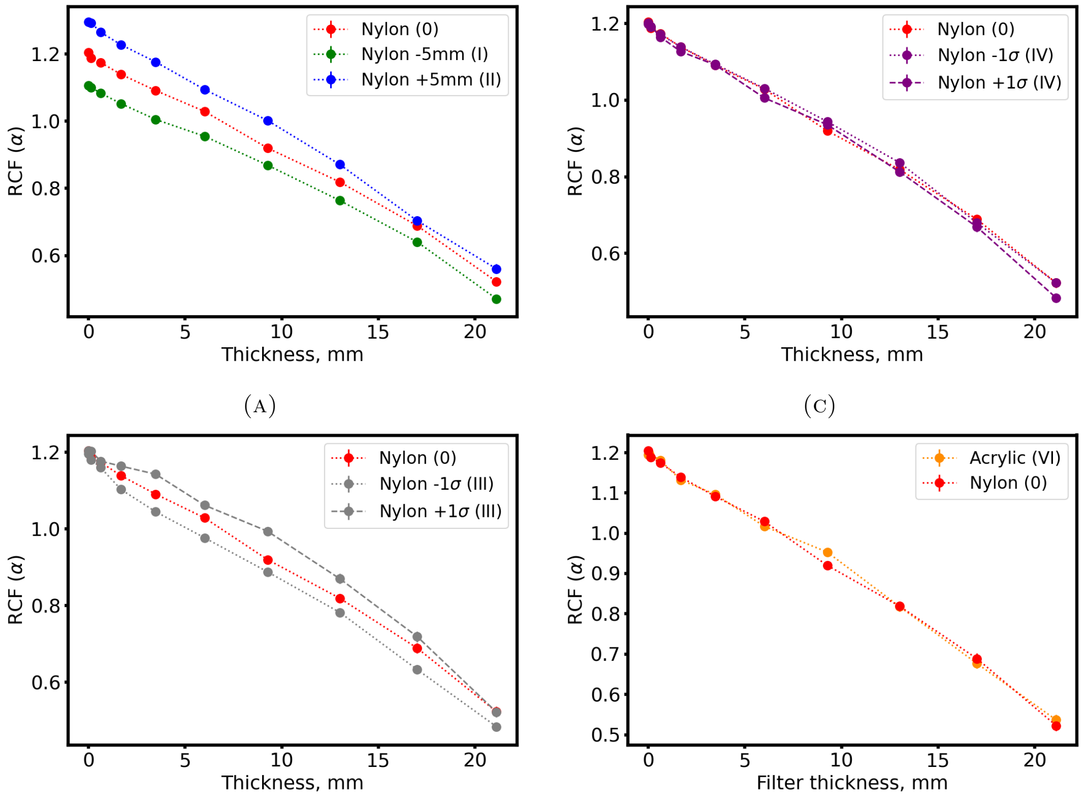

(A)

(C)

(B)

(D)

Figure 8.2: The α correction factor as a function of filter thickness as calculated for (A) simulations I and II, (B) simulation III, (C) simulation IV and (D) simulation VI. The α correction factor used for simulation 0 is shown by the red data points in all plots. This is the same RCF as that used for simulation V. Information about each simulation can be found in Table 8.1 and in the main text.

The RCF used for simulations III and IV is shown in Figure 8.2b. The x+1σ is shown by the dashed grey line and the x-1σ by the dotted grey line. The α is larger for all filters compared to simulation 0 with x+1σ. This is as expected because if the filters are thicker, more x-rays are attenuated so the detector response is reduced. Therefore in order for the simple simulation to match the full simulation, the RCF is larger to increase the detector response measured. Conversely, for the filters that had the thicknesses decreased by 1σ, the α is smaller than the unchanged measurement. This is because the detector response will be larger than expected due to the thinner filters allowing more x-rays than expected to pass through. Hence the RCF must be smaller to account for the higher than expected detector responses. These results are as expected and show that the RCF is adapting to changes in filter thickness in order to calculate for the error.

Figure 8.2c shows α for simulation IV. The α for x+1σ is shown by the purple dashed line and the α for x-1σ is shown by the purple dotted line. In each data set the α is plotted as a function of the expected thickness (x rather than $x \pm 1\sigma$). Therefore the α values for $+\sigma$ are slightly lower than simulation 0 because the actual thickness value should lie to the right of the x where a smaller α is needed. Similarly the $-\sigma$ are slightly higher than simulation 0 because these points should lie to the left of each x where α is larger.

The final RCF plot is that showing the difference between the α using Nylon (simulation 0) and Acrylic (simulation VI) as the calibration material. This is shown in Figure 8.2d. The Acrylic α is shown in orange. There is little difference between the correction factors suggesting minimal effect of the calibration material on the calculation of α. For simulation V, the RCF for simulation 0 was used for x=0.05 mm and x=0.14 mm so is not shown in a separate plot.

8.4 Reconstruction, Z_{eff} and ρ response to systematic errors

The reconstructions for each simulation are shown in Figure 8.3. The red line is the reconstruction for simulation 0. The dashed black line shows the simulated spectrum. Generally there was little change to the reconstructions upon visual inspection with all systematic errors not influencing the general spectrum shape. The percentage difference for simulation 0 and simulation 0 with $\pm 1\sigma$ was 2.2%. As given in Table 8.1, percentage differences ranged from 4.6-2.3%. Therefore all reconstructions were slightly outside the random error 1σ range however the differences were fractionally small.

The reconstruction for the simulation for each of the systematic error investigations was compared to the reconstruction for simulation 0 to evaluate the change in the calculation of Z_{eff} and ρ. The percentage chance of the material being explosive, $p(X)$, was also calculated (see Section 7.7.1 for details of the calculation). For simulation 0 the C3 value was (3.12±0.11)$\times10^4$ counts and from this Z_{eff} was calculated as 7.11±0.14. The C9 value for simulation 0 was (0.97±0.01)$\times10^4$ counts and from this ρ was calculated as (1.43±0.03) g cm^{-3}. The percentage likelihood the material was explosive was $p(X)$=99.4%.

The C3, C9, Z_{eff}, ρ and $p(X)$ values were calculated from the reconstruction for each systematic error simulation. The results are summarised in Table 8.1. For each simulation the Z_{eff}, ρ and $p(X)$ values were compared those for simulation 0 to determine how much of an effect the systematic error had on the material identification. For all simulations POM was identified as explosive to $p(X)$ >98%.

8.4.1 Simulation I and II: x-ray tube alignment

For simulation I the Z_{eff} value was 6.95±0.14 and ρ=1.40±0.03 g cm^{-3}. The Z_{eff} was consistent to 0.81σ and ρ 0.71σ to simulation 0. For simulation II the Z_{eff} was 7.02±0.14 and ρ was (1.46±0.03) g cm^{-3}. These were 0.45σ and 0.71σ respectively from the ρ value for simulation 0 (as above, the Z_{eff} and ρ values were 7.11±0.14 and (1.43±0.03) g cm^{-1} for simulation 0). The change in alignment was offset by the RCF effectively so that the atomic number and density calculations from simulation 0 were retained to $<1\sigma$. The material was also identified as explosive with $p(X)$=99.3%, only 0.1% less than simulation 0. Therefore a change in x-ray beam position of ±5 mm did not affect the measurement of the material properties nor the categorisation of the material.

8.4.2 Simulation III and IV: Filter thickness

For simulation III (filter thicknesses changed by x±1σ reconstructing using x) Z_{eff}=6.93±0.14 for the maximum C3 recorded, and Z_{eff}=7.12±0.14 for the minimum C3 recorded. These values are consistent to 0.91σ and 0.05σ respectively. ρ was (1.46±0.03) g cm^{-3} for the maximum C9 value and (1.39±0.03) g cm^{-3} for the minimum C9 value. These values were consistent with the simulation 0 results to 0.71σ and 0.94σ respectively. The $p(X)$ values were 98.8% and 98.1% which were slightly less than the 99.4% for simulation 0 but still within a 98% likelihood detection threshold. For simulation IV (filter thicknesses changed by x±1σ and reconstructed using x±1σ) a similar change in Z_{eff} and ρ was observed. The only difference was the minimum value of Z_{eff} (corresponding to maximum C3) was 6.91±0.14 and this was consistent to 1.01σ with simulation 0. The $p(X)$ values were 99.0% and 99.4%.

This suggests that, although there is a change in the Z_{eff} and ρ values when x±1σ thicknesses are considered, the change is caused by the different filter thicknesses used rather than a discrepancy between the actual filter thicknesses and the thicknesses used in the reconstruction

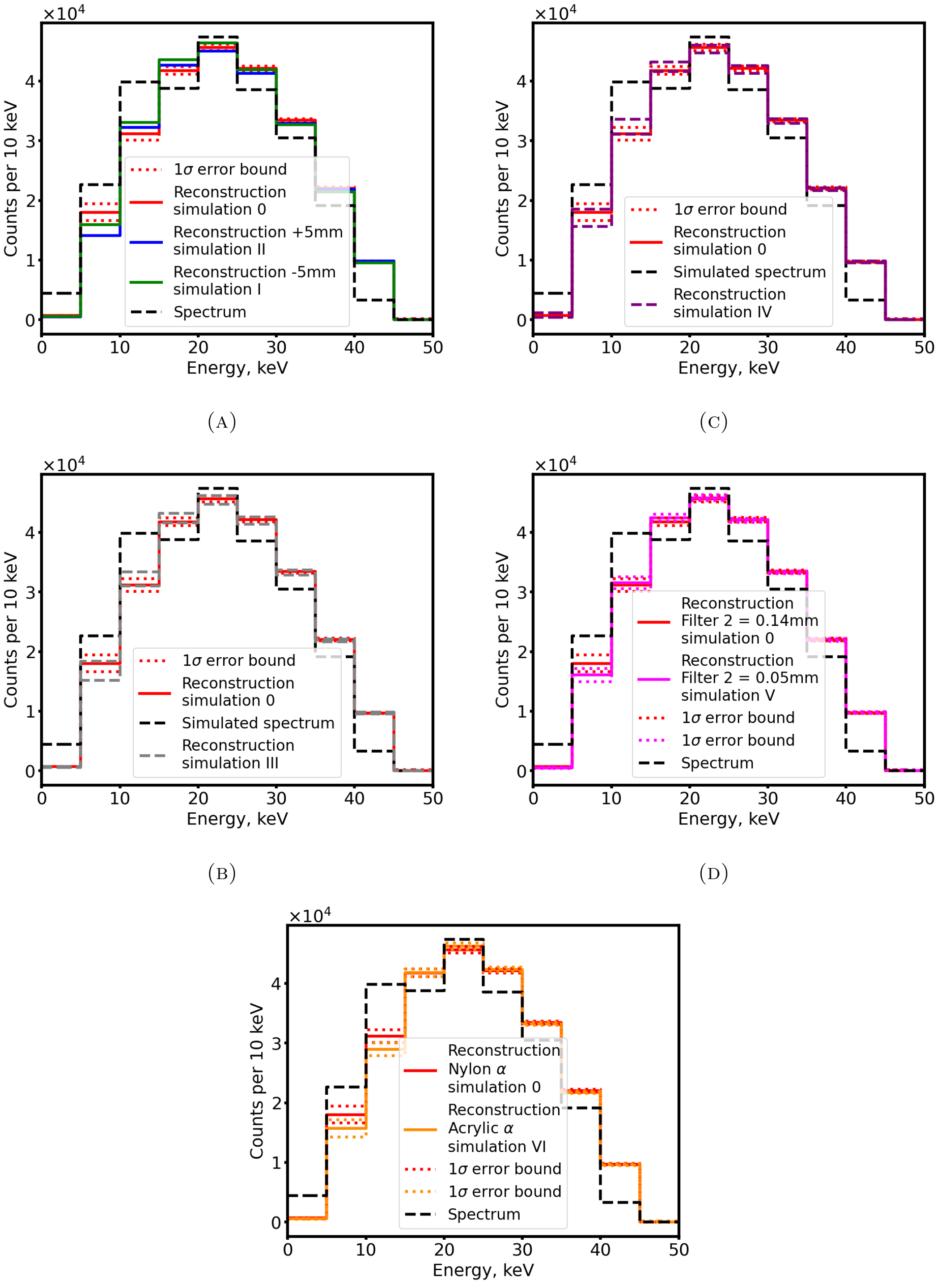

(A) (C)

(B) (D)

(E)

Figure 8.3: Reconstructions for (A) simulations I (green line) and II (blue line), (B) simulation III (grey line), (C) simulation IV (purple lines), (D) simulation V (pink line) and (E) simulation VI (yellow line). The reconstruction for simulation 0 is shown by the solid red line and the simulated spectrum is shown by the black dashed line. 1σ error bounds for the reconstructions are given by the dotted line.

model. This suggests that a much larger source of error is the choice of filter thicknesses in the reconstruction model. This will be discussed in more depth in Section 9.3. Nonetheless, all values considered here are consistent with the simulation 0 results to $\sim 1\sigma$ hence do not affect the measurement of the material properties.

The maximum and minimum C3 and C9 values in both simulation III and IV were caused by a -σ change in the thickness for filters C and F. This suggests these filters are most sensitive to errors in the thickness. Of course, not all possible combinations of x$\pm 1\sigma$ filters have been investigated so absolute quantification of this error is not possible using this simulation. However, this is something that could be investigated most efficiently by repeated experimental trials.

8.4.3 Simulation V: Filter B thickness

The Z_{eff} and ρ values for simulation V (where filter B=0.05 mm) were 7.08±0.14 and 1.44±0.03 g cm^{-3}, consistent with simulation 0 to 0.15σ and 0.24σ respectively. The material was categorised as explosive with a percentage likelihood of $p(X)$=99.4%. Hence changing filter B from 0.14 mm to 0.05 mm did not change the measurement of Z_{eff} and ρ nor the classification of the material. Therefore the mistake in the thickness of filter B on experiment day 2 had a negligible effect on with spectrum reconstructions of PVDF and PTFE.

8.4.4 Simulation VI: Calibration material

Finally, for simulation VI (Acrylic used as the calibration material) Z_{eff}=7.32±0.15 and (ρ=1.41±0.03) g cm^{-3}. These values were consistent with simulation 0 to 1.02σ and 0.47σ respectively. Therefore the calculated values of Z_{eff} and ρ were preserved between the Nylon and Acrylic calibration material datasets to $\sim 1\sigma$. Again, the classification of the material as explosive was preserved with $p(X)$=99.4%.

8.5 Summary and recommendations for static systematic errors

The magnitude of the systematic error effects investigated in this chapter were chosen to be within limits that may go unnoticed to the experimenter. If a combination of changes occurred at once, for example an x-ray tube misalignment and a filter thickness error, this could also change the result. Therefore it is still worth considering how these errors could be reduced. A more precise alignment of the x-ray beam would be necessary to decrease the alignment effect. Experiments should utilise a mechanical alignment system incorporating lasers to ensure the beam is pointing exactly at the object centre. Additionally, higher-spec filters could be used where the manufacturing tolerance is smaller, particularly for filters C and F.

8.6 Time varying systematic errors

The detector response can vary as a function of time even with no change to the experimental geometry. This is because environmental effects such as ambient temperature [60], operating time and external noise can all change the CdTe detector response. Additionally, temperature and power supply deviations can change the x-ray tube output spectrum [128].

A series of experimental measurements were performed in order to quantify the change in detector response over the course of each experimental day. The detector response was measured for a 10 mm thick HDPE sample and a 3 mm thick tin sample at different times throughout the day. The backscatter spectra acquired for each material are shown in Figure 8.4. Although the energy integrated detector response was similar for both materials, the backscatter spectra were very different. The HDPE spectrum is dominated by x-ray scattering whereas the tin spectrum is dominated by characteristic x-ray emission.

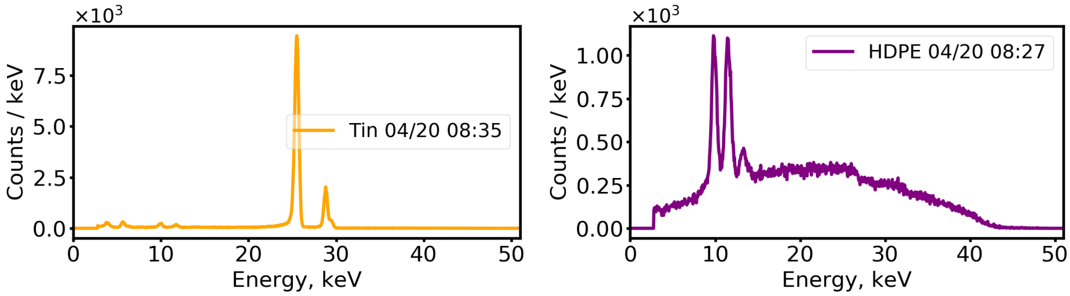

(A) Tin

(B) HDPE

FIGURE 8.4: Experimental backscatter spectra for (A) 3 mm tin sample and (B) 10 mm HDPE sample. Both spectra were acquired at the start of the first experimental day (at 08:35 and 08:27 respectively).

Figure 8.5 shows the detector response as a function of time on both experiment days for HDPE and Tin. Over the course of the first experimental day (4th February 2020) the detector response for both tin and HDPE showed a 1.5% and 1.1% variation respectively. The highest detector response for both was the first measurement of the day at 08:30. The lowest detector response for both was the last measurement of the day at 16:30. For the second experimental day (5th February 2020) the detector response for tin and HDPE showed a 5.2% and 6.1% variation respectively. Similarly to the previous day, the detector response was highest for the earliest measurement and lowest for the latest measurement. For both days the two materials followed the same trend. On day 1 the response remained fairly constant

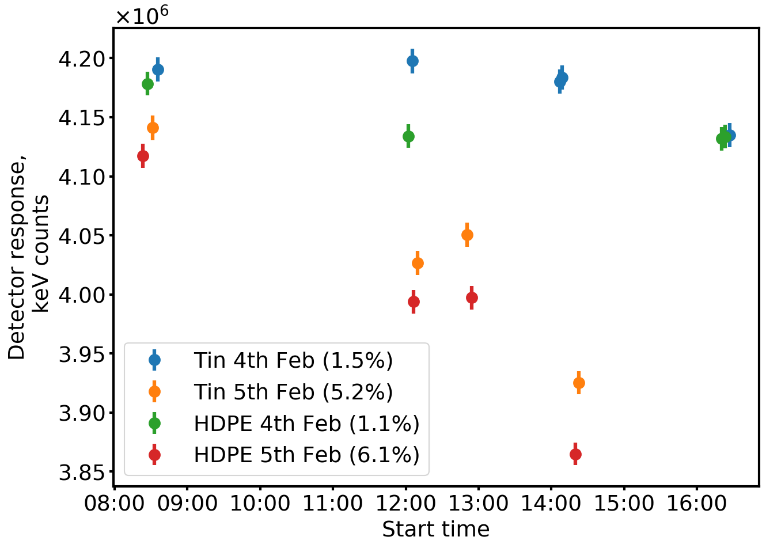

FIGURE 8.5: Detector response as a function of time for calibration materials HDPE and Tin on two experimental days. The percentage difference between the maximum and minimum recorded response is given in brackets in the legend.

over time but on the second day the response decreased as a function of time. Differences were thought to be because of the different energies of x-rays being scattered (or emitted in the case of Tin) from the sample. This suggests an energy dependent factor to the variation of the detector response.

The difference between the two experimental days may be due to differences in the air temperature. Local weather sources record different air temperatures [129]: on the 4th February it was 6° at 08:20 and 9° at 16:20, and on the 5th it was 5° at 08:20 and 8° at 14:20. As the experiment was performed outside, it was likely to be sensitive to weather changes. Studies in a temperature controlled environment would however be necessary to prove and quantify this.

As discussed in Section 4.7.3, changes to the detector response of $>1\%$ can have a considerable impact on the reconstruction. In the method proposed in this work, the calibration measurement for each filter was only performed once throughout the day. Therefore this did not account for the time-variation of the detector response. Commercial systems are also often used in outdoor environments so it is unlikely that the effects of temperature changes could be removed. Instead they should be corrected for in the calibration process. To improve this, calibrations should be done regularly throughout the day so the RCF can be acquired in real time. For the proof-of-concept study presented in this work, this was too time consuming as each RCF takes 660 s of acquisition time plus additional time to change the filters over, by which time environmental effects could change the detector response further. However, this is something to bear in mind when considering how the system could be scaled up to a commercial system.

8.7 Chapter summary

The effect of different systematic errors was investigated using modified full geometry simulations. The effects investigated were the x-ray tube alignment, errors in the filter thickness and the calibration material used to calculate the RCF. All errors investigated in this section were suitably corrected for by the RCF. All Z_{eff} and ρ values calculated where within 1.01σ from the unchanged simulation values. For all systematic errors considered, none changed the categorisation of the POM material as explosive as in all cases the percentage likelihood was $>$98%. Time-varying changes to the detector response were also studied and variation was found between experimental days. This was thought to be due to environmental effects such as the air temperature, however further testing is required to fully understand this. More frequent measurements of the RCF was recommended to reduce this effect which is likely to be an issue in field backscatter systems.

Chapter 9

Discussion

This chapter gives a critical evaluation of the main results of this thesis. Firstly, the results are evaluated within the wider field of research. Then improvements to the method are discussed namely the reconstruction model, choice of filter thicknesses and the reconstruction method choice. The x-ray tube input spectrum used in the Geant4 simulations is also discussed in detail. Application of the technique to other situations such as higher energy x-ray beams, samples of variable thickness, multi-layer samples and variable source-to-detector distances are all covered. Finally the chapter is concluded with a short discussion of how the technique could be scaled up to a commercial backscatter system. Future experiments planned to achieve this are presented in chapter 10.

9.1 Perspectives

This work has demonstrated accurate identification of illicit materials using an x-ray backscattering technique employing a novel spectrum reconstruction method. In the organic material range ($3 \leq Z_{eff} \leq 16$) materials were correctly identified to within $<0.5 Z_{eff}$ and $<0.12\rho$ g cm^{-3} of their data sheet values. In the explosive material range ($6.5 \leq Z_{eff} \leq 8.0$ and $1.4 \leq \rho \leq 2.0$ g cm^{-3}) materials were identified to within $0.1 Z_{eff}$ and 0.04 g cm^{-3}. Both of the explosive simulant materials were detected at greater than 95% probability. All of these results are extremely promising and show a substantial improvement on the basic organic/inorganic material separation that is currently possible on commercial x-ray backscatter systems.

Most academic research into improving material identification in x-ray backscatter imaging using energy integrating detectors has focused on improving image contrast between materials. Techniques have involved using collimator devices such as a twisted slit collimator [5, 130] and a "lobster eye" lens [131], and optimisation of detector systems for rapid detection [132].

Additionally, a research group at K.N. Toosi University of Technology, Iran have proposed a method of material discrimination using detector rise times [133]. The results are promising in simulation but are yet to be tested experimentally due to the requirement for detectors with sub-nanosecond response times.

Company research is also an active field with development projects at Rapiscan Systems and American Science and Engineering (AS&E). Projects have focused on handheld backscatter systems [70, 134, 135], detector development [14, 136–138] and timing techniques such as time-of-flight backscatter imaging [70, 114, 139, 140]. Improved material discrimination capabilities in a field application have not yet been demonstrated. To the author's knowledge this is the first work that actively quantifies material properties such as atomic number and density using an energy integrating detector system.

The most similar work was an investigation into material identification quantification carried out by a research group at CEA LETI, Grenoble, France [16, 17]. The aim of the work was to develop a system capable of determining Z_{eff} and ρ of organic materials, particularly explosives. The system used a CdTe detector operating in photon counting mode and a 120 kVp x-ray tube. A multivariate analysis learning method combined with a material database was used. Measured spectra were compared to known simulated spectra from a database and used to extract Z_{eff} and ρ information. Further details can be found in reference [17] by C. Paulus *et al.*

The material discrimination capabilities of the technique in reference [17] are illustrated in Figure 9.1 which is Figure 10 in the paper by C. Paulus *et al.* [17]. The acquisition time was 30 min per material. Overall the accuracy of the technique based on the data points shown in Figure 9.1 was $<0.9Z_{eff}$ and <0.08 g cm^{-3}. These values were acquired from inspection of Figure 9.1 as no values were quoted in the text in reference [17]. Table 9.1 shows a comparison of the Z_{eff} and ρ values for the materials that were studied in the present work and by C. Paulus *et al.* (POM, PVDF and PTFE). The measurements from C. Paulus *et al.* are shown as a range calculated by reading off the maximum and minimum values for each material in Figure 9.1. No uncertainties are quoted as none were provided in the text in reference [17].

Table 9.1 shows that for POM the present work calculated the Z_{eff} to within 1σ of the true value, however the range of values given by C. Paulus *et al.* were just less of the true value by 0.02 Z_{eff}. In addition, the ρ calculated in this work was 1.4σ away from the true value and for C. Paulus *et al.* the density range given was too high by 0.02 g cm^{-3}. For PVDF both the Z_{eff} and ρ values were within 1σ for this work. For C. Paulus *et al.* the Z_{eff} true value was within the quoted range, however the ρ value was 0.05 g cm^{-1} higher than the upper limit of the quoted range. Lastly for PTFE the Z_{eff} value calculated in this work was within 1σ of the true value, however for C. Paulus *et al.* the Z_{eff} was $0.35Z_{eff}$ higher than the upper limit of the quoted range. For ρ, both methods calculated values that were lower than the true value. Based on these three materials, the technique presented in this work calculated more Z_{eff} and ρ values to within 1σ of their true values compared to the work by C. Paulus *et al.*

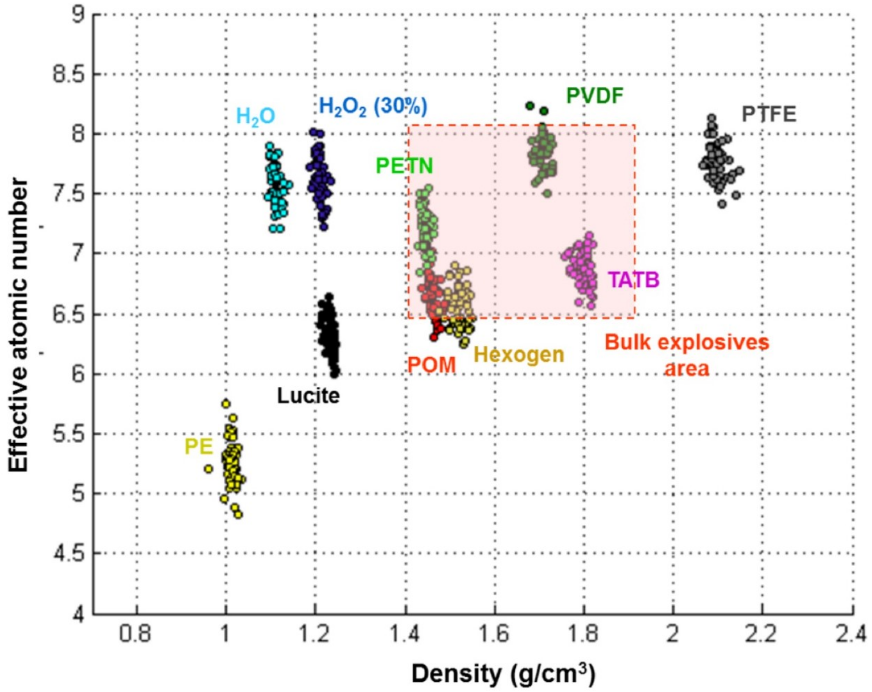

FIGURE 9.1: Material identification capabilities of the x-ray backscatter detection system based on CdTe detector photon counting measurements presented by C.Paulus *et al.* from the CEA LETI group in Grenoble, France [16, 17]. This figure has been reproduced from [17] Figure 10.

Material	Z_{eff}			Density, g cm^{-3}		
	This work	C. Paulus *et al.* [17]	True value	This work	C. Paulus *et al.* [17]	True value
POM	7.00 ± 0.14	6.28 - 7.01	7.03	1.37 ± 0.03	1.43 - 1.49	1.41
PVDF	8.08 ± 0.19	7.48 - 8.23	7.97	1.80 ± 0.05	1.68 - 1.73	1.78
PTFE	8.35 ± 0.20	7.40 - 8.13	8.48	2.08 ± 0.06	2.06 - 2.15	2.20

TABLE 9.1: Calculated Z_{eff} and ρ values by the method presented in this thesis and by C.Paulus *et al.* in reference [17]. The values for C.Paulus *et al.* were acquired by reading off the maximum and minimum data points for each material in Figure 9.1. The results for this work are taken from those in Table 7.9. The methods are compared in the main text.

The main advantage of the C. Paulus *et al.* work over the work presented in this thesis is the data is independent of sample thickness, something that was not considered in this project. The main disadvantages are a longer acquisition time (30 min compared to 600 s) and the fact that an energy resolving detector is used meaning scaling up to an industrial backscatter system for cargo scanning would be impractical with current technology.

Other material determination methods using x-ray scattering have been developed however have not so far reached an advanced stage of development. A system design was proposed by Y.S. Ham and C. F. Poranski in 1996 which uses multiple angles and energy integrating detector to calculate Z_{eff} and ρ but was not developed further beyond the initial design [141]. This system required measurements at multiple scattering angles so may have been impractical to scale up to an industrial system. Additionally, there exists a body of work on extracting atomic number information using Rayleigh to Compton ratio techniques but this has only been applied to backscatter imaging using mono-chromatic synchrotron sources or mono-chromatised x-ray beams [142–144]. Long acquisition periods and energy resolved detectors were required in both cases.

When considering this work in the perspective of the wider field of research, the main advantages however are that the method is (relatively) quick compared to existing methods, can achieve a similar accuracy (albeit with a uniform sample thickness). Importantly, it does not require a photon-counting detector, hence provides a potentially cheaper alternative to most methods. The disadvantage of the work is that more work needs to be done on investigating the effect of the sample thickness on the material identification capabilities. Another advantage of the technique is the calibration process developed does not require energy information either and can be easily applied to any scatter geometry.

9.2 Reconstruction model

9.2.1 Attenuation coefficient sampling

The reconstruction model was based on the attenuation of a polychromatic x-ray source through each thickness of filter. The process describing the attenuation is a complex function of x-ray energy and filter thickness and depends on the properties of the filter material. To create the reconstruction model, this function was sampled at different energies and filter thicknesses using a quadrature method [89]. The function was sampled at energies $E{=}\{E_1, E_2, ..., E_i\}$ and $x{=}\{x_1, x_2, .., x_j\}$. The reconstruction model, the $\mathbf{W}$, matrix was

$$\mathbf{W} = \sum_{i=1}^{m} \sum_{j=1}^{n} E_i e^{-\mu(E_i)x_j} \tag{9.1}$$

where E_i is the bin-centre energy of bin i and x_j is the filter thickness of filter j. The index i runs from 1 to m where m is the number of bins and j runs from 1 to n where n is the number of filters. Both m=10 and n=10 in this work. The E values were chosen evenly over the energy range and x was chosen by calculating the thickness of aluminium at which 10% of x-rays were transmitted for each energy. This was done to ensure even bin spacing across

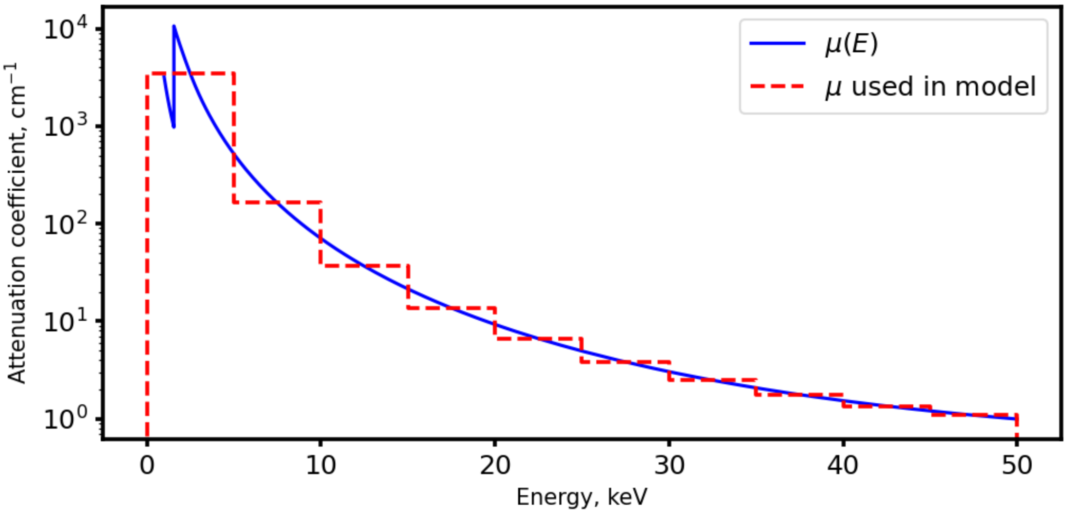

FIGURE 9.2: Attenuation coefficient for aluminium as a function of energy shown in blue. The assumed attenuation function used in the model is shown by the red dashed line. The variation between the two is greatest the lower the energy. All data for $\mu(E)$ was taken from the NIST XCOM database [52].

the spectrum, which seemed a reasonable starting point given that this was the first test of the technique. Useful reconstructions were obtained from this which allowed the atomic number and density of the material to be estimated to high accuracy.

One issue with the reconstruction model is that for low energies <10 keV, using the midpoint energy is less representative of all the energies in that bin because the attenuation coefficient changes very rapidly. Figure 9.2 shows the attenuation coefficient for aluminium μ as a function of energy between 0 and 50 keV. As before all data was taken from the NIST XCOM database [52]. The blue line shows $\mu(E)$ as a continuous function of energy. The red dashed line shows the μ used in the reconstruction model. The lower the energy the less representative the $\mu(E_C)$ of the function $\mu(E)$ due to the larger gradient of $\mu(E)$.

To reduce these errors, one could consider a non-linear bin sampling such that areas where the attenuation coefficient varied rapidly there were more bins, for example an exponential distribution of bins. This could also suit the energy spectrum reconstruction performed in this work as there is more structure to the spectrum on the low energy side due to scattering of characteristic x-rays compared to the high energy side which is smoother due to bremsstrahlung scattering.

9.2.2 Choice of filter thickness

The thickness of filter used was also a major consideration in the reconstruction model. Based on the availability of materials and the knowledge that filters should be neither too thick nor too thin, filters corresponding to a 10% transmission percentage at each bin centre energy were chosen. However, a more precise choice of filter thickness may yield better results, because as seen in Section 8.4.2, changing the filter thickness can change the reconstruction outcome. When choosing filter thicknesses, there are many different constraints that should be considered.

- Filters should be chosen so that the difference in intensity between subsequent energies is maximum to produce the greatest contrast in the intensity measurement vector.
- Filters should be minimum thickness to reduce scattering.
- Filters should be minimum thickness to increase the signal to noise ratio.
- The thinnest filters (for example filters A, B, C) should be as thick as possible to minimise thickness errors and increase filter stability. For example, filter A was 0.0066 mm in the experiment, however increasing the thickness to 0.009 mm would make the filter more stable and the error in the thickness would be less as a percentage.
- Other practical considerations include the type of material used and the cost of manufacture.

Figure 9.3 shows the intensity difference between bin centre energies for neighbouring bins as a function of filter thickness. The intensity difference was calculated as

$$I_{diff}(x) = e^{-\mu(E_{i+1})x} + e^{-\mu(E_i)x}. \tag{9.2}$$

For all energies, the intensity difference increased with increasing filter thickness up to a maximum point, then decreased with increasing filter thickness, The filter thickness

E_{j+1}-E_j, keV	x_{max}	$I_{diff}(x_{max})$, %	x_{used}	$I_{diff}(x_{used})$, %
7.5 - 2.5	0.009	81.9	0.0066	80.4
12.5 - 7.5	0.12	50.4	0.14	49.7
17.5 - 12.5	0.43	34.9	0.63	32.4
22.5 - 17.5	1.03	26.0	1.68	22.7
27.5 - 22.5	1.96	20.0	3.47	16.5
32.5 -27.5	3.21	15.7	6.0	12.4
37.5 -32.5	4.74	12.5	9.26	9.4
42.5 - 37.5	6.45	9.9	13.0	7.3
47.5 - 42.5	8.23	7.9	17.0	5.6
47.5 - 50.0	9.61	3.4	21.1	2.2

TABLE 9.2: Approximate intensity difference between detector response measurements as a function of filter thickness.

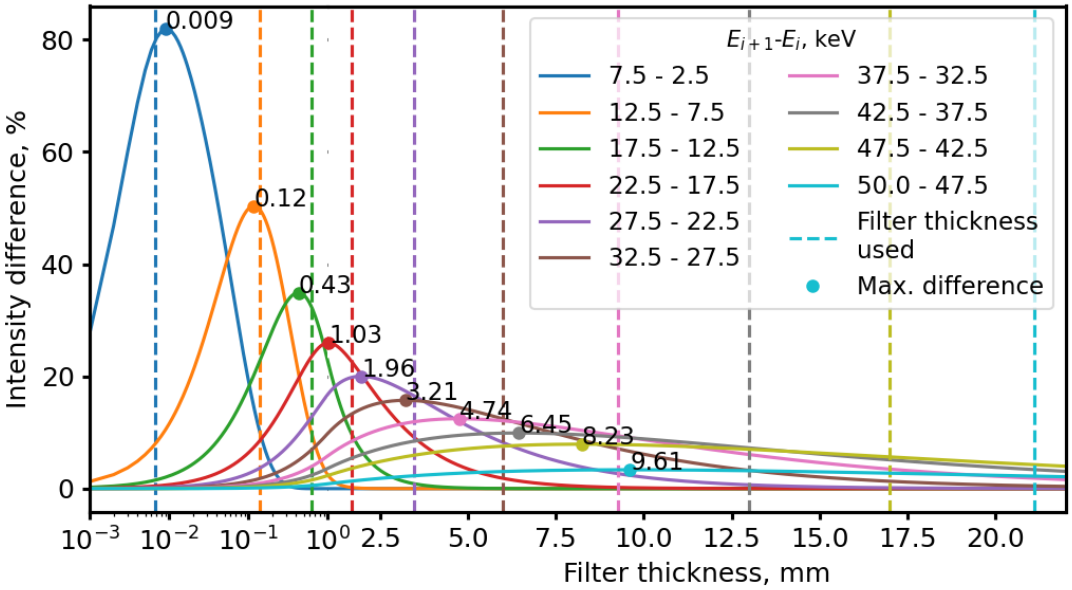

FIGURE 9.3: Difference in intensity between bin centres as a function of filter thickness. One way to improve the reconstruction is to pick filters which maximise the intensity difference between filters. The maximum difference is shown by the point and written next to it for each difference. All distances are given in mm. All energies are given in keV. The vertical dashed line is the filter thickness that was used in this work.

corresponding to the maximum intensity difference (x_{max}) is given on the annotation on each of the maximum points. The vertical dashed lines show the filter thickness that was actually used (x_{used}). Table 9.2 gives the x_{max}, $I_{diff}(x_{max})$, x_{used} and $I_{diff}(x_{used})$ for each E_{j+1}-E_j. For the first two filters, the thickness of maximum intensity and the thickness used was similar (0.009 mm compared to 0.0066 mm for filter A, 0.12 mm compared to 0.14 mm for filter B). After this though, the filter thickness used was larger than the filter thickness of maximum intensity, and the difference between the two increased with increasing energy. However, for no energy was the intensity difference substantially lower than the maximum difference for the filters used. Even for bin 10 the maximum intensity difference is 3.4% at a filter thickness of 9.61 mm but 2.2% at the 21.1 mm actually used.

Based on these findings, improvements to the method should involve using thinner filters, particularly for the higher energy bins in order to improve the signal to noise ratio and hence reduce the percentage error in the reconstruction. Additionally, using thinner filters will also reduce scattering and hence reduce the amount of data correction required (the RCF will be larger). Nonetheless, practical considerations such as material availability, geometry constraints and cost may mean that the filter that maximises the intensity difference may not be the best to use. It ultimately depends on the application.

9.3 Reconstruction method choice

In this work the Tikhonov regularisation method was used with the regularisation parameter chosen by the L-curve method based on the total error in the data. However, there are other algorithms using different methods for regularisation available. For example the algebraic reconstruction technique (ART) method [89, 100], conjugate gradient least square method (CGLS) [89, 99, 145] and methods based on matrix singular value decomposition, for example the TSVD method (truncated singular value decomposition) [89]. Reconstruction methods ART, CGLS and TSVD were all investigated as alternatives to the Tikhonov method by comparing the resulting spectra as will be discussed in this section. Algorithms will be briefly discussed, but for a more complete guide to their formulation, see the given references for each method.

The ART and CGLS methods are iterative methods where the regularisation is controlled by the number of iterations. The solution starts off smooth and as the iteration number increases, smoothing decreases. In x-ray CT applications, iterative methods have been shown to reconstruct images with a larger signal to noise ratio. Less radiation dose is required to produce a similar quality image when compared to other methods such as filtered back-projection [146], therefore are most suited to this application, particularly for materials with low photon statistics (those with Z_{eff} >10). The best number of iterations to run for is decided by the user. The ART method (also known as Kacsmarz's method) is a simple and widely used iterative algorithm. However ART is associated with a slow convergence speed hence more iterations need to be run before the optimum solution is achieved, taking up more computational time [89]. CGLS is a faster algorithm that converges in fewer iterations.

The SVD method is a method that involves solving the equation $\vec{b} = \mathbf{A}\vec{x}$ by finding the matrix singular value decomposition (SVD) of $\mathbf{A}$ and using this to calculate the inverse of $\mathbf{A}$. This is analogous to finding the different frequency components of the solution. The truncated version of the SVD (TSVD) is where higher frequency components in the SVD of $\mathbf{A}$ are not included in the solution. The higher frequency components are those corresponding to the noise in the data, so including these will result in a nonsensical solution similar to having too small a regularisation parameter in the Tikhonov algorithm. The regularisation in the TSVD algorithm is based on a user choice of how many frequency components to include. The disadvantage of the TSVD method is that the SVD must be calculated initially and for very large $\mathbf{A}$, this can be a computationally intensive task [89]. However for the 10×10 matrices considered in this work, this is a trivial calculation and there many computational tools that can calculate the SVD efficiently (for example [147]).

The response data from the full geometry (FG) simulations of POM and PVC were reconstructed using the ART, CGLS and TSVD algorithms in addition to the Tikhonov algorithm to compare method performances. A comparison of the results is shown in Figure 9.4 for (A) POM and (B) PVC. The average energy and percentage difference compared with the simulated spectrum are given in Table 9.3 for each method. Consider the POM reconstruction shown in Figure 9.4a. The average energies are similar (between 23.0 and 23.6 keV) and the % difference has a small range of 12.7-15.0%, showing similar reconstruction shapes for each method. For PVC, as shown in Figure 9.4b there is a greater difference between the performances of the different reconstruction methods, with the TSVD method showing the greatest similarity (16.2% difference) and closest average energy (25.5 keV) to the spectrum. This is due to the close agreement of the TSVD solution in bins 2 and 3 compared to the other methods. This suggests that the TSVD method may be a better choice for reconstructing spectra for materials with $Z_{eff} > 10$. However, this is based on just one material and hence would require further investigation across a wider range of samples.

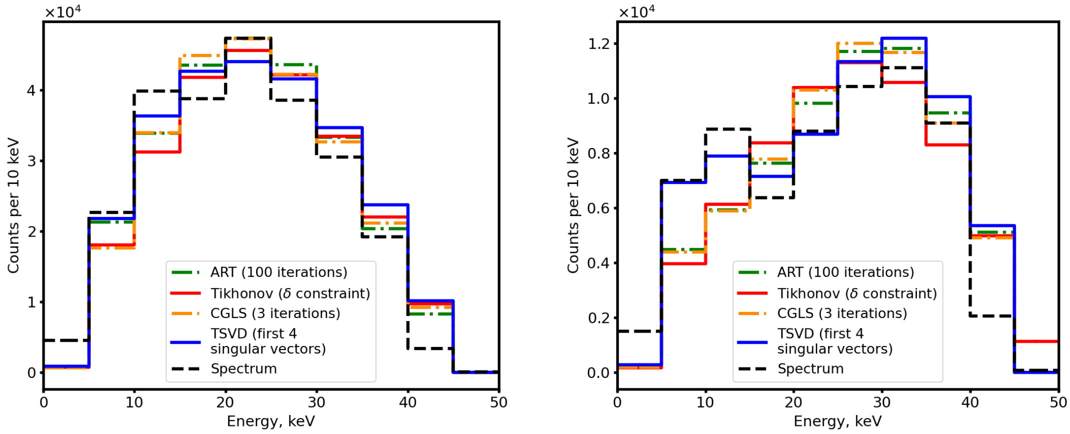

(A) POM (B) PVC

FIGURE 9.4: Full simulation geometry spectrum reconstruction for (A) POM and (B) PVC. Four different reconstruction algorithms were used: ART (green), Tikhonov (red), CGLS (yellow) and TSVD (blue). The overall spectrum shapes were reproduced but there were differences between the absolute number of counts that have been reconstructed in each bin. Information about each spectrum is provided in Table 9.3.

Method	POM		PVC	
	Avg. energy keV	d, %	Avg. energy keV	d %
Tikhonov	23.6	15.0	26.3	25.4
ART	23.0	12.0	26.3	22.7
CGLS	23.3	13.6	26.2	23.2
TSVD	23.3	12.7	25.5	16.2
Spectrum	21.8	-	23.8	-

TABLE 9.3: Average energy and % difference compared to the simulated spectrum for reconstructions of POM and PVC using the Tikhonov, ART, CGLS and TSVD algorithms. The spectrum reconstructions are shown in Figure 9.4.

Convergence speed and algorithm speed was not an issue as only one data set was being reconstructed at a time. However, when considering scaling this up to a system acquiring thousands of datasets a second, as is the case on a commercial system, reconstruction time will be more of a consideration. In this case it would be best to use the CGLS algorithm as it converges in the fewest iterations of the methods tested. However, CGLS requires the number of iterations to be chosen by the user so could be harder to automate. All reconstruction algorithms will have advantages and disadvantages and ultimately the choice of algorithm will depend on the application and which features are a priority.

9.4 Simulation input x-ray spectrum

The full geometry simulation (FG) was validated against experimental data in order to quantify how well the experiment data were reproduced. As discussed in Section 6.4.4, in general good agreement was seen between the simulated and experimental spectra. Upon inspection of the spectra, differences were seen in the region below 10 keV and between 25-35 keV (see Figure 6.6). This was because the input spectrum used in the simulation was the x-ray source measured using the CdTe detector. It was concluded that the simulation could be improved by using an input spectrum without the CdTe detector effects in the spectrum.

Spectrum processing software could be used such as Amptek XRS-FP software [148] which removes the Cd and Te escape events from the spectrum by a stripping algorithm [61], or by Monte Carlo simulation [149, 150]. Alternatively, x-ray tube spectral models could be used instead of an experimental measurement. The x-ray spectrum simulation program *SpekCalc* [151] for example, which calculates photon spectra from tungsten x-ray tubes, or theoretical calculation based on characteristic x-ray and bremsstrahlung photon yields [152] using model results (for example [153, 154]).

9.5 Measurements with higher energy beams

As discussed in Section 2.3.5, with a maximum beam energy of 50 keV it is not possible to acquire density information from a backscatter spectrum for materials with Z_{eff} >10. This is because there is no clear relationship between the backscattered intensity and density even in a theoretical case due to the influence of the atomic number. In order to find density information for materials with Z_{eff} >10, higher energy x-ray beams are required. In commercial systems, 200 keV x-ray tubes are used, so in theory higher densities can be measured.

Using Equation 2.14 in Section 2.3.2 and the attenuation coefficient data from the NIST database [52], the scatter intensity as a function of density was calculated for a beam energy of E=200 keV. Figure 9.5 shows the scatter intensity as a function of density (normalised to the largest point). The red points show the scatter intensity at different densities based on the theoretical calculation. The scatter intensity increased with increasing density. A $\mathrm{y = mln(x) + c}$ function was fit to the data and is shown by the black line on Figure 9.5. The fit parameters were m=0.453±0.011 and c=0.519±0.006 and the χ^2_{red} was 1.68. This shows that the density can be approximated for all organic materials ($Z_{eff} \leq$16) using an energy of 200 keV.

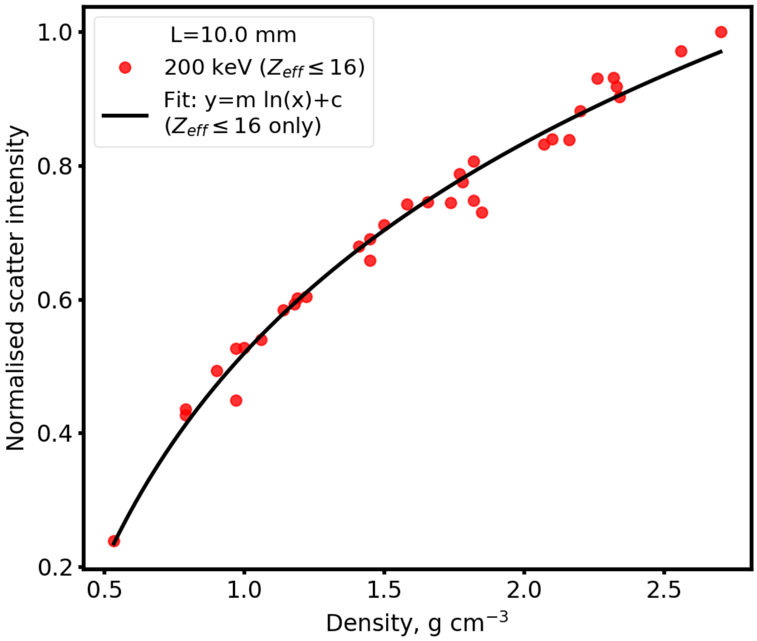

FIGURE 9.5: Scatter intensity as a function of density for E=140 keV. Data points shown are for $Z_{eff} \leq$16. A $\mathrm{y = mln(x) + c}$ equation has been fit to the data for both energies. The fit parameters for the fit were m=0.453±0.011 and c=0.519±0.006 and χ^2_{red}=1.68.

Atomic number information can still be calculated using the scatter intensity at 10 keV using a 200 keV beam. However, as seen in the 50 keV, the accuracy to which Z_{eff} is calculated decreases with increasing Z_{eff}. For example the Z_{eff} for POM was calculated as 7.00±0.14 but for PVC it was 14.42±0.72. The percentage error is 2.5 times higher for PVC than POM. Increasing the energy by which the atomic number calculation is done can improve the accuracy for larger atomic numbers because the larger atomic numbers no longer lie in the plateau of the curve.

Figure 9.6 shows the scatter intensity (as calculated using Equation 2.14) as a function of Z_{eff}. When $Z_{eff} \leq$8 there is a non-linear relationship with Z_{eff}, however from $Z_{eff} \leq$8 an exponential relationship with Z_{eff} is observed. This is because for materials with $Z_{eff} >$8, photo-electric absorption is the dominant interaction at 30 keV and photo-electric absorption depends on Z_{eff} as discussed in Section 2.2. For Z_{eff} $\leq$8, Compton scattering is dominant which depends on density rather than Z_{eff}.

The relationship $\mathrm{y = Ae^{-b(x-8.00)} + c}$ was fit to the data in Figure 9.6 with 8$\leq$ Z_{eff} $\leq$25 and the fit parameters were A=1.74±0.09, b=0.23±0.01 and c=0.024±0.008 with χ^2_{red}=0.002. This suggests that more accurate Z_{eff} information can be acquired using the scatter information at 30 keV for 8$\leq$ Z_{eff} $\leq$20 so can be used in conjunction with the 10 keV information to calculate Z_{eff} more accurately. It is also worth noting that as the energy of the x-ray beam increases, the Z_{eff} corresponding to the transition between the non-linear and linear region increases meaning Z_{eff} information becomes available for higher Z_{eff} materials as the x-ray beam energy is increased.

For materials in the explosive range, it is best to use E <30 keV as 6.5$\leq$ Z_{eff} $\leq$8.0 lies in the non-linear part otherwise. Additionally, this analysis would only work with a higher energy x-ray beam, where the 30 keV was the low energy region of the spectrum. In this work the relationship between the number of counts at 30 keV and Z_{eff} did not follow the expected trend. This was thought to be due to additional detector effects and scattering in the 30 keV region which meant the relationship between the measured intensity and energy deviated from what was expected theoretically.

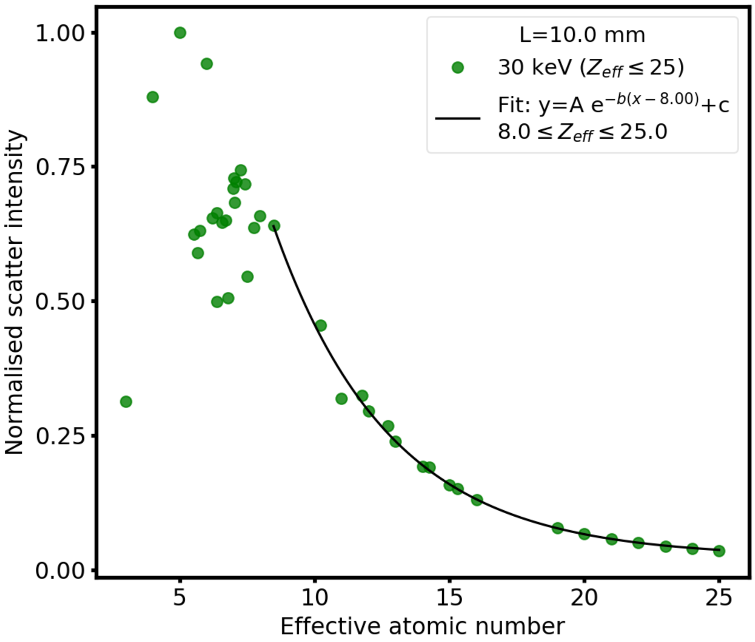

FIGURE 9.6: Scatter intensity as a function of Z_{eff} for E=30 keV. Data points shown are for Z_{eff} $\leq$25. A y=$Ae^{-b(x-8.00)}$+c function has been fit in the region 8$\leq$ Z_{eff} $\leq$25. The fit parameters are A=1.74±0.09, b=0.23±0.01 and c=0.024±0.008. The χ^2_{red} was 0.002.

9.6 Accounting for the sample thickness

The sample thickness was not considered in this work as all samples tested and simulated were 10 mm thick. As discussed in Section 2.3.7, increasing the sample thickness increases the intensity of the backscattered beam, up to a plateau thickness. The relationship between Z_{eff} and C3 depends on the thickness, particularly for materials with Z_{eff} <8. The relationship between ρ and C9 depends on the thickness for all materials. This is a particular downside with this method of material identification and should be addressed in future work so a wider range of samples can be identified.

To the author's knowledge there is no present solution to measuring the thickness of a material using x-ray backscatter imaging with a single detector at a single scattering angle. Backscatter imaging has been used to measure material thickness but in the case where the material is known, for example measuring aeroplane skin thickness which is made from aluminium [155].

A method for thickness estimation currently employed in x-ray transmission imaging for material discrimination and thickness determination is a method called "basis material decomposition" [156]. This method uses the fact that the total attenuation coefficient of any material $\mu(E)$ can be written as a linear sum of the attenuation coefficient of known materials i,

$$\mu(E) = \sum_i L_i \mu_i, \tag{9.3}$$

where L_i is the equivalent length of material i. A set of basis materials are chosen and the coefficients L_i can be found by acquiring energy spectrum measurements. The value of the coefficients L_i can be linked to the material properties such as Z_{eff} and ρ [59].

Future work should investigate if there is a similar functional form that could be used for backscatter imaging, although the situation is likely to be complicated by the fact that the backscatter process is a three step process (attenuation of the primary beam, scattering, and then attenuation of the secondary beam) compared to a single step for transmission imaging, so many more basis materials would be needed. Other techniques for eliminating the material thickness in backscatter imaging which use multiple detector angles such as the method presented by C. Paulus *et al.* [17] (discussed in Section 9.1) could be adapted for use in this technique.

Another possibility would be to use a method of mathematical constraints to estimate the material thickness. As shown in Figure 2.14, for thicker samples the scatter intensity is higher for both E=10 and 50 keV. If the scatter intensity for a 50 mm sample were used to calculate the Z_{eff} and ρ values using the fit equations for a 10 mm sample then the Z_{eff} would be calculated as much too small, and the ρ much too large. The fact that no material with a very low Z but very high ρ is physically possible could be used as an indicator that a larger material thickness is likely. Again, this is in a very early stage of development so much more work is needed in this area to understand if this would work in practice.

9.7 Material shielding effects

A common issue in backscatter imaging is the effect of material in front of the object of interest. This could be an object behind a cargo container wall for example. Typical cargo container walls are made from steel and are approximately 3 mm in thickness. This can alter the backscatter spectrum obtained because the steel can attenuate both the primary and secondary x-ray beams resulting in a reduction in detected x-rays particularly at low energies. This could change the material properties, in particular increasing the value of Z_{eff} that is measured. A steel attenuation parameter could be added into the reconstruction model so that the terms of $\mathbf{W}$ also account for attenuation through steel as well as the sample. Another approach could be to incorporate the steel into the calibration process for determining the RCF. Again, future work should also involve investigation into what the exact effects of this are.

9.8 Source-to-object and object-to-detector distances

Another problem encountered in x-ray backscatter imaging is the problem of unknown source-to-object distance. Backscatter scans only produce 2-dimensional images so it is impossible to tell the depth of an object within a cargo container. The depth of the object can affect the scattered energy spectrum because the depth of the scattering interaction changes the scattering angle to the detector and the attenuation of the scattered beam. As all measurements in this work were performed at a fixed depth, this was not investigated but would be important for scaling up to a field backscatter system. As for the material shielding effects discussed in Section 9.7, accounting for this effect could involve an additional parameter in the reconstruction model.

9.9 Scaling up to a field backscatter system

Looking to the future of this research, the ultimate aim is to create a working commercial x-ray backscatter system that can provide improved material identification in real time to improve the accuracy and efficiency by which illicit materials such as explosives can be detected. This work as shown by proof of concept that improved identification is possible using a detector filtration method under certain experimental conditions. Discussion in this section will focus on the main error considerations when thinking about scaling up the method to a 200 keV field backscatter system. Further design ideas will be presented in Chapter 10.

The main experimental error in this work was the random error in the data collection. The only way to reduce this significantly is to increase the data acquisition time. Although x-ray backscatter systems operate with a significantly higher x-ray flux compared to the 50 keV x-ray tube used in this work, the time the x-ray beam spends illuminating each pixel of the image is 7 orders of magnitude less at approximately 10-20 μs [139]. The result is a lower signal-to-noise ratio (SNR) than in this experiment. For example, in one research setting, a person carrying a steel plate was scanned with a 160 keV x-ray beam at a distance of 15 m [77, 127]. The SNR for the steel plate was 77.2. From the data in Table 7.1 in Section 7.2 the SNR in the experiment ranged from 224 for PVC to 410 for POM.

To achieve the same SNR, measurements would need to be acquired for approximately 3 times longer at 30-60 μs for Z<10 material such as POM. For Z>10 materials like PVC, it is likely that even longer acquisition times will be required because the SNR for PVC was shown to produce an overly smooth spectrum reconstruction using Tikhonov regularisation even at a SNR of 224, as discussed in Section 7.4. In order to have the same SNR as POM, the PVC acquisition time needed to be 2.8 times longer than POM in this experiment, therefore one could reasonably expect acquisition times of up to 90-180 μs needed for PVC to achieve the same quality of reconstruction.

This is one of the main drawbacks to the technique when considering it for scaling up to a commercial backscatter system. Scans would take 3 times longer hence still cause delays at ports and security checkpoints. However in some cases the benefits of improved identification may outweigh the disadvantages of the higher acquisition time. Such a case may be if a vehicle is detected as suspicious during an ordinary backscatter scan, a secondary acquisition could be performed using the detector filter method. A typical backscatter scan takes between 10-60 s. If this were increased by up to 9 times to 90 s-9 min, this would still be considerably shorter than a manual search which can take several hours [13]. Additionally, the second scan may only need to be performed on part of the vehicle where the suspicious material was detected which would significantly reduce the scan time.

9.10 Summary and recommendations

The presented technique provides superior Z_{eff} resolution for 10 mm material samples compared to a similar technique presented by C. Paulus *et al.* [17] ($<0.1 Z_{eff}$ compared to $<0.9 Z_{eff}$) at a faster acquisition time (600 s compared to 30 min) and importantly does not require an energy resolving detector. Testing the technique on different sample thicknesses and different source-to-detector distances should be a subject of future work. In addition, future work should also consider the effect of material such as steel container walls being in front of the sample.

In order to optimise the reconstruction process, it is recommended that thinner filters be used in order to increase the difference in intensity between filters and maximise the signal to noise ratio. Additionally non-linear bin spacing in the reconstruction warrants investigation to improve the reconstruction in the areas where there are more spectrum features. Other reconstruction algorithms should be investigated, for example TSVD, which shows in initial investigation to improve the reconstruction for low SNR materials, or CGLS which has a short reconstruction time so may be beneficial when having to reconstruct spectra for many different image pixels.

The presented technique could calculate the density only for materials with Z_{eff} <10 due to theoretical limitations. X-ray sources with a maximum energy of 200 keV can be used instead to calculate the density for all organic materials ($Z_{eff} \leq$16). The scatter intensity at 30 keV could also be used to improve the Z_{eff} resolution in the 8$\leq Z_{eff} \leq$16 range in the case of a 200 keV beam being used.

Finally, the largest source of error in the presented work was the random error. In order to reduce this it would be necessary to increase the acquisition time by up to 9 times with present equipment. This requirement would reduce the efficiency of the scan in a field environment, and hence it is envisaged that the presented technique would be used as a secondary inspection upon detection of a suspicious item.

Chapter 10

Proposed future experiments and development

Future work should focus on building on this proof of concept study to apply the technique to higher energy x-ray beams more similar to those used on commercial systems. Three propositions for future experiments will now be discussed. This includes a test system similar to the 50 keV set-up presented in this thesis but using a 200 keV x-ray beam. Some preliminary tests have already been completed for this. Other experiments include a multi-detector experiment at 200 keV. Ideas for future detector development are also presented.

10.1 200 kV test system

Preliminary work on a test backscatter system using a 200 kV x-ray beam has already been completed. The set-up consisted of a single Gadox detector (with density 180 $\mathrm{mg\,cm^{-2}}$), collimated 200 kVp x-ray source and material test piece arranged in a backscatter configuration. The detector was coupled to a Hamamatsu R1307 3 inch photo-multiplier tube (PMT) [157]. The applied PMT voltage was 950 V. The active area of the detector was 200×200 mm. A photograph of the set-up is shown in Figure 10.1. In this set-up the sample test piece was 1 m away from the source collimator and the sample-to-detector distance was 1.4 m. The sample test pieces were 20×25 mm in area. The detector filters were placed on a shelf directly in front of the detector. A mix of copper and aluminium filters were used to achieve a 10% attenuation at each bin centre over the 0-200 keV energy range. Initial testing was completed in March 2020, however a complete set of test data has not yet been acquired due to restricted laboratory access during the pandemic.

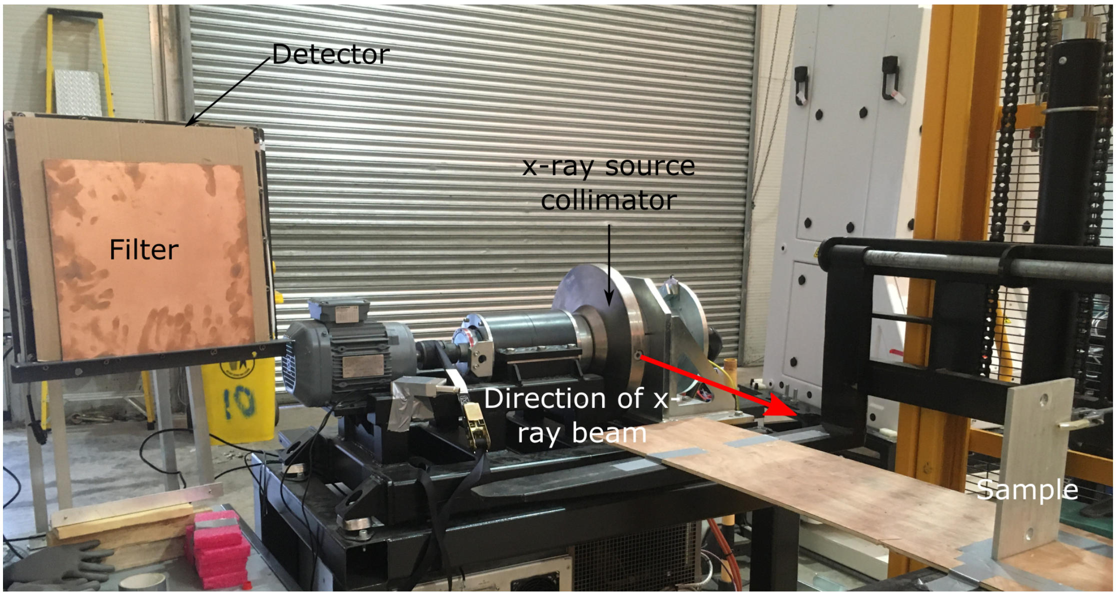

FIGURE 10.1: Photograph of the set-up used to perform preliminary testing work on a higher energy backscatter geometry. The experiment used a 200 kVp x-ray tube and Gadox detector. The x-ray source collimator, detector, detector filter and sample are shown. The direction of the x-ray beam is indicated by the red arrow annotation. A mix of aluminium and copper detector filters were used. See the main text for more details.

Initial tests showed the detector response had a dependence on ambient temperature. A response decrease of approximately -0.04% per minute was observed for calibration measurements acquired over a 2 hour period between 9 am and 11 am. The PMT was thought to be causing the change as the PMT gain varies as a function of temperature [157]. This is an important issue to be aware of and gain correction methods used in field systems [136], or regular calibrations should be considered in order to reduce the effect of time-varying systematic errors on the detector response.

Future work should include measurements of plastic materials at the 200 keV beam energy using the set-up discussed here. Spectra should be reconstructed in the same way as in the 50 keV test. Properties of the reconstructed spectra such as the number of counts in the 10 and 30 keV and 140 keV bins should be used to determine atomic number and density properties following Section 9.5. Similar to the 50 keV set-up, calibration measurements should also be performed. A simple simulation of the 200 keV geometry should also be performed so the RCF can be calculated by the method discussed in this thesis. This simulation would require a beam profile measurement, although this may be more difficult to acquire owing to the 200 keV beam's larger spot size and higher power compared to the 50 keV. Alternatively, a calculated beam profile derived from spectrum models, as discussed in Section 9.4, may be more appropriate.

10.2 Multi-detector test on an M60 system

One issue with the proof-of-concept study and the 200 kV test system outlined in Section 10.1 is that only one detector is used so each filtered response measurement must be acquired individually, increasing the acquisition time greatly. Some field systems such as the M60 have multiple backscatter detectors (similar to that shown in Chapter 3 Section 3.4), hence one method that should be tested is whether multiple filtered detector response measurements can be acquired simultaneously. The diagram in Figure 10.2 shows one way this could be achieved. This is based on the 14-detector backscatter panel of the test backscatter system discussed in Section 3.1. Fourteen different thicknesses of material could be placed across the detector array as shown in Figure 10.2 and the detector response could be recorded for each detector. This would allow fourteen intensity measurements to be acquired simultaneously and allow reconstruction of a fourteen bin energy spectrum.

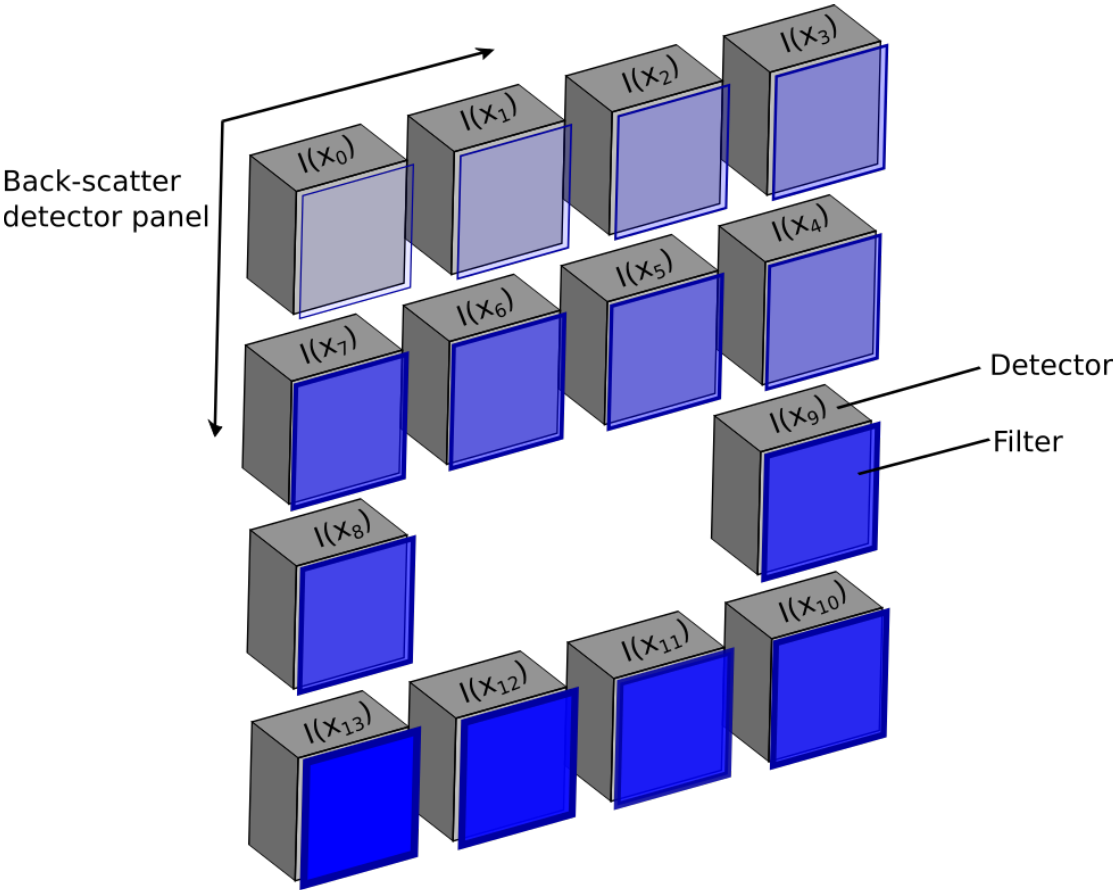

FIGURE 10.2: A schematic diagram of the backscatter detector panel of the test M60 backscatter system similar to that shown in Chapter 3, Figure 3.3a. The detector panel consists of fourteen individual detectors. These detectors are represented by a grey cube in the diagram. To acquire multiple filtered detector response measurements simultaneously, filters of different thickness could be placed over each detector. The filters are shown in blue and the opacity of the filter gives an indication of the filter thickness. The intensity recorded by each detector is written as $I(x_i)$ where i is the detector number ranging from 0 to 13.

Simple geometry simulations of the set-up would need to run and calibration measurements performed so the RCF could be determined for accurate reconstructions. Other systematic errors not encountered in the single detector system could be multiple scattering from one detector to another, so this would need to be studied closely to determine if the RCF approach could suitably correct for this.

The results of this experiment would be able to show what energy resolution and hence material identification capabilities are possible on a real backscatter system. If successful, rolling out the technique across backscatter systems such as this would be relatively simple and inexpensive as only minor hardware modifications are required to accommodate the filters. This could be a very promising development in improving material identification on commercial systems if successful.

10.3 Detector development

An issue still remaining with the multi-detector idea in Section 10.2 is that the scan acquisition time would still have to be larger than standard as a lot of the signal is lost through absorption in the filters. A way around this would be a different detector design where detectors are stacked longitudinally along the scattered beam direction. This way detectors in front act as filters for the detectors behind so less signal is lost. The “transXend” detector design developed by I. Kanno [25] could be used to implement this. Additionally, optimally segmented scintillator detectors such as those developed in [138, 158] could be used as an alternative.

Chapter 11

Conclusions

X-ray backscatter imaging has revolutionised the detection of contraband concealed in vehicles and cargo, however it has long suffered from poor material identification capabilities. This thesis has proposed a novel technique for improving identification of illicit materials in x-ray backscatter imaging. This work presented is the first application of the spectrum reconstruction technique to x-ray backscatter imaging.

A 50 keV x-ray beam and a CdTe detector operated in energy-integration mode were used to measure the backscattered x-ray spectrum of five plastic samples with a fixed 10 mm sample thickness. The samples tested were two explosive simulants and three inert materials. During the data acquisition process, ten different measurements of the backscattered beam were acquired each with a different thicknesses of filter material in front of the detector. By modelling as an inverse problem the energy spectrum was calculated mathematically from the set of detector response measurements. A calibration process was developed in this work and implemented to account for scattering and systematic errors to ensure valid energy spectra were calculated. The calculated energy spectra were in good agreement with spectra acquired using an energy resolving detector under the same conditions.

The reconstructed energy spectra were used to estimate the effective atomic number (Z_{eff}) and density (ρ) of the material, and to classify the materials as explosive or inert. Relationships between the number of counts in the reconstructed spectrum between 10-15 keV and Z_{eff}, and 40-45 keV and ρ, were derived using a simulated data set. Using these relationships, thresholds for explosive materials were derived and the Z_{eff} and ρ of the experimentally tested materials was estimated.

The Z_{eff} of all experimentally tested materials was calculated to within $0.5Z_{eff}$ and 0.12 $\mathrm{g\,cm^{-3}}$ of the data sheet value. In the explosives material range this was improved to $0.1Z_{eff}$ and 0.04 $\mathrm{g\,cm^{-3}}$. Both explosive simulant materials were identified to a greater than

95% confidence level. Further analysis of the simulated data suggested a maximum true positive detection rate of 100% and a 7% false positive detection rate. These results demonstrated material identification is possible to high accuracy without the use of energy-resolving detectors which previous studies had relied upon. The result is a substantial improvement on the basic organic/inorganic material separation that is currently achievable on commercial backscatter systems.

The study successfully demonstrated improved identification of materials under a particular set of conditions. Next stages in development should focus on investigating a wider range of experimental conditions such as variable sample thickness and variable source-to-object distances. Improvements to the existing technique such as more regular calibrations, algorithm development and the use of different thicknesses of filter should also be investigated to optimise the technique. Future experiments using 200 keV x-ray beams with single and multiple detectors should also be performed to further understand how the technique could be scaled up for eventual use on field backscatter systems.

Appendix A

Simulation validation by spectrum comparison

The following appendix contains all the spectra used for validation of the full geometry simulation discussed in Section 6.4. The materials POM, HDPE, Nylon and PVC were used for validation. Simulated and experimental spectra were compared for all ten filter measurements and one unfiltered measurement for all materials.

A.1 POM

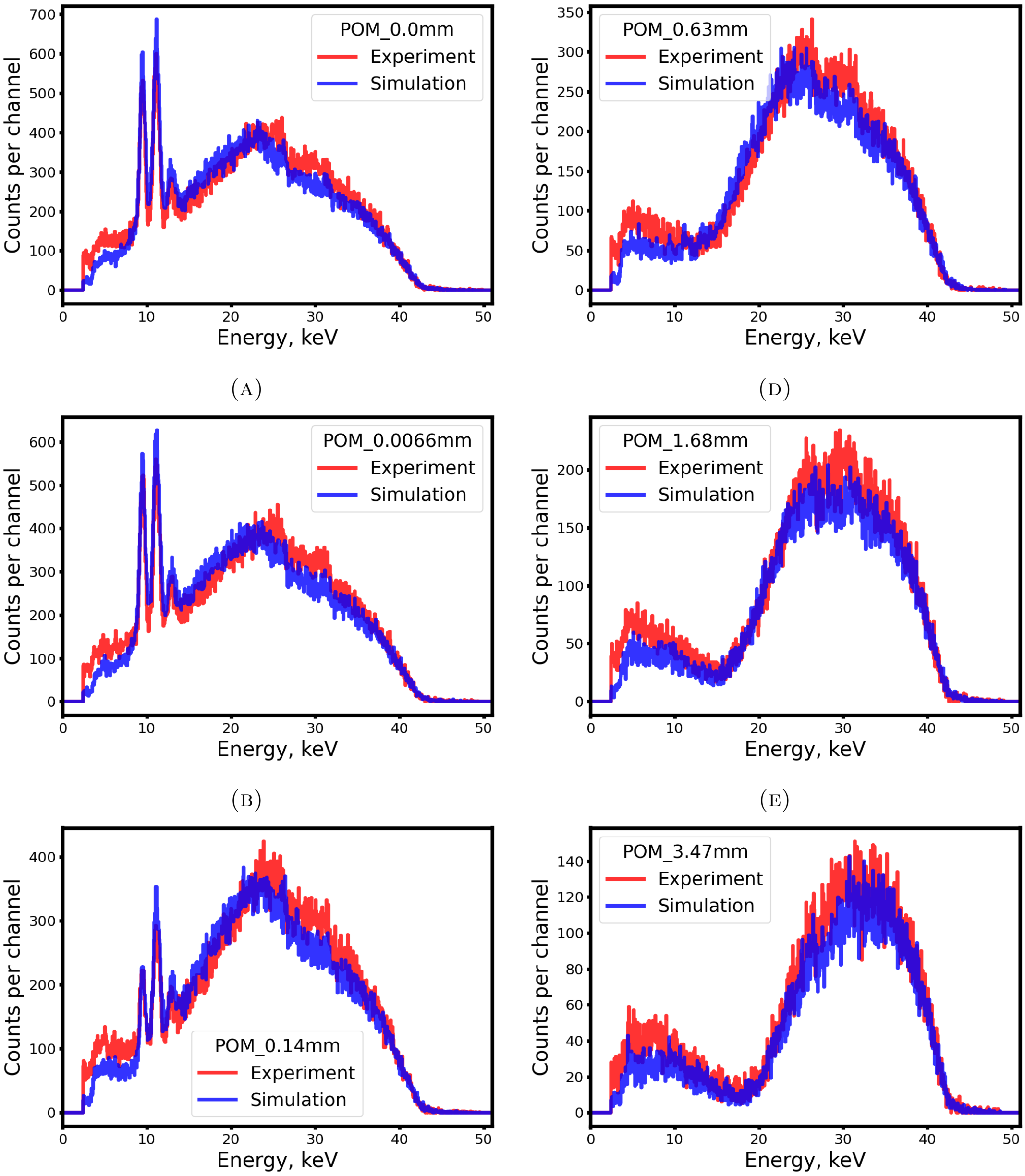

(A) (D) (B) (E) (C) (F)

FIGURE A.1: Simulation and experiment comparisons for 10 mm POM. Figures shown are (A) No filter, (B) Filter A (0.0066 mm), (C) Filter B (0.14 mm), (D) Filter C (0.63 mm), (E) Filter D (1.68 mm) and (F) Filter E (3.47 mm).

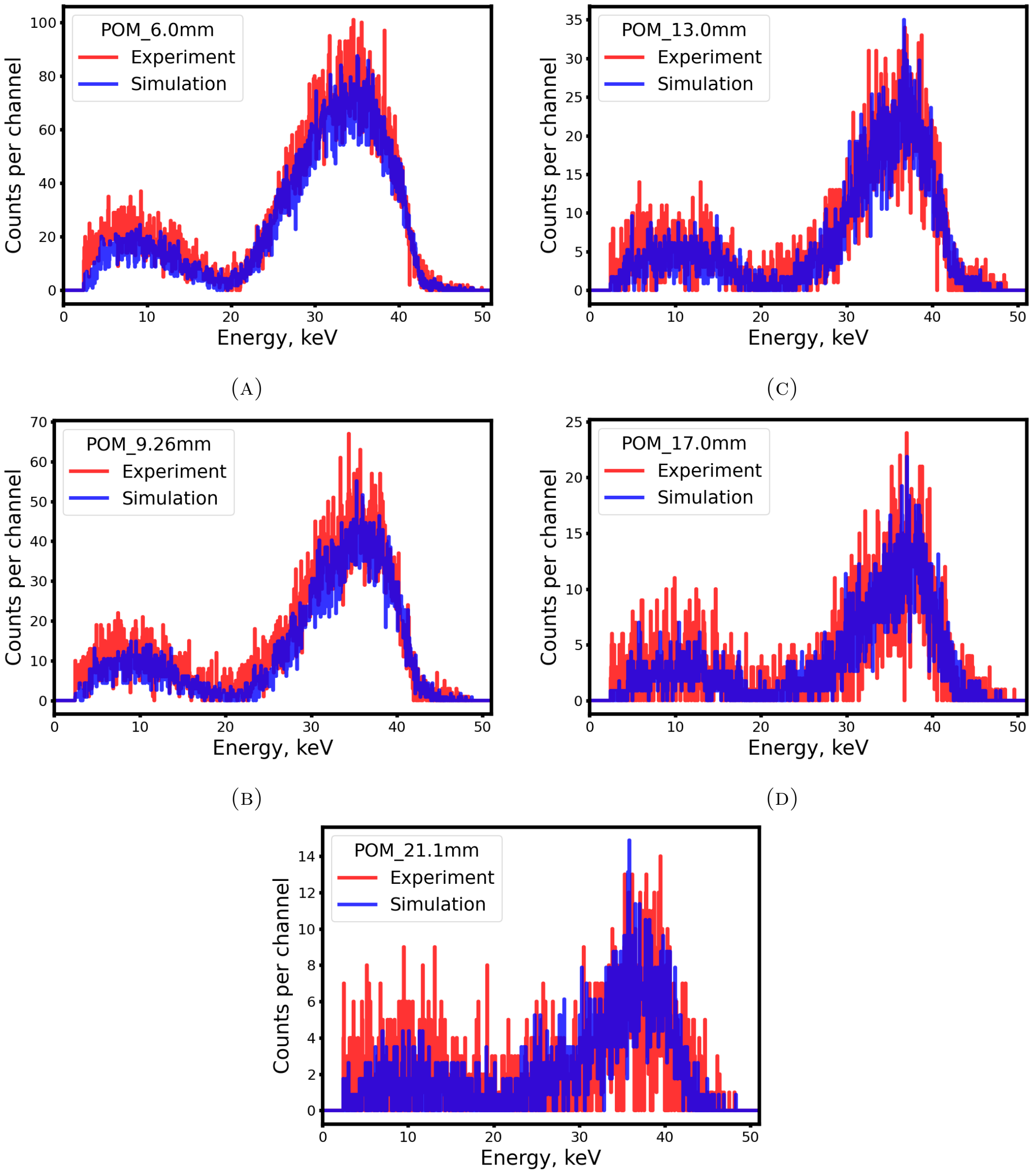

(A) (C)

(B) (D)

(E)

Figure A.2: Simulation and experiment comparisons for 10 mm POM. Figures shown are (A) Filter F (6.0 mm), (B) Filter G (9.26 mm), (C) Filter H (13.0 mm), (D) Filter I (17.0 mm) and (E) Filter J (21.1 mm).

A.2 HDPE

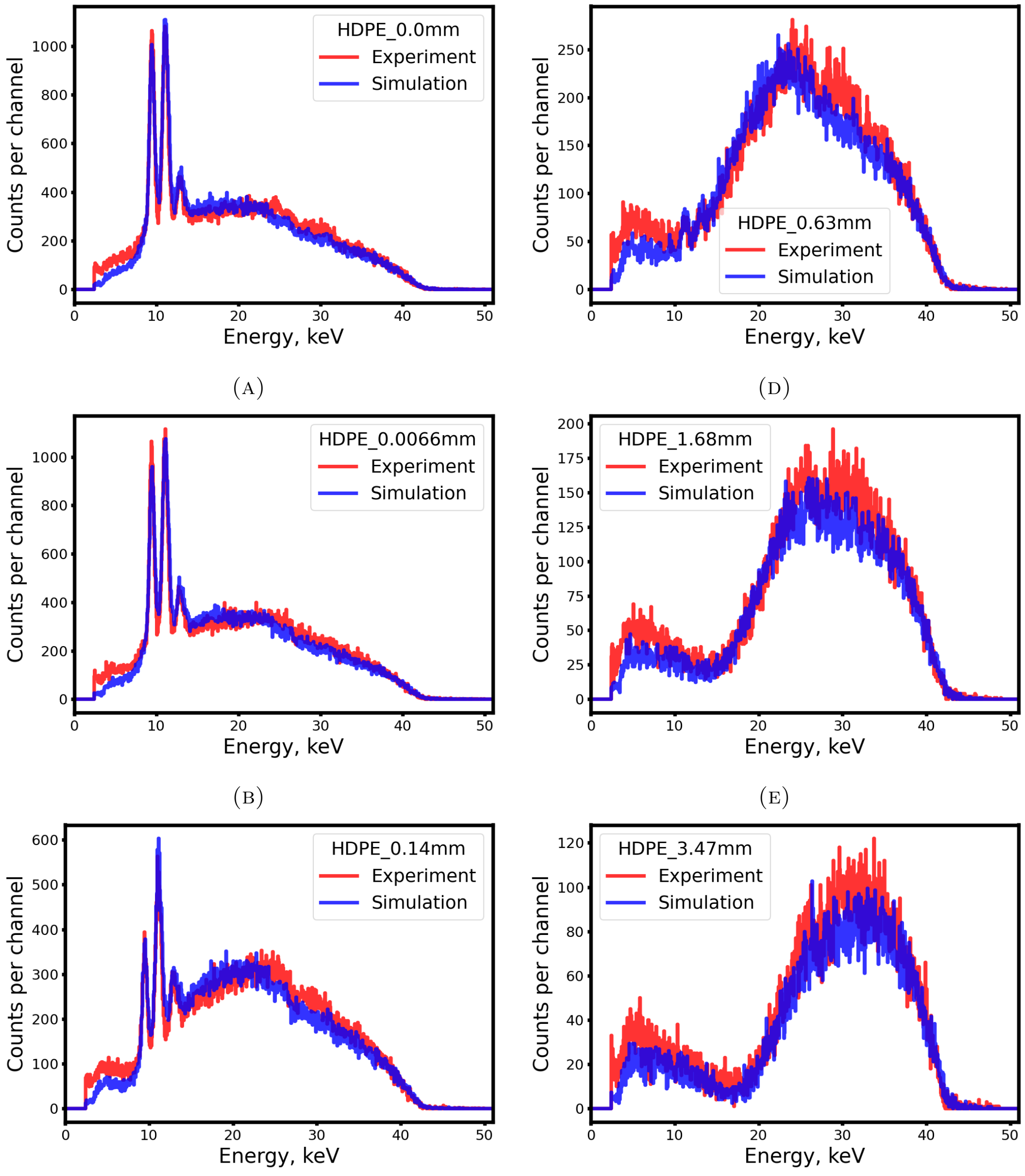

(A) (D)

(B) (E)

(C) (F)

FIGURE A.3: Simulation and experiment comparisons for 10 mm HDPE. Figures shown are (A) No filter, (B) Filter A (0.0066 mm), (C) Filter B (0.14 mm), (D) Filter C (0.63 mm), (E) Filter D (1.68 mm) and (F) Filter E (3.47 mm).

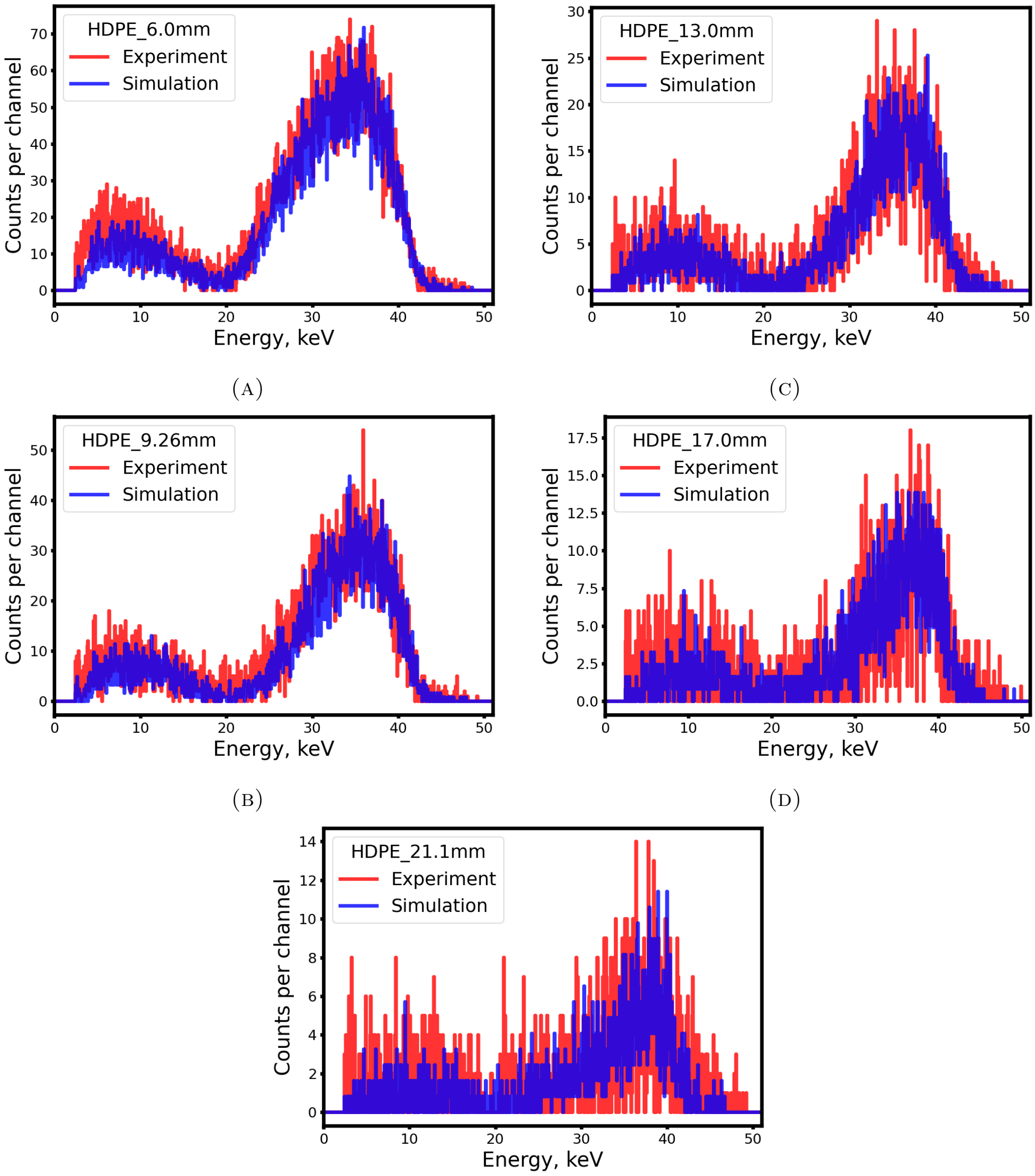

(A)

(C)

(B)

(D)

(E)

Figure A.4: Simulation and experiment comparisons for 10 mm HDPE. Figures shown are (A) Filter F (6.0 mm), (B) Filter G (9.26 mm), (C) Filter H (13.0 mm), (D) Filter I (17.0 mm) and (E) Filter J (21.1 mm).

A.3 Nylon

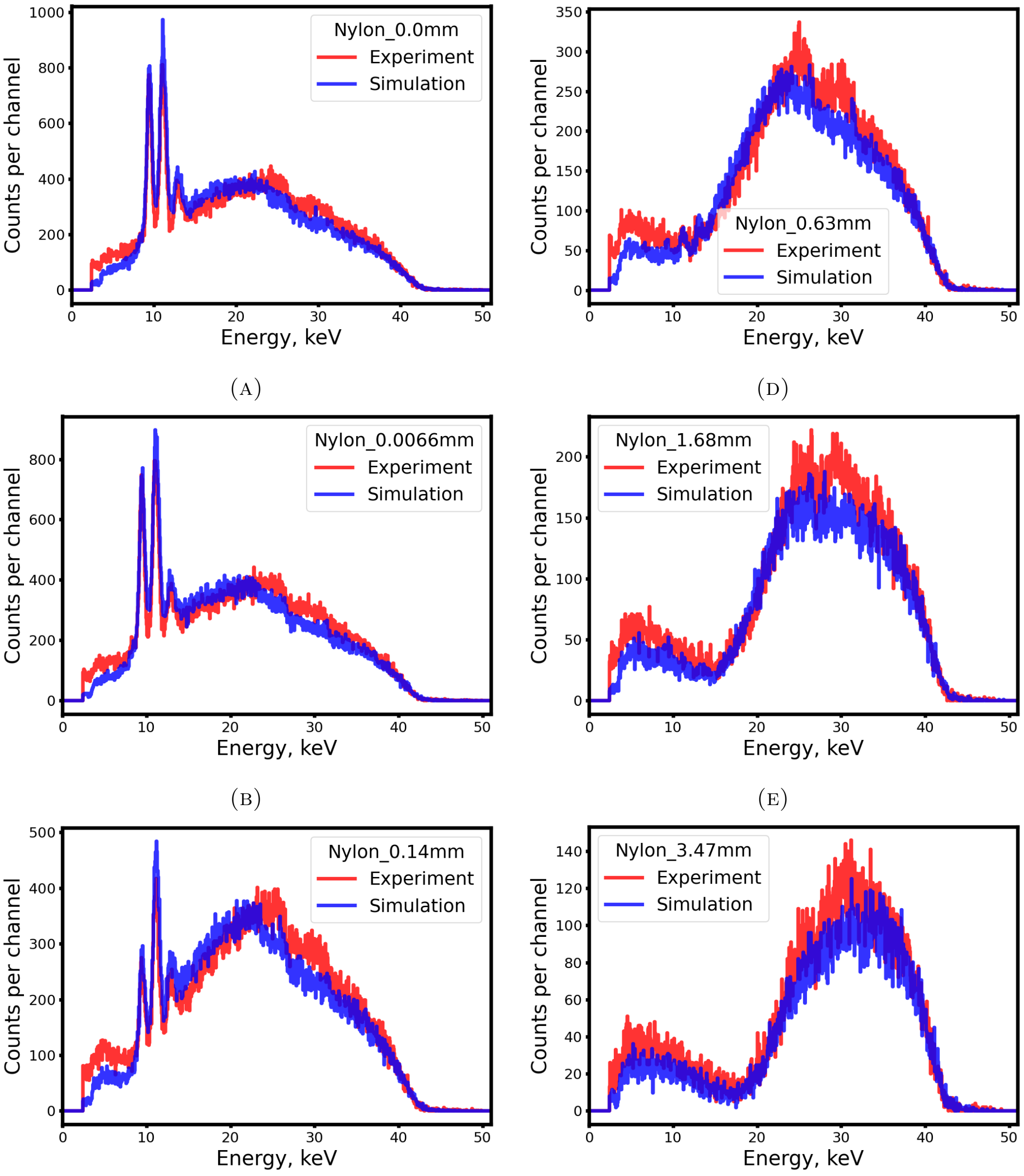

(A) (D)

(B) (E)

(C) (F)

FIGURE A.5: Simulation and experiment comparisons for 10 mm Nylon. Figures shown are (A) No filter, (B) Filter A (0.0066 mm), (C) Filter B (0.14 mm), (D) Filter C (0.63 mm), (E) Filter D (1.68 mm) and (F) Filter E (3.47 mm).

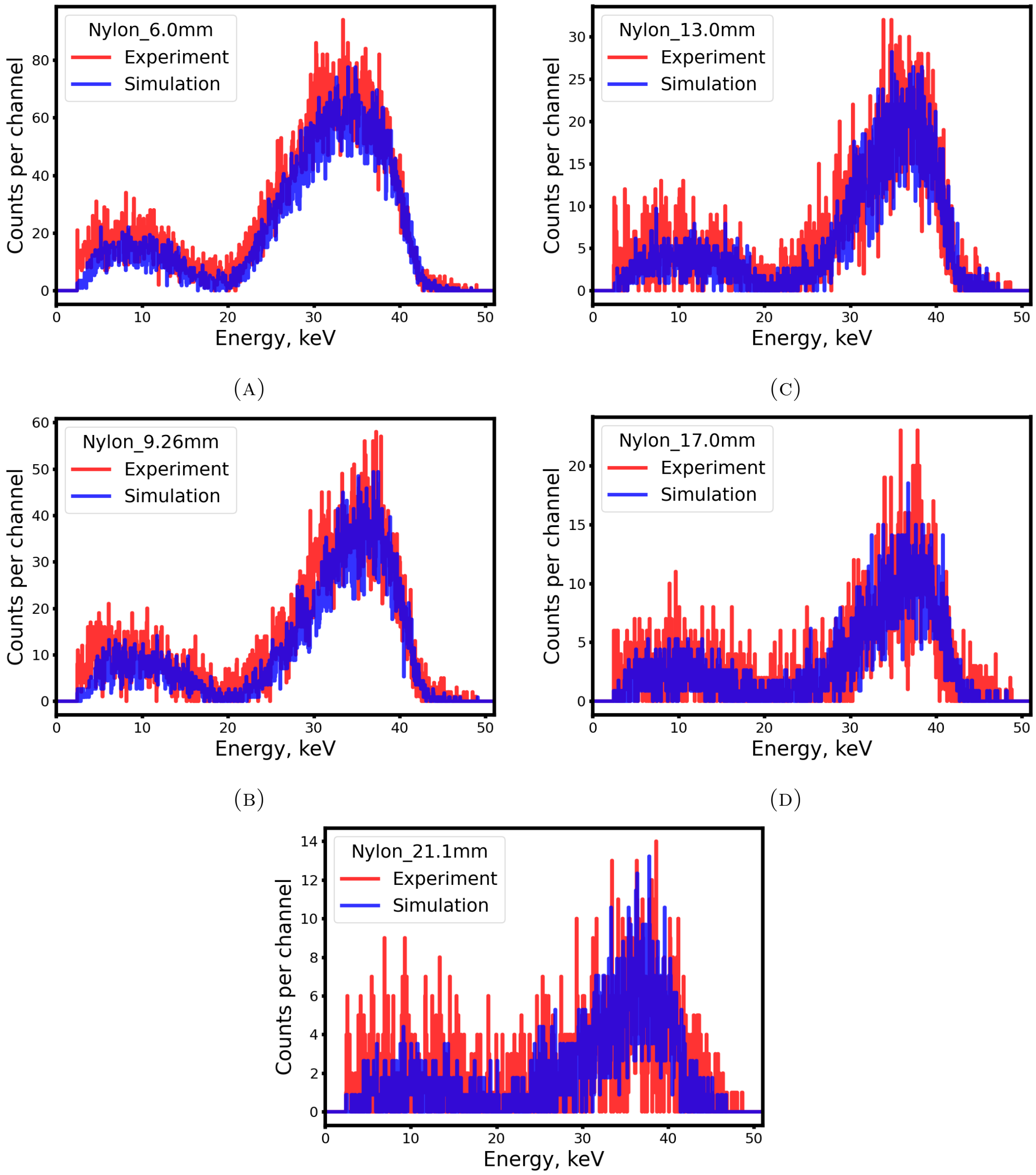

(A) (C)

(B) (D)

(E)

Figure A.6: Simulation and experiment comparisons for 10 mm Nylon. Figures shown are (A) Filter F (6.0 mm), (B) Filter G (9.26 mm), (C) Filter H (13.0 mm), (D) Filter I (17.0 mm) and (E) Filter J (21.1 mm).

A.4 PVC

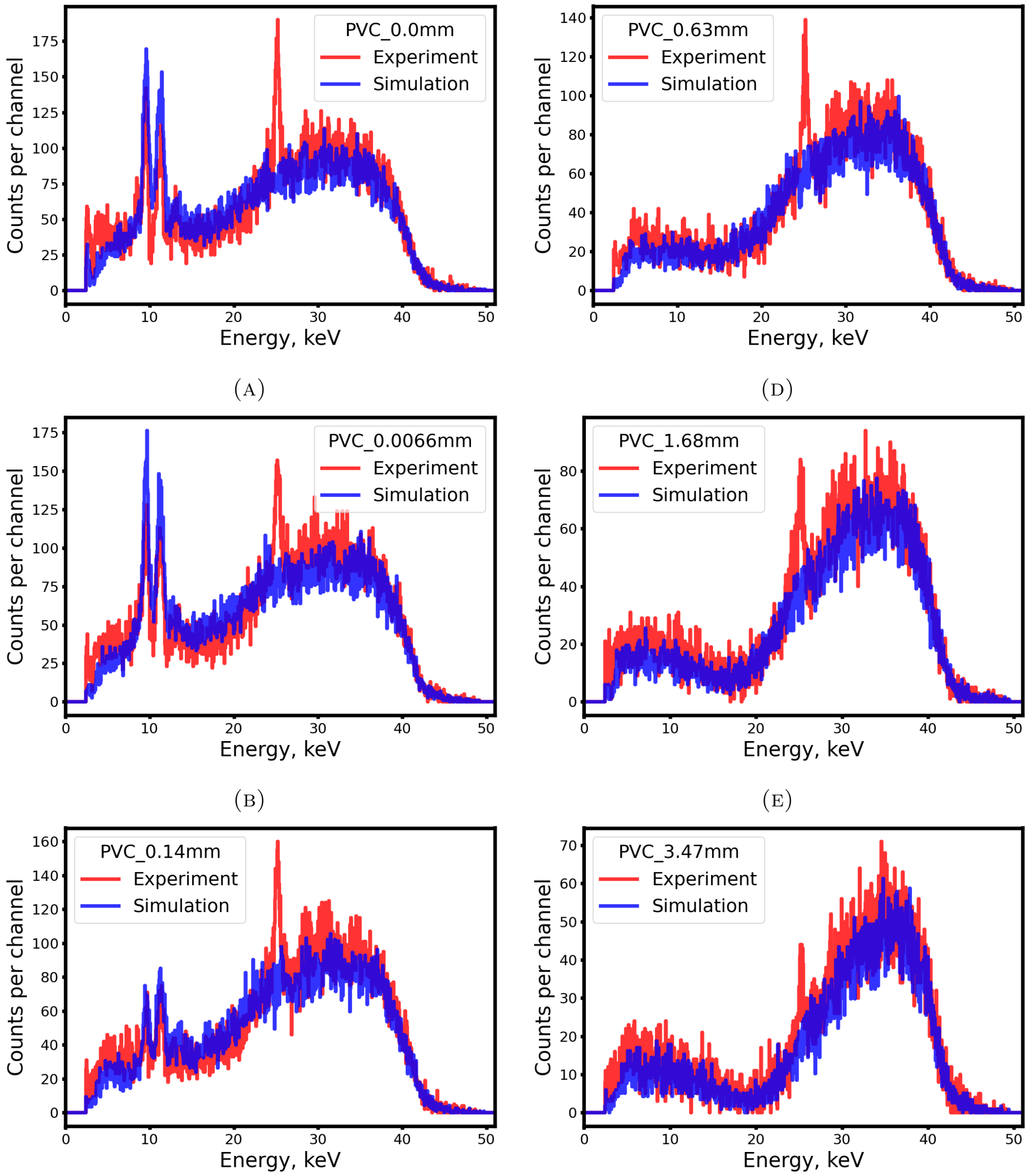

(A) (D)

(B) (E)

(C) (F)

FIGURE A.7: Simulation and experiment comparisons for 10 mm PVC. Figures shown are (A) No filter, (B) Filter A (0.0066 mm), (C) Filter B (0.14 mm), (D) Filter C (0.63 mm), (E) Filter D (1.68 mm) and (F) Filter E (3.47 mm).

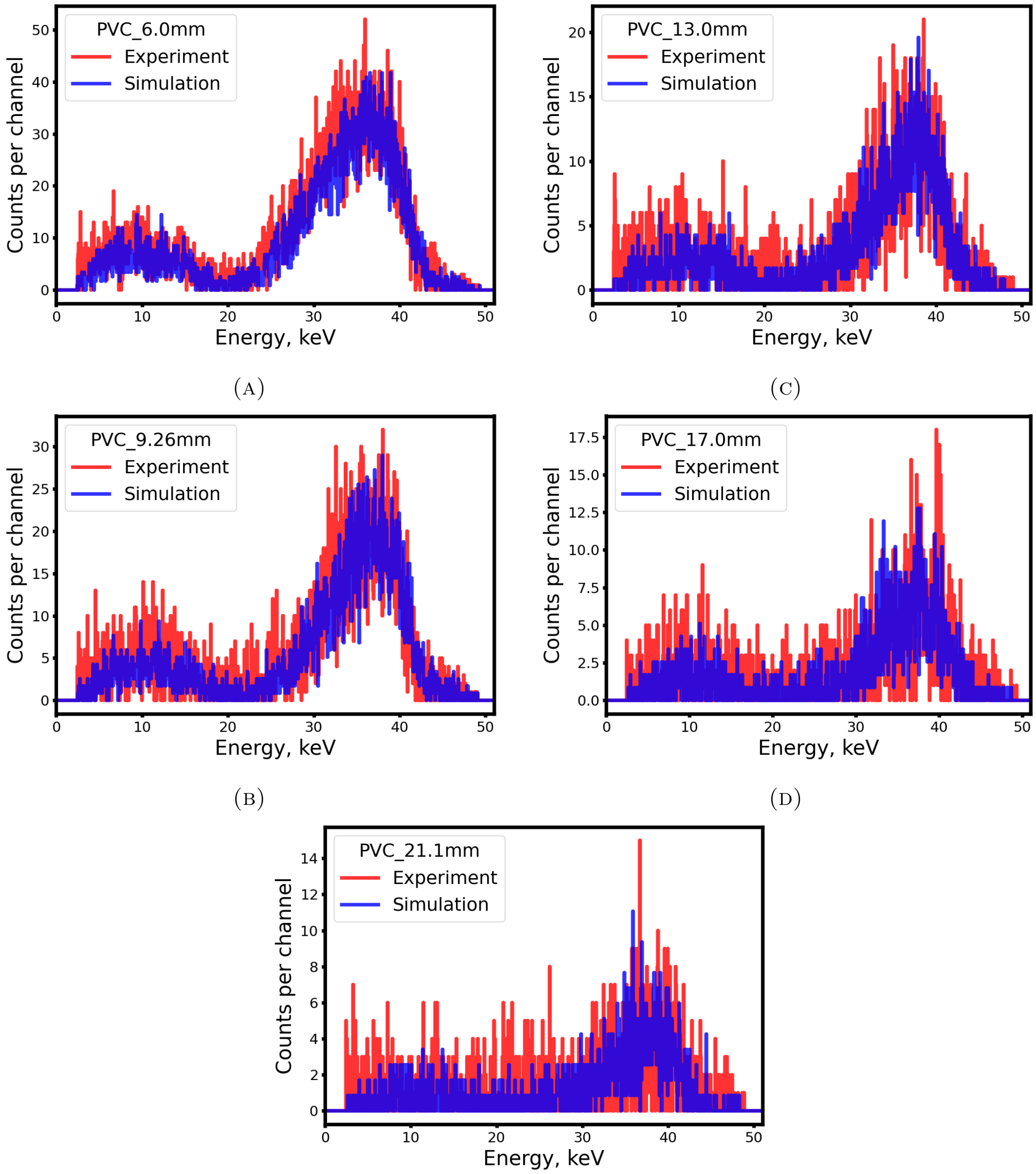

(A)

(C)

(B)

(D)

(E)

FIGURE A.8: Simulation and experiment comparisons for 10 mm PVC. Figures shown are (A) Filter F (6.0 mm), (B) Filter G (9.26 mm), (C) Filter H (13.0 mm), (D) Filter I (17.0 mm) and (E) Filter J (21.1 mm).

This page is intentionally left blank.

Appendix B

Experiment CdTe spectra and response measurements

This appendix gives the raw CdTe spectra and detector response measurements for all experimentally tested materials. The detector response measurement was acquired by integrating the spectrum as discussed in Section 5.5.2. The detector response measurements were used to reconstruct the experimental energy spectra as discussed in Figure 7.4. Also included are the spectra and response measurements for Acrylic and Nylon. These were used as calibration measurements on the two experimental days and were used to calculate the RCF as discussed in Section 5.7. The detector response measurements for each material are given in Table B.1 at the end of this appendix.

B.1 HDPE

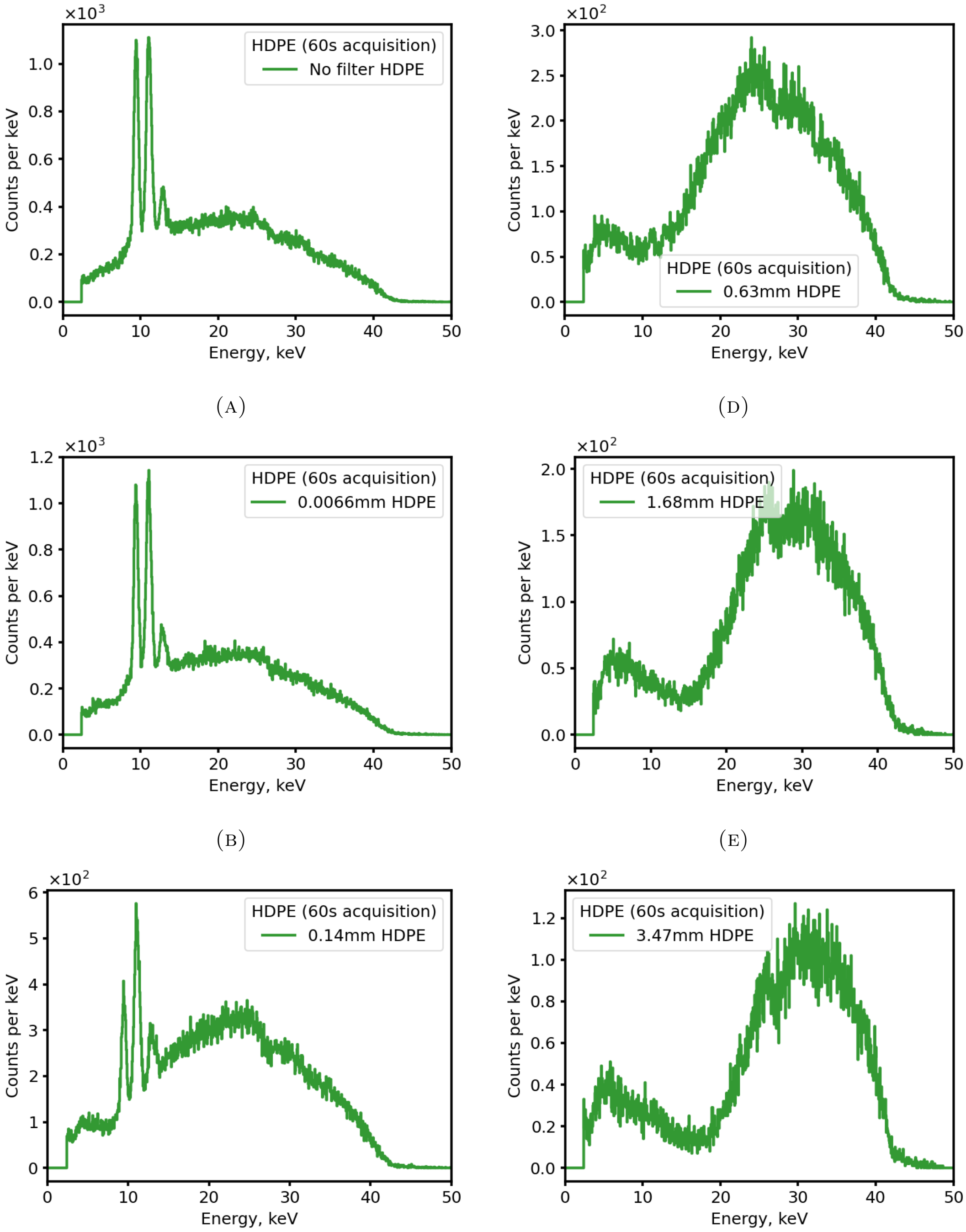

(A) (D)

(B) (E)

(C) (F)

FIGURE B.1: Experimental CdTe spectra for 10 mm HDPE. Figures shown are (A) No filter, (B) Filter A (0.0066 mm), (C) Filter B (0.14 mm), (D) Filter C (0.63 mm), (E) Filter D (1.68 mm) and (F) Filter E (3.47 mm).

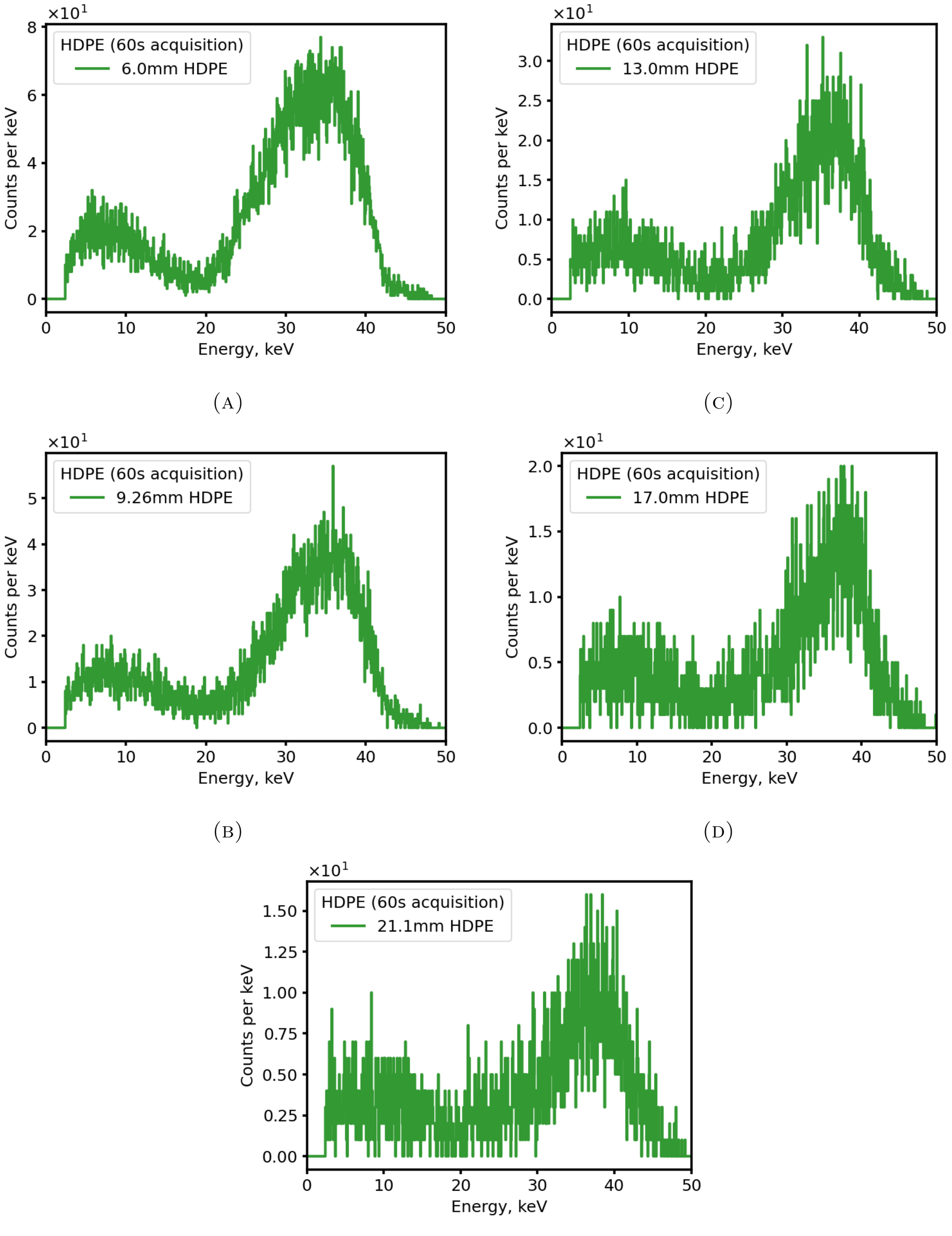

(A)

(C)

(B)

(D)

(E)

Figure B.2: Experimental CdTe spectra for 10 mm HDPE. Figures shown are (A) Filter F (6.0 mm), (B) Filter G (9.26 mm), (C) Filter H (13.0 mm), (D) Filter I (17.0 mm) and (E) Filter J (21.1 mm).

B.2 POM

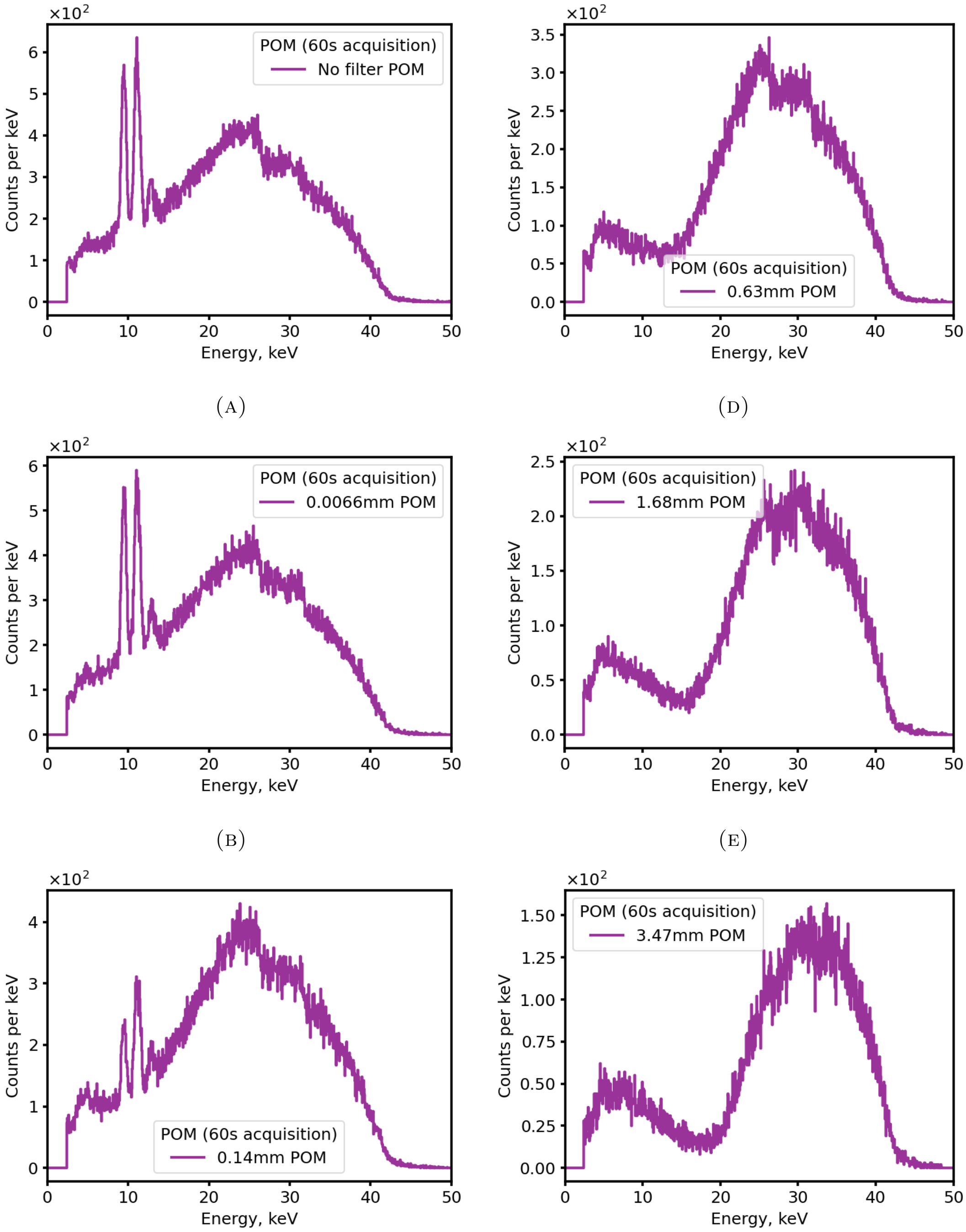

(A)

(D)

(B)

(E)

(C)

(F)

FIGURE B.3: Experimental CdTe spectra for 10 mm POM. Figures shown are (A) No filter, (B) Filter A (0.0066 mm), (C) Filter B (0.14 mm), (D) Filter C (0.63 mm), (E) Filter D (1.68 mm) and (F) Filter E (3.47 mm).

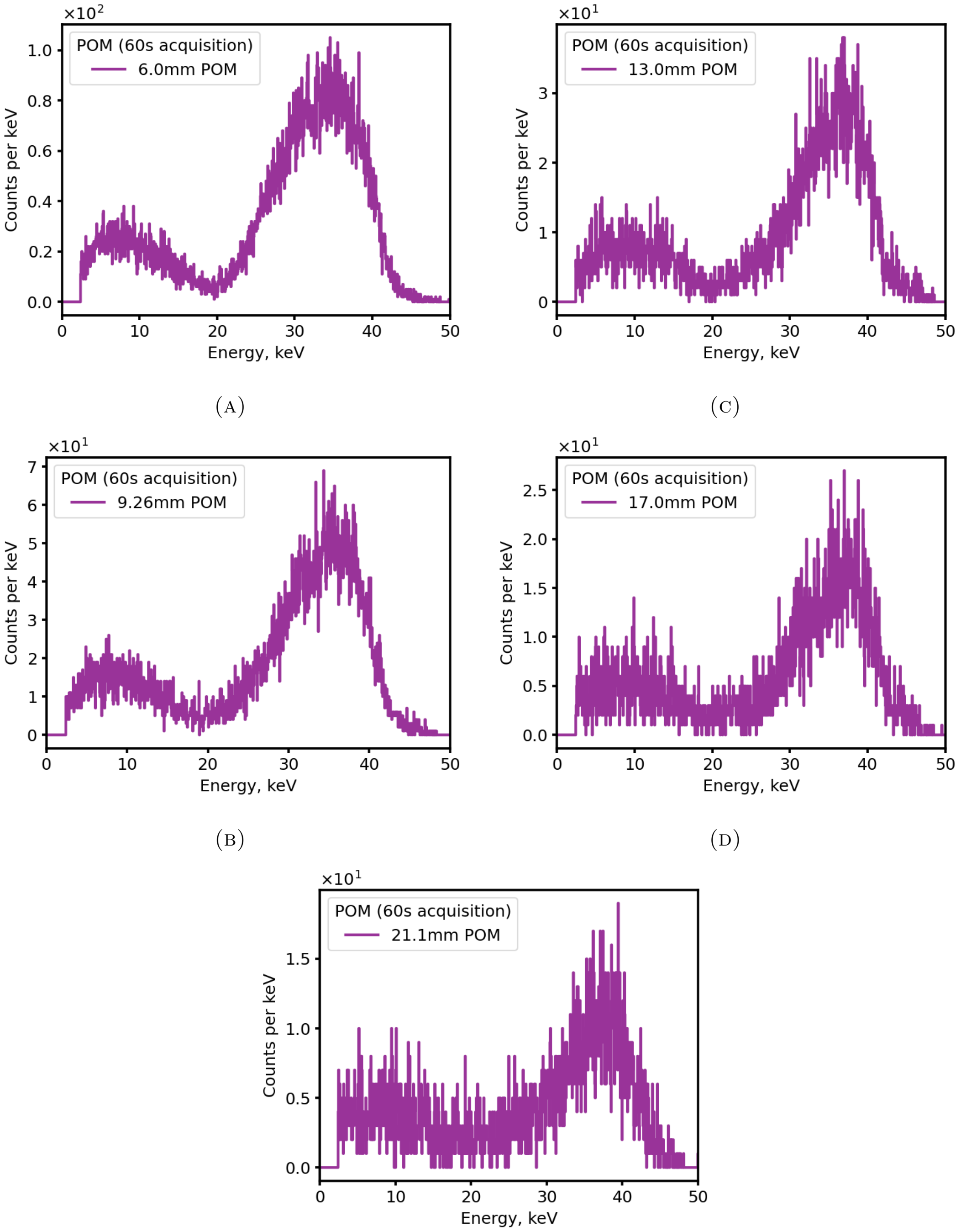

(A) (C)

(B) (D)

(E)

FIGURE B.4: Experimental CdTe spectra for 10 mm POM. Figures shown are (A) Filter F (6.0 mm), (B) Filter G (9.26 mm), (C) Filter H (13.0 mm), (D) Filter I (17.0 mm) and (E) Filter J (21.1 mm).

B.3 PVC

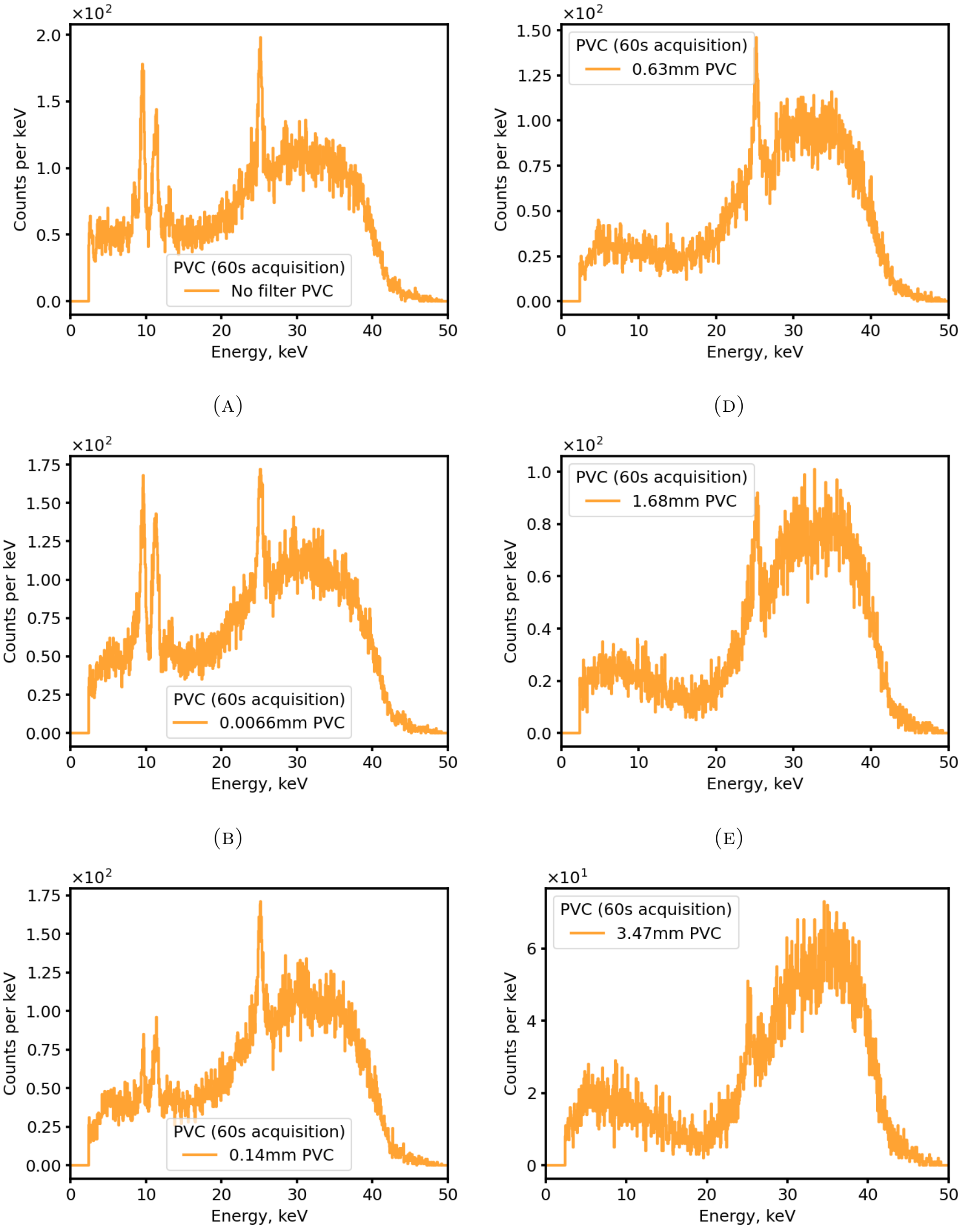

(A) (D)

(B) (E)

(C) (F)

FIGURE B.5: Experimental CdTe spectra for 10 mm PVC. Figures shown are (A) No filter, (B) Filter A (0.0066 mm), (C) Filter B (0.14 mm), (D) Filter C (0.63 mm), (E) Filter D (1.68 mm) and (F) Filter E (3.47 mm).

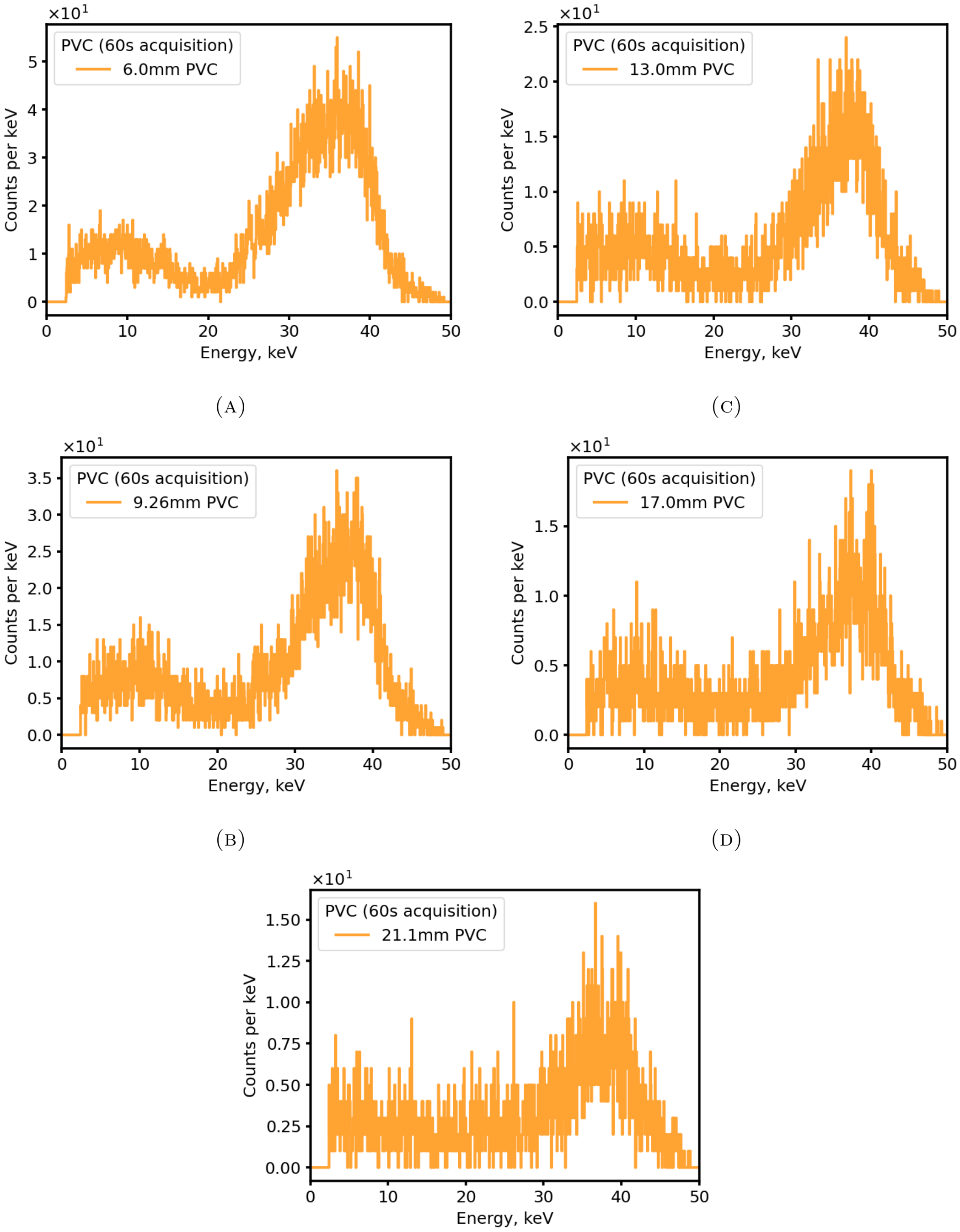

(A) (C)

(B) (D)

(E)

FIGURE B.6: Experimental CdTe spectra for 10 mm PVC. Figures shown are (A) Filter F (6.0 mm), (B) Filter G (9.26 mm), (C) Filter H (13.0 mm), (D) Filter I (17.0 mm) and (E) Filter J (21.1 mm).

B.4 PVDF

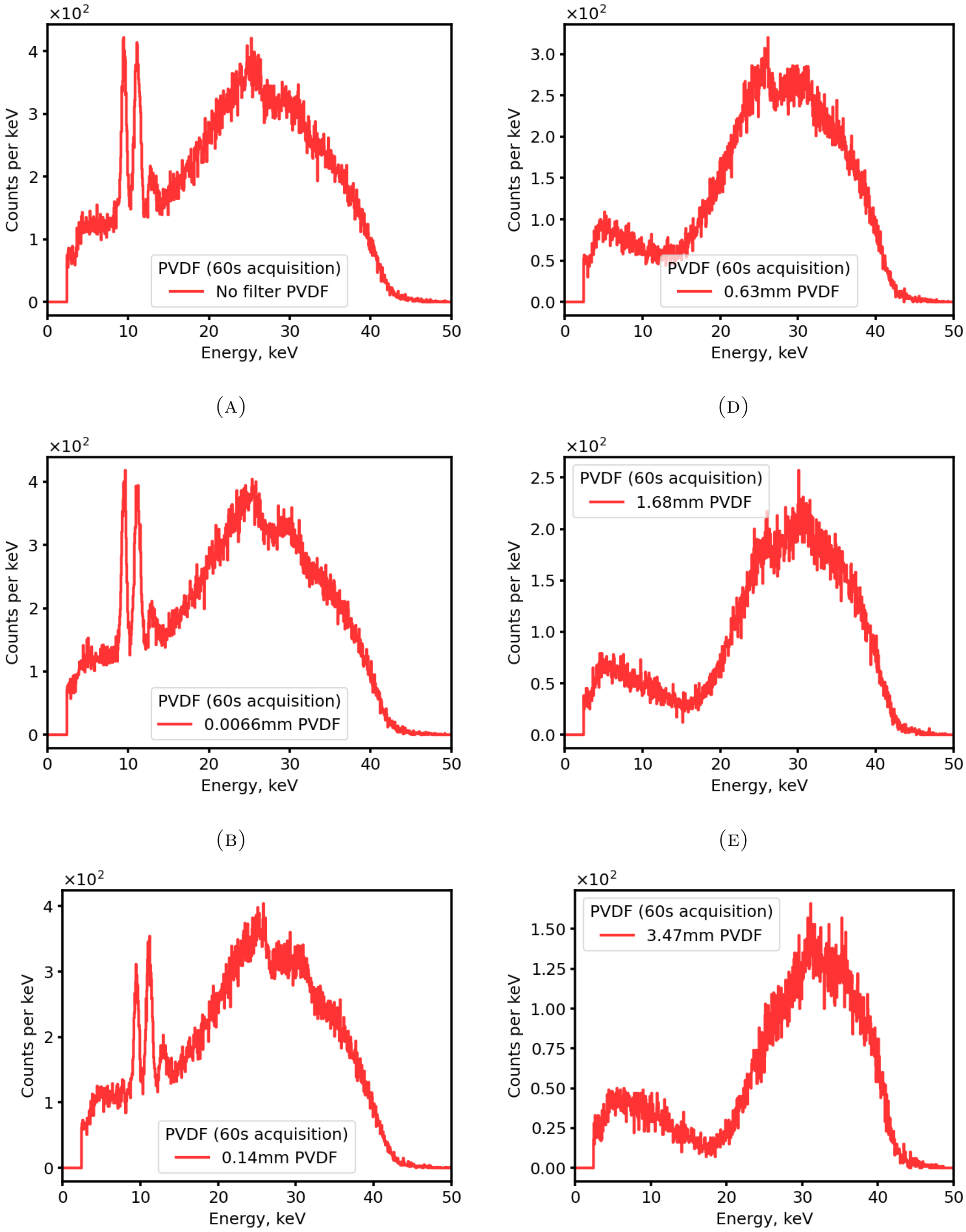

(A) (D)

(B) (E)

(C) (F)

Figure B.7: Experimental CdTe spectra for 10 mm PVDF. Figures shown are (A) No filter, (B) Filter A (0.0066 mm), (C) Filter B (0.14 mm), (D) Filter C (0.63 mm), (E) Filter D (1.68 mm) and (F) Filter E (3.47 mm).

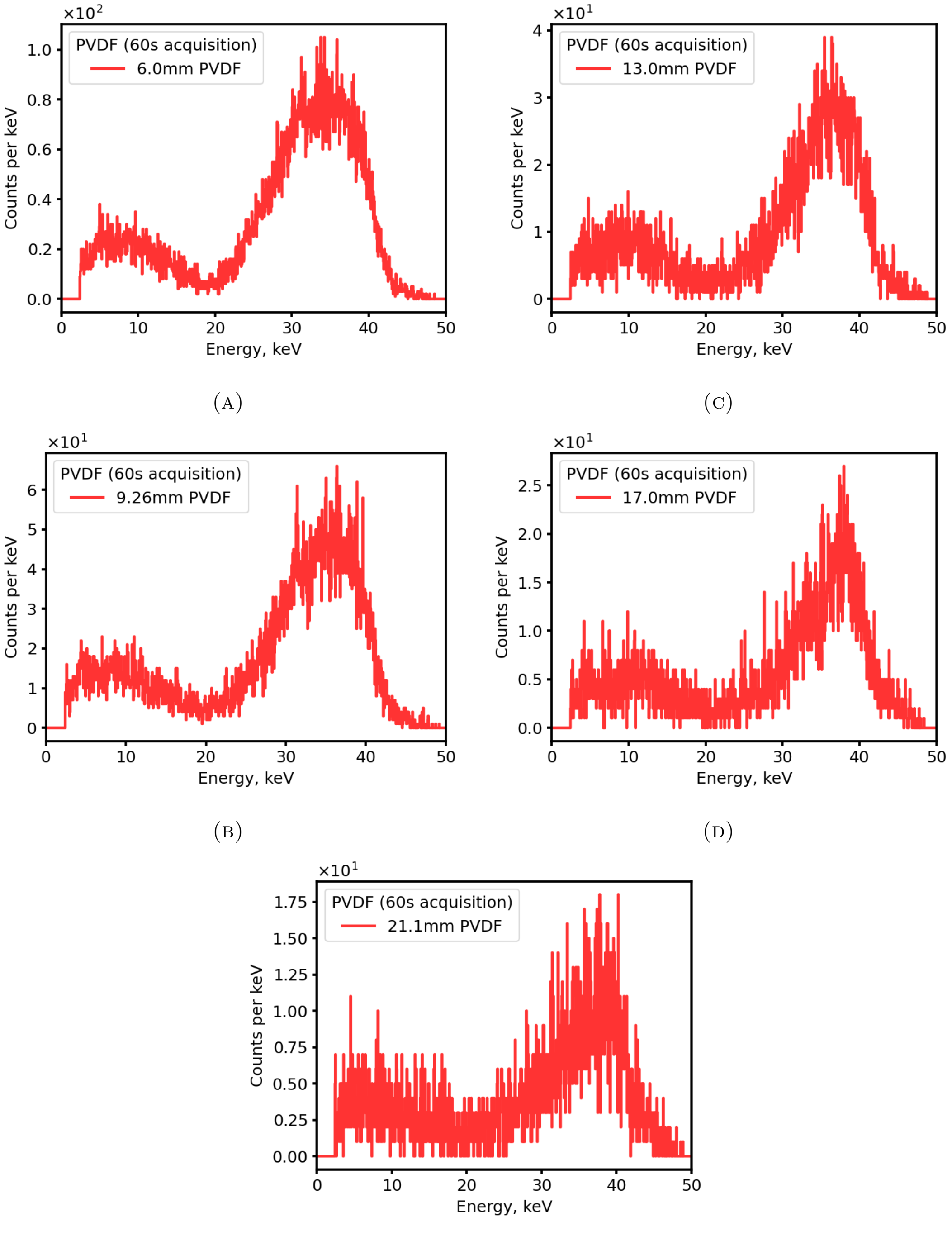

(A)

(C)

(B)

(D)

(E)

FIGURE B.8: Experimental CdTe spectra for 10 mm PVDF. Figures shown are (A) Filter F (6.0 mm), (B) Filter G (9.26 mm), (C) Filter H (13.0 mm), (D) Filter I (17.0 mm) and (E) Filter J (21.1 mm).

B.5 PTFE

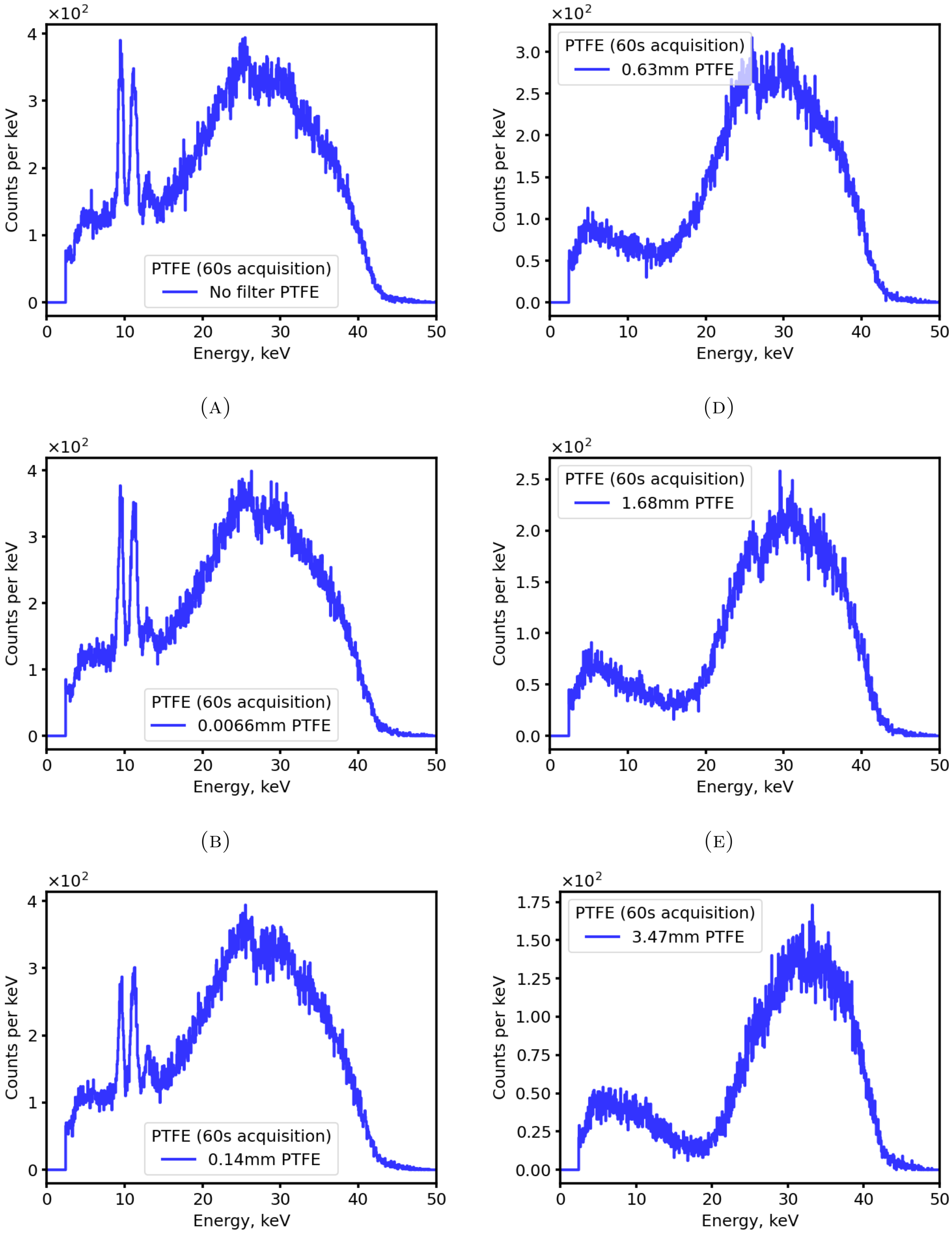

(A) (D)

(B) (E)

(C) (F)

Figure B.9: Experimental CdTe spectra for 10 mm PTFE. Figures shown are (A) No filter, (B) Filter A (0.0066 mm), (C) Filter B (0.14 mm), (D) Filter C (0.63 mm), (E) Filter D (1.68 mm) and (F) Filter E (3.47 mm).

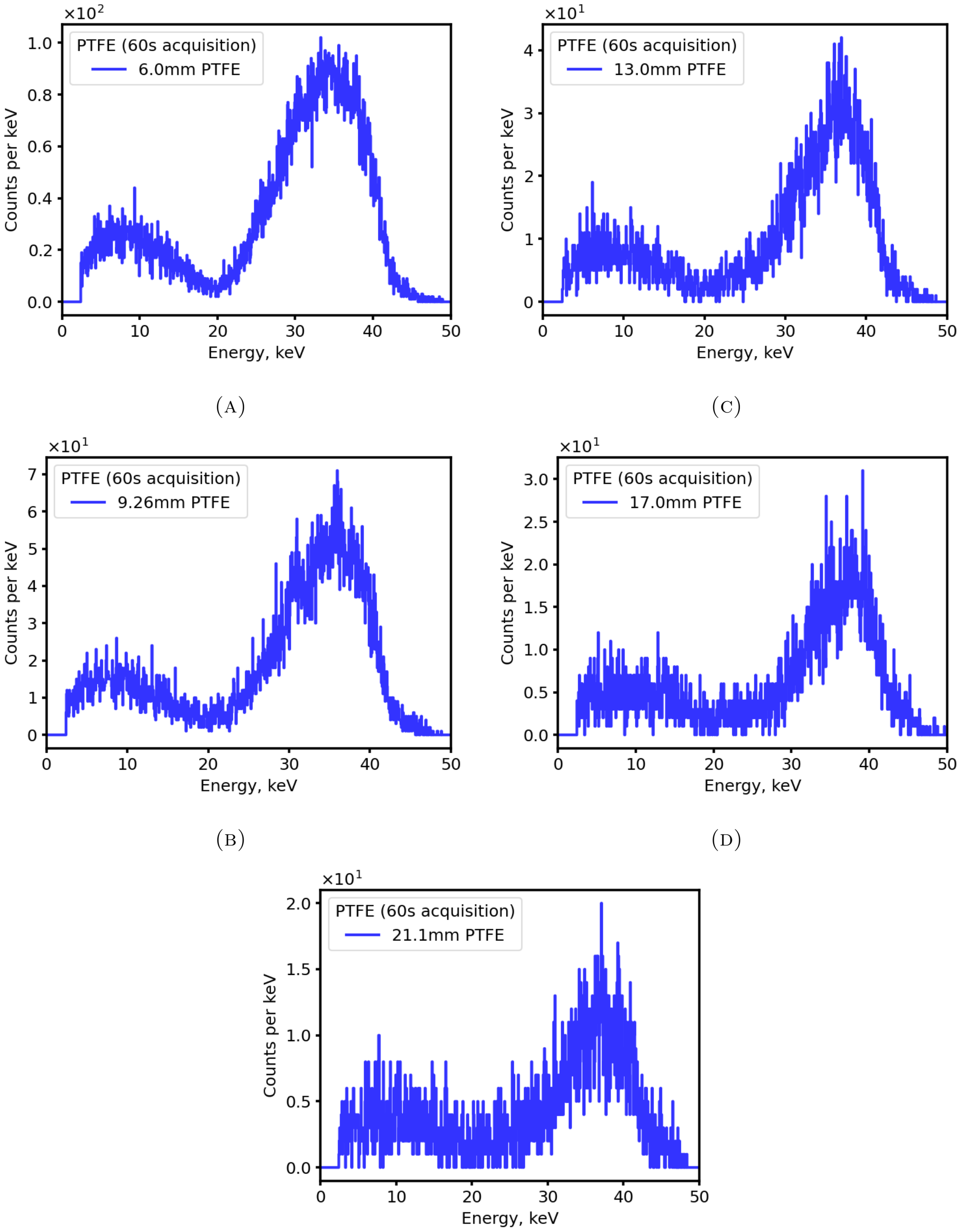

(A) (C)

(B) (D)

(E)

Figure B.10: Experimental CdTe spectra for 10 mm PTFE. Figures shown are (A) Filter F (6.0 mm), (B) Filter G (9.26 mm), (C) Filter H (13.0 mm), (D) Filter I (17.0 mm) and (E) Filter J (21.1 mm).

B.6 Nylon

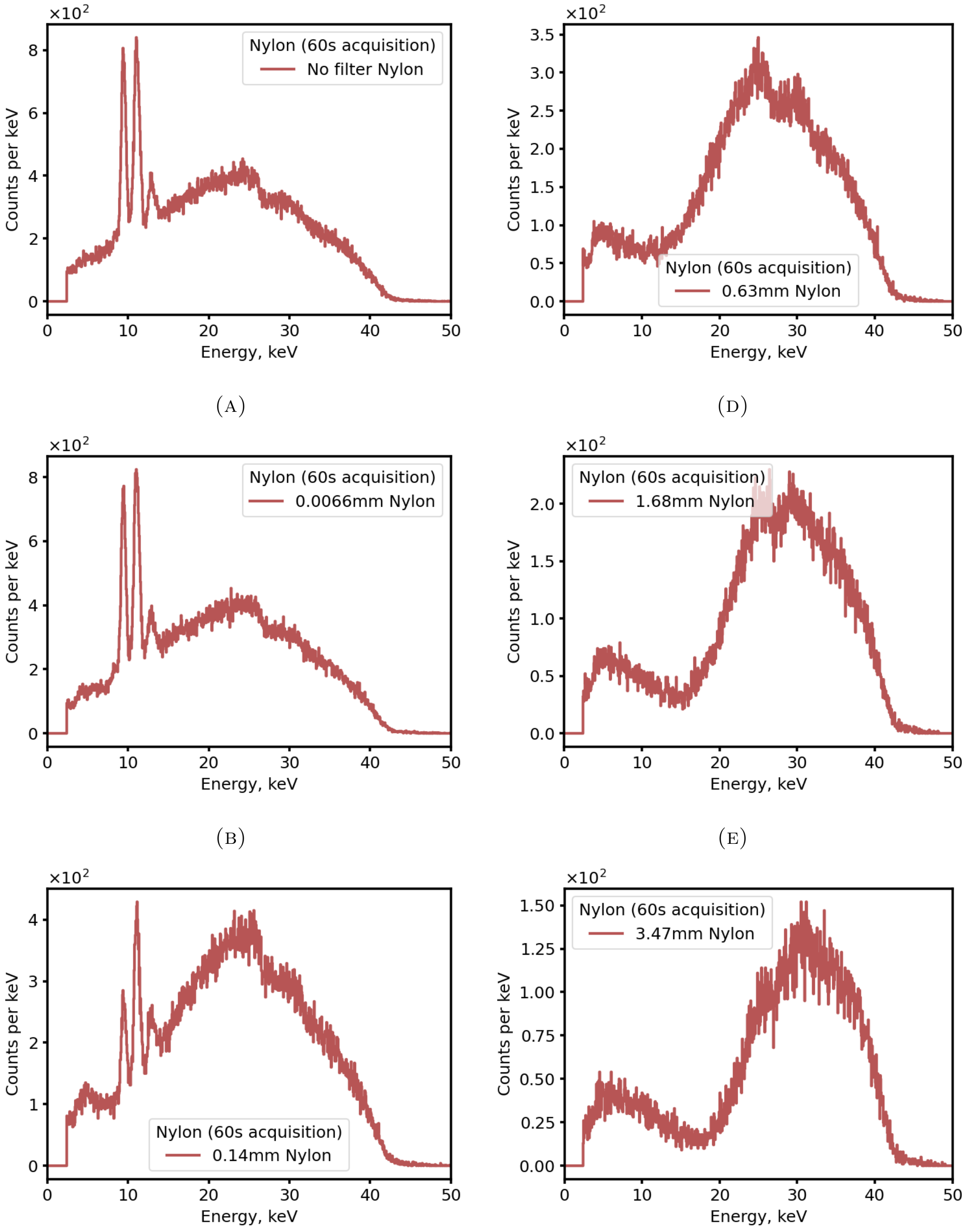

(A)

(D)

(B)

(E)

(C)

(F)

FIGURE B.11: Experimental CdTe spectra for 10 mm Nylon. Figures shown are (A) No filter, (B) Filter A (0.0066 mm), (C) Filter B (0.14 mm), (D) Filter C (0.63 mm), (E) Filter D (1.68 mm) and (F) Filter E (3.47 mm).

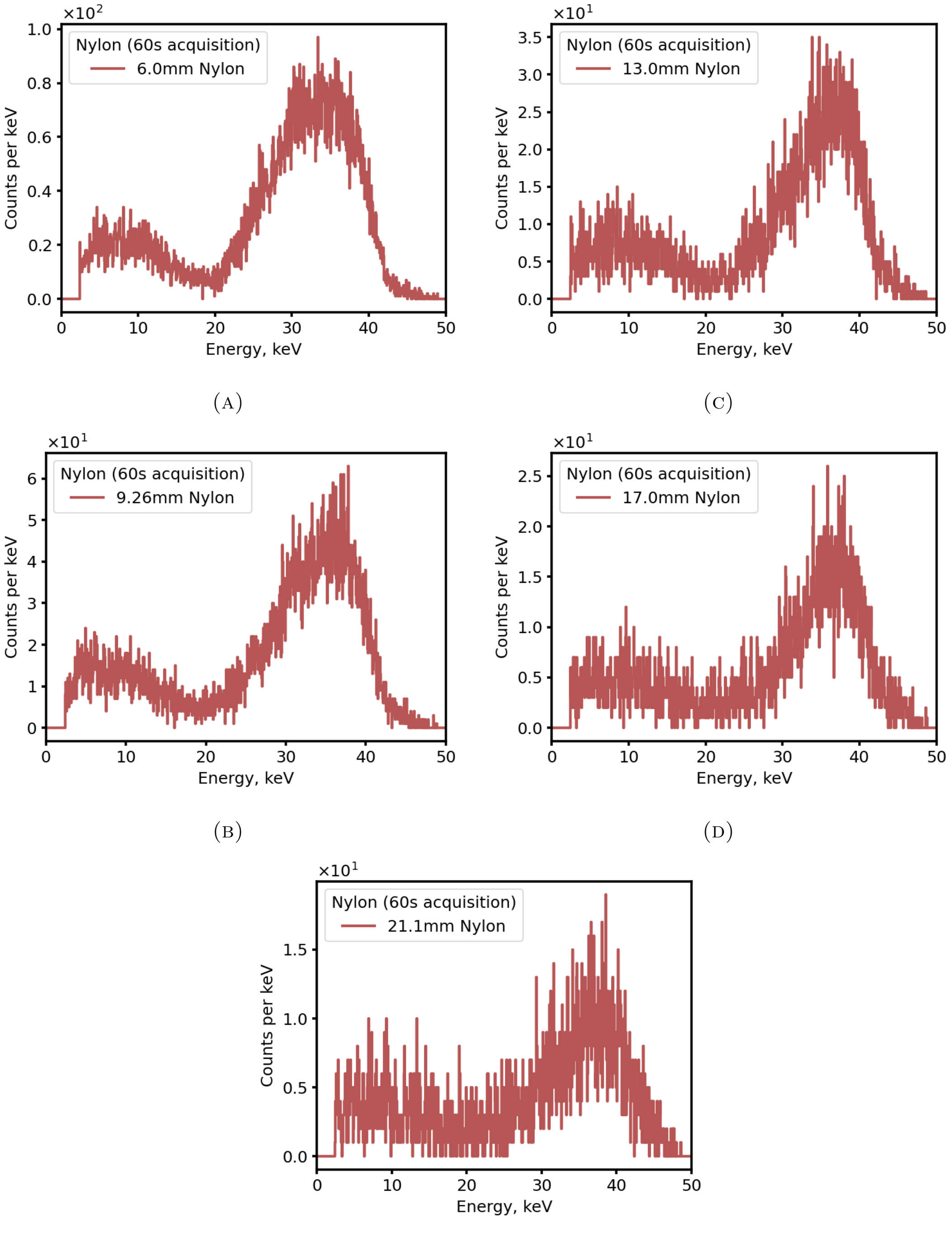

(A) (C)

(B) (D)

(E)

FIGURE B.12: Experimental CdTe spectra for 10 mm Nylon. Figures shown are (A) Filter F (6.0 mm), (B) Filter G (9.26 mm), (C) Filter H (13.0 mm), (D) Filter I (17.0 mm) and (E) Filter J (21.1 mm).

B.7 Acrylic

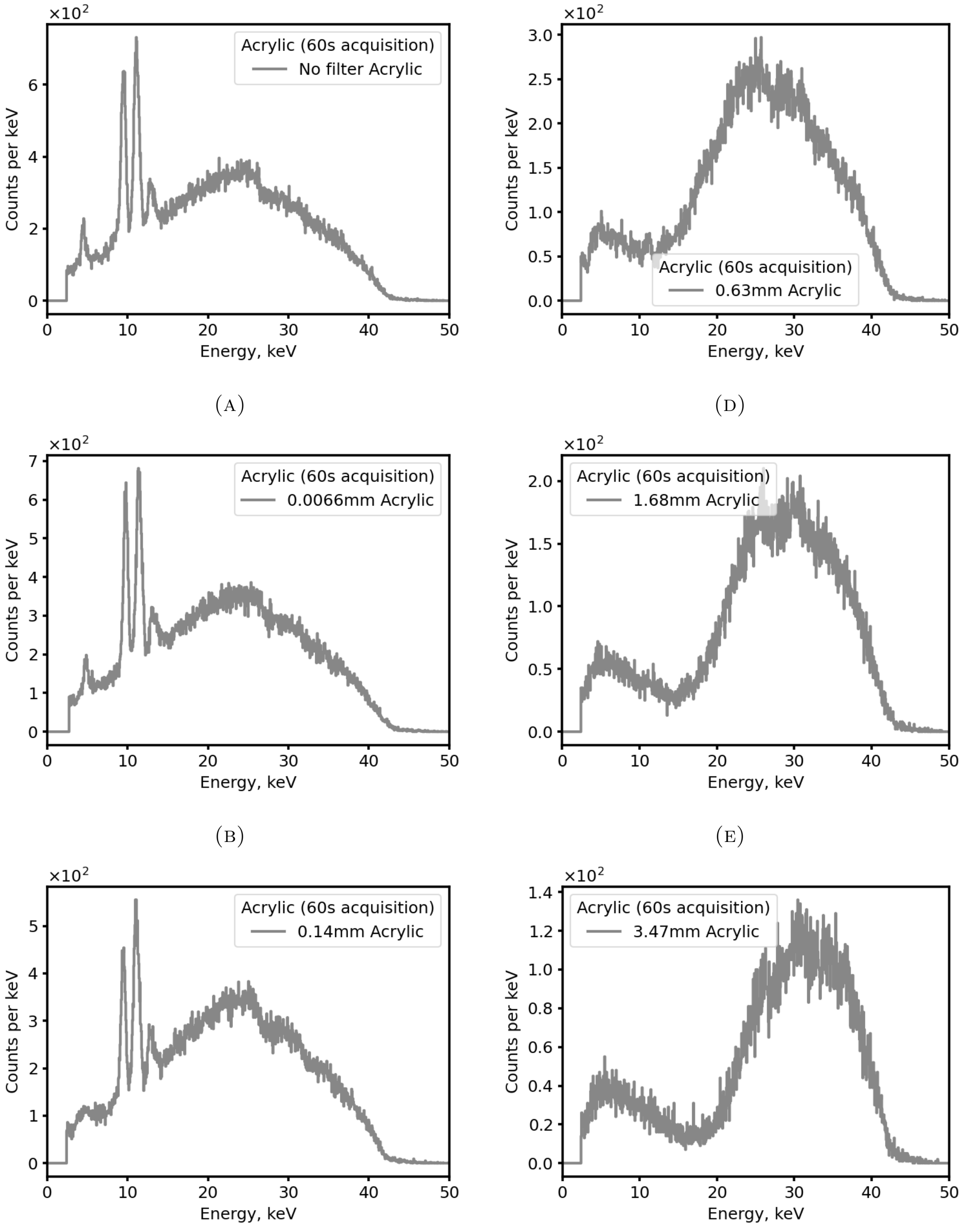

(A) (D)

(B) (E)

(C) (F)

FIGURE B.13: Experimental CdTe spectra for 10 mm Acrylic. Figures shown are (A) No filter, (B) Filter A (0.0066 mm), (C) Filter B (0.14 mm), (D) Filter C (0.63 mm), (E) Filter D (1.68 mm) and (F) Filter E (3.47 mm).

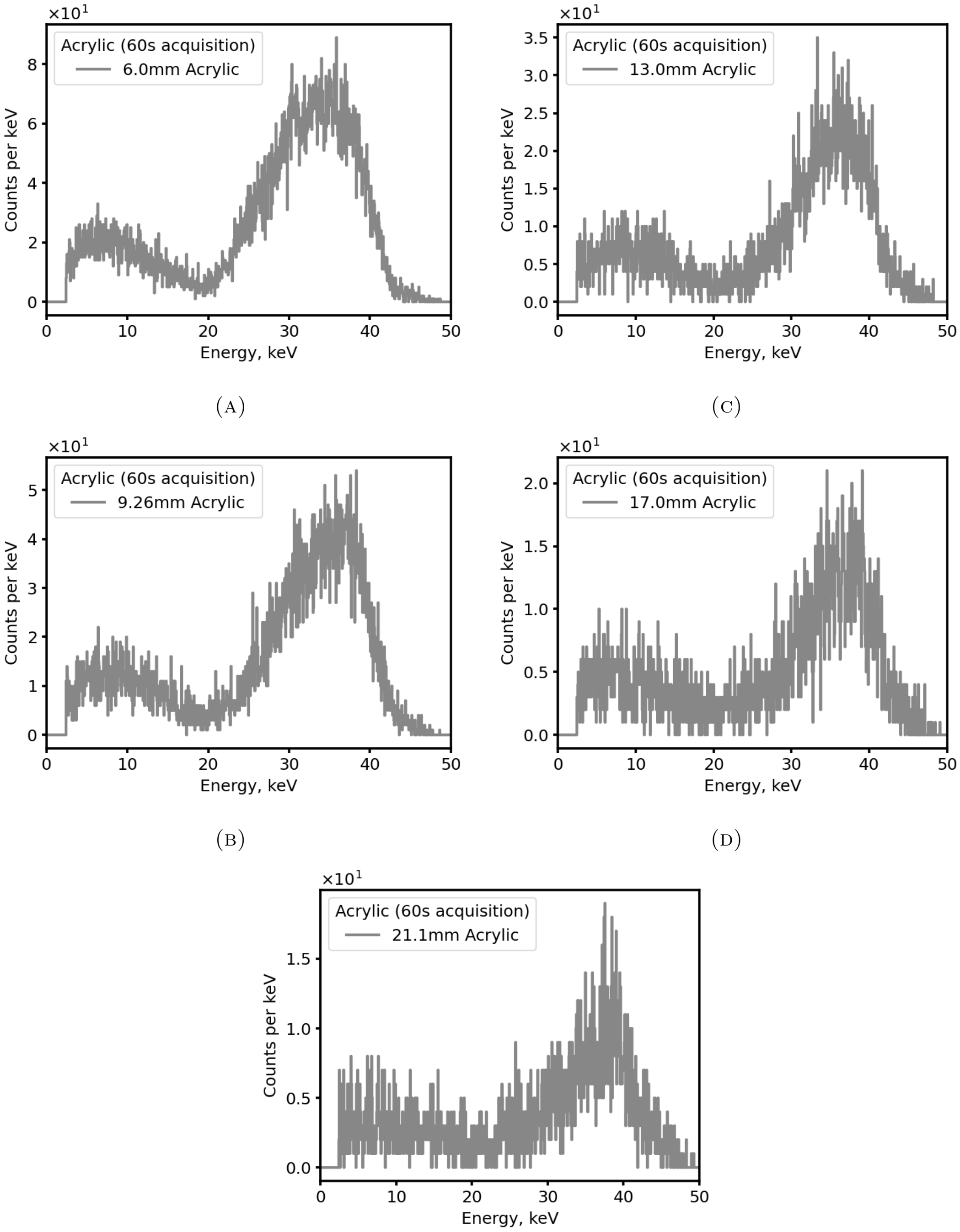

(A) (C)

(B) (D)

(E)

FIGURE B.14: Experimental CdTe spectra for 10 mm Acrylic. Figures shown are (A) Filter F (6.0 mm), (B) Filter G (9.26 mm), (C) Filter H (13.0 mm), (D) Filter I (17.0 mm) and (E) Filter J (21.1 mm).

#	Filter	Detector response, keV counts						
	thickness, mm	HDPE Fig. B.1 & B.2	POM Fig. B.3 & B.4	PVC Fig. B.5 & B.6	PVDF Fig. B.7 & B.8	PTFE Fig. B.9 & B.10	Nylon Fig. B.11 & B.12	Acrylic Fig. B.13 & B.14
-	0.0	4078810 ±10234	4393687 ±11028	1449413 ± 6966	3953920 ±10677	3966833 ± 10799	4437810 ± 10887	3939308 ± 10344
A	0.0066	4065524 ± 10248	4400294 ± 11053	1453432 ± 6986	3964043 ± 10698	3968253 ± 10810	4446224 ± 10922	3976195 ± 10449
B	0.14	3500271 ± 9817	3984703 ±10699	1352015 ± 6840	3823433 ±10559	3866892 ± 10717	3909599 ± 10477	3733519 ± 10164
C	0.63	2573085 ± 8851	3119818 ± 9784	1130030 ± 6430	2915302 ± 9562	2974933 ± 9700	2984742 ± 9518	2632864 ± 9000
D	1.68	1768409 ± 7664	2221614 ± 8536	880324 ± 5871	2117005 ± 8401	2187999 ± 8562	2085272 ± 8266	1846453 ± 7839
E	3.47	1082871 ± 6332	1397867 ± 7087	600559 ± 5118	1347702 ± 6996	1415669 ± 7164	1281835 ± 6806	1154308 ± 6514
F	6.0	601557 ± 5108	793964 ± 5695	376929 ± 4395	778816 ± 5661	827300 ± 5802	724986 ± 5475	648054 ± 5255
G	9.26	355249 ± 4287	459243 ± 4674	242690 ± 3862	446767 ± 4637	479826 ± 4761	420824 ± 4536	384151 ± 4406
H	13.0	197885 ± 3666	243962 ± 3873	149512 ± 3453	247201 ± 3891	257303 ± 3942	228053 ± 3804	206460 ± 3711
I	17.0	129367 ± 3348	154776 ± 3474	109501 ± 3253	150655 ± 3458	163010 ± 3523	148061 ± 3440	128637 ± 3345
J	21.1	98011 ± 3191	110760 ± 3246	86646 ± 3131	105864 ± 3232	110547 ± 3257	107479 ± 3239	96344 ± 3183

TABLE B.1: Experimental detector responses for each filter and material calculated from the spectra in Figures B.1-B.14.

Appendix C

Experiment reconstruction data

This appendix gives the numerical values for the Tikhonov reconstructions in all channels for HDPE, POM, PVC, PVDF and PTFE experimental data. All data is shown in Table C.1. The data is displayed in the main text in Section 7.4 Figure 7.3. The C3 and C9 values used in the analysis are given in the main text in Table 7.5 and Table 7.4.

Energy, keV	Counts				
	HDPE	POM	PVC	PVDF	PTFE
0-5	996 ± 88	494 ± 63	98 ± 15	119 ± 78	0 ± 85
5-10	26962 ± 1918	14143 ± 1411	2781 ± 346	8109 ± 1026	5865 ± 1098
10-15	48412 ± 1277	32488 ± 1092	6424 ± 330	21821 ± 1036	19888 ± 1093
15-20	50811 ± 841	43519 ± 720	9488 ± 244	34564 ± 648	32837 ± 681
20-25	43003 ± 644	45143 ± 531	1305 ± 172	41833 ± 497	40741 ± 534
25-30	33223 ± 447	40450 ± 400	11556 ± 139	41414 ± 402	41383 ± 427
30-35	23491 ± 332	31794 ± 314	10325 ± 119	34609 ± 316	35474 ± 334
35-40	14468 ± 279	21003 ± 239	8062 ± 86	23854 ± 229	25039 ± 246
40-45	6369 ± 156	9444 ± 136	5264 ± 54	11288 ± 133	12222 ± 143
45-50	0 ± 217	0 ± 206	2290 ± 96	0 ± 212	0 ± 226

Table C.1: Spectrum reconstruction data for HDPE, POM, PVC, PVDF and PTFE..

This page is intentionally left blank.

Bibliography

[1] B. C. Towe and A. M. Jacobs. X-ray backscatter imaging. *IEEE Transactions on Biomedical Engineering*, 28(9), 1981.

[2] R. S. Holt, M. J. Cooper, and D. F. Jackson. Gamma-ray scattering techniques for non-destructive testing and imaging. *Nuclear Instruments and Methods in Physics Research*, 221:98–104, 1984.

[3] R. D. Speller and J. A. Horrocks. Photon scattering - a 'new' source of information in medicine and biology? *Physics in Medicine and Biology*, 36(1):1–6, 1991.

[4] W. L. Dunn and A. M. Yacout. Corrosion detection in aircraft by x-ray backscatter methods. *Applied Radiation and Isotopes*, 53:625–632, 2000.

[5] S. Kolkoori, N. Wrobel, U. Zscherpel, and U. Ewert. A new X-ray backscatter imaging technique for non-destructive testing of aerospace materials. *NDT&E international*, 70:41–52, 2015.

[6] D. O'Flynn, C. Crews, N. Fox, B. P. Allen, M. Sammons, and R. D. Speller. X-ray backscatter sensing of defects in carbon fibre composite materials. In *Proceedings of SPIE*, 2017.

[7] M. Spannuth, M. Esmaeili, S. Gunn, D. M. Ponce-Marquez, H. Torsteinsen, and A. Voll. X-ray backscatter imaging in an oil well. In *Society of Petroleum Engineers Annual Technical Conference and Exhibition*, 2014.

[8] A. Balamesh, M. Salloum, and S. Abdul-Majid. Feasibility of a new moving collimator for industrial backscatter imaging. *Research in Nondestructive Evaluation*, 29(3):143–155, 2017.

[9] J. Callerame. X-ray backscatter imaging: Photography through barriers. *Powder Diffraction*, 21(2):132–135, 2006.

[10] D-C. Dinca, J. R. Schubert, and J. Callerame. X-ray backscatter imaging. In *Proceedings of SPIE 6945*, 2008.

[11] G. Zentai. X-ray imaging for homeland security, 2008. IEEE International Workshop on Imaging Systems and Techniques - IST 2008, Chania, Greece September 10-12 2008.

[12] Rapiscan Systems and AS&E. Mini Z - Handheld Z backscatter imaging system for detecting drugs and contraband. Online, 2021. Available at https://www.rapiscan-ase.com/products/handheld-inspection/mini-z-screening-system Accessed: 11/08/2021.

[13] Rapiscan Systems and AS&E. Effective, non-destructive vehicle searches - how to avoid unneccessary destruction when searching for drugs and currency, 2020. Available at https://info.rapiscan-ase.com/drug-interdiction-damage-control Accessed: 18/08/2020.

[14] E. J. Morton and A. F. Kotowski. Mobile imaging system and method for detection of contraband, 2018. US Patent No. US9958569B2.

[15] N. Faderl. Fast decay solid-state scintillators for high-speed x-ray imaging. *Proceedings of SPIE - Electro-Optical and Infrared Systems: Technology and Applications XVI*, 11159, 2019.

[16] A. S. Lalleman, G. Ferrand, B. Rosse, Isabelle Thfoin, Rene Wrobel, J. Tabary, N. B. Pierron, F. Mougel, C. Paulus, and L. Verger. A dual X-ray backscatter system for detecting explosives: Image and discrimination of a suspicious content. *IEEE Nuclear Science Symposium Conference Record*, 2011.

[17] C. Paulus, J. Tabary, N. Billon Pierron, J.-M. Dinten, E. Fabiani, F. Mathy, F. Mougel, J. Rinkel, and L. Verger. A multi-energy X-ray backscatter system for explosives detection. *Journal of Instrumentation*, 3, 2013.

[18] L. Verger, E. Gros d'Aillon, O. Monnet, G. Montémont, and B. Pelliciari. New trends in gamma-ray imaging with CdZnTe/CdTe at CEA-Leti. *Nuclear Instruments and Methods in Physics Research*, 571:33–43, 2007.

[19] S. Del Sordo, L. Abbene, E. Caroli, A. M. Mancini, A. Zappettini, and P. Ubertini. Progress in the development of CdTe and CdZnTe semiconductor radiation detectors for astrophysical and medical applications. *Sensors*, 9:3491–3526, 2009.

[20] A. Frank, G. Geus, and P. Schall. X-ray detection system, 2001. European Patent Office Patent No. EP1186909A2.

[21] R. D. Macdonald. Design and implementation of a dual-energy x-ray imaging system for organic material detection in an airport security application. In *Proceedings of SPIE*, pages 31–41, 2001.

[22] V. Rebuffel, J. Rinkel, J. Tabary, and L. Verger. New perspectives of X-ray techniques for explosives detection based on CdTe/CdZnTe spectometric detectors. *Journal of Instrumentation*, 8, 2013.

[23] M. Myronakis, P. Huber, M. Lehmann, R. Fueglistaller, M. Jacobson, Y-H. Hu, P. Baturin, A. Wang, M. Shi, T. Harris, D. Morf, and R. Berbeco. Low-dose megavoltage cone-beam computed tomography using a novel multi-layer imager (MLI). *Medical Physics*, 47(4), 2020.

[24] I. Kanno, S. Maetaki, H. Aoki, S. Nomiya, and H. Onabe. Low exposure X-ray transmission measurements for contrast media detection with filtered X-rays. *Journal of Nuclear Science and Technology*, 40(7):457–463, 2003.

[25] I. Kanno, R. Imamura, K. Mikami, A. Uesaka, M. Hashimoto, M. Ohtaka, K. Ara, S. Nomiya, and H. Onabe. A current-mode detector for unfolding x-ray energy distribution. *Journal of Nuclear Science and Technology*, 45(11):1165–1170, 2008.

[26] I. Kanno, Y. Yamashita, E. Kanai, T. Ogawa, and K. Shinsho. Two-dimensional "transXend" detector for third-generation energy-resolved computed tomography. *Journal of Nuclear Science and Technology*, 53(2):258–262, 2016.

[27] T-H. Tsai, T. Hamaguchi, H. Iramina, M. Nakamura, and I. Kanno. Filter-based energy-resolved X-ray computed tomography with a clinical imager. *Journal of Nuclear Science and Technology*, 56(2):210–220, 2019.

[28] T-H. Tsai, T. Hamaguchi, and I. Kanno. Performance improvement of the filter-type "transXend" energy-resolving detector by considering noise sensitivity. *Journal of Nuclear Science and Technology*, 55(6):663–371, 2018.

[29] Y. Maruyama, T. Hamaguchi, T-H. Tsai, and I. Kanno. Response function estimation with fine energy bins for the energy-resolved computed tomography using a transXend detector. *Journal of Nuclear Science and Technology*, 55(2):199–208, 2018.

[30] T. M. Buzug. *Computed Tomography: From Photon Statistics to Modern Cone-Beam CT*. Springer, 2008.

[31] C. A. Macdonald. *An introduction to x-ray physics, optics and applications*. Princeton University Press, 2017.

[32] W. J. Duffin. *Electricity and Magnetism*. McGraw-Hill Book Company, 4th edition, 1990.

[33] H. A. Kramers. On the theory of x-ray absorption and of the continuous x-ray spectrum. *Philosphical Magazine*, 46, 1923.

[34] A. Thompson, D. Attwood, E. Gullikson, M. Howells, K. J. Kim, J. Kirz, J. Kortright, I. Lindau, Y Liu, R. Pianetta, A. Robinson, J. Scofield, J. Underwood, D. Vaughan, G Williams, and H. Winick. *X-ray Data Booklet Table 1-3*. Lawrence Berkley National Laboratory, 2011.

[35] Amptek Inc. Choosing the anode material. https://www.amptek.com/-/media/ametekamptek/documents/products/choosing the anode material in an x-ray tube.pdf (Accessed: 16/07/2020).

[36] N. Langhoff, A. Simionovici, V. Arkadiev, T Čechák W. Knüpfer, and J. Leonhardt. *X-ray sources*, chapter 2. Springer, 2006.

[37] A. Górecka-Drazga. Miniature x-ray sources. *Journal of Microelectromechanical systems*, 26(1), 2017.

[38] Amptek Inc. Mini-X X-ray tube system for XRF, 2018. http://amptek.com/products/mini-x-ray-tube/2016.

[39] C. Turner, A. Reyes, H. K. Pew, M. W. Lund, M. Lines, P. Moody, and S. Voronov. Mobile miniature x-ray source, 2001. US Patent No. 6661876B2.

[40] G. F. Knoll. *Radiation Detection and Measurement*. John Wiley and Sons, 3rd edition, 2000.

[41] K. S. Krane. *Introductory Nuclear Physics*. John Wiley and Sons, 2nd edition, 1998.

[42] M. J. Cooper, P. E. Mijnarends, N. Shiotani, N. Sakai, and A. Bansil. *X-ray Compton scattering*. Oxford Science Publications, 2004.

[43] D. V. Rao, R. Cesareo, A. Brunetti, G. E. Gigante, T. Akatsuka, T. Takeda, and Y. Itai. Doppler broadening calculations of compton scattering for molecules, plastics and tissues, and a few biological materials in the x-ray region: An analysis in terms of compton broadening and geometrical energy broadening. *Journal of Physical and Chemical Reference Data*, 33(3):627, 2004.

[44] E. M. A. Hussein. *Radiation Mechanics Principles and Practice*, chapter 3, pages 42–53. Elsevier, 2007.

[45] O. Klein and Y. Nishina. Über die Streuung von Strahlung durch freie Elektronen nach der neuen relativistischen Quantendynamik von Dirac. *Zeitschrift für Physik*, 52:853–868, 1929.

[46] E. Storm and H. I Israel. Photon cross sections from 1 kev to 100 MeV for elements Z=1 to Z=100. *Atomic Data and Nuclear Data Tables*, 7(6):656–681, 1970.

[47] D. T. Cromer and J. B. Mann. Compton scattering factors for spherically symmetric free atoms. *Journal of Chemical Physics*, 47, 1967.

[48] L. B. Mendelsohn and B. J. Bloch. Atomic L-shell Compton profiles: Calculations for atoms and comparison with experiment. *Physical Review A*, 12, 1975.

[49] R. A. Bonham. Calculation of total inelastic x-ray scattering cross sections. *Physical Review A*, 23, 1981.

[50] R. Ribberfors and K.-F. Berggren. Incoherent x-ray scattering functions and cross sections by means of a pocket calculator. *Physical Review A*, 26, 1982.

[51] J. H. Hubbell, Wm. J. Veigele, E. A. Briggs, R. T. Brown, D. T. Cromer, and R. J. Howerton. Erratum: Atomic form factors, incoherent scattering functions and photon scattering cross sections. *Journal of Physical and Chemical Reference Data*, 6, 1977.

[52] M. J. Berger, J. H. Hubbell, S. M. Seltzer, J. Chang, J. S. Coursey, R. Sukumar, D. S. Zucker, and K. Olsen. XCOM: Photon cross sections database, 2010. Available: http://physics.nist.gov/xcom.

[53] A. Beer. *Grundriss des photometrischen Calcüles*. Vieweg, 1854.

[54] R. Nowotny. XMuDat: Photon attenuation data on PC, 1998. Technical Report number IAEA-NDS-195, International Atomic Energy Agency, Vienna, Austria.

[55] V. P. Singh, N. M. Badiger, and N. Kucuk. Determination of effective atomic numbers using different methods for some low-Z materials. *Journal of Nuclear Chemistry*, 2014, 2014.

[56] A. H. El-Kateb, R. A. M. Rizk, and A. M. Abdul-Kader. Determination of atomic cross-sections and effective atomic numbers for some alloys. *Annals of Nuclear Energy*, 27:1333–1343, 2000.

[57] A. Levet and Y Özdemir. Determination of effective atomic numbers, effective electron numbers, total atomic cross-sections and buildup factor of some compounds for different radiation sources. *Radiation Physics and Chemistry*, 130:171–176, 2017.

[58] S. R. Manohara, S. M. Hanagodimath, K. S. Thind, and L. Gerward. On the effective atomic number and electron density: A comprehensive set of formula for all types of materials and energies above 1 keV. *Nuclear Instruments and Methods in Physics Research B*, 266:3906–3912, 2008.

[59] A. Brambilla, A. Gorecki, A. Potop, C. Paulus, and L. Verger. Basis material decomposition method for material discrimination with a new spectroscopic x-ray imaging detector. *Journal of Instrumentation*, 12, 2017.

[60] R. Redus, A. Huber, J. Pantazis, T. Pantazis, and D. Sperry. Design and performance of the X-123 compact X-ray and gamma-ray spectroscopy system. In *IEEE Nuclear Science Symposium Conference Record*, 2006.

[61] R. H. Redus, J. A. Pantazis, T. J. Pantazis, A. C. Huber, and B. J. Cross. Characterization of cdte detectors for quantitive x-ray spectroscopy. *IEEE Transactions on Nuclear Science*, 56(4), 2009.

[62] O. Limousin. New trends in CdTe and CdZnTe detectors for X- and gamma-ray applications. *Nuclear Instruments and Methods in Physics Research A*, 504:24–37, 2003.

[63] S. Miyajima. Thin CdTe detector in diagnostic x-ray spectroscopy. *Medical Physics*, 30(5), 2003.

[64] J. Rinkel, G. Beldjoudi, V. Rebuffel, C. Boudou, P Ouvrier-Buffet, G. Gonon, L. Verger, and A. Brambilla. Experimental evaulation of material identification methods with CdTe X-ray spectrometric detector. *IEEE Transactions on Nuclear Science*, 58(5), 2011.

[65] L. Lawson. Flux maximisation techniques for Compton backscatter depth profilometry. *Journal of X-ray Science and Technology*, 4:18–36, 1993.

[66] H. Toyama, A. Higa, M. Yamazato, T. Maehama, R. Ohno, and M. Toguchi. Quantitative analysis of polarization phenomena in CdTe radiation detectors. *Japanese Journal of Applied Physics*, 45(11), 2006.

[67] R. Redus. Charge trapping in XR-100T-CdTe and -CZT detectors - Application note ANCZT-2 Rev. 3, 2007.

[68] G. Gilmore and J. Hemmingway. *Practical gamma-ray spectroscopy*. John Wiley and Sons, 1995.

[69] J. B. Binks. *The Theory and Practice of Scintillation Counting*, volume 27. Pergamon Press, 1964.

[70] A. Arodzero, J. Callerame, D-C. Dinca, R. Sud, L. Grodzins, M. Rommel, P. Rothschild, J. Schubert, M. Couture, J. M. Denker, and J. E. Everett. Hand-held x-ray detection system using wavelength shifting fiber-coupled scintillation detectors, 2019. United States Patent No. US 10209372.

[71] M. Procter. *Radiation detector technical reference manual*. Rapiscan Systems, 2012.

[72] A. Chalmers. Single-sided x-ray inspection of vehicles using AS&E's Z-Backscatter Van. In *Proceedings of SPIE 5199 - Penetrating Radiation Systems and Applications V*, 2003.

[73] M. Nikl. Scintillation detectors for x-rays. *Measurement science and technology*, 17:37–54, 2006.

[74] P. A. Rodnyi. *Physical processes in inorganic scintillators*, chapter 3. CRC Press, St. Petersburg, Russia, 1997.

[75] C. Michail, I. Valais, I. Seferis, N. Kalyvas, S. David, G. Fountos, and I. Kandarakis. Measurement of the luminescence properties of Gd2O2S:Pr,Ce,F powder scintillators under x-ray radiation. *Radiation Measurements*, 70:59–54, 2014.

[76] S. Das, J. Saini, and A. K. Dubey. Measurement of decay time constant of a plastic scintillator by a delayed coincidence method. In *Proceedings of the DAE-BRNS Symposium on Nuclear Physics*, volume 60, pages 1068–1069, 2015.

[77] L. Grodzins and P. J. Rothschild. X-ray backscatter mobile inspection van, 2013. United States Patent No. 2013/0343520 A1.

[78] N. Carrington. Private communication, September 2019. Rapiscan Systems.

[79] Rapiscan Systems and AS&E. ZBV - Mobile Z backscatter cargo and vehicle screening system. Online, 2021. Available at https://www.rapiscan-ase.com/products/mobile/zbv-cargo-and-vehicle-screening Accessed: 11/08/2021.

[80] Rapiscan Systems and AS&E. Z portal for passenger vehicles - Multi-view, multi-technology, cargo and vehicle screening system. Online, 2021. Avaible at https://www.rapiscan-ase.com/products/portal/z-portal-for-passenger-vehicle-screening Accessed: 11/08/2021.

[81] Rapiscan Systems and AS&E. Z portal for trucks and cargo - Multi-view, multi-technology, cargo and vehicle screening system. Online, 2021. Available at: https://www.rapiscan-ase.com/products/portal/z-portal-for-trucks-cargo-screening Accessed: 11/08/2021.

[82] Rapiscan Systems and AS&E. EAGLE P60 ZBx - Advanced, multi-technology, multi-view, drive-through portal. Online, 2021. Available at https://www.rapiscan-ase.com/products/portal/eagle-p60-zbx-multi-technology-cargo-inspection Accessed: 11/08/2021.

[83] Rapiscan Systems and AS&E. EAGLE M60 ZBx - Advanced, mobile inspection system with combinational imaging. Online, 2021. Available at https://www.rapiscan-ase.com/products/mobile/eagle-m60-zbx-multi-technology-cargo-inspection Accessed: 11/08/2021.

[84] M. Dabas, A. Tabbagh, and J Tabbagh. 3-D inversion in subsurface electrical surveying. *Geophysical Journal International*, 119(3):975–990, 1994.

[85] P. C. Hansen, J. G. Nagy, and D. P. O'Leary. *Deblurring Images: Matricies, Spectra and Filtering*. Society for Industrial and Applied Mathematics, 2006.

[86] D. Margalit and J. Rabinoff. *Interactive Linear Algebra*. Georgia Institute of Technology, 2019.

[87] A. N. Tikhonov and V. Y. Arsenin. Solutions of ill-posed problems. *Society of Industrial and Applied Mathematics Review*, 21(2), 1979.

[88] R. C. Aster, B Borchers, and C. H. Thurber. *Parameter Estimation and Inverse Problems*, volume 90. International Geophysics, 2005.

[89] P. C. Hansen. *Discrete Inverse Problems: Fundamentals of Algorithms*. Society for Industrial and Applied Mathematics, 2010.

[90] P. C. Hansen. *Rank-Deficient and Discrete Ill-Posed Problems: Numerical Aspects of Linear Inversion*. Society for Industrial and Applied Mathematics, 1998.

[91] N. C. Nguyen. A note on tikhonov regularization of linear ill-posed problems. http://www.mit.edu/ cuongng/Site/Publication_files/Tikhonov06.pdf (Accessed 02/06/2020).

[92] O. Scherzer. The use of Morozov's discrepancy princple for Tikhonov regularization for solving nonlinear ill-posed problems. *Computing*, 51:46–60, 1993.

[93] J. L. Castellanos, S. Gómez, and V Guerra. The triangle method for finding the corner of the L-curve. *Applied Numerical Mathematics*, 43(4):359–373, 2002.

[94] I. Kanno and T. Kuroyama. Estimation of the sugar content of fruit by an energy-resolved computed tomography using a material decomposition method. *Journal of Nuclear Science and Technology*, 58(5), 2021.

[95] I. Kanno and K. Yamada. Energy-resolved computed tomography with a response-function-less transxend detector. *Journal of Nuclear Science and Technology*, 2021. Published online on 20th July 2021.

[96] R. Redus. CdTe measurement of x-ray tube spectra: Escape events - Application note ANCDTE1 Rev A1, 2008.

[97] A. Querol, S. Gallardo, J. Ródenas, and G. Verdú. Application of Tikhonov and MTSVD methods to unfold experimental X-ray spectra in the radiodiagnostic energy range. In *32nd Annual Internation Conference of the IEEE EMBS*, 2010.

[98] A. Querol, S. Gallardo, J. Ródenas, and G. Verdú. Application of the MTSVD and Tikhonov unfolding methods for reconstruction of primary X-ray spectra of

mammography equipment with silicon detector. *Nuclear Technology*, 175:63–72, 2011.

[99] M. R. Hestenes and E. Stiefel. Methods of conjugate gradients for solving linear systems. *Journal of Research of the National Bureau of Standards*, pages 409–436, 1952.

[100] F. Natterer and F. Wübbeling. *Mathematical Methods in Image Reconstruction*. Society for Industrial and Applied Mathematics, 2001.

[101] L. A. Feldkamp, L. C. Davis, and J. W. Kress. Practical cone-beam algorithm. *Journal of the Optical Society of America A*, 1(6):612–619, 1984.

[102] L. Landweber. An iteration formula for Fredholm integral equations of the first kind. *American Journal of Mathematics*, 73(3):651–624, 1951.

[103] Amptek Inc. *Complete x-ray and gamma-ray spectrometer*, 2019. http://www.amptek.com/pdf/x123cdte.pdf.

[104] Amptek Inc. DPPMCA display and acquisition software, 2019. http://amptek.com/products/dpp-mca-display-acquisition-software.

[105] Amptek Inc. Mini-X control software v1.0.0.10 - updated Feb. 25 2016, 2016. Available at: https://www.amptek.com/internal-products/obsolete-products/mini-x-x-ray-tube-software (Accessed 16/03/2021).

[106] Velmex Inc. BiSlide. https://www.velmex.com/Products/BiSlide/ (Accessed 14/09/2021).

[107] D C Radford. Background subtraction from in-beam HPGe coincidence data sets. *Nuclear Instruments and Methods in Physics Research*, 361:306–316, July 1995.

[108] M.-M. Bé, V. Chisté, C. Dulieu, E. Browne, V. Chechev, N. Kuzmenko, R. Helmer, A. Nichols, E. Schönfeld, and R. Dersch. Table of Radionuclides (Vol. 1-A = 1 to 150): 241Am, 2004. Available at https://ftp.cdc.gov/pub/FOIAREQ/168372-A45.pdf (Accessed 19/01/2021).

[109] M.-M. Bé, V. Chisté, C. Dulieu, E. Browne, V. Chechev, N. Kuzmenko, R. Helmer, A. Nichols, E. Schönfeld, and R. Dersch. Table of Radionuclides (Vol. 1-A = 1 to 150): 133Be, 2004. Available at https://ftp.cdc.gov/pub/FOIAREQ/168372-A45.pdf (Accessed 19/01/2021).

[110] M. O. Krause and J. H. Oliver. Natural widths of atomic K and L levels, Kalpha x-ray lines and several KLL Auger lines. *Journal of Physical and Chemical Reference Data*, 8(2):329–338, 1979.

[111] J. Allison, K. Amako, J. Apostolakis, P. Arce, M. Asai, T. Aso, E. Bagli, A. Bagulya, S. Banerjee, G. Barrand, B.R. Beck, A.G. Bogdanov, D. Brandt, J.M.C. Brown, H. Burkhardt, Ph. Canal, D. Cano-Ott, S. Chauvie, K. Cho, G.A.P. Cirrone, G. Cooperman, M.A. Cortés-Giraldo, G. Cosmo, G. Cuttone, G. Depaola, L. Desorgher, X. Dong, A. Dotti, V.D. Elvira, G. Folger, Z. Francis, A. Galoyan, L. Garnier, M. Gayer, K.L. Genser, V.M. Grichine, S. Guatelli, P. Guèye, P. Gumplinger, A.S. Howard, I. Hřivnáčová, S. Hwang, S. Incerti, A. Ivanchenko, V.N. Ivanchenko, F.W. Jones, S.Y. Jun, P. Kaitaniemi, N. Karakatsanis, M. Karamitros, M. Kelsey, A. Kimura, T. Koi, H. Kurashige, A. Lechner, S.B. Lee, F. Longo, M. Maire, D. Mancusi, A. Mantero, E. Mendoza, B. Morgan, K. Murakami, T. Nikitina, L. Pandola, P. Paprocki, J. Perl, I. Petrović, M.G. Pia, W. Pokorski, J.M. Quesada, M. Raine, M.A. Reis, A. Ribon, A. Ristić Fira, F. Romano, G. Russo, G. Santin, T. Sasaki, D. Sawkey, J.I. Shin, I.I. Strakovsky, A. Taborda, S. Tanaka, B. Tomé, T. Toshito, H.N. Tran, P.R. Truscott, L. Urban, V. Uzhinsky, J.M. Verbeke, M. Verderi, B.L. Wendt, H. Wenzel, D.H. Wright, D.M. Wright, T. Yamashita, J. Yarba, and H. Yoshida. Recent developments in Geant4. *Nucl. Instr. Meth. Phys. Res. A*, 835:186 – 225, 2016.

[112] E. J. Price. *Validation of clinical image quantification and dosimetry using 3D printed anthropomorphic phantoms*. PhD thesis, University of Manchester, 2019.

[113] N. Calvert. *Time-of-flight Compton scatter imaging for cargo security*. PhD thesis, University College London, 2016.

[114] N. Calvert, E. J. Morton, and R. D. Speller. Preliminary Monte Carlo simulations of linear accelerators in time-of-flight Compton scatter imaging for cargo security. *Crime Science*, 2(2), 2013.

[115] S. Huang, X. Wang, Y. Chen, J. Xu, T. Tang, and B. Mu. Modeling and quantitive analysis of x-ray transmission and backscatter imaging aimed at security inspection. *Optics Express*, 27, 2019.

[116] Geant4 collaboration. Low energy electromagnetic physics - Livermore, 2020. Available at https://geant4.web.cern.ch/node/1619 (Accessed 20/09/2021).

[117] G.A.P. Cirrone, G. Cuttone, F. Di Rosa, L. Pandola, F. Romano, and Q. Zhang. Validation of the Geant4 electromagnetic photon cross-sections for elements and compounds. *Nuclear Instruments and Methods in Physics Research Section A: Accelerators, Spectrometers, Detectors and Associated Equipment*, 618:315–322, 2010.

[118] V. Ivanchenko, J. Apostolakis, A. Bagulya, H. Ben Abdelouahed, R. Black, A. Bogdanov, H. Burkhard, S. Chauvie, P. Cirrone, G. Cuttone, G. Depaola, F. Rosa,

Z. Francis, V. Grichine, P. Gumplinger, P. Gueye, S. Incerti, A. Ivanchenko, and C Zacharatou. Recent improvements in Geant4 electromagnetic physics models and interfaces. *Progress in Nuclear Science and Technology*, 2:898–903, 10 2011.

[119] J. Apostolakis, S. Giani, M. Maire, P. Nieminen, M. Pia, and L. Urban. Geant4 low energy electromagnetic models for electrons and photons. *European Organisation for Nuclear Research*, 11 1999.

[120] Geant4 collaboration. GEANT4 Materials Database, 2021. Available at https://geant4-userdoc.web.cern.ch/UsersGuides/ForApplicationDeveloper/html/Appendix/materialNames.html (Accessed 25/09/2021).

[121] D. Thain, T. Tannenbaum, and M. Linvy. Distributed computing in practice: The Condor experience. *Concurrency and Computation: Practice and Experience*, 17:323–356, 2005.

[122] T. Pantazis, J. Pantazis, A. Huber, and R. Redus. The historical development of the thermoelectrically cooled X-ray detector and its impact on the portable and hand-held XRF industries (February 2009). *X-ray spectrometry*, pages 90–97, 2010.

[123] A. Basit, M. R. Siddique, S. M. Mirza, S. U. Rehman, and M. Y. Hamza. Study of CdTe detection efficiency for medical applications using Geant4-based stochastic simulations. *Journal of Radiological Protection*, 38:1483–1500, 2018.

[124] J. B Kortright and A. C. Thompson. X-ray data booklet: Section 2.1 X-ray emission energies, 2011. Available at https://xdb.lbl.gov/Section1/Sec_1-2.html (Accessed 15th July 2020).

[125] PVC Forum South East Europe. Stabilisers, 2021. http://www.seepvcforum.com/en/content/17-stabilisers (Accessed 16/09/2021).

[126] Plastics Europe. Polyolefins - about plastics, 2021. Availble at https://www.plasticseurope.org/en/about-plastics/what-are-plastics/large-family/polyolefins (Accessed 16/07/2021).

[127] P. Rothschild, J. Schubert, W. J. Baukus, W. Wade Sapp Jr, R. Schueller, J. Callerame, and W. R. Cason. X-ray inspection based on scatter detection, 2009. United States Patent No. 7551715 B2.

[128] E. L. Nickoloff and H. L. Berman. Factors affecting x-ray spectra. *Radiographics*, 13(6), 1993.

[129] timeanddate.com. Past weather in Stoke-on-Trent, England, United Kingdom - February 2020, 2020. Available at https://www.timeanddate.com/weather/uk/stoke-on-trent/historic?month=2&year=2020 (Accessed 29/04/2021).

[130] S. Kolkoori, N. Wrobel, K. Osterloch, U. Zscherpel, and U. Ewert. Novel X-ray backscatter technique for detection of dangerous materials: Application to aviation and port security. *Journal of Instrumentation*, 8, 2013.

[131] J. Xu, X. Wang, B. Mu, Q. Zhan, Q. Xie, Y Li, Y Chen, and Y. He. A novel biometric X-ray backscatter inspection of dangerous materials based on a lobster-eye objective. *Proceedings of SPIE Security + Defense, Edinburgh, UK*, 2016.

[132] B. Yang, X. Wang, H. Shen, J. Xu, K. Xiong, and B. Mu. Design of x-ray backscatter imaging system for vehicle detection. *Proceedings of SPIE Security + Defense, Online*, 2020.

[133] R. Faezeh, A. S. Sadat, B. Esmaiel, and D. M. Vahid. Comparison of the time behaviour in the separation of light and heavy materials in X-ray backscattered method as a diagnostic tool in inspection. *Nuclear Instruments and Methods in Physics Research A*, 812:86–91, 2016.

[134] P. Rothschild, L. Grodzins, P. Bradshaw, and L. Wainwright. Hand-held x-ray backscatter imaging device, 2013. United States Patent No. 2013/0195248 A1.

[135] E. Grant, J. Lee, and P. Leung. Handheld backscatter imager, 2015. United States Design Patent No. US D724216 S.

[136] E. J. Morton. Multiple energy detector, 2020. United States Patent No. 10578752.

[137] P. Rothschild and H. D Kellogg. System and kit for x-ray backscatter imaging with removable detector, 2019. World Intellectual Property Organization - International Publication Number WO 2019/152900 A1.

[138] A. Arodzero, J. Callerame, D-C. Dinca, R. Sud, L. Grodzins, M. Rommel, P. Rothschild, and J. Schubert. Spectral discrimination using wavelength-shifting filber-coupled scintillation detectors, 2017. United States Patent No. US 9658343 B2.

[139] E. J. Morton. Time of flight backscatter imaging system, 2013. United States Patent No. 8582720 B2.

[140] N. Calvert, M. M. Betcke, A. N. Deacon, A. J. Gleeson, C. Hill, P. A. McIntosh, L. O. Mitchell, E. J. Morton, J. Ollier, M. G. Procter, and R. D. Speller. Feasibility study of time-of-flight Compton scatter imaging using picosecond length X-ray pulses. *IEEE Transactions on Nuclear Science*, 61(6):3702 – 3710, 2014.

[141] Y. S. Ham and C. F. Poranski. Method and apparatus for determing both density and atomic number of a material composition using Compton scattering, 1996. Navy Case No. 76676.

[142] A. Yoneyama, M. Kawamoto, and R. Baba. Novel Zeff imaging method for deep internal areas using back-scattered X-rays. *Nature Reasearch - Scientific Reports*, 9, 2019.

[143] M. Donativi, S. Quarta, R. Cesareo, and A. Castellano. Rayleigh to Compton ratio with monochromatic radiation from an X-ray tube (preliminary results). *Nuclear Instruments and Methods in Physics Research B*, 264:189–193, 2007.

[144] F. Li, Z. Liu, T. Sun, C. Yang, Y. Sun, W. Sun, J. He, and X. Ding. A confocal three-dimensional micro X-ray scattering technology based on Rayleigh to Compton ratio for identifying materials with similar density and different weight percentages of low-Z elements. *Radiation Physics and Chemistry*, 112:163–168, 2015.

[145] A. Bjorck. *Numerical Methods for Least Squares Problems*. Society for Industrial and Applied Mathematics, 1996.

[146] A. Mileto, L. S. Guimaraes, C. H. McCollough, J. G. Fletcher, and L. Yu. State of the art in abdominal CT: The limits of iterative reconstruction algorithms. *Radiology*, 293(3), 2019.

[147] NumPy. API reference - numpy.linalg.svd, 2021. https://numpy.org/doc/stable/reference/generated/numpy.linalg.svd.html Accessed 28/07/21.

[148] Amptek Inc. XRS-FP quantitative XRF analysis software, 2021. https://www.amptek.com/internal-products/obsolete-products/xrs-fp-quantitative-xrf-analysis-software Accessed 28/07/21.

[149] M. Moralles, D.A.B Bonifacio, M. Bottaro, and M.A.G Pereria. Monte Carlo and least-squares methods applied in unfolding of X-ray spectra measured with Cadmium Telluride detectors. *Nuclear Instruments and Methods in Physics Research A*, 580:270 –273, 2007.

[150] M. M. Nasseri. Determination of tungsten target parameters for transmisison X-ray tube: A simulation study using GEANT4. *Nuclear Engineering and Technology*, pages 795–798, 2016.

[151] G. Poludniowski, G. Landry, F. DeBlois, P. M. Evans, and F. Verhaegen. SpekCalc: A program to calculate photon spectra from tungsten anode x-ray tubes. *Physics in Medicine and Biology*, 54:433–438, 2009.

[152] V. Rackwitz, U. Panne, and V-D Hodoroaba. Calculation of X-ray tube spectra by means of photon generation yields and a modified Kramers background for side-window X-ray tubes. *X-Ray Spectrom*, 41:264–272, 2012.

[153] M. S. Prasad and D. C. Joy. Measurements of absolute x-ray generation efficiency for selected K, L and M-Lines. *Scanning*, 25:210–215, 2003.

[154] G. H. McCall. Calculation of x-ray bremsstrahlung and characteristic line emission produced by a maxwellian electron distribution. *Journal of Physics D: Applied Physics*, 15:823–831, 1982.

[155] T. Jensen and J. N. Gray. Material thickness measurements using Compton backscatter. *Review of Progress in Quantitative Nondestructive Evaluation*, 12, 1993.

[156] L. A. Lehmann, R. E. Alvarez, A. Macovski, W. R. Brody, N. J. Pelc, S. J. Riederer, and A. L. Hall. Generalized image combinations in dual KVP digital radiography. *Medical Physics*, 8(5):659–667, 1981.

[157] Hamamatsu Photonics. Photomultiplier tubes R1307, R1307-1 - For scintillation counting, especially for gamma camera 76mm (3 inch) diameter, 8 stage, head-on type bialkali photocathode photomultiplier tubes, 2021. Availble at https://www.hamamatsu.com/eu/en/product/type/R1307-01/index.html Accessed 18/08/2021.

[158] K. Weinfurther, J. Mattingly, E. Brubaker, and J. Steel. Model-based design evaluation of a compact, high-efficiency neutron scatter camera. *Nuclear Instruments and Methods in Physics Research A: Accelerators, Spectrometers, Detectors and Associated Equipment*, 883:115–135, 2018.